

Stefan Rößler

Magnetic imaging of static and dynamic states in systems of reduced dimensions

Magnetic imaging of static and dynamic states in systems of reduced dimensions

Dissertation
zur Erlangung des Doktorgrades
des Fachbereichs Physik
der Universität Hamburg

vorgelegt von
Stefan Rößler

Hamburg
2014

Gutachter der Dissertation:

Prof. Dr. Hans Peter Oepen
Universität Hamburg, Germany

Prof. Dr. André Thiaville
Universite Paris-Sud & CNRS, France

Gutachter der Disputation:

Prof. Dr. Hans Peter Oepen
Universität Hamburg, Germany

Prof. Dr. Kornelius Nielsch
Universität Hamburg, Germany

Datum der Disputation:

7.1.2015

Vorsitzender des Prüfungsausschusses:

Prof. Dr. Michael Rübhausen

Vorsitzende des Promotionsausschusses:

Prof. Dr. Daniela Pfannkuche

**Dekan der Fakultät für Mathematik,
Informatik und Naturwissenschaften:**

Prof. Dr. Heinrich Graener

Berichte aus der Physik

Stefan Rößler

**Magnetic imaging of static and dynamic states
in systems of reduced dimensions**

Shaker Verlag
Aachen 2015

Bibliographic information published by the Deutsche Nationalbibliothek

The Deutsche Nationalbibliothek lists this publication in the Deutsche Nationalbibliografie; detailed bibliographic data are available in the Internet at <http://dnb.d-nb.de>.

Zugl.: Hamburg, Univ., Diss., 2015

Copyright Shaker Verlag 2015

All rights reserved. No part of this publication may be reproduced, stored in a retrieval system, or transmitted, in any form or by any means, electronic, mechanical, photocopying, recording or otherwise, without the prior permission of the publishers.

Printed in Germany.

ISBN 978-3-8440-3523-0

ISSN 0945-0963

Shaker Verlag GmbH • P.O. BOX 101818 • D-52018 Aachen

Phone: 0049/2407/9596-0 • Telefax: 0049/2407/9596-9

Internet: www.shaker.de • e-mail: info@shaker.de

Abstract

Within this thesis, static and dynamic states in magnetic systems of reduced dimensions are investigated by means of the advanced magnetic imaging technique “scanning electron microscopy with polarization analysis” (SEMPA). After a short introductory overview of the historical development of storage media, its current status is described with a focus on random-access memory (RAM). The basic concepts of modern non-volatile storage devices based on magnetism are introduced and the physical mechanisms behind the phenomena that are used to manipulate and access the data are discussed.

Magnetic imaging is a powerful, yet illustrative tool to further explore the physics behind these mechanisms. After a short overview of the history and current status of magnetic imaging techniques, the working principle of SEMPA is explained. The imaging capabilities of SEMPA are used to investigate the current-driven stationary displacement of a magnetic vortex core confined in a square permalloy element. The full set of spin-transfer torque parameters is obtained from the measurement. In the course of the investigation, the physical origin of the nonadiabatic contribution ($\beta = 0.12 \pm 0.02$) is explored. It is shown to consist of one component that depends on the intrinsic properties of the material (29 %) and one component that depends on the divergence of the magnetic texture (71 %).

A concept for enhancing the temporal resolution of SEMPA into the regime of one nanosecond is presented. The feasibility of the concept is proven by observing the gyration of a magnetic vortex core that is excited by a high-frequency field ($f = 70$ MHz). From the elliptic shape of the movement pattern, the resonance frequency of the square permalloy element that contains the vortex core is derived.

In another project of this thesis, the interplay between ferromagnetic and ferroelectric domain walls is investigated. In 20 nm thick $\text{Co}_{40}\text{Fe}_{40}\text{B}_{20}$ on BaTiO_3 , the ferromagnetic domain walls are pinned on top of the ferroelectric ones. Two types of magnetic 90° domain walls are identified: Charged walls are created after an external field was applied parallel to the ferroelectric domain walls. When the field is applied perpendicular to the ferroelectric domain walls, uncharged walls are created. The width of both wall types is compared with SEMPA. The width is found to be enhanced by 500 % for the charged walls (≈ 770 nm) compared to the uncharged walls (≈ 150 nm).

The thesis concludes with a theoretical chapter in which the uniaxial anisotropy is derived that emerges when a magnetic film is prepared on top of a rippled substrate. The strength of the anisotropy is calculated for an alignment of the magnetization along the hard in-plane axis, perpendicular to the ripple pattern. Two magnetic configurations are considered: In the wavy configuration, the local magnetization follows the ripple structure of the film. In the uniform configuration, a rigid magnetization is present. A thickness-dependent transition between both states is identified. The results are compared to experimental studies.

Kurzfassung

Im Rahmen dieser Arbeit werden statische und dynamische Zustände in magnetischen Systemen reduzierter Dimensionen mittels Rasterelektronenmikroskopie mit Polarisationsanalyse (SEMPA) untersucht. Zunächst wird ein kurzer einführender Überblick über die historische Entwicklung und den aktuellen Stand der magnetischen Speichermedien, mit einem Fokus auf „random-access memory“ (RAM), gegeben. Die grundlegenden Konzepte moderner, magnetischer, nichtflüchtiger Speichermedien werden eingeführt. Die physikalischen Mechanismen, die sich hinter den Phänomenen verbergen, welche verwendet werden um auf einzelne Bits zuzugreifen und sie zu manipulieren werden erläutert.

Die magnetische Bildgebung ist ein leistungsstarkes und dennoch illustratives Werkzeug, um die Physik hinter diesen Mechanismen weiter zu erforschen. Nach einem kurzen Überblick über die Geschichte und den aktuellen Stand der magnetischen Abbildungsverfahren wird die Funktionsweise des SEMPA erläutert. Die bildgebenden Fähigkeiten des SEMPA werden verwendet, um die stationäre Verschiebung einer magnetischen Wirbelstruktur, die in einem Quadrat aus Permalloy eingeschlossen ist, durch einen Gleichstrom zu untersuchen. Aus der Messung wird der volle Satz der „spin-transfer torque“ Parameter bestimmt. Im Zuge dieser Untersuchung wird der physikalische Ursprung des nichtadiabatischen Beitrages ($\beta = 0.12 \pm 0.02$) untersucht. Es wird gezeigt, dass dieser aus zwei Komponenten besteht: eine, die nur von den inneren Eigenschaften des Materials abhängt (29%) und eine, die von der Divergenz der magnetischen Textur bestimmt wird (71%).

Ein Konzept zur Verbesserung der Zeitauflösung des SEMPA in den Bereich von einer Nanosekunde wird vorgestellt. Die Zuverlässigkeit des Konzepts wird durch Beobachtung der Kreisbewegung eines von einem Hochfrequenzfeld (70MHz) angeregten magnetischen Wirbelkerns nachgewiesen. Aus der elliptischen Form des Bewegungsmusters wird die Resonanzfrequenz des magnetischen Quadrates abgeleitet, welches den Wirbelkern beinhaltet.

In einem weiteren Projekt dieser Arbeit wird das Wechselspiel zwischen ferromagnetischen und ferroelektrischen Domänenwänden untersucht. In 20 nm dickem $\text{Co}_{40}\text{Fe}_{40}\text{B}_{20}$ auf BaTiO_3 sind die ferromagnetischen Wände an die ferroelektrischen Wände gekoppelt. Zwei Arten von magnetischen 90° Domänenwänden werden in diesem System identifiziert: Geladene Wände entstehen, nachdem ein externes Magnetfeld parallel zu den ferroelektrischen Domänenwänden angelegt wird. Ungeladene Wände hingegen entstehen, wenn das Feld senkrecht zu den ferroelektrischen Domänenwänden angelegt wird. Die Breite der beiden Wandtypen wird mittels SEMPA verglichen und es zeigt sich, dass die geladenen Wände ($\approx 770\text{nm}$) um einen Faktor fünf breiter sind als die ungeladenen Wände ($\approx 150\text{nm}$).

Diese Arbeit schließt mit einem theoretischen Abschnitt. In diesem wird die uniaxiale Anisotropie abgeleitet, die entsteht, wenn ein magnetischer Film auf einem gewellten Substrat hergestellt wird. Die Stärke der Anisotropie wird für eine Ausrichtung der Magnetisierung entlang der harten Richtung innerhalb der Filmebene, senkrecht zu der Wellenstruktur, berechnet. Zwei magnetische Konfigurationen werden behandelt: In der welligen Konfiguration folgt die Magnetisierung der welligen Struktur des Filmes und in der gleichförmigen Konfiguration ist die Magnetisierung starr in eine Richtung gerichtet. Ein Schichtdicken-abhängiger Übergang zwischen beiden Konfigurationen wird hierbei identifiziert. Die Ergebnisse werden mit experimentellen Arbeiten verglichen.

Contents

1	Introduction	1
2	Magnetic Imaging	11
2.1	Historical Overview	11
2.2	Scanning Electron Microscopy with Polarization Analysis	13
2.2.1	Measuring the Spin Polarization of Secondary Electrons	14
2.2.2	SEMPA Imaging With a LEED Detector	16
2.2.3	SEMPA in Comparison	23
3	Spin-Transfer-Torque Parameters for a Magnetic Vortex Core	25
3.1	Micromagnetics	25
3.1.1	Torques and Energies in Micromagnetics	26
3.1.2	Effective Field	27
3.1.3	Damping	30
3.1.4	Spin-Transfer	31
3.1.5	Summary	35
3.2	Previous Experimental Work on the Spin-Transfer-Torque Parameters	36
3.3	Using a Vortex Core to Determine All Spin-Transfer-Torque Parameters	37
3.3.1	Theoretical Approach	39
3.3.2	Micromagnetic Simulations of the Current-Induced Vortex Core Displacement	42
3.3.3	Sample Preparation	44
3.4	Vortex Displacement in Iron Alloys	48
3.5	Vortex Displacement in Permalloy	51
3.5.1	SEMPA Measurements	52
3.5.2	Material Properties Obtained by Ferromagnetic Resonance	56
3.5.3	Determination of all Spin-Transfer-Torque Parameters	59
3.5.4	Experimental Sources of an Oersted Field	66
3.6	Summary	71
4	Time-Resolved Magnetic Imaging	73
4.1	Time-Resolved Magnetic Imaging	73
4.1.1	Photon-Based Techniques	73
4.1.2	Electron-Based Techniques	75
4.1.3	Scanning Probe Techniques	76
4.2	Time-Resolved SEMPA	76
4.3	Technical Improvement of the Setup	78

4.4	Time-Resolved Measurements	80
4.4.1	Time-Resolved SEM	82
4.4.2	Time-Resolved SEMPA	83
4.5	Summary and Outlook	90
5	Interaction Between Ferroelectric and Ferromagnetic Domain Walls	93
5.1	Charged Walls	95
5.2	Uncharged Walls	100
5.2.1	Determination of Wall Width	100
5.2.2	Experimental Broadening	102
5.2.3	Wall Width in Theory and Experiment	106
5.3	Summary	107
6	Uniaxial Anisotropy of a Rippled Magnetic Film	109
6.1	Model System and Possible Magnetic Configurations	110
6.2	Stray Field Energy	113
6.2.1	Surface and Volume Magnetic Charges	113
6.2.2	From Charges to Energy	117
6.3	Exchange Energy	122
6.4	Comparison of the Energy Contributions	124
6.5	Comparison of Model Values to Experimental Data	127
6.5.1	Permalloy on Diamond	127
6.5.2	Cobalt on Magnesium Oxide	128
6.5.3	Permalloy, Cobalt, and Iron on Silicon	129
6.6	Summary	133
7	Appendix	135
7.1	Evaluation Tools for SEMPA Data	135
7.1.1	Determination of the Vortex Core Position from SEMPA Data	135
7.1.2	Determination of Position and Orientation of the Magnetic Structure	138
7.2	Correction of Current Density for Parasitic Shunt Resistances	140
7.3	Raw Data of SEMPA Images	142
	References	145
	Publications	175
	Acknowledgement	177

1 Introduction

The Information Society

The document you are holding in your hands is a child of the information age¹. The information contained within this document was mainly obtained (by measurement), researched, and evaluated with the help of “information and communications technology” (ICT) [1], which is an integral part of this age [2]. In modern digital ICT, information is thought of as “data”, which consists of single binary digits (bits)². The development of the information society is closely entangled with the rapid development of the technological equipment [5, 6]. The technical equipment is required to conduct three basic operations on information. These are [5]:

1. communication - the transmission of information through space
2. storage - the transmission of information through time
3. computation - the meaningful transformation of information

This thesis is mainly dedicated to the improvement of the direct connection between the latter two of these operations: The non-permanent storage of information prior to, in between, or directly after computation³. Today, the high-speed primary memory is well-separated from the slower to access secondary memory, which is endowed with a much higher capacity. While the primary memory is only required to transmit data through a time span of a few milliseconds, the high-capacity secondary memories are used to transmit huge amounts of data over periods of many years⁴.

In the following sections, the history of primary storage devices will be recapitulated, starting with a short digression into secondary storage. The path towards universal memory devices will be explored. Universal memories unite fast access times with high-density storage capabilities and therefore have the possibility to replace primary and secondary storage media altogether. The physical effects behind promising candidates for universal memory will be investigated throughout this thesis. Let us now start with a short summary of the technological development of storage media during the beginning of the information age: the digital revolution.

¹Maybe you are even reading in on some sort of electronic device, which is also a child of this age.

²Putting the nomenclature of “bits” into context with the definition of information as the absence of uncertainty [3], each bit of optimally compressed data reduces the uncertainty by one half [4]. Picture this as cutting the full scale of “letters from an alphabet or pixels from a color scale” [5] into half. The bit state of “0” or “1” yields the information whether the letter of interest is part of the first half (A-M) or the second half (N-Z) of the alphabet and hence reduces the uncertainty by half.

³In this context, it is irrelevant whether the computation is done in an application specific sense (for instance to display the information on a screen) or for general purpose [5].

⁴The whole situation is very similar to the way information is stored and processed within the human brain. While the primary memory corresponds to the human short term, or working memory, the secondary memory can be related to the brain’s long term memory [7].

The Digital Revolution

Although the digital revolution spawned the information age, just as the industrial revolution initiated the industrial age, it can not really be assigned to a specific point in time. Instead, it consists of a series of technological breakthroughs that occurred during the last century. These milestones irreversibly changed the way in which information was stored.

In the middle of the last century, digital information was mainly stored in punch cards [8]. While carrying around a punch card might sound like a secure way to transport information, it is probably not the fastest one⁵ since punch cards have a very limited capacity. Although punch cards were still in use up to the modern ages, for instance in the presidential election of the United States, more advanced technologies have since been developed.

The earliest ways to improve the storage capacity were based on the phenomenon of magnetism. Magnetic tape (1952) provided a dramatic increase in storage density: “a 10.5 inch diameter reel of tape could hold the equivalent of more than 35,000 punched cards” [12]. The tape storage, however, only allowed for a sequential access to the data, because the positioning of the tape head to an arbitrary place took several seconds. The increasing demand for faster access times lead to the development of hard disk drives (1956) where the data is stored “less than a second from management’s reach” [13]. Today, disk and tape storage media are still being used as mass storage devices. In the year 2007, the two major components of world’s total capacity to store information were PC hard disk drives (42 %) and digital tape storage (21 %) [5]. Modern hard disk drives operate at 10.000 rotations per minute [14], which means that any given data bit passes the read/write head every 6 milliseconds.

The access times of mass storage devices, however, have never been able to keep up with the exponentially increasing computation power of the central processing units (CPU). The invention of the transistor in 1947 [15] and the integration of a huge number of transistors onto a small plate (known as an integrated circuit, IC) around 1960 [16], were the starting points of a development in which the number of transistors, and therefore the computing power, doubled roughly every two years [16].

The Concept of Temporary Storage

To resolve the discrepancy between CPU computation speed and the access times of mass storage devices, additional levels of temporary memory are required. The first level is the primary memory, which is located closest to the CPU. One key feature of primary memory devices is “random access”, meaning that any random memory cell can be accessed within an equal amount of time. This gave them their name “random-access memory” (RAM). During the beginning of the transistor age, magnetic core memory (see Fig. 1.1a) was the most commonly used form. In magnetic core memory, data is stored in small magnetic rings that are threaded onto an array of wires [17]. Two binary states are defined by the direction in which the magnetization curls within these rings. Each of the rings can be addressed individually since it only switches when all of its crossing wires are carrying current. Magnetic core memory is a three-dimensional memory system with access times close to one microsecond [17].

⁵The sentence “Never underestimate the bandwidth of a station wagon full of tapes hurtling down the highway” [9] might however also be applied to a station wagon full of modern nano-punch cards [10, 11].

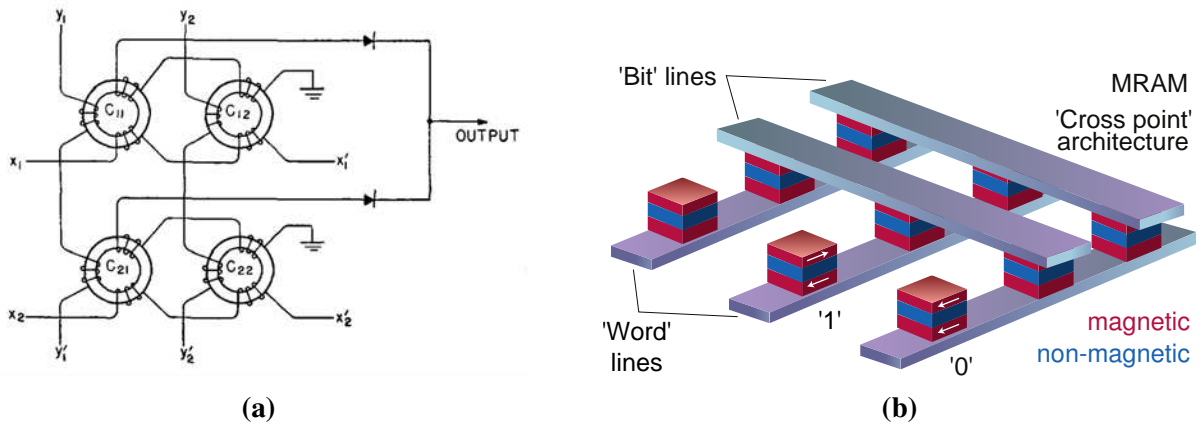


Figure 1.1: Sketches of two chronologically well-separated types of magnetic random-access memory. (a) Ancient magnetic core memory (around 1950, image reproduced from [17]). The data is stored in the flux rotation within magnetic rings (four rings are visible). To change the state of ring C_{11} , a current is sent through wires x_1 and y_1 . The field that is produced by the two wires, which are wound around the magnetic storage core like a coil, is sufficient to switch the magnetization in ring C_{11} . Rings C_{12} and C_{21} only experience half the field, which is not sufficient to switch them (they are “half-select”). To read the state of a core, the writing procedure has to be repeated while the signal on the “output” circuit is monitored. If the flux inside the ring changes an inductive voltage is observed, which does not happen if the flux stays constant. One can therefore distinguish whether the ring has switched or not and has destructively read its state. When the state of the ring is of further importance, it needs to be re-written. (b) Modern magnetic random access memory (MRAM around 2005, image slightly modified from [18]). In MRAM, the data is stored in layer stacks that lie between two crossing arrays of wires. Each stack consists of three layers: a free layer (top, magnetic) which stores the information, a separation layer (middle, non-magnetic), and a reference layer (bottom, magnetic) which is required for the readout operation. “For writing, current pulses are sent through one line of each array, and only at the crossing point of these lines is the resulting magnetic field high enough to orient the magnetization of the free layer. For reading, the resistance between the two lines connecting the addressed cell is measured.” [18]. The resistance of the state “1” with anti-parallel orientation of the magnetization in the two layers can be up to ten times [19] the resistance of the “0” state with parallel orientation because of the tunnel magnetoresistance effect [20, 21].

Technology	Existing					In development
	DRAM	SRAM	NOR flash	MRAM	FeRam	STT-RAM
Read speed (ns)	10	1	10	3 – 20	20 – 80	2 – 20
Write speed (ns)	10	1	1000	3 – 20	50	2 – 20
Cell size (F^2)	6 – 10	50 – 120	4 – 8	16 – 40	15 – 34	6 – 20
Node F (nm)	22 [22]	22 [22]	45 [23]	90 [24]	130 [25]	45 [26]
Non-volatile	no	no	yes	yes	yes	yes
Idle power	high	low	none	none	none	none
Endurance	10^{16}	10^{16}	10^5	$> 10^{15}$	10^{12}	$> 10^{15}$

Table 1.1: Performance of random-access memory devices (data from Refs. [24, 27, 28], for a description of the technologies see main text). The size of a cell containing a single bit is given in units of the technology node (or design rule) F . Then quantity of F^2 gives the areal number of (crossing) metal wires that are required for the layout and is process independent. The areal size of a single memory cell can be determined by multiplication of the cell size by the squared technology node F^2 . In 2013 the 14 nm technology node was reached in CPU fabrication by Intel [29]. The endurance gives the maximum number of read/write cycles that a device can sustain. The major drawbacks of existing techniques are evident. DRAM has a high power consumption and volatility. The power consumption is reduced in SRAM but only at the cost of a lower storage density. NOR flash suffers from a low endurance and a very slow write speed. MRAM and FeRAM start to encounter scaling problems when going to smaller technology nodes. Details about these issues can be found in the main text.

One drawback of magnetic core memory is that each memory cell is reset during the inductive readout process [17] (for details see caption of Fig. 1.1). In the late 1960’s magnetic core memory was replaced by the newly-developed dynamic random access memory (DRAM) [30, 31]. DRAM offered a higher storage density and even faster access times (see Tab. 1.1). In DRAM, data is stored as the charge of a capacitor, which is always subjected to a small leakage current and therefore needs to be recharged every few milliseconds. An alternative to DRAM that does not need to be refreshed periodically is static RAM (SRAM). In SRAM, data is stored in the state of a flip-flop, which takes up the sixfold place compared to a single transistor. This means that SRAM is not suitable for high-density data storage because its cost per byte is too high. Although the power consumption in the idle state is greatly reduced for SRAM, the data is still inevitably lost when the memory is no longer powered.

Yet another way to store data electronically is using a floating gate transistor (FGMOS)⁶. In an FGMOS, the floating gate is well-separated from all conductive channels by a highly resistive material. It is charged by “hot electrons” [32, 33] that hop across the barrier. It is uncharged by the application of a sufficiently high voltage to allow for quantum tunneling (Fowler-Nordheim tunneling [34]) of the electrons out of the gate. This method of data storage is used in “electrically erasable programmable read-only memory” (EEPROM) and in flash memory

⁶A metal–oxide–semiconductor field-effect transistor (MOSFET) is most commonly used in a floating-gate transistor, hence the “MOS” in FGMOS.

[35]. Although EEPROM and flash are considered non-volatile, they suffer from dramatically slow write speed and a very low endurance (see Tab. 1.1, in which NOR flash⁷ is listed as an example).

Fast and Non-Volatile Temporary Storage

During the past decades, alternative approaches of storing data in a randomly accessible, yet non-volatile⁸ way have been introduced. These technologies are termed “non-volatile random-access memory” (NVRAM). A few selected examples are discussed in this section.

A modern NVRAM technology, very similar to the early non-volatile magnetic core memory, is magnetic random-access memory (MRAM, see Fig. 1.1b). In MRAM, the data is stored in the orientation of the single domain state in a ferromagnetic layer. The unfavorable induction-based readout mechanism of magnetic core memory (see Fig. 1.1a) is replaced by a magneto-resistive approach [37, 38]. Modern MRAMs [39–41] make use of the tunnel magnetoresistance (TMR) [20, 21], which occurs in magnetic tunnel junctions (MTJs) [42–45]. These MTJs consist of three layers that are stacked on top of each other: A free layer for storing the information, a reference layer with fixed magnetization for the readout procedure, and an insulating layer between the two. The resistance of the stack is much higher when the magnetization of the two ferromagnetic layers is aligned anti-parallel, than it is for a parallel alignment of the magnetization; a result of the TMR [20, 21].

The writing process of the MRAM technology is yet very similar to the magnetic core memory, although some improvements have been applied [41]. Fundamental challenges however remain in the scaling of an MRAM system. As the cell size scales down, the switching field of the free layer and hence the writing current increases [18, 24]. Together with a downscaling of the conduction lines, this leads to a tremendous increase in heat generation [18, 24]. Sharing the writing current over multiple conduction lines is a possible solution but may result in increased error rates. This is due to the unintended switching of a neighbouring element that is not in the center of the current-carrying lines and hence experiences less stray field (it is “half-select”) but switches nonetheless because of local variations in bit shapes and therefore anisotropy [24]. Alternative approaches of decreasing the writing current include a channeling of the magnetic induction, heat assisted recording, microwave excitation, or using antiferromagnetic layers instead of ferromagnetic ones and switching them by a spin-flop process [18]. Despite all of these problems, the MRAM technology has reached the 90 nm technology node [24] and the 65 nm node will soon be reached [46–48]. In the lab, cells with diameters of 40 nm were already produced [49] and dimensions below 20 nm are within reach [50]. Currently a “fab” (semiconductor fabrication plant) that is dedicated to the fabrication of MRAM cells is being built in Russia [51].

Another solution to the scaling problem of MRAM lies in changing the writing procedure from field-induced to current-induced switching [52, 53]. Since this is quite a fundamental change, the resulting memory is given a new name: “spin-transfer torque random-access mem-

⁷The internal characteristics of NOR flash are similar to that of a NOR gate, which implements a logical NOR. The name was given in contrast to NAND flash, which resembles the logical NAND.

⁸One might be tempted to say “persistent” instead of “non-volatile” to avoid the negation. The term “persistent memory” is however already being used in informatics to name something slightly different [36].

ory” (STT-RAM) [54–56]. “As predicted by the spin-transfer theory [53], there is an asymmetry as a function of the direction of current bias, so that domains in the two magnetic layers can be aligned antiparallel by currents flowing in one direction, and then reoriented parallel by reversing the current flow” [57]. For switching from anti-parallel to parallel alignment this can be understood in a simple picture: The electrons flow into the memory cell through the fixed layer and become “spin-polarized”, which means that the majority of the spins of the conduction electrons (responsible for charge transport) are aligned parallel to the localized electrons (responsible for magnetism). The conduction electrons keep a certain amount of their spin polarization as they pass through the thin and nonmagnetic spacer layer. When the conduction electrons enter the free layer they are initially aligned anti-parallel to the localized electrons. The conduction electrons, however, tend to align their spin with the localized electrons. The conservation of spin angular momentum during this alignment causes a back-action on the localized electrons (and therefore the magnetization) [50] which it experiences as a torque, the spin-transfer torque.

One big advantage of switching by current instead of field is the improved scalability of the system. The strength of the spin-transfer torque does not depend on the total current that is sent through the structure, but only on its density. This means that the total current decreases as the device is scaled down [24]. The critical current densities that are needed are, however, still relatively high [24]. Although STT-MRAM devices have already been built in 2005 [58] and have reached the 45 nm technology node in 2009 [26], industrial production has not yet been started. The technique is expected to be scalable down to the 8 nm node and will “outperform [...] SRAMs from the 15 nm process node” on [59].

There are however also alternatives of storing data in a non-volatile way that do not include any magnetic materials. One of those is ferroelectric random access memory (FeRAM). “In an FeRAM, information is stored by the polarization direction in a ferroelectric film and the stored datum is read out using the polarization reversal current” [60, p. 4]. Although FeRAM has been around for quite a while (since 1992 [61]), it plays a rather minor role in modern data storage. Reasons for this are evident from Tab. 1.1: It has a low storage capacity (and therefore a high cost per byte) because the polarization current is proportional to the area of the capacitor [60, p. 4] and therefore the layout can not be scaled down so easily. Additionally, although improvements have been made during the last few years, its endurance is still rather limited [60].

Yet another alternative that is in development is “phase-change random-access memory” (PRAM)⁹. In PRAM, a phase transition is induced, for instance by local heating of a phase-change material (PCM) [62]. The phase transition can be reversed by local melting, which is achieved by heating and quenching of the region [62]. Between two phases, a difference in conductivity of up to three orders of magnitude can be present [63]. This dramatic change in resistance is utilized for the reading process. While the properties of PRAM are very similar to those of FeRAM (which is listed in Tab. 1.1), it also suffers from a low endurance [24]. PRAM has currently reached the 20 nm technology node [64].

⁹The values for PRAM are not listed in Tab. 1.1 because there is no space left. They can however be found in Wolf *et al.* [24] and are very similar to the values of FeRAM apart from a slightly smaller cell size and an even worse endurance.

One thing all of the previously discussed NVRAM technologies have in common is the involvement of materials that are not part of the standard CMOS¹⁰ procedures. These materials need to be applied separately after fabrication as a back-end of (production) line (BEOL) process. This fact establishes a certain investment barrier, which delays their introduction to industrial fabrication as long as they are not clearly favorable to the other techniques listed in Tab. 1.1.

The non-volatility of RAM will have a large impact on modern information and communication technology. Imagine a personal computer with a non-volatile RAM (NV-RAM). It can be switched off and on instantaneously in less than a second¹¹. It will not be affected by data loss due to power blackouts anymore. One can only start to imagine how many man-hours are wasted by people who are waiting for their computer to start up, to shut down, or by doing work that they already did but was lost because someone ran over the power cable. On top of all that, a personal computer using NV-RAM will consume less power because the data within the RAM does not need to be refreshed every few milliseconds [65].

Towards Universal Memory

Most of the technologies that were presented in the previous section are candidates for a universal memory [24, 66]. A new memory technology has the chance to become “universal” when it combines the benefits of all other memory technologies. A universal memory would render the dissociation between mass storage devices and random access memories unnecessary, as it could replace both. To be able to do so it needs to combine high density, fast read and write times, low power consumption, non-volatility, and high endurance.

There is, however, yet another candidate for universal memory which is not listed in Tab. 1.1 as it can not be considered as random access memory. The preliminary technology that is quite similar to traditional tape memory is called “racetrack memory” (RTM) [67]. Three major differences to tape memory are its miniature size, the increased number of read/write heads, and the way the information is passed along the heads [67]. In RTM, the information is stored in a ferromagnetic wire either in the orientation of domains with a well-defined size, or as the presence or absence of a magnetic domain wall (DW).

To read the information, all domain walls within the wire are collectively pushed along the wire with an electric current. The movement of the domain walls is again induced by spin-transfer torques, exactly as the magnetization switching in MRAM [67]. The orientation of domains or the presence of domain walls is sensed by an MTJ that is either directly attached to or located in close vicinity to the racetrack. To write information, a domain is switched by a magnetic field pulse and domain walls are subsequently created or annihilated [67, 68]. One big advantage of the technique is that the ferromagnetic wire can in principle be arbitrarily bent or curled up. By curling the wires all three dimensions of space can be used, which tremendously increases the areal storage density [67]. In terms of functionality RTM is often compared to a shift register [69].

Current issues with RTM lie within the fabrication of the three-dimensional “racetracks”, in achieving a uniform DW displacement and motion for all DWs within the wire through the re-

¹⁰Complementary metal–oxide–semiconductor.

¹¹Depending on the time that is required for memory check while booting up.

duction of pinning centers (certain positions where DW motion uncontrollably stops), and in reducing the threshold current that is required for DW motion [28]. Although RTM is a very promising technique, its industrial development has only just begun [68, 70]. Theoretically, the interaction between an electrical current and the local magnetization is however very well described by a few fundamental equations [52, 53, 71–74] (reviews can be found in [75, 76]). Within the theoretical framework, three basic parameters are important for current-induced domain wall motion (in RTM), or current-induced domain switching (in STT-RAM) [50]:

- α - The Gilbert damping constant α of the magnetic system is a measure for the rate at which an excited magnetic system loses its energy. “The mechanisms by which this occurs include coupling of the magnetization field to spin waves, eddy currents, and lattice vibrations, and the effects of polycrystalline structure, strains, and crystal defects such as voids, interstitial atoms, and “foreign” atoms” [77]. Due to the latter effects, α is often used as a measure for the quality (purity) of a magnetic film.
- u - The spin drift velocity u gives the efficiency of the interaction between current and magnetization. The spin drift velocity is proportional to the current density as well as to the degree of spin polarization of the electrons within the current [73, 74].
- β - The so called “nonadiabatic” parameter β is a complex phenomenological parameter, which “turned out to modify the threshold current and the terminal velocity of [a domain] wall significantly” [78]. The origin and behavior of the β parameter will be explored throughout the third chapter of this thesis.

The Scope of this Thesis

The first experimental study of this thesis (chapter 3) is dedicated to the reliable determination and separation of the above-mentioned parameters (α, β, u) for a given material system. The parameters are experimentally obtained by observing the deflection of a magnetic vortex core while a continuous current of electrons flows through it. A vortex is a magnetic texture very similar to a water swirl (or water vortex). In a magnetic vortex, the in-plane magnetization curls around a central core region where it points out of the film plane. The size of the core region is only a few nanometers [79].

One of the measured parameters (β) is dramatically increased due to the swift rotation in the core region [80]. The result is compared to measurements of β in a “magnetic spin wave” [81, 82], which is similar to a very shallow water-surface wave structure. In a spin wave the magnetization varies on a much larger length scale of a few micrometers. The comparison is used to separate the contribution to β that stems from the swiftness, from the one that stems from intrinsic material properties [80]. The other parameters (α and u) are, within error, not altered by the swiftness. The simultaneous determination of all three parameters is important because an entanglement of the three can not yet be excluded [82].

The measurements that are presented in the first experimental chapter (chapter 3) would not have been possible without a sophisticated tool for magnetic imaging [80]. The observation of magnetic systems by magnetic imaging has become a powerful technique in modern experimental research [83]. The historical development of magnetic imaging is reviewed in chapter 2. The

chapter completes with a description of the imaging technique that has been used to conduct the measurements presented in this thesis. This technique of “scanning electron microscopy with polarization analysis” (SEMPA) is a very suitable tool to produce high-fidelity images of magnetic surfaces [83]. The capabilities of SEMPA to resolve the in-plane magnetization vector with a high resolution allow for the quantitative analysis of a magnetic system [84].

A growing desire in modern research lies within the observation of the dynamic reaction of a magnetic system to ultra-fast perturbations. The ongoing investigation of switching mechanisms in small magnetic elements will help to further reduce the read and write times of magnetic memory devices [85]. An extension of SEMPA imaging into the time domain would therefore greatly extend the scope of application for the technique. Usually SEMPA “videos” can only be obtained with a time-resolution (the time between two frames) of minutes due to the large integration time of a single image. We however developed a technique (TR-SEMPA) that allows us to obtain SEMPA videos of a magnetic texture with a time-resolution down to one nanosecond [86].

The experimental approach of how to improve the temporal resolution of SEMPA so dramatically (by ten orders of magnitude) and a first proof of principle are presented in chapter 4. The first video that was ever obtained with TR-SEMPA shows the field-driven rotational gyration of a magnetic vortex core around its field-free equilibrium position. The observation of this “harmonic” gyration yields an alternative approach for determining two of the parameters that are mentioned above (α and β) [87, 88].

The magnetic imaging capabilities of SEMPA were also used to elucidate the interaction between ferroelectric and ferromagnetic materials (chapter 5). The high spatial resolution of SEMPA is used to observe two distinct types of magnetic 90° domain walls that occur in one and the same system: “charged” and “uncharged” walls. The beauty of the system is that the type of wall can easily be switched by a magnetic field of only a few millitesla [89]. Both walls show a slightly different internal structure, but the main difference is their width, which is one order of magnitude larger for the charged wall than for the uncharged wall. Another interesting fact is that the magnetic domain walls are strongly coupled to their ferroelectric counterparts. This makes it possible to move the ferromagnetic walls along with the ferroelectric ones [90, 91]. As the ferroelectric domain walls can easily be manipulated by electric fields, this effect could be utilized in future RTM devices. Ferroelectric domains can also be used to change the orientation of ferromagnetic domains from in-plane to out-of-plane by switching their anisotropy axes. This fact finds an interesting application in logic devices [24].

The thesis concludes with a theoretical chapter (chapter 6). The calculation describes how a rippled substrate can break the symmetry in a magnetic film and affect its magnetic properties, in this case the uniaxial magnetic anisotropy. The topic was already explored in my diploma thesis [92], where the foundations of the theory have been developed¹². Being able to control the anisotropy by modifying the substrate gives us an extrinsic control of the stability of memory cells. There are two important aspects that have to be considered regarding the stability of an element [93–95]: The stability against random switching induced by thermal fluctuations and the stability against intended switching by field or current. While the first one should be as high as possible, the second one usually should be as low as possible. Both are however

¹²The diploma thesis also includes SEMPA images of the anisotropy-induced deformation of a vortex state on top of a rippled substrate.

connected and the optimum value of the anisotropy is the result of a compromise. By adjusting the waviness of an underlying substrate, a wide range of values can be set for the uniaxial anisotropy within the film plane.

In summary, this thesis shows how magnetic imaging provides a fundamental contribution to our understanding of the nature of magnetic materials. The importance of imaging techniques in the exploration and unraveling of the secrets of nature was summarized by Edward O. Wilson as follows: “The search for the ultimate has been aided through direct visual observation by steady advances in the resolving power of microscopes. This technological enterprise satisfies [an] elemental craving: to see all the world with our own eyes.” [96].

2 Magnetic Imaging

The first observation of magnetic domains in the early 1930's [97, 98]¹ established the importance of magnetic imaging. It not only proved the previously discussed domain theory [71, 101, 102] right, but also provided a means of directly observing the behavior of these domains, for instance under the influence of external magnetic fields. Since these early days, a great variety of techniques that allow for the visual representation of a magnetic system have been developed [83, 103].

After a short overview of the history of magnetic imaging, an appreciation of modern magnetic imaging is provided by considering the technique of scanning electron microscopy with polarization analysis (SEMPA). The combination of magnetic imaging and theoretical modeling is a powerful tool that allows us to investigate, develop, and expand the fundamental theories of magnetism.

2.1 Historical Overview

The visualization of magnetic domains was first performed in 1931 when v. Hámos and Thiessen [97] and Bitter [98] allowed “small magnetized particles in suspension [...] to settle on a magnetic surface” [98]. As those particles aligned along the stray field generated at domain boundaries, the first demonstration of the domain configuration at the surface of a given sample was performed (see Fig. 2.1a). Since then, the Bitter technique has been improved by using smaller particles and more sophisticated microscopes [108, 109] (see Fig. 2.1a). Additional improvements in polishing allowed to separate the effects that are “characteristic of the polished surface and not of the interior” [100] from the ones that truly stem from the magnetic configuration [100].

Nowadays, the magnetization can be visualized by a variety of techniques utilizing different effects. Magneto-optical methods that make use of the Faraday effect [110–112] (in transmission, see Fig. 2.1b) or Kerr effect [113] (in reflection) have been developed. The latter can be carried out in parallel mode, often using visible light [114–116] or in scanning mode using laser light [117–119].

An improvement in resolution can be achieved by using light of lower wavelengths *i.e.* X-rays. The element-specific X-ray magnetic circular dichroism (XMCD) characterizes a magnetization-dependent absorption of transmitted X-rays [120, 121]. The discovery of XMCD has led to the development of the scanning transmission X-ray microscope (STXM) [122] and the full-field transmission X-ray microscope (TXM, see Fig. 2.1c) [106, 123, 124], operated in

¹One may argue that the “true domain patterns” [99] were only observed some years later when an electrolytic polishing of the sample surface was introduced by Williams, Bozorth and Shockley in 1949 [100].

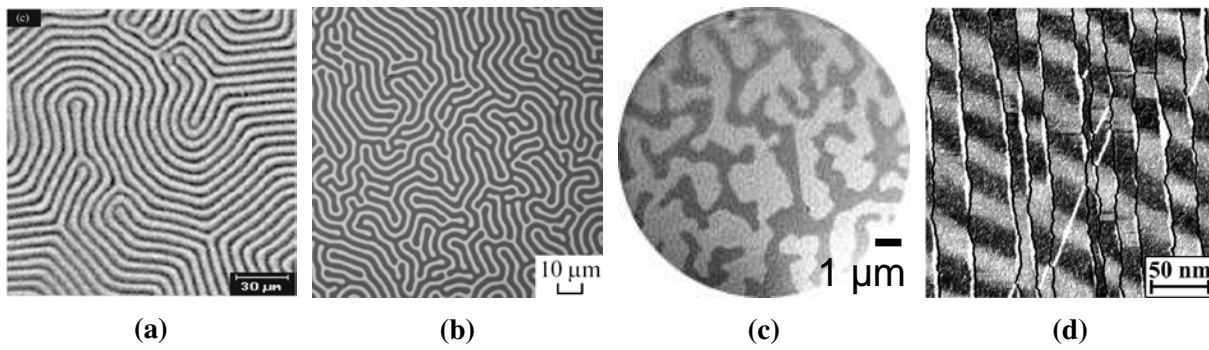


Figure 2.1: Some examples of images obtained with various magnetic imaging techniques. All images show the out-of-plane contrast. In (a) the black-and-white contrast marks domains (white) and domain walls (black), whereas in the other images black and white areas represent the two opposing magnetization directions ($m_z = \pm 1$). (a) Modern Bitter image of the domain structure in $\text{Y}_{2.6}\text{Sm}_{0.4}\text{Fe}_{3.8}\text{Ga}_{1.2}\text{O}_{12}$ [104]. (b) Domain structure of a polished magnetite crystal visualized utilizing the Faraday effect [105]. (c) Element-specific TXM image of the magnetic XMCD signal at the L_3 Fe edge in a $[4 \text{ \AA} \text{ Gd} / 4 \text{ \AA} \text{ Fe}]_{75}$ multilayer [106] (d) SP-STM image of 1.95 ML Fe on W(110) recorded with a GdFe tip [107].

parallel mode. The effect can also be used for lens-less holographic techniques where the real-space image is reconstructed from the hologram via Fourier transform (FTH) [125]. The XMCD is further used to obtain magnetic contrast in photo-electron emission microscopy (XPEEM) [126–128].

However, also purely electron-based techniques have been developed [129]. In (scanning) transmission electron microscopy (TEM) [130–132] or (STEM) [133], the deflection of electrons that have passed through a thin sample induced by the Lorentz force is measured. The deflection of reflected electrons by the Lorentz force can also be utilized to obtain magnetic contrast in scanning electron microscopy (SEM) [134]. Another option is measuring the polarization of the secondary electrons that are emitted from sample atoms excited by an electron beam. This is carried out in scanning electron microscopy with polarization analysis (SEMPA), which will be discussed in the next section. By working with a spin-polarized incident beam, it is also possible to make use of the Pauli exclusion principle [135] upon diffraction, which is utilized in spin-polarized low energy electron microscopy (SPLEEM) [136].

An entirely different approach to magnetic imaging, which allows for even higher lateral resolution, is based on scanning probe techniques [137]. In magnetic force microscopy (MFM) [138] a small ferromagnetic tip is used to probe the magnetostatic forces above a sample surface. By bringing a ferromagnetic tip close enough to the surface to allow for a tunneling current to flow, the local electronic density of states can be probed, which is done in spin-polarized scanning tunneling microscopy (SPSTM, see Fig. 2.1d) [139]. Sensitivity to local magnetic fields in AFM can also be achieved by attaching a single spin to the AFM tip and monitoring its Zeeman splitting by optically detecting the magnetic resonance signal [140–142]. Using a scanning-probe technique allows to surpass the diffraction limit that is limiting the resolution in optical techniques [143]. This is put into practice in scanning near field optical microscopy (SNOM) [144].

Further details and a profound discussion and comparison of different imaging techniques can be found in [83, 103].

2.2 Scanning Electron Microscopy with Polarization Analysis

The discovery of the electron as a particle by J.J. Thomson in 1897 [145, 146] and of its wave-like nature by de Broglie in 1924 [147] led to a flourishing development of experimental techniques that make use of the electron to investigate the properties of physical objects. One of these techniques is “scanning electron microscopy” (SEM). In an SEM, electrons are accelerated to a few thousand volts and focused to a tiny spot of a few nanometers on the surface of an object of interest [148]. The number of electrons that are reflected (backscattered electrons, BSE) or emitted (secondary electrons, SE) from the object as the beam is scanned across its surface, yields information about the surface topology and several physical properties² of the given object [149].

However, electrons have additional properties that can be of interest for experimental investigations. A very important one is the quantum mechanical property of “spin”, which was discovered in 1922 for a silver atom by Gerlach and Stern [150] and ascribed to the electron by Pauli [135] and Uhlenbeck and Goudsmit [151]. In 1976 it was found, that the spins of secondary electrons that are emitted from a magnetic material are preferentially aligned along a certain direction [152]. The degree of this alignment along a given quantization axis y , the spin polarization P_y is defined as the imbalance in spin of a number of electrons N [153, p. 52]:

$$P_y = \frac{N_{\uparrow} - N_{\downarrow}}{N_{\uparrow} + N_{\downarrow}} \quad (2.1)$$

Here N_{\uparrow} (N_{\downarrow}) represents the integer number of electrons with spin parallel (anti-parallel) to the y -axis and $N_{\uparrow} + N_{\downarrow} = N$ is the total number of electrons. It was later discovered that the spin polarization P_y reflects the “average valence-electron spin density within the solid” for secondary electrons above a certain energy threshold [154]. The polarization and the number of secondary electrons that are emitted from a sample depend on their kinetic energy E [155]. This dependence is quite similar for all $3d$ -ferromagnets [83, p. 141] [84]. The dependence of P_y and N on energy is shown for the example of a fully saturated Iron sample ($m_y = 1$) in Fig. 2.2a [155]. The number of electrons is peaked at low energies around 2-3 eV while the polarization has its maximum for the lowest energies [155].

The low energy secondary electrons can therefore be used as a source of information about the magnetic moment of a given substance. Due to the small dimension of the electronic wave function ($\lambda \leq 1 \text{ \AA}$ for $E \geq 100 \text{ eV}$ electrons³), electron beams possess the opportunity to probe the magnetic moment with a high spatial resolution. To this end it is however required to be able to determine the spin polarization of the secondary electrons. Several means of determining the spin polarization will be discussed in the following section.

²Apart from topographic effects, a change in the number of electrons that are obtained can be induced by a change in material, electrical potential or by magnetic stray fields.

³ λ is the “de Broglie” wavelength, given by $\lambda = h/p$ with Planck’s constant h and the momentum of the electron p [147] [157, p. 4].

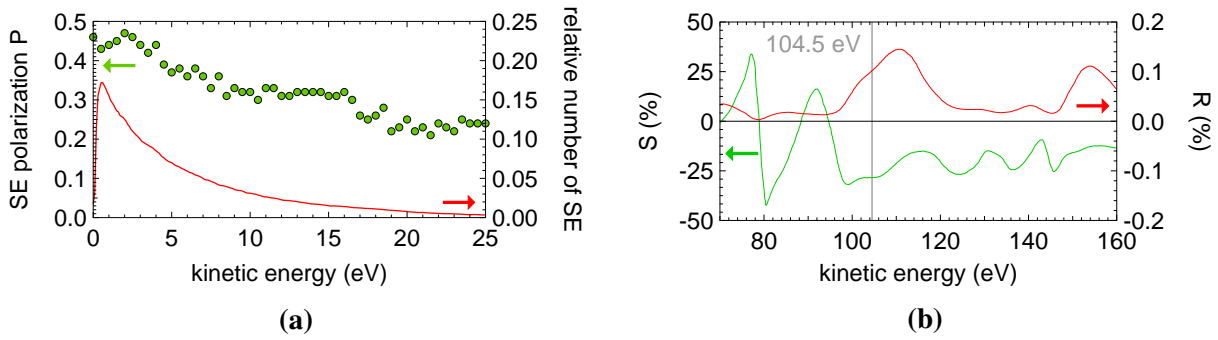


Figure 2.2: (a) Emission of secondary electrons from a clean Fe(110) single crystal that is saturated along the [100] direction (data from Refs. [84, 155]). The crystal was excited by a primary beam of 2 kV that hits the surface at an angle of 60° . Secondary electrons are collected from within a cone of 3° around the surface normal. The number of secondary electrons and the polarization parallel to the [100] direction are shown. (b) Sherman function S and reflectivity R for the scattering of electrons at the W(001) surface (data from Refs. [84, 156]). The Sherman function describes the asymmetry in scattering of a fully polarized beam into two opposing (2,0) LEED spots. The reflectivity gives the number of electrons that are scattered elastically. Finding a range where the product of R and S is maximized is desired for the application of a LEED detector in SEMPA imaging. The optimum working point as derived by Kirschner [156] is indicated by a gray line.

2.2.1 Measuring the Spin Polarization of Secondary Electrons

The most important contribution to the determination of the magnetic moment and therefore the spin of the electron was made by Mott [158] in 1929. Mott developed a theory about the scattering of fast electrons at atomic nuclei [158]. He found that the scattering angle of electrons at atomic nuclei is spin dependent: “Suppose an electron, about whose spin direction we know nothing, falls on a nucleus and is scattered through a given angle; we now know that its spin axis is more likely to be in one direction than another.” [158].

The scattering asymmetry of the electrons is generated by the spin-orbit interaction. Assuming a Coulomb potential, the part of the Hamilton operator H_{SO} that is responsible for this effect is proportional to [156, p. 30]:

$$H_{SO} \propto \frac{Z}{r^3} (\mathbf{s} \cdot \mathbf{l}) \quad (2.2)$$

The strength of the spin-orbit interaction is proportional to the number of electrons of the nucleus Z and therefore strongest around heavy atoms. The strength of the interaction grows with $1/r^3$, which means that the interaction takes place in close vicinity of the atomic nucleus [156]. It further depends on the dot product between the electron spin \mathbf{s} and its angular momentum $\mathbf{l} = \mathbf{r} \times \mathbf{p}$.

Based on the idea of Mott [158], analyzers for the spin polarization of electrons have been constructed [159]. This finally led to development of the scanning electron microscope with polarization analysis (SEMPA), which was first built in 1984 by Koike and Hayakawa [160,

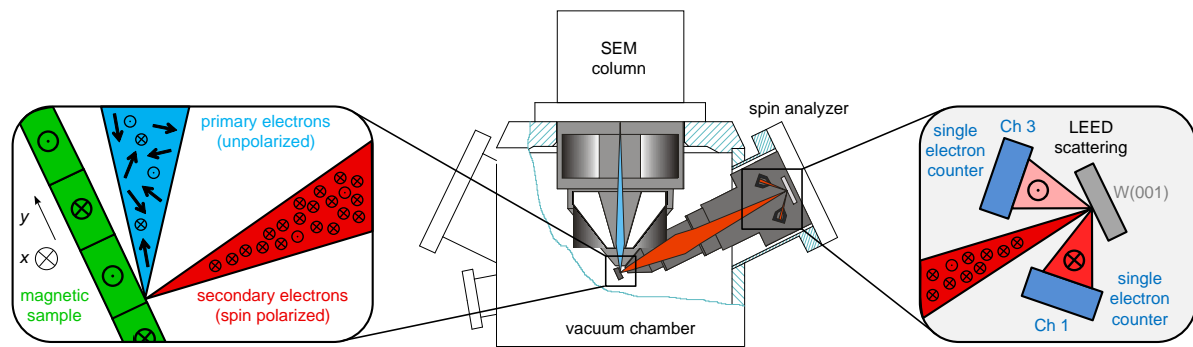


Figure 2.3: Working principle of SEMPA (modified image from Ref. [84]). A beam of unpolarized electrons (blue) is focused into a certain spot of a magnetic sample (green). The column of a of an ultrahigh vacuum scanning electron microscope (UHV-SEM) is most conveniently used for the generation of the incident beam. The secondary electrons (red) that are emitted from the magnetic sample (green) are spin polarized up to a certain degree. Their axis of spin polarization \otimes is aligned anti-parallel to the magnetization \odot at the point of their origin. The spin polarization of the secondary electrons is measured with a spin analyzer. In this example a LEED (low energy electron diffraction) detector is used. The secondary electrons are slightly accelerated (~ 100 V) and then scattered at a W(001) surface. The intensity of two opposing (2,0) LEED spots shows an asymmetry if the spin polarization of the secondary electrons is perpendicular to the axis that connects these two spots and lies within the scattering plane. In this example more electrons are registered in the lower counter (Ch 1). One can therefore conclude that the projection of the magnetization vector on the x -axis (the component m_x) at the point where the beam is currently focused is negative. Two additional counters, positioned along the axis which is perpendicular to the plane of this figure, yield information about the y component of the magnetization vector m_y . With SEMPA, two components of the magnetization vector \mathbf{m} can be measured simultaneously.

[161]. The working principle of SEMPA is illustrated in Fig. 2.3. SEMPA combines the high spatial resolution of a scanning electron microscope with the ability to determine the distribution of magnetic moments within the sample by measuring the spin polarization of the secondary electrons. Since electrons need to be accelerated to high energies to be analyzed in a detector of the Mott type [158], the experimental setup of Koike and Hayakawa [160] was rather large. Until now, various improvements have been made to Mott detectors that led to a more compact design [162–168].

However, other types of detectors have since been developed [169]. They work at lower energies and are therefore inherently smaller. The most common ones make use of spin-dependent scattering of electrons at a surface, which is again due to the spin-orbit interaction. One type is based on low-energy diffuse scattering (LEDS) of the polarized electrons at a polycrystalline Au film [170, 171]. The LEDS type of detector is currently in operation at the SEMPA of the National Institute of Standards and Technology (NIST) [169].

Another type of the smaller detectors is based on low-energy electron diffraction (LEED) at a W(001) single crystal [172, 173]. The first implementation of the LEED detector in SEMPA was done by Oepen and Kirschner [174, 175]. A detector of the LEED type is being used at the

SEMPA machines of the Institute of Applied Physics in Hamburg [176], one of which was used to conduct the measurements that are presented in this thesis.

Common to all spin detectors is the fact that only the projection of the electron polarization on the plane perpendicular to the direction of the incident SE beam is measured. The SEMPA at NIST has two detectors available that are aligned perpendicular to each other and a beam splitter, which allows for a simultaneous measurement of all three magnetization components [177]. A different method for getting access to all three components of the magnetization is by rotating the electron spin on its way through the detector [178, 179].

Since a detector of the LEED type was used to obtain the data that is presented in this thesis, a detailed description of the working principle of SEMPA is given based on this type of detector in the following section.

2.2.2 SEMPA Imaging With a LEED Detector

A schematic illustration of our SEMPA machine, which uses a LEED detector for the analysis of spin polarization, is shown in Fig. 2.3. The secondary-electron beam is diffracted at the (001) surface of a tungsten crystal in normal incidence [84]. The spin-dependent intensities of four (2,0) LEED spots are simultaneously monitored by four micro-channel plates [180–182] and the respective electronic devices that discriminate and count the single-electron pulses. Scattering at a single crystal in contrast to an amorphous material requires a very clean surface, which makes UHV⁴ conditions necessary within the detector. The important aspects in maximizing the efficiency of this type of detector and therefore the quality of the acquired images as well as some characteristic experimental requirements are discussed in this section. The discussion will deal with the different parts of the experimental setup as they follow along the path of the electrons (see also Fig. 2.3). Let us therefore start at the electron gun, which is required for the generation of an electron beam.

Generation of the Electron Beam

An electron gun is required to generate a primary current of unpolarized electrons that is used to probe the magnetic properties of the surface of interest. The most important aspects of the electron gun are:

- A high beam current (high number of primary electrons). The number of secondary electrons (SE) that are generated is directly proportional to the beam current. More SE lead to a reduction in the imaging time and/or to a decrease in the statistical error of the resulting image. Both is beneficial for SEMPA.
- A small beam diameter resulting in a high resolution. While this is somewhat contrary to the previous point, a trade-off between a high beam current and a high resolution has to be found.

⁴UHV = Ultra-high vacuum. In SEMPA the pressure should at least be in the 10^{-10} mbar range.

- The generation of a beam with the above-mentioned characteristics at a low accelerating voltage. A low accelerating voltage U_a is preferred in SEMPA, as the number of secondary electrons that are emitted from the sample (SE yield) increases with decreasing U_a (for electron energies above something like 600 eV) [183, p. 153 f].
- The ability to work at a (relatively) high working distance. The electron gun shares the half-space above the sample with the spin-detector. The front end of both devices has a certain spatial dimension, which means that they can not both be brought infinitely close to the sample for geometrical reasons. In our setup, a working distance of 8 mm is given for both columns by the geometry [84].
- The primary electron gun needs to be able to work under and maintain UHV. This means that it needs to be bakeable and must not contain any materials that degas under UHV conditions.
- SEMPA images require longer imaging times than SEM images. The Gun therefore needs to be particularly stable, which means that thermal drift has to be minimized to acquire a stable beam position.

These requirements are fulfilled very well by the UHV version of the Zeiss Gemini system [84]. For a beam current of 1 nA and a working distance of 8 mm at $U_a = 3$ kV a resolution of 7.5 nm is specified [84]. For SEMPA imaging, the gun is currently operated at 6 kV and produces a beam current of about 5 nA [184]. A beam current of 5 nA corresponds to 3×10^{10} incident electrons per second.

In our setup, the beam of primary electrons hits the surface of any plain sample at an angle of $\theta = 65^\circ$ with respect to the surface normal. While this decreases the maximum resolution in y direction by a factor of 2.4 (see chapter 5.2.2), it increases the secondary electron yield by a factor of 2-4 (with respect to normal incidence) [183, p. 156]. Since it is not possible to position both, the SEM column and the spin-detector, in a position where they can operate at normal incidence, it is favorable to deviate from normal incidence with the SEM column rather than with the spin-detector [84]. The reasons for this will become clear later on in this section. For high-resolution SEM imaging it is however possible to tilt the sample stage towards normal incidence and to reduce the working distance to 1 - 2 mm. In this mode the in-lens detector of the Zeiss Gemini system is used for imaging.

Interaction with the Sample Surface

The primary electron beam generates two types of electrons when interacting with the surface of a sample: Backscattered electrons (BSE) and secondary electrons (SE) [183]. The backscattered electrons have (per definition) an energy of more than 50 eV. They are considered as electrons that stem from the primary beam, which may have undergone several processes of energy loss. The main peak in the BSE distribution stems from electrons that are elastically scattered from the surface. Depending on the sample material this peak shows at approximately 90 % of the energy of primary electrons [183, p. 149]. The BSE are unpolarized electrons of the primary beam, they therefore carry no spin-information about the sample and only contribute to the background signal of a SEMPA image if they are detected.

As a result of the high kinetic energy of BSE, almost none of them are detected in SEMPA for two reasons: First, as in billiard, BSE are mostly reflected under an angle that is opposite to their angle of incidence [183, p. 147]. Second, due to their high kinetic energy, the accelerating voltage of the spin detector is not sufficient to change their trajectory sufficiently so that they can enter the spin detector. Only a small percentage of the BSE is reflected close enough to the surface normal of the sample to be able to reach the tungsten crystal. For this small percentage of BSE, however, another filtering mechanism applies. Because of the energy filtering capabilities of the spin-detector, the BSE are scattered at an angle that does not allow them to enter the electron counters⁵.

The secondary electrons are (per definition) electrons with an energy below 50 eV. Since SE are emitted directly from the sample material, they carry spin-information about the sample, *i.e.* they are spin polarized. The spin of the secondary electrons is aligned anti-parallel to the magnetization at their point of origin [154]. The degree of spin polarization depends on their energy (see Fig. 2.2a). In $3d$ transition metals, the spin polarization is higher for electrons of lower energy. This is due to a scattering of the minority electrons into the holes of the d -bands on their way to the surface [185]. The level of high polarization for low-energy electrons coincides with a peak in the secondary electron distribution (see Fig. 2.2a), which is beneficial for SEMPA. In addition to this decrease for lower energies, smaller features are superimposed to the distribution of polarization with energy. These effects are a result of the band-structure of the material [84].

The number of secondary electrons that are emitted into a certain direction follows Lambert's cosine law [183, p. 162]. This means that the number of SE that are detected in a given segment of space is proportional to $\cos \theta$ (θ is again being measured with respect to the surface normal) and is hence maximal along the surface normal. The number of electrons that are registered can therefore be maximized when the spin detector is positioned in normal take-off geometry [84].

Scattering at the Tungsten Crystal

The SE that are generated at the surface of the sample are guided towards and into the spin detector by a gradient in potential of 56 V mm^{-1} that extends into the experimental chamber. The gradient is generated by the first acceleration lens of the spin detector [84]. The beam of SE is then parallelized by a drift tube and directed towards the (001) surface of a tungsten single crystal. A quadrupole optics allows for the adjustment of the beam position, which is required to maximize the number of electrons that find their way through the detector and into the counting system [84].

When the SE reach the tungsten crystal they are scattered at the W(001) surface. The number of electrons that are elastically scattered with respect to the number of incoming electrons is defined as the reflectivity R . The reflectivity depends on the kinetic energy of the incoming electrons and has a maximum of $R = 0.11 \%$ at 110 eV for the (2,0) beams [186, p. 85] (see also Fig. 2.2b). However, not only the reflectivity depends on the SE energy, but also the probability that an electron of a given spin direction is predominantly scattered into one of two opposing (2,0) beams. The asymmetry in scattering amplitudes, the Sherman function S [187],

⁵Details on the energy filtering capability of the spin detector are given in the following section "Scattering at the Tungsten Crystal" and in [84].

is generated by a difference in the differential cross section σ for electrons of two opposing spin directions [186, p. 12]:

$$S = \frac{\sigma_{\uparrow} - \sigma_{\downarrow}}{\sigma_{\uparrow} + \sigma_{\downarrow}} \quad (2.3)$$

The cross section for this process shows an interference pattern, the peaks of which are determined by the electronic wavelength λ and the position of which hence depends on the kinetic energy of the incident electrons [186, p. 12]. The interference pattern is slightly shifted along the θ -axis for electrons of two opposing spin directions due to the spin-orbit term (see Eq. (2.1)). The energy dependence of the Sherman function S of the (2,0) beams is shown in Fig. 2.2b. It shows several zero crossings for energies below 95 eV. Above 95 eV it stays negative, showing a region where S has its maximal values around 100 - 120 eV.

The total asymmetry $A = PS$ that shows in the intensity of two opposing LEED beams is a product of the polarization of the incident beam P and the Sherman function S . In terms of the number of electrons N that are registered in each of the beams the asymmetry A is defined for a fully polarized beam ($P = 1$, $A = S$) as [153, p. 56]:

$$A = \frac{N(2,0) - N(\bar{2},0)}{N(2,0) + N(\bar{2},0)} \quad (2.4)$$

However neither the asymmetry, nor the reflectivity alone determine the quality of a LEED detector. A good measure for the quality of a given detector is the error in the measured polarization ΔP that can be obtained. Assuming Poisson statistics, the error is given by [153, p. 243]:

$$\Delta P = \sqrt{\frac{1}{NS^2}} \quad (2.5)$$

Where $N = N(2,0) + N(\bar{2},0)$ is the number of electrons that are counted in two opposing LEED beams and is proportional to the reflectivity R . A is the above-mentioned asymmetry. Minimizing the error therefore means maximizing the quantity [84]

$$F_m = 2RS^2 \quad (2.6)$$

which is known as the ‘‘figure of merit’’ that was ultimately defined to obtain a measure for the quality of a Mott detector [186, p. 84]. To maximize F_m , one has to select an energy window in which the secondary electrons are allowed to pass. The fact that emission angle and incident energy of the electrons are entangled in LEED scattering comes in handy in solving this issue [84]. The energy window can be defined by inserting an aperture in front of the electron counters [84]. As a result of that, incoming electrons with a kinetic energy that is too high (low) are diffracted at the tungsten crystal under an angle that is too high (low) to allow for them to pass through the aperture. While the size and the distance of the aperture from the tungsten crystal

defines the width of the energy window, its angular position determines the relative position of the energy window.

A working point where the figure of merit is maximized lies at 104.5 eV [186, p. 86]. At this energy, the Sherman function S shows a shoulder and the reflectivity R is close to its peak value (see Fig. 2.2b). For fully polarized electrons ($P = 1$), the values $A = 0.28 \pm 0.02$ and $R = 2.2 \times 10^{-3}$ were obtained, resulting in $F_m = 1.7 \times 10^{-4}$ [186, p. 86]. Values for Mott detectors are in the range of $F_m = 0.2 - 1.0 \times 10^{-4}$ and for LEDS detectors $F_m = 1.0 - 2.0 \times 10^{-4}$ [169].

The energy of 104.5 eV is chosen as the central energy of the energy window in our system and defines the angle of $\theta = 40.64^\circ$ at which the centers of the apertures are located [84]. A SE polarization of $P = 1$ is however rather hypothetical, so that the dependence of SE polarization on energy (see Fig. 2.2a) has to be taken into account when a detector setup is designed [84]. Additionally, the transmission function, which defines the probability that an electron of a certain energy is transmitted into the electron counters, has to be optimized with respect to SE polarization P , reflectivity R , and asymmetry A [84]. Details on how this was done can be found in Ref. [84].

Since the process of LEED scattering is very surface sensitive, the tungsten crystal needs to be cleaned quite frequently [184]. Over time, the surface of the crystal becomes covered with hydrogen atoms originating from residual gas. The tungsten crystal is cleaned by flash heating to a temperature of 2500 K for about ten seconds [188, 189]. At a base pressure of 3×10^{-10} mbar (mainly hydrogen), constant imaging conditions can be maintained for one hour after flash cleaning [184]. By now, the base pressure of our chamber is at 3×10^{-11} mbar and even longer imaging times are possible.

Counting of Electrons

As discussed above, the electron multipliers are positioned behind an aperture. The aperture only allows for electrons to pass that are scattered under an particular angle and therefore have a particular energy. Additionally two retarding grids are installed behind the aperture [84]. While the first grid is set to the scattering potential, the second one is set to a voltage that is close to the sample ground (-102 V relative to the tungsten crystal) [176]. As a result of the negative potential, the SE generated at the tungsten crystal can not reach the electron counters and therefore do not contribute to the background signal (they do not carry any spin information about the sample). Additionally, a part of the inelastically scattered electrons is suppressed [84, 176].

While the majority of SEMPA machines detects electrons using channeltrons [190], the “SEMPA II” machine in Hamburg, at which this thesis was conducted, makes use of multi-channel plates (MCP) [180–182]. There are several reasons for this [176]: The width of the electrical pulse generated by the arrival of an electron at the plate is smaller for an MCP than for a channeltron (5 ns compared to 20 ns). Additionally, the dead-time is reduced to the range of the pulse duration, because the probability that an electron hits the same channel as the previous electron is very low. Both circumstances lead to an increase in the maximum count rates that can be processed of possibly up to 100 MHz [176]. Another reason for the usage of MCPs is their smaller size, which allows for a reduction of the total size of the spin detector so that

it can be placed within the main chamber, rendering the pumping and maintenance of an extra detection chamber unnecessary [176].

To increase the MCP lifetime and further reduce the probability of hitting the same channel twice, an additional lens for de-focusing is placed in front of the MCP. It spreads the (2,0) LEED beam and causes a more uniform illumination of the MCP assembly.

When an electron arrives at the MCP, an electrical pulse is generated and transmitted to a counter card which is connected to the measurement computer. The measurement software then increases the count of the array cell that corresponds to the current position of the electron beam by one (see next section).

Image Formation

The formation of an image in SEMPA is similar to the formation of an image in SEM (which is described in Ref. [148]) with the distinction that four detectors instead of one are active during the imaging process. The data of each of the four single-electron counters is simultaneously stored in a separate two-dimensional array while the primary electron beam is scanned across the surface. Like in SEM, the position of the active cell of these arrays (the cell that the data is written into) is correlated to the position of the primary electron beam on the surface of the sample.

Two parameters need to be defined before the imaging process is started. The size of the array and the time that is reserved for data collection in each of its cells, which is often denoted as the “pixel dwell time”. Common values in SEMPA imaging lie between 50 and 500 for one dimension of the array and a pixel dwell time in the range of 10 - 20 ms.

The data within each of the four arrays can be visualized as a grayscale image, which is exemplary shown for a SEMPA measurement of an iron whisker in the upper row of Fig. 2.4. Each pixel of the image is directly correlated to one cell of the array. The brightness of a pixel is proportional to the integer number (the number of electrons that were counted) that is stored in the corresponding cell. The four images consist of 128×128 pixel² and each single pixel was recorded for 10 ms. The whole data acquisition took 2 min and 44 s.

As the probability of an electron to be deflected into one of the four counters depends on its spin direction, each of the four channel images holds information about the spin-polarization of the secondary electrons. The brightness within an image is however additionally modulated by the mechanisms that give rise to contrast in conventional SEM imaging [191], which is in most cases mainly the topography of the surface. The topography-induced modulation is approximately the same for each of the four channels. It can hence be separated from the magnetic contrast. For instance summing up the intensities I of all four images eliminates the magnetic information from the resulting image, as it is the same as treating the four counters as one single detector:

$$I_{\text{Sum}} = I_1 + I_2 + I_3 + I_4 \quad (2.7)$$

The surface topography of the iron whisker is clearly visible in this “Sum” image in Fig. 2.4.

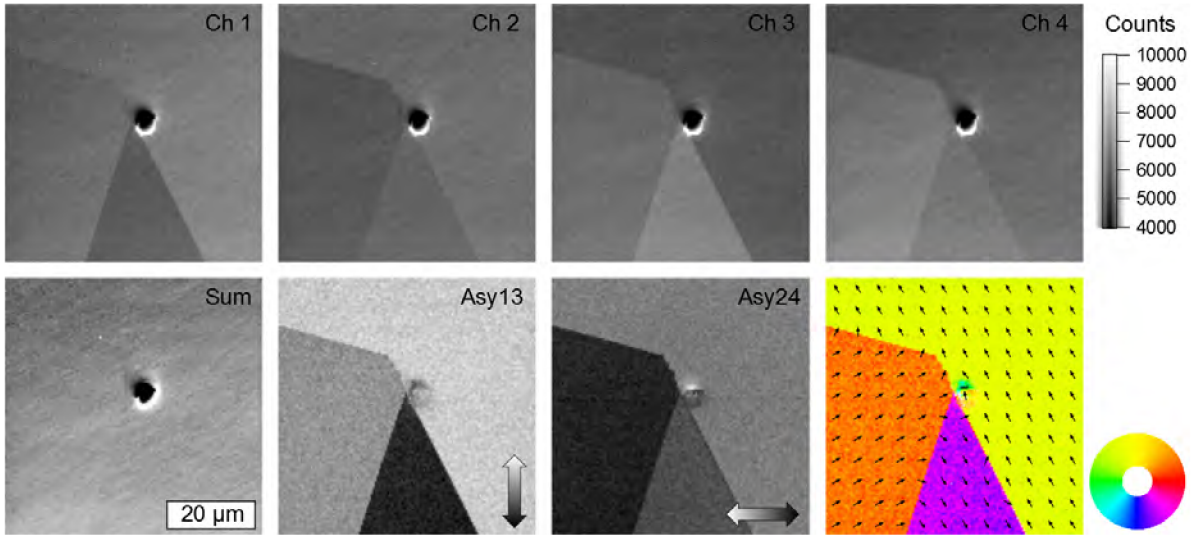


Figure 2.4: SEMPA images of an iron whisker. The images consist of 128×128 pixel² and were taken with a pixel dwell time of 10 ms. The raw images of the four channels are shown in the upper panels. In the four channels the magnetic contrast (triangular shaped structures) is overlain by the contrast due to topography or material (best seen at the dirt particle in the center of the images). When the intensity of the four channels is summed up (Sum) according to (2.7), the magnetic contrast is suppressed while the topographical and material contrast remains. When the asymmetry between two opposing channels (Asy13 and Asy24) is calculated by (2.8) and (2.9), the topographical contrast is strongly reduced and the magnetic contrast remains. The application of a color coding to the angular information that is contained within the asymmetry images (according to the color wheel) yields the false-color image that is shown in the bottom right corner.

The magnetic information (the asymmetry of (2.4)) can be extracted by subtracting the intensities that are recorded in two opposing counters:

$$I_{\text{Asy13}} = \frac{I_1 - I_3}{I_1 + I_3} \quad (2.8)$$

$$I_{\text{Asy24}} = \frac{I_2 - I_4}{I_2 + I_4} \quad (2.9)$$

These asymmetry images show a quantity proportional to the projection of the in-plane magnetization vector (\mathbf{m}_x and \mathbf{m}_y) on the axis perpendicular to the connection line between two opposing LEED spots. The asymmetry images contain information about the domain structure of the sample, which is clearly visible in Fig. 2.4. In these images the asymmetry amounts to 6.7%. The asymmetry information can be translated into a map of the in-plane magnetization angle θ when the experimental asymmetry E is known:

$$\theta = \arctan 2 \left(\frac{I_{\text{Asy24}} - E_{\text{Asy24}}}{I_{\text{Asy13}} - E_{\text{Asy13}}} \right) \quad (2.10)$$

For the determination of the experimental asymmetry E , a non-magnetic region of the sample or a two-dimensional histogram of the two asymmetry images can be used [83, p. 147] [192, 193]

(an example is also shown in chapter 5). The determination of E is crucial for the generation of the angle-map, as it is usually of the same order of magnitude as I . Since these additional parameters are required for the generation of an angle-map, the usage of the asymmetry images is often preferable because they are obtained directly from the raw data.

2.2.3 SEMPA in Comparison

Compared to other techniques of domain observation, SEMPA is a rather sophisticated one. It requires high-level technological equipment, very good vacuum conditions, and high-quality samples with a very clean surface [103, p. 104]. When these requirements are however fulfilled one has access to a “powerful tool for the investigation of magnetic domain structures in ultrathin films” [83, p. 164]. This tool allows for the determination of the orientation of the magnetization vector with very high precision. In modern machines, the magnetization vector can be probed with an angular resolution of 4° [84] and a spatial resolution of down to 3 nm [194]. All three components of the magnetization vector are thereby basically accessible [177–179]. Another pronounced characteristic of SEMPA is its sensitivity to the magnetization in the topmost surface layers below 1 nm [103, p. 105].

Since electrons are used as the carrier of information in SEMPA, the strength of externally applied magnetic fields is limited. With some additional modifications and a locally strongly confined magnetic field it is however possible to perform SEMPA measurements in magnetic fields of up to 100 mT [195].

The imaging capabilities of SEMPA are applied to experimental systems in chapters 3, 4, and 5 of this thesis.

3 Spin-Transfer-Torque Parameters for a Magnetic Vortex Core

The stationary displacement of a magnetic vortex core by an electric current yields information on the interaction between electrical currents and magnetization patterns. This information can be used to optimize magnetic storage devices, in which the writing process relies on spin-transfer torque (see chapter 1). Using a robust measurement scheme [196], all of the relevant spin-transfer torque parameters α , β and u were obtained [80]. Before the measurement principle is discussed, a review of the theoretical background will be given, starting with the theory of micromagnetics.

3.1 Micromagnetics

The theory of micromagnetics enables the description of magnetism on the length scale from one nanometer up to several micrometers [103]. It is thus useful for the study of magnetic domains, domain walls and vortices. In this section the theory of micromagnetics will be derived, starting at the atomic level.

On the atomic level, the magnetic moment μ is quantum-mechanically generated by the spin of the electron μ_S as well as by its orbital motion around the atomic nucleus μ_L . Both are connected to their appropriate quantum numbers S and L via the respective g -factors

$$\mu = \mu_S + \mu_L = -\frac{e}{2m_e}(g_S \mathbf{S} + g_L \mathbf{L}) \quad (3.1)$$

While the g factor of the electron is almost exactly equal to $g_S = 2$ [197], the orbital g factor equals $g_L = 1$. In “ferromagnetic substances [...] the orbital motion electively contributes something like 10 percent and the spin motion 90 percent of the saturation magnetization“ [198]. The contribution of the orbital motion is therefore sometimes neglected.

With respect to the total angular momentum $J = L + S$, the magnetic moment can further be expressed as:

$$\mu = -\frac{e}{2m_e} g_J J = -\mu_B g_J \frac{J}{\hbar} \quad (3.2)$$

Where g_J is the Landé g -factor of the electron and $\mu_B = \frac{e\hbar}{2m_e}$ the Bohr magneton. A first approximation on the way to micromagnetics in solid state materials is to only consider the total magnetic moment of an atom, instead of all the single magnetic moments of the contributing electrons. The magnetic moment of the atom is located at the respective lattice site

and is strongly coupled to the neighboring moments by the exchange interaction. A variation in the orientation of the magnetic moments therefore occurs on a length scale larger than one lattice constant. The physical property that is used to describe this length scale is either the magnetostatic or the magnetocrystalline exchange length l_{ms} or l_{mc} , whichever is shorter [199]:

$$l_{\text{ms}} = \sqrt{\frac{2A}{\mu_0 M_s^2}} \quad (3.3)$$

$$l_{\text{mc}} = \sqrt{\frac{A}{K_u}} \quad (3.4)$$

In the calculation of the exchange length, the exchange stiffness A is compared to the saturation magnetization M_s , or the uniaxial anisotropy K_u respectively. For the 3d transition metal ferromagnets Iron, Cobalt, and Nickel, the exchange length is of the order of a few nanometers and thereby larger than the lattice constant which is of the order of a few Å. Thus, a variation of the magnetic moments will occur on a scale that is larger than a few lattice constants. This justifies the final approximation on the way to micromagnetics: The discrete magnetic moments μ are replaced by a continuous vector field \mathbf{M} [200]:

$$\mathbf{M} = \frac{N}{V} \mu_{\text{B}} g \mathbf{S} \quad (3.5)$$

In this approximation N spins \mathbf{S} in a unit volume V are considered to be parallel to each other. The continuous vector field \mathbf{M} is often denoted as “the magnetization”. The magnetization is a measure for the average density of the magnetic moments.

For the sake of simplicity, the vector \mathbf{M} is commonly replaced by the unit vector $\mathbf{m} = \mathbf{M}/M_s$. The quantity M_s hereby denotes the saturation magnetization per unit volume, which is achieved when all magnetic moments point in the same direction.

3.1.1 Torques and Energies in Micromagnetics

The temporal evolution of the magnetization \mathbf{m} at zero temperature can be fully described when the torque \mathbf{T} on the magnetization is known. A torque occurs when the direction of the magnetization vector deviates from its energetic minimum position. A variety of mechanisms contribute to the total energy of the magnetization. Their respective effects on the magnetization can be represented by their individual torques, which was first done in 1935 by Landau and Lifshitz [71]. They introduced an effective torque $\mathbf{T}_{\text{field}}$, which is due to an effective field that arises as a combination of all the energetic contributions. This description leads to a spiraled motion of the magnetic moment around the direction of the effective field. An additional damping term causes a decrease of the amplitude of the spiraled motion over time until the magnetization is aligned with the effective field. The theory was developed further by Brown [201, 202].

Twenty years later Gilbert [77, 203] added an alternative formulation of the phenomenological damping term $\mathbf{T}_{\text{damping}}$, which is the formalism that is most commonly used today. The effect of an electron current on the local magnetization, which was first predicted in the seventies [204], was only introduced half a century later. It can be described as an additional torque,

the spin-transfer torque \mathbf{T}_{st} [53, 73, 74, 205]. The temporal evolution of the magnetization \mathbf{m} , given by the total torque it is subjected to, can be written as

$$\frac{\partial \mathbf{m}}{\partial t} = \mathbf{T} = \mathbf{T}_{\text{field}} + \mathbf{T}_{\text{damping}} + \mathbf{T}_{\text{st}} \quad (3.6)$$

A detailed description of the individual torques is given in the following sections.

3.1.2 Effective Field

The torque caused by external and internal fields that are combined as an effective field \mathbf{H}_{eff} is given as

$$\mathbf{T}_{\text{field}} = -\gamma \mathbf{m} \times \mu_0 \mathbf{H}_{\text{eff}} \quad (3.7)$$

with the gyromagnetic ratio γ . The gyromagnetic ratio γ is defined as the ratio of the magnetic dipole moment to the angular momentum of an electron

$$\gamma = g \cdot \frac{e}{2m_e} \quad (3.8)$$

including the Landé factor g and the charge e and mass m_e of the electron.

The effective field \mathbf{H}_{eff} consists of the external field \mathbf{H}_{ext} , the exchange field \mathbf{H}_{ex} , the demagnetization field \mathbf{H}_{d} , and the anisotropy field \mathbf{H}_{a} . Although the magneto-crystalline anisotropy and the exchange energy do not give rise to a real physical field, their influence on the magnetization can be described as a field-like contribution [206]. Details on the individual field contributions will be given in the following sections.

External Field

The energy that arises from an external magnetic field \mathbf{H}_{ext} is given by an integral over the scalar product of the magnetization and the external field in the unit volume V :

$$E_{\text{ext}} = -\mu_0 M_s \int \mathbf{m} \cdot \mathbf{H}_{\text{ext}} dV \quad (3.9)$$

The energy due to an external field reaches its minimum when the magnetization is aligned along the direction of the external field. It is also called “Zeeman energy” after the Dutch physicist Pieter Zeeman.

Exchange Field

The exchange interaction tends to align two neighboring spins \mathbf{S}_i and \mathbf{S}_j either parallel or anti-parallel to each other. The exchange energy E_{ex} between these two spins is given by [207, 208]:

$$E_{\text{ex}} = -2J_{ij} \mathbf{S}_i \cdot \mathbf{S}_j \quad (3.10)$$

A parallel alignment of the spins (ferromagnetism) is observed when the exchange integral J_{ij} is positive. When the exchange integral J_{ij} is negative, an anti-parallel alignment between the individual spins (antiferromagnetism) is preferred. Expressing the effect of the exchange interaction as a field-like contribution is most conveniently done by comparing (3.10) to the energy of a spin \mathbf{S}_i in an external field, the effective “exchange field” \mathbf{H}_{ex} [209]:

$$E_{\text{ex}} = \mu_0 g \mu_B \mathbf{S}_i \mathbf{H}_{\text{ex}} \quad (3.11)$$

The exchange field that is experienced by \mathbf{S}_i stems from all the surrounding spins \mathbf{S}_j . The contributions of each of these spins to the effective field therefore need to be summed up:

$$\mathbf{H}_{\text{ex}} = \frac{2}{\mu_0 g \mu_B} \sum J_{ij} \mathbf{S}_j \quad (3.12)$$

As the exchange integral J_{ij} quickly diminishes as the distance between two atoms increases, it is usually sufficient to take into account the interaction with the nearest neighbors. The quantum-mechanically motivated exchange field \mathbf{H}_{ex} corresponds to the molecular field that was once introduced by Pierre Weiss to explain the existence of ferromagnetism at room temperature [102, 210].

In the continuum approximation the exchange field \mathbf{H}_{ex} can be derived from the exchange energy as [200]:

$$\mu_0 \mathbf{H}_{\text{ex}} = \frac{2A}{M_s^2} \nabla^2 \mathbf{m} \quad (3.13)$$

The exchange integral J is converted to the exchange stiffness A by [200]:

$$A = \frac{2nJS^2}{a} \quad (3.14)$$

This conversion incorporates the physical properties of the crystal lattice, the lattice constant a and the type of the lattice $n = 1$ for sc, $n = 2$ for bcc, and $n = 4$ for fcc, in the exchange stiffness A .

Demagnetization Field

The demagnetizing field H_d is caused by changes in the continuous magnetization that give rise to magnetic charges. A variation in the direction of the magnetization causes a magnetic volume charge:

$$\rho_m = -\mu_0 M_s \nabla \cdot \mathbf{m} \quad (3.15)$$

The introduction of a surface gives rise to another magnetic charge, the surface charge:

$$\sigma_m = \mu_0 M_s \mathbf{n} \cdot \mathbf{m} \quad (3.16)$$

A surface charge is generated when a component of the magnetization vector \mathbf{m} points parallel to the surface normal \mathbf{n} . The demagnetizing field at point \mathbf{r} can be obtained by integrating over surface and volume charges [199, 202]:

$$\mu_0 H_d(\mathbf{r}) = -\frac{\mu_0}{4\pi} \int \frac{(\mathbf{r} - \mathbf{r}') \rho_m(\mathbf{r}')}{|\mathbf{r} - \mathbf{r}'|^3} dV' + \frac{\mu_0}{4\pi} \int \frac{(\mathbf{r} - \mathbf{r}') \sigma_m(\mathbf{r}')}{|\mathbf{r} - \mathbf{r}'|^3} dS' \quad (3.17)$$

The demagnetizing field causes an energy E_d proportional to its magnitude and depends on its relative orientation to the magnetization:

$$E_d = -\frac{\mu_0 M_s}{2} \int \mathbf{H}_d \mathbf{m} dV \quad (3.18)$$

As a self-energy, the demagnetization energy differs from the Zeeman energy by a factor of 1/2 [199]. The demagnetizing field causes a torque that tends to align the magnetization in a direction in which magnetic charges are reduced. This alignment, however, also reduces the demagnetizing field itself. A more detailed discussion on the origin and physics of magnetic charges at hand of an experimental sample system is given in chapter 6.

Anisotropy Field

When the energy of the magnetization in a given material depends on its orientation in real space, the material is said to exhibit magnetic anisotropy. The anisotropy might be caused by the shape of the sample, crystal symmetry, stress, or directed atomic pair ordering [209]. A material can exhibit an anisotropy along one or more axes which are referred to as “easy axes”. The most simple case is the first order of the magneto-crystalline uniaxial anisotropy where the anisotropy energy E_a is given as [199]:

$$E_a = K_u [1 - (\mathbf{m} \cdot \mathbf{k})^2] \quad (3.19)$$

The anisotropy energy is equal to $K_u > 0$ and maximal, when the magnetization \mathbf{m} is oriented perpendicular to the unit vector \mathbf{k} representing the easy axis. To classify whether the anisotropic behavior of a material is dominated by the magneto-crystalline anisotropy or by the shape anisotropy the quality factor Q is introduced:

$$Q = \frac{K_u}{\frac{\mu_0}{2} M_s^2} \quad (3.20)$$

Materials with $Q \ll 1$ are classified as “soft magnetic” whereas materials with $Q > 1$ are classified as “hard magnetic”. A comparison of the anisotropy energy (3.19) to the Zeeman energy (3.9) yields the anisotropy field H_a [211]:

$$\mu_0 \mathbf{H}_a = \frac{2K_u}{M_s} (\mathbf{m} \cdot \mathbf{k}) \mathbf{k} \quad (3.21)$$

The anisotropy field tends to align the magnetization with the easy axis.

3.1.3 Damping

If the micromagnetic equation (3.6) only consisted of a torque that is due to an effective field, it would cause the magnetization to gyrate around the direction of this field forever. Since this is not the case in realistic materials, a friction term was phenomenologically introduced into the equation to allow for the dissipation of energy. This damping torque has to fulfill two requirements:

1. It should cause “the magnetization to spiral in towards the effective field without increasing the precession rate” [77].
2. It must preserve the magnitude of the magnetization at any time.

In the original formulation of Landau and Lifshitz [71], the damping torque is of the form:

$$T_{LL} = -\eta [\mathbf{m} \times (\mathbf{m} \times \mathbf{H}_{\text{eff}})] \quad (3.22)$$

The strength of the damping is parametrized by a phenomenologically introduced dimensionless damping parameter η . A slightly different formulation of the damping torque was later introduced by Gilbert [77, 203]:

$$T_{\text{Gilbert}} = \alpha \mathbf{m} \times \frac{\partial \mathbf{m}}{\partial t} \quad (3.23)$$

Both formulations fulfill the requirements that are stated above. “The difference between the two is usually very small and almost all theoretical” [212] and “experiment cannot distinguish the two” [212]. While both formalisms are used in literature, there is a tendency towards Gilbert damping in modern literature as it “is often considered as the more fundamental one” [199].

It was later discovered that the intrinsic origin of damping lies within the spin-orbit coupling [213–215]. “As the magnetization precesses, the spin-orbit interaction changes the energy of the electronic states, pushing some occupied states above the Fermi level and some unoccupied states below the Fermi level” [214]. This leads to the creation of electron-hole pairs near the Fermi level. While these electron-hole pairs relax by lattice scattering, energy is dissipated to the lattice. The intrinsic damping is anti-proportional to the spin-relaxation rate τ_{sr} [216].

Additionally, the damping is enhanced extrinsically by two-magnon-scattering at impurities and interfaces [217–219]. The damping constant is thereby a good measure for the quality of a given film system [220].

If not stated otherwise, the formulation of Gilbert [77, 203] (3.23) will be used throughout this thesis. It has to be noted that also the torque caused by an effective field (3.7) is slightly different in the formulation of Landau and Lifshitz [71]. Using the formulation of Gilbert for the damping mechanism, equation (3.7) is denoted as the “Landau-Lifshitz-Gilbert equation” or short “LLG”.

3.1.4 Spin-Transfer

The main contribution to the magnetization in a $3d$ transition metal ferromagnet (Co, Fe, Ni) stems from the strongly localized electronic $3d$ states that exhibit a high density of states and a high polarization around the Fermi level [209]. The main contribution to charge transport, however, comes from the $4s$ states that make up the conduction band [209]. The spins of the electrons in the respective states are coupled via the s - d exchange interaction [52, 221]. This coupling enables the transfer of spin momentum from one to the other, a phenomenon entitled as “spin-transfer”.

Adiabatic Spin-Transfer

The phenomenon of spin-transfer causes electrons that pass through a ferromagnetic region to become spin polarized. This means that they become aligned with the majority spin of the localized electrons around the Fermi level. When the conduction electrons flow through a region where the spin of the localized electrons (and therefore the magnetization) changes they will experience a torque, as the s - d exchange interaction tends to align them with the localized electrons. Since the total spin momentum has to be conserved, the localized electrons experience an identical torque in the opposite direction (after Newton’s third law: *actio = reactio*) [52, 53]. A torque on the local magnetization is hence exerted by a spin polarized current.

It has been found that this torque has to be expressed as an additional term in the Landau-Lifshitz-Gilbert equation (LLG) and can not be included in the effective-field term [205]. The additional torque was derived under the assumption that the spin of the $4s$ conduction electrons is parallel to the spin of the localized $3d$ electrons at every point inside the magnetic material and is therefore denoted as the “adiabatic spin-transfer torque” [74, 205]:

$$\mathbf{T}_{\text{st}} = (\mathbf{u} \cdot \nabla) \mathbf{m} \quad (3.24)$$

Its strength scales with the spin drift velocity \mathbf{u} , which “directly represents the rate of spin angular momentum transfer from the conduction electrons to the local moments” [222]. It is further proportional to the derivative of the magnetization pattern in the direction of the spin drift velocity \mathbf{u} , which is parallel to the technical current direction [73, 74]¹:

$$\mathbf{u} = \frac{g\mu_B P}{2eM_s} \mathbf{j} \quad (3.25)$$

The spin drift velocity is proportional to the Landé factor g , the current spin polarization P , the density of the traversing current j , and anti-proportional to the saturation magnetization M_s . It has to be noted that \mathbf{j} is parallel to the technical current direction and therefore anti-parallel to the electron flow.

The adiabatic spin-transfer torque is present not only at interfaces between magnetic and unmagnetic materials [223–225] but also in regions where the magnetization varies, like domain walls and vortices [226].

¹In the framework of Zhang and Li [73], the spin drift velocity is defined slightly different as $u/(1 + \xi^2)$, with ξ being the nonadiabatic parameter (see next section). The definition of Thiaville *et al.* [74] which is given in (3.25) will be used throughout this thesis.

Nonadiabatic Spin-Transfer

In realistic materials, a slight mistracking may be present between the localized electrons and the conduction electrons. This mistracking gives rise to yet another torque contribution, the “nonadiabatic spin-transfer torque” [73, 74], which has to be added to (3.24) as another separate term:

$$\mathbf{T}_{\text{st}} = (\mathbf{u} \cdot \nabla) \mathbf{m} - \beta \mathbf{m} \times [(\mathbf{u} \cdot \nabla) \mathbf{m}] \quad (3.26)$$

The strength of the mistracking is parametrized by a phenomenologically introduced parameter β . It is directly evident from (3.26) that the nonadiabatic torque is perpendicular to the adiabatic one. Because of the similar geometry compared to the torque that is caused by an effective field (3.7), the nonadiabatic spin-transfer torque is often called the “field-like torque” [50].

There are two major contributions that produce mistracking in a magnetic structure: One caused by spin relaxation processes β_{sr} and one that is truly nonadiabatic and nonlocal in nature β_{na} [78]:

$$\beta = \beta_{\text{sr}} + \beta_{\text{na}} \quad (3.27)$$

The spin relaxation term β_{sr} can be derived in the limit of a slowly varying magnetization, which is often denoted as “the adiabatic limit” [75, 78]. The adiabatic approximation is valid when the magnetization varies on a length scale that is greater than the spin diffusion length λ_{sd} [73, 74]. This length can be seen as the length on which a non-equilibrium spin population propagates before it relaxes toward equilibrium. The spin diffusion length is connected to the spin relaxation time τ_{sr} [216, 227] and the diffusion constant D_0 via $\lambda_{\text{sd}} = \sqrt{D_0 \tau_{\text{sr}}}$ [228]. Spin diffusion lengths in metallic ferromagnets and their alloys range from 3-4 nm in permalloy ($\text{Ni}_{80}\text{Fe}_{20}$) up to 60 nm in cobalt (tabulated values can be found in Ref. [229]).

Theoretical considerations show that the spin relaxation term β_{sr} is of the order of the damping constant α [230, 231]. Its physical origin lies within spin-flip scattering and spin-orbit interaction with impurities [75, 232–235]. The spin-flip contribution can be determined by $\beta_{\text{sr}} = \hbar / (J \tau_{\text{sr}})$ [73]. The spin relaxation time τ_{sr} describes the time delay in which the spin of the conduction electrons follows the temporally varying magnetization, a phenomenon known as “breathing Fermi surface” [236].

The truly nonadiabatic contribution β_{na} is dominant in structures where a large magnetization gradient is present. Its magnitude is proportional to the domain wall resistance [73, 237]. Depending on the steepness of the magnetization gradient, which is proportional to the width of a domain wall, several physical mechanisms come into play [76]. For magnetic textures with an extension below 10 nm, like vortex structures, the nonadiabaticity is increased by spin diffusion [238–240]. The magnitude of the diffusion current however strongly depends on the internal structure of the magnetic texture or the domain wall. It has for instance a much higher significance for vortex walls compared to transverse walls [238–240].

For even narrower walls with dimensions smaller than 5 nm ballistic spin-mistracking further increases the nonadiabaticity [241, 242]. This is the truly “nonadiabatic” process which physically stems from the fact that the variation in the magnetic structure is too swift for the spins

of the conduction electrons to follow. Its strength decays exponentially as the width of the wall increases [241].

Going even further, when the domain wall only consists of one or two atomic layers, the reflection of electrons leads to momentum transfer which also contributes to the nonadiabatic contribution [237].

All these processes contributing to β_{na} are nonlocal in their nature and thereby actually go beyond of what can be described in the framework of the Landau-Lifshitz-Gilbert equation. However, “For all but extreme cases, these contributions can be captured through effective values of local parameters” [76].

The description used here, as well as some of the aforementioned derivations have been obtained using the *s-d* model, where the conduction electrons are clearly discriminated from the localized spins. “However, in reality, this separation of degrees of freedom is not always so obvious; since in an itinerant picture, all electronic bands contribute to both conduction and magnetism with different weights” [75].

Further information on spin-transfer torques can be found in one of the several review articles that have been written on this topic [76, 78, 243–249].

Spin-Orbit Torque

For material systems with a strong spin-orbit interaction that is induced by a lack of inversion symmetry, an additional torque arises [250, 251]. A strong spin-orbit interaction leads to the generation of a non-equilibrium spin density by a passing current, a phenomenon known as the “Edelstein effect” [252]. In a relativistic picture, the non-equilibrium spin density gives rise to an additional torque on the magnetization, the “spin-orbit torque” [253]. The spin-orbit torque can not be included in the conventional formalism of spin-transfer torques as it has a different symmetry and origin [250]:

- It does not depend on the magnetization gradient.
- It is independent of the magnetic configuration.
- It is distributed homogeneously through regions where the interfaces do not change.
- It does not involve the transfer of spin angular momentum from conduction electrons to localized electrons.
- It transfers orbital momentum from the lattice to the spin system.

Instead of expanding the mechanism of spin-transfer torques, the spin-orbit torque can rather be described as an additional effective magnetic field [253], the direction of which depends “on the orientation of the applied current relative to the crystallographic axes” [251].

The strong spin-orbit interaction can however also have an effect on the “conventional” spin-transfer torques by increasing β_{sr} through an increase in the spin-flip rate $1/\tau_{sf}$ [250]. In the material systems discussed in this chapter, the spin orbit interaction is rather weak and spin-orbit torques can hence be neglected.

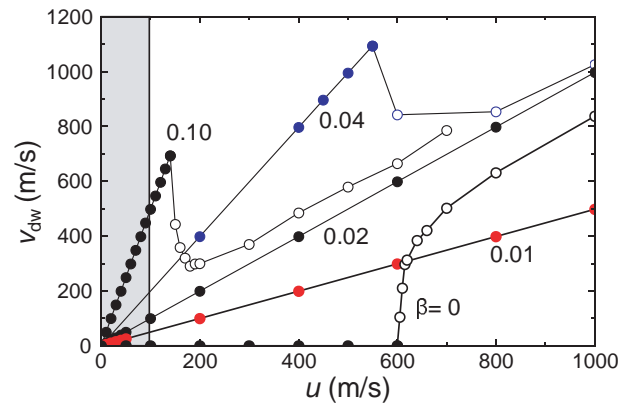


Figure 3.1: Velocity of a transverse domain wall, simulated for a small and perfect wire (reproduced from [74]) for different values of the nonadiabatic parameter β . The shaded area highlights the experimentally available range for the spin drift velocity u . Starting from zero, the domain wall velocity v_{dw} increases proportional to β/α as expected from (3.28). A critical value of u is observed where the wall velocity suddenly deviates from this behavior and approaches a tangent of unity. This point can be regarded similar to the Walker breakdown field in field driven motion [254, 255]. The nucleation of vortices is denoted by open symbols and can be observed above this critical point, causing the terminal velocity to be reduced.

Velocity of Néel Walls Driven by Spin-Transfer

One of the most important properties for technical spin-transfer torque applications (for instance Racetrack memory [67, 68], see chapter 1) is the velocity that can be reached by a magnetic domain wall that is driven by an electric current. The domain wall velocity was addressed in the very first publications that included the nonadiabatic contribution [73, 74]. In the framework of the Landau-Lifshitz-Gilbert equation, the effect of spin-transfer torques on domain walls was evaluated by micromagnetic simulations (for a transverse wall and a vortex wall in an in-plane system) [74] and by theoretical considerations (for a symmetric Néel wall) [73]. Both yielded similar results, which are shortly summarized here and displayed in Fig. 3.1. It has to be noted that different results are obtained when Landau-Lifshitz damping is considered instead of Gilbert damping, which might be a way to experimentally distinguish between the two formalisms [212]. This chapter will however concentrate on the results that were obtained with Gilbert damping

Let us first consider the case of pure adiabatic spin-transfer ($\beta = 0$, compare also Fig. 3.1). In this case the adiabatic spin-transfer torque initially leads to a movement and a cumulative distortion of the domain wall [73]. The distortion increases until it completely absorbs the adiabatic spin angular momentum and the domain wall stops [73]. It can only be moved further by increasing the current density j and thereby the spin drift velocity $u \propto j$. Above a critical value u_c the Walker breakdown [254, 255] sets in resulting in “the periodic injection of antivortices at wire edges, which cross the wire width and are expelled” [74]. Supported by this mechanism, the domain wall motion continues. When u is increased above the critical value, the speed of the domain wall v_{dw} approaches the spin drift velocity $v_{\text{dw}} = u$.

Let us now consider the case of adiabatic and nonadiabatic spin-transfer ($\beta \neq 0$, compare also Fig. 3.1). In this case an initial finite wall velocity is sustained, even as the domain wall becomes distorted. In the idealized model without extrinsic pinning no threshold current is found for the wall motion [74]. However, as u is increased further, the Walker breakdown occurs and the velocity tends toward $v_{\text{dw}} = u$. In the regime below the Walker breakdown the wall velocity v_{dw} increases linearly with u as [73, 74, 256]:

$$v_{\text{dw}} = \frac{\beta}{\alpha} u \quad (3.28)$$

It is proportional to the parameter of nonadiabaticity β , the inverse of the Gilbert damping α and the spin drift velocity u which is directly proportional to the density of the driving current j . The linear dependence between wall velocity and current density below the Walker breakdown has been found in numerous experiments [257–260]. Equation (3.28) is still valid when the additional nonlocal spin-transfer torque β_{na} is considered [239], which was not included in the original determination. It is however important to note that the effective β_{na} depends on the exact magnetic configuration [239] and will therefore change as the domain wall transforms during its movement. The parameter of nonadiabaticity β can thus not be considered as a material property when nonlocal effects are taken into account.

For the optimization of the domain wall velocity v_{dw} at a given current density one has to:

- maximize the spin drift velocity u . This means using a magnetic material which simultaneously has a high current spin polarization P and a low saturation magnetization M_s .
- maximize the (effective) parameter of nonadiabaticity β .
- minimize the Gilbert damping α .

It is therefore important to acquire a measurement scheme that allows for a simultaneous and independent determination of all three quantities u , α , and β . The idea, theoretical modelling, and the experimental implementation of such a scheme will be discussed in the following sections.

3.1.5 Summary

In the previous sections the evolution of the magnetization \mathbf{m} under external influences was described in the framework of the Landau-Lifshitz-Gilbert equation. The action and origin of the individual torques induced by damping T_{damping} , internal and external fields T_{field} and electric currents T_{st} has been discussed. The Landau-Lifshitz-Gilbert equation can now be written in its full form [53, 71, 73, 74, 77, 203, 205]

$$\frac{\partial \mathbf{m}}{\partial t} = \mathbf{T}_{\text{field}} + \mathbf{T}_{\text{damping}} + \mathbf{T}_{\text{st}} \quad (3.29)$$

$$\frac{\partial \mathbf{m}}{\partial t} = -\gamma \mathbf{m} \times \mu_0 \mathbf{H}_{\text{eff}} + \alpha \mathbf{m} \times \frac{\partial \mathbf{m}}{\partial t} - u \frac{\partial \mathbf{m}}{\partial x} + \beta u \mathbf{m} \times \frac{\partial \mathbf{m}}{\partial x} \quad (3.30)$$

with the parameters

- γ , the gyromagnetic ratio;
- $\mu_0 \mathbf{H}_{\text{eff}}$, the effective field;
- α , the Gilbert damping;
- u , the current-induced spin drift velocity;
- β , the parameter of nonadiabaticity.

We have seen that the important parameters for the optimization of domain wall velocities in spintronic devices are the spin-drift velocity u , the Gilbert damping constant α , and the parameter of nonadiabaticity β . The following sections will focus on the experimental determination of these three parameters.

3.2 Previous Experimental Work on the Spin-Transfer-Torque Parameters

The early experimental work after the theoretical prediction of the nonadiabatic spin-transfer torque [73, 74] mainly concentrated on the determination of the new and unknown β parameter in the soft magnetic permalloy ($\text{Ni}_{80}\text{Fe}_{20}$). Most of the times the other two parameters were not determined for the sample system at hand, but literature values were taken if they were required.

In the first experiments, depinning processes of domain walls in thin magnetic nanowires were investigated. Properties like the velocity [261] or depinning fields or currents [262–265] of a domain wall were measured. In other experiments the magnitude of the Walker-breakdown field [245, 260] or the precessional frequency of domain walls beyond that field [261, 266] were determined. From all these properties a wide range of β values ranging from 0.007 to 4.1 were deduced, mostly in comparison to a 1D model [74].

It soon became clear that a lot of factors influence the behavior of magnetic domain walls in thin nanowires and that the 1D model has its limitations [245]. The depinning processes are influenced by the exact geometry of the pinning potential [265] whereas the wall velocity also depends on edge roughness [74]. The properties extracted from depinning fields or wall velocities further depend on the type and chirality of the magnetization pattern in the wall region [267–269]. They are also influenced by the current density distribution throughout the wire leading to Joule heating [270–273] and Oersted fields [274]. In pulsed experiments the temporal shape of incoming current pulses also plays an important role [275, 276]. Additionally, transformations of a domain wall may occur under high current densities and alter the results [277].

Nowadays it is furthermore known that β is not a material constant, but consists of further contributions that depend on the exact structure of the magnetization pattern that is investigated. As theoretically discussed in chapter 3.1.4, the contributions are most conveniently split in an adiabatic part β_{sr} , which indeed only depends on material parameters, and a truly nonadiabatic part β_{na} , which depends on the magnetic texture [78]:

$$\beta = \beta_{\text{sr}} + \beta_{\text{na}} \quad (3.31)$$

While the first contribution does not depend on the width of a domain wall, the latter very well does. An experimental approach to separate the two contributions therefore lies in the investigation of magnetic patterns in which the spatial variation of the magnetization happens on very different length scales. It is furthermore important that all three parameters that are relevant for spin-transfer torque are determined [278]. These include the spin-drift velocity u and/or current spin polarization P as well as the Gilbert damping α .

A shallow variation of the magnetic texture, leading to a small gradient of the magnetization, is found in spin waves with wavelengths of a few μm [279]. When a current is sent through a film carrying a spin wave, the frequency of the spin wave is shifted and the effective damping changes [280, 281]. While the shift in frequency is proportional to the spin-drift velocity u , the change in the effective damping, which is seen in a deviation of α , can be connected to β . It is therefore possible to obtain all three parameters simultaneously [81, 82]. The value of β that has been determined in these experiments corresponds to β_{sr} , as the variation of the magnetization happens on a length scale that is far above the spin-diffusion length of permalloy.

A very swift variation of the magnetic texture (with a rotation of 180° over a few nm), leading to a strong gradient of the magnetization, is found in vortex cores [79, 282]. The nonadiabaticity has been obtained from the behavior of vortices under the influence of current pulses [283] and harmonically oscillating currents [88]. It was found to be strongly increased compared to β_{sr} which indicates a dominating contribution of β_{na} for the vortex structure. However, the simultaneous measurement of all three crucial parameters for a vortex core still remained an open question as the above-mentioned experiments lack a direct determination of the spin-drift velocity [88, 283].

A method to obtain all relevant parameters for a magnetic vortex core, as well as its experimental implementation, is discussed in the following sections.

3.3 Using a Vortex Core to Determine All Spin-Transfer-Torque Parameters

A robust measurement scheme for the determination of the β parameter and spin-drift velocity as defined in the Landau-Lifshitz-Gilbert equation (3.29) was proposed by Benjamin Krüger in 2010 [196]. Krüger suggested to probe the current-induced displacement of a magnetic vortex core that is confined within a square structure, a configuration also known as the Landau state. The experimental setup is shown in Fig. 3.2a.

A vortex is a magnetic configuration where the magnetization curls around a central point. In the central core of such a vortex structure, the magnetization is tilted out of the film plane to save exchange energy. The lateral dimension of that core region is approximately 10 nm [79, 284, 285]. Its size depends on the ratio of exchange stiffness and saturation magnetization [286, 287].

There are four possible magnetic configurations for the Landau state. They can be described by two binary properties: The sense of rotation c and the polarity p of the vortex core (Fig.

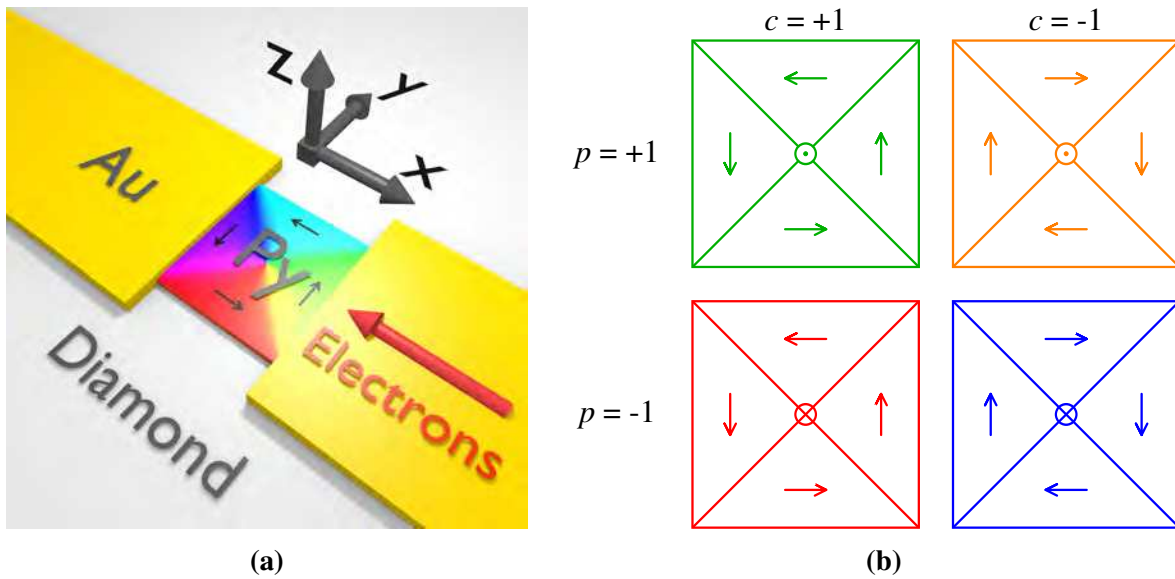


Figure 3.2: (a) Schematic of the experimental setup. A permalloy square with an edge length of $5\mu\text{m}$ and a height of roughly 10nm is placed on top of a diamond substrate. It is contacted by gold leads on two edges, which allows for sending continuous currents of ultrahigh densities ($j > 1 \times 10^{12} \text{A m}^{-2}$) through the nanostructure [288]. The most probable magnetic configuration for a nanostructure of these dimensions is the Landau state. The Landau state consists of four domains where the magnetization lies parallel to the edges of the structure with vortex core in their middle. The four possible configurations of a magnetic vortex state are shown in (b). The first unique property of a magnetic vortex is the direction c in which the magnetization curls around the core region. Imagine looking at the structure from above the substrate ($+z$ direction). A clockwise rotation of the magnetization around the core is now defined as positive c . The second unique property is the out-of-plane direction of the core magnetization, the core polarity p . It is defined as positive when the central magnetization points away from the substrate (represented by \odot) and as negative when the core magnetization points towards the substrate (represented by \otimes).

3.2b). A displacement of the vortex core is caused by the adiabatic and nonadiabatic spin-transfer-torque contributions (see chapter 3.1.4) as well as by the Oersted field, that is generated by the electric current. All those contributions show a different dependence on core polarity p and sense of rotation c . Probing the displacement for different c, p -states therefore allows for a separation of all the contributions.

In contrast to a moving domain wall there is no intrinsic pinning in the dynamics of a confined vortex, which means that no intrinsic threshold current is expected for the vortex motion [289]. By using a large structure (several μm) instead of a thin wire, the larger distance of the manipulated magnetic structure (vortex core) to the edges of the nanostructure, additionally leads to a decrease in external pinning. Using a larger structure furthermore improves the accuracy of the measurement as the displacement of the vortex core induced by a given current density increases proportional to the size of the structure [196].

The vortex state is the energetic ground state for permalloy squares with an edge length l greater than 100 nm and a thickness t above 10 nm [290, 291]. The parameters of $l = 5 \mu\text{m}$ and $t = 10 \text{ nm}$ that are chosen for the experiment, therefore ensure a high probability for the creation of a vortex state after a demagnetization procedure. A demagnetization of the structure will be required to switch between different c, p -states.

3.3.1 Theoretical Approach

The theoretical approach for the determination of the spin-transfer torque parameters by measuring the displacement of magnetic vortices is thoroughly discussed in [196, 292]. A short summary of the most important points will be given in this section.

When a constant electric current flows through a magnetic vortex structure, there are several forces at work that act on the vortex core and change its equilibrium position [196]. A change in equilibrium position leads to a damped spiral motion of the vortex core around its new energy minimum, which is completed after a few nanoseconds [293].

As long as the vortex core keeps its static structure during the movement and does not deform, it can be considered as a quasiparticle. The steady state motion of the rigid magnetization pattern can then be described by the equation of Thiele [72]. The forces that are due to the spin-transfer torque have been added to the Thiele equation by Thiaville *et al.* [74]. The modified version of the Thiele equation reads [74]

$$\mathbf{F} + \mathbf{G} \times (\mathbf{v} - \mathbf{u}) + \overline{\overline{D}}(\alpha\mathbf{v} - \beta\mathbf{u}) = \mathbf{0} \quad (3.32)$$

with the spin drift velocity \mathbf{u} and the velocity of the vortex core \mathbf{v} . The gyrovector \mathbf{G} is written in polar coordinates, with the angle of the in-plane magnetization ϕ and the angle of the out-of-plane magnetization θ , as an integral over the magnetic volume V [72, 87]:

$$\mathbf{G} = -\frac{\mu_0 M_s}{\gamma_0} \int dV \sin(\theta) (\nabla\theta \times \nabla\phi) \quad (3.33)$$

$$= -p \frac{2\pi}{\gamma_0} \mu_0 M_s t \cdot \mathbf{e}_z =: G_0 \cdot \mathbf{e}_z \quad (3.34)$$

With $\gamma_0 = \mu_0 \gamma$. In the last term, the integral was carried out for the vortex structure. The gyrovector points in $\pm z$ direction depending on the polarity of the vortex core p . Its magnitude is proportional to the film thickness t .

The dissipation dyadic $\overline{\overline{D}}$ is a tensor of second order (3×3 matrix). It is given as [72]:

$$\overline{\overline{D}} = -\frac{\mu_0 M_s}{\gamma_0} \int dV (\nabla\theta \otimes \nabla\theta + \sin^2(\theta) \nabla\phi \otimes \nabla\phi) \quad (3.35)$$

For the rigid vortex core the dissipation tensor is diagonal². The diagonal elements are [87]:

$$D_{xx} = D_{yy} =: D_0 \approx -\frac{2\pi}{\gamma_0} \mu_0 M_s t \frac{\ln(l/a)}{2} \quad (3.36)$$

$$D_{zz} = 0 \quad (3.37)$$

²Diagonal means that all entries outside the diagonal equal zero.

The diagonal elements of the dissipation tensor show a logarithmic dependence on the edge length of the structure l and the lower bound of the integration a , which is “in the order of magnitude of the radius of the vortex core” [87].

The modified Thiele equation (3.32) has the simple solution $\mathbf{v} = (\beta/\alpha)\mathbf{u}$, which for instance gives the velocity of a vortex domain wall (VW) that moves through a wire [74] (compare (3.28) on p. 35). The movement of the domain wall sustains “as long as the restoring force keeping the vortex in the wire can balance the gyrotropic term. Otherwise, the VW transforms into a TW by lateral expulsion of the vortex.” [74]³.

When the vortex core is however confined within a structure, for instance a square, it can not sustain a linear motion in one direction without being expelled from the structure. One solution to the Thiele equation is then found when a harmonic excitation is assumed (for instance $\mathbf{u} = \mathbf{u}_0 \cdot \sin(\omega t)$) [87]. The vortex core then moves around its equilibrium position on an elliptical or circular orbit [87]. The exact shape of the orbit depends on the ratio between the excitation frequency and the resonance frequency of the vortex state [294].

When a stationary direct current is applied, as shown in Fig. 3.2a, the position of the vortex core changes until all contributing forces are balanced [196]. The vortex core then reaches a new steady state equilibrium position where its velocity equals zero. Note that all experimental access to the damping parameter α is lost as soon as the velocity reaches zero (see (3.32)). For a direct current in x direction ($\mathbf{u} = ue_x$) the deflecting forces that are due to the current can directly be obtained from (3.32) by setting $\mathbf{v} = 0$ as:

$$\mathbf{F}_{\text{curr}} = \begin{pmatrix} D_0\beta u \\ G_0 u \end{pmatrix} \quad (3.38)$$

In realistic sample systems, the current flow will not be homogeneous and the effect of an additional inhomogeneous Oersted field has to be considered. The physical origin of the Oersted field (including additional mechanisms that give rise to an Oersted field) is discussed in chapter 3.5.4 on page 66. The Oersted field has to lie in a direction that is perpendicular to the current flow. The Oersted field can hence consist of a y - and of a z -component. The z -component of the Oersted field has no influence on the position of the vortex core. The y -component will affect the size of the vertical domains where the magnetization is aligned parallel to the field. Thus, the vortex core is deflected in $\pm x$ direction. The deflecting force that is caused by the Oersted field can be approximated by a homogeneous field H in y direction as [196]:

$$\mathbf{F}_{\text{field}} = \begin{pmatrix} \mu_0 M_s H l t c \\ 0 \end{pmatrix} \quad (3.39)$$

The direction of this force depends on the sense of rotation of the vortex core c . It is proportional to the film thickness t , the length of the square element l and the field strength H .

Since the core is confined within a nanostructure, restoring forces arise once the core is deflected from its equilibrium position. With the core not being in the center, each two opposing domains are of different size and their flux is no longer being compensated. This gives rise to

³TW means transverse wall.

a restoring force \mathbf{F}_{rest} that can be calculated from the magnetostatic energy. It is, for small deflections, proportional to the radius of the core deflection (as for an harmonic oscillator) [87]

$$\mathbf{F}_{\text{rest}} = \begin{pmatrix} -m\omega_r^2 x \\ -m\omega_r^2 y \end{pmatrix} \quad (3.40)$$

with the parabolic confining potential $V = \frac{1}{2}m\omega_r^2(x^2 + y^2)$ [87]. In equilibrium, the sum of all forces equals zero: $\sum F_i = \mathbf{F}_{\text{curr}} + \mathbf{F}_{\text{field}} + \mathbf{F}_{\text{rest}} = 0$. By inserting (3.38), (3.39), and (3.40) and solving for x and y , the equilibrium position of the vortex core is obtained [196]:

$$\begin{pmatrix} x \\ y \end{pmatrix} = -\frac{|G_0|}{m\omega_r^2} \begin{pmatrix} \tilde{H}c + \left|\frac{D_0}{G_0}\right| \beta u \\ up \end{pmatrix} \quad (3.41)$$

with

$$\tilde{H} := \frac{\gamma}{2\pi} \mu_0 H l \quad (3.42)$$

By measuring the displacement vector, one gets access to the spin drift velocity u and the β parameter. The spin drift velocity is directly accessible from the displacement in y direction when the strength of the confining potential is known. Its strength can be determined from micromagnetic simulations, which will be discussed in the following section. The direction of the y displacement further yields information about the polarity of the vortex core p ; an effect that is particularly important to determine the core polarity from a SEMPA image, which shows the magnetization pattern in the film plane⁴.

For the determination of the nonadiabaticity β the contribution of the Oersted field has to be eliminated. It is therefore most convenient to compare the displacement trajectories dx/dy that arise when the density of the constant driving current is varied for two vortex states with opposing sense of rotation c . By adding up those trajectories direct access to β is obtained:

$$\beta = \frac{1}{2} \frac{G_0}{D_0} \left(p \cdot \frac{dx}{dy}(c, p) + p \cdot \frac{dx}{dy}(-c, p) \right) \quad (3.43)$$

With this formula β can be determined directly from the measured data. No knowledge of the spin drift velocity or other material parameters is required. Only one micromagnetic simulation needs to be conducted to determine the geometrical factor G_0/D_0 . It will be shown in the following section that this factor slightly depends on the saturation magnetization M_s (and thereby temperature), the film thickness t and the lateral dimensions of the square l . Due to this weak dependance, small errors in M_s , t or l have almost no effect on the precision with which β is determined.

⁴The only way to visualize a small percentage of the out-of-plane component of the magnetization with the SEMPA machine that was used throughout this thesis is by tilting the sample. This was not done as it is experimentally very difficult and yields no additional information.

3.3.2 Micromagnetic Simulations of the Current-Induced Vortex Core Displacement

As discussed in the previous chapter, micromagnetic simulations are required to obtain the ratio of G_0/D_0 that is essential for the determination of the β parameter. The numerical calculation of the magnetic configuration with the lowest energy (for certain boundary conditions) is being performed since 1965 [295]. Micromagnetic simulations of current-induced vortex core displacement have been mainly performed by Benjamin Krüger⁵. The freely available codes OOMMF [296] (calculating on the CPU) and MICROMAGNUM [297, 298] (calculating on the GPU) were used as simulational tools. Both codes solve the Landau-Lifshitz-Gilbert equation including the spin-transfer torque terms numerically. The results obtained with both of the tools were consistent, but MICROMAGNUM obtained them a lot faster due to its parallel processing capabilities. An example for the simulation of the Landau state in a permalloy square is shown in Fig. 3.3.

The problem at hand, however, could not be calculated directly for the following reasons: To calculate the correct value for β , it is critical to determine the exact ratio between the magnitude of two geometrical factors (see (3.43)): the gyrovector G_0 (defined in (3.34)) and the diagonal element of the dissipation tensor D_0 (defined in (3.36)). Both properties are obtained by integrating over the gradient of the out-of-plane component of the magnetization [87]. Since the out-of-plane component is strongly peaked in the center of the vortex core (Fig. 3.3d), its gradient might very well be underestimated when oversized cells are used in the simulation. Regarding permalloy, a cell size of about 2 nm in x and y direction was found to be sufficiently small [292]. For the system at hand, with a thickness of about 10 nm, “it is a reasonable approximation that the magnetization is independent of the z coordinate” [196]. It is therefore sufficient to use only one cell in z direction, whose thickness equates with the thickness of the film.

Using a cell size of 2 nm \times 2 nm \times 10 nm for the system shown in Fig. 3.2a would translate to an amount of 6.25 M simulation cells. A reasonable computation time can be obtained for systems of roughly 100 k cells [196]. To obtain an estimate of the geometrical factors, despite the large size of the structure (edge length $l = 5 \mu\text{m}$), simulations were conducted for structures of $l = 500 - 1700 \text{ nm}$. Additionally, the saturation magnetization M_s and film thickness t were varied, to make it possible to account for a change of these values during the experiment and to allow for an appropriate adjustment of the geometric factors. While t will be reduced due to subsequent ion milling in SEMPA, M_s might be altered as the temperature is increased by joule heating during each measurement cycle.

To obtain the geometrical factors, the deflection of the vortex core was simulated under the application of a small direct current. Since no Oersted field is included in the computational

⁵*I. Institut für Theoretische Physik, Universität Hamburg - currently employed at the Institut für Physik, Johannes Gutenberg Universität Mainz.*

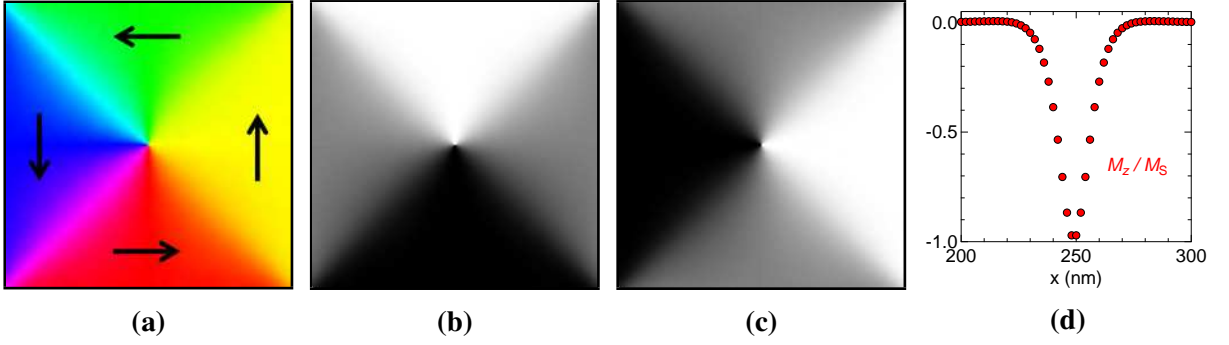


Figure 3.3: Micromagnetic simulation of a $500 \text{ nm} \times 500 \text{ nm} \times 10 \text{ nm}$ sized permalloy structure obtained with OOMMF [296] using a cell size of $2 \text{ nm} \times 2 \text{ nm} \times 10 \text{ nm}$. Illustration of the (a) in-plane angle, (b) x -component, (c) y -component, and (d) a line profile of the z -component of the magnetization vector, taken in the center of the structure. In this case the vortex structure has a positive sense of rotation $c = +1$ and a negative core polarity $p = -1$. While the out-of-plane component is not accessible with our setup, the first three images can similarly be obtained by SEMPA. No magnetic fields or electric currents were applied in this simulation. Fig. (d) shows that a lateral cell size of 2 nm is sufficiently small to allow for at least one cell to show the full out-of-plane magnetization in the center of the vortex core.

code, a comparison of the deflection amplitude to (3.41) directly yields the desired parameters. The resulting values were best fitted by [80]

$$\begin{aligned} \frac{D_0}{G_0} = \frac{1}{2} \ln \left(\frac{1.85}{\text{nm A}} l (M_s + 220 \text{ kA m}^{-1}) (97 \text{ nm} - t) \right) \\ + \frac{27.7}{\mu\text{A m}} l (M_s - 550 \text{ kA m}^{-1}) (t + 2 \text{ nm}) \end{aligned} \quad (3.44)$$

for the ratio of the diagonal element of the dissipation tensor and gyrovector and

$$2\pi f_{\text{res}} = \frac{mw_r^2}{G_0} = \frac{\gamma}{2\pi} \left(1.8\mu_0 M_s \frac{t}{l} + 130 \text{ pJ m}^{-1} \cdot \frac{t + 8.5 \text{ nm}}{M_s t l^2} \right) \quad (3.45)$$

for the prefactor of (3.41), which is equal to the resonance frequency of the vortex core when damping is small ($\alpha^2 \ll 1$, see (12) in [87]).

A graphical representation of (3.44) and (3.45) for a parameter space that contains the values which are expected during the measurement of the vortex core displacement in SEMPA is shown in Fig. 3.4. The parameter D_0/G_0 , which is important to determine the value of β , shows only a slight dependance on the parameters M_s and t that might change between SEMPA measurements due to ion milling. The resonance frequency, however, shows a stronger dependence on M_s and t . This primarily stems from its almost linear dependence on thickness [293] and saturation magnetization; the second term in (3.45) is only a small adjustment. As a consequence of these dependencies, one has to have a good measure of thickness and saturation magnetization when trying to determine the spin-drift velocity or the Oersted field contribution from measuring the current-induced displacement of a vortex core.

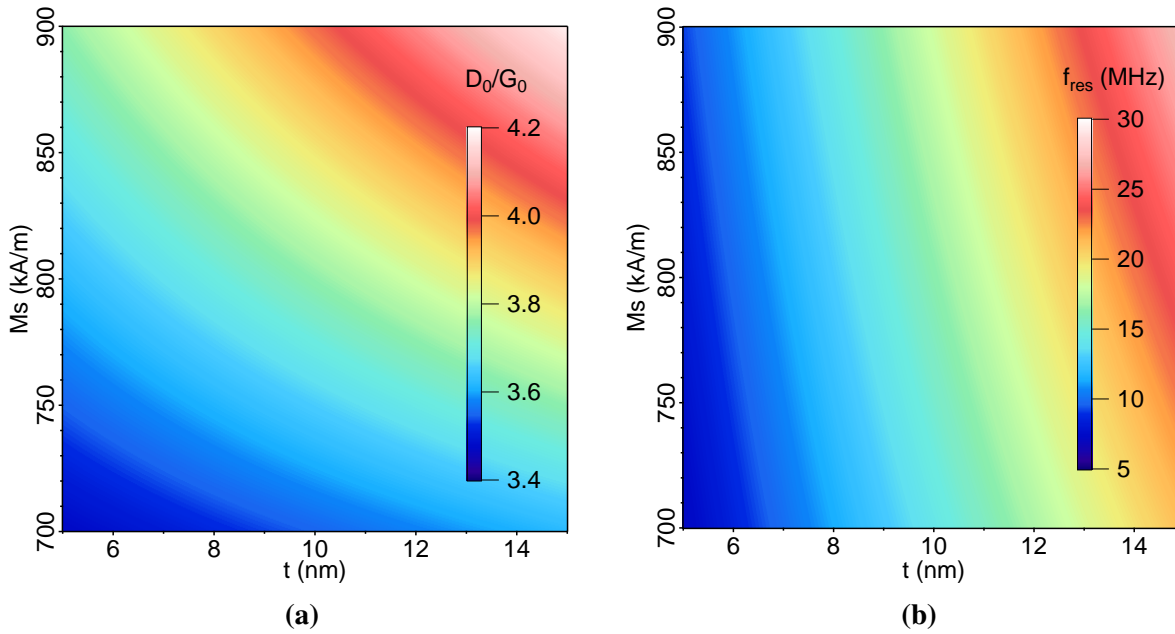


Figure 3.4: Resulting values for the geometric factors of a square, with an extrapolated length of $l = 5 \mu\text{m}$, plotted over the parameter space that could possibly manifest in the measurements. (a) Ratio of the diagonal element of the dissipation tensor and gyrovector calculated from (3.44). The ratio shows only a small derivation of $\pm 10\%$ over the whole parameter space. (b) Resonance frequency of the vortex core calculated from (3.45). It is strongly influenced by film thickness and saturation magnetization. The resonance frequency increases as the confining potential gets stronger for thicker films or for a larger saturation magnetization.

3.3.3 Sample Preparation

To allow for the application of ultrahigh current densities ($j \geq 10^{12} \text{A m}^{-2}$) over extended times (several hours) [288], the samples are prepared on a single-crystalline diamond substrate, which is thermally highly conductive [299]. Commercial diamond cuboids with a size of $2 \text{mm} \times 2 \text{mm} \times 0.5 \text{mm}$ (see Fig. 3.6a) are used with their (100) surfaces superpolished [300] by “Almax easyLab” [301]. The polishing results in an RMS⁶ roughness of 0.16 nm [302]. An excellent polishing of the surface without the appearance of any significant polishing lines is required to prevent the emergence of a substrate induced anisotropy (see chapter 6). Prior to preparation, the diamonds are swept clean with foam tipped swabs under the application of ethanol and distilled water. Subsequently to cleaning, as many manual preparation steps as possible are conducted in a laminar flow cabinet to keep the diamonds clean.

In the first preparation step two opposing bonding pads with an area of approximately 0.4mm^2 are created in the center of the diamond surface (Fig. 3.5a). To this end a thin copper mask is used. The mask contains a circular hole through which a $20 \mu\text{m}$ broad bar runs. The mask is positioned on the diamond and secured with a titanium latch. Then it is placed upside down in a vacuum chamber and the whole chamber is pumped to a base pressure of

⁶root mean square

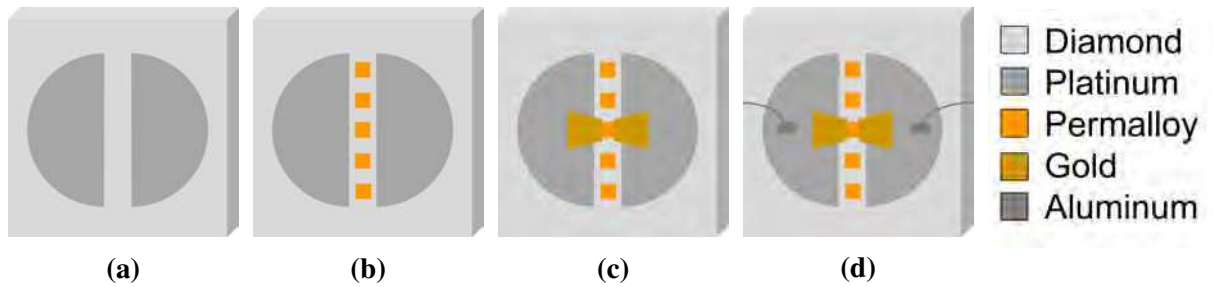


Figure 3.5: Schematic display of the sample synthesis. The samples are prepared on a single-crystalline diamond substrate. (a) Bonding pads consisting of platinum with an underlying adhesive layer of chromium are thermally evaporated through a copper mask. (b) Magnetic material is deposited through a Si_3N_4 mask with square holes (cut with focused ion beam) resulting in the creation of square elements on the diamond surface (size greatly exaggerated). (c) Another mask that has been cut with a laser is aligned above one of the square elements. Subsequently a thin gold film is evaporated through the mask, closing the gap between the square and the platinum pads without covering too much of the magnetic nanostructure. (d) Finally each platinum pad is connected to the sample holder through bonding with thin aluminum wires.

1×10^{-7} mbar, which usually happens overnight. A chromium target, located 20 cm below the sample, is then heated by electron bombardment until chromium atoms or small clusters start to evaporate into the vacuum (thermal evaporation). By detecting the change of mass in a quartz oscillator that is mounted at the same height as the sample, the thickness of the deposited chromium film is monitored. When a thickness of 10 nm is reached the process is stopped. The chromium target is then *in-situ* replaced by a gold target and the whole process is repeated until a gold layer of 10 - 20 nm is added to the chromium layer. The chromium layer increases the adhesion of the highly conductive gold film to the diamond substrate, which makes this film system optimal for contacting samples by wire bonding.

In the second step the magnetic nanostructures are prepared (Fig. 3.5b). Square holes with an edge length of $5 \mu\text{m}$ are milled into a Si_3N_4 membrane (Fig. 3.6a) with a focused ion beam (FIB). The membrane is then placed upon the diamond and aligned with an optical microscope using a light source shining from beyond the diamond. A magnetic film is then brought onto the sample through the mask in the same way as described in the previous step. After evaporation, the position of the structures and their behavior under the influence of magnetic fields is inspected with a magneto-optical Kerr microscope. This way the structure with the highest probability to show a Landau state after demagnetization is identified and the mobility of the vortex core is ensured.

In the third step the structure of choice is brought in contact with the bond pads (Fig. 3.5c). Two rectangular or slightly trapezoidal holes with a separation of $4 \mu\text{m}$ are laser cut into a Si_3N_4 mask. Since, in contrast to ion milling, no metallic layer is needed for laser cutting, the mask remains slightly transparent for light in the optical range. This allows for an alignment of the mask with the optical microscope, while, again, the light source is placed below the sample. The mask is then placed in a position, where the separating bar between the two trapezoidal holes covers the middle of the selected magnetic square element. A 20 - 30 nm thick gold film

Magnetic material	t_i (nm)	Contact material	t_i (nm)	R_i (Ω)	Ref. No.
Fe	12	Gold	15	201	372
Fe ₅₄ Co ₃₉ Si ₇	12	Gold	15	329	363
Ni ₈₁ Fe ₁₉	12	Gold	15	359	361

Table 3.1: Tabular overview of the samples that have been prepared on diamond substrates and investigated with SEMPA. The initial thicknesses t_i of the materials involved as well as the initial resistances R_i of the samples are given. The differences in resistance are mainly caused by differently sized overlap regions of the gold contacts.

is then evaporated the same way as in the steps before, closing the gap between the selected square and the bonding pads. Successful operation is confirmed by measuring the resistance between the two bonding pads, which should be of a few hundred Ohms.

Finally, the two contact pads are bonded to the sample holder with aluminum wire bonds (Fig. 3.5d) and the sample holder is transferred into the SEMPA chamber.

Prepared Samples

A variety of samples was prepared for the investigation with SEMPA. Not every sample, however, remained intact during the whole preparation process due to the following reasons:

- Nanowires are very sensitive to electrostatic discharge (ESD). Small amounts of charges that may accumulate on pliers, hands, bonding wires, Si₃N₄ membranes, the sample holder, or the fixing springs are sufficient to destroy the sample. Although ESD-safe equipment is used, the danger of a discharge can never be completely avoided.
- The third step of the sample synthesis (Fig. 3.5c) is very delicate. In order to find the magnetic structures, the mask has to be moved across the sample. If small particles of dirt or dust accumulate between mask and sample, they scratch across the surface while the mask is moved. This may damage the magnetic structures.
- After the mask for the evaporation of gold contacts has been aligned as described above, the sample holder has to be transferred into the evaporation chamber. The holder needs to be rotated by 180° in order to be placed upside down for the evaporation process. This may cause the mask to shift by a few hundred nanometers, so that the evaporated gold contacts (or at least one of them) no longer touch the magnetic square structure.

Three of the samples that have been successfully prepared and investigated with SEMPA will be discussed in the following sections. Their individual composition is shown in Tab. 3.1. Different in-plane materials were chosen to investigate the material dependence of the spin-transfer torque parameters.

Sample Setup for SEMPA

To be able to conduct SEMPA measurements at ultrahigh current densities ($10^{11} - 10^{12} \text{ A m}^{-2}$) [288], the diamond substrate is pressed to a polished copper plate by two screws (see Fig. 3.7a).

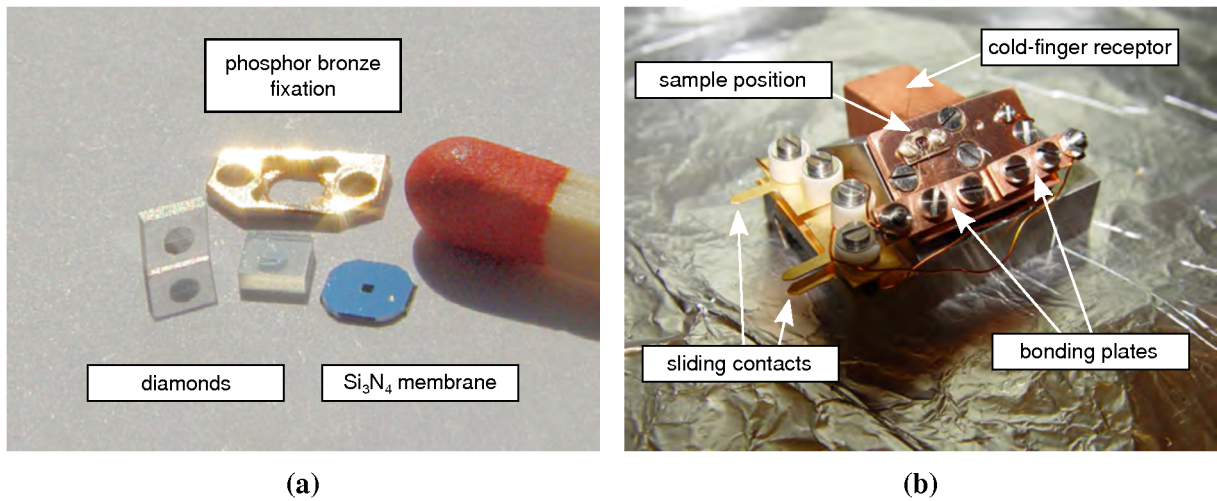


Figure 3.6: Photographic images of the experimental sample setup. (a) Bottom left: single-crystalline diamond substrates with two half-moon shaped bonding pads on top of their (100) surface. Top: phosphor bronze sheet that can be used for a gentle fixation of the substrate. Bottom right: silicon frame holding a thin Si_3N_4 membrane (within the square region in the center), which is used as a shadow mask for the fabrication of nanostructures. The head of a match is shown for size comparison. (b) The sample holder, ready to be transferred into SEMPA. Compared to (a), the bottom (silver) part of the sample holder is roughly of the size of a conventional match box. The diamond sample is fixated on a copper plate using the phosphor bronze fixation. The sample is wire bonded to two bonding plates, which are connected to sliding contacts with copper wires. A copper block, containing a thread for the reception of a cold finger, is attached to the back of the copper plate. The copper plate is thermally insulated against the sample holder by four small glass balls (diameter ≈ 0.2 mm).

Additionally to the screws, a sheet made out of phosphor bronze (Fig. 3.6a) can be used to avoid damaging the substrate⁷ by distributing the force over a larger area (see Fig. 3.6b). After fixation of the substrate, a connection to the sample holder is established by wire bonding from the bonding pads on the diamond surface to two copper bonding plates. The bonding plates are attached to the sample holder and connected to sliding contacts (see Fig. 3.6b). Reliable parameters for wire bonding⁸ (Force / Time / Power) are (3 / 8 / 3) for Pt/Cr/Diamond and (3 / 4 / 3) for copper. A slight roughening of the copper prior to bonding is recommended to allow for a better adhesion of the bonding wire.

A copper block with a thread is attached to the back of the copper plate, for the reception of a cold finger (see Fig. 3.6b). By cooling with liquid nitrogen or helium, or by heating, this allows for a variation of the sample temperature in the range of 40 - 400 K.

An image that has been obtained with SEM showing a diamond that has been fixated with screws is displayed in Fig. 3.7a. Two M1 screws are pressing against two opposing corners of

⁷When using sapphire (Al_2O_3) as a substrate a strong fixation with screws may break off the edges of the substrate. By using the sheet for fixation, the force is distributed over a larger area and damage to the substrate can be avoided. Using the phosphor bronze sheet for the fixation of a diamond substrate is easier but not mandatory.

⁸Manual Wire Bonder, Model No. 4123/4/6/9 by Kulicke and Soffa Industries Inc.

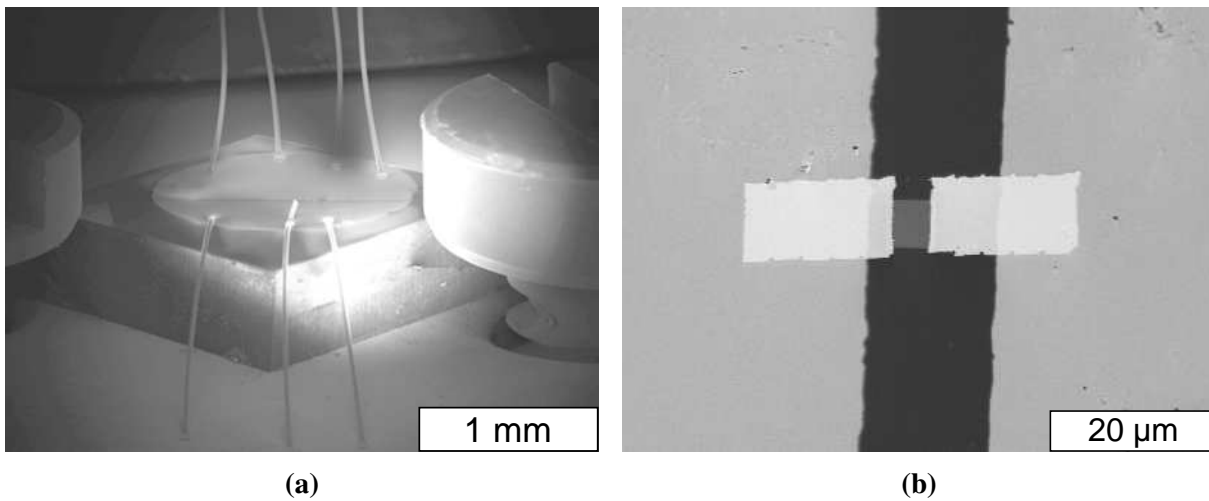


Figure 3.7: (a) SEM image of one of the first samples that was transferred into SEMPA. A diamond substrate is firmly attached to a copper plate by two M1 screws. Four bonding wires are connected to the upper bonding pad, three to the lower one. The isolation channel is visible in the center of the diamond; it is located between both bonding pads and runs from the left to the right. As it turned out later, a rotation of the diamond by 90° (with the isolation channel running from top to bottom) is favorable when an electric potential is applied: The number of secondary electrons that reach the spin detector is then less dependent on the potential that is applied to the sample. (b) SEM image of the isolation channel in the center of the diamond for the iron sample. The square iron structure is located within the isolating channel. Two gold leads that contact the square from both sides are clearly visible as the brightest region of this image.

the substrate without touching the metallic bonding pads in the central region of the diamond. Each of the two bonding pads is connected by 3-4 bonds of $25\ \mu\text{m}$ thick aluminum wire. A single aluminum wire bond can carry a current of up to 400 mA before failing. A zoom into the central region of the diamond surface is shown in Fig. 3.7b for the iron sample. Two Pt/Cr bonding pads, separated by a $20\ \mu\text{m}$ wide isolating channel, are visible. The square iron structure is located in the center of the isolating channel. Thin gold leads are connecting it to the bonding pads on two sides. The resistance of this particular sample is $201\ \Omega$.

3.4 Vortex Displacement in Iron Alloys

The displacement of a magnetic vortex core by a magnetic field or an electric current has been investigated for samples made of pure iron and the soft-magnetic alloy $\text{Fe}_{54}\text{Co}_{39}\text{Si}_7$. Since magnetic vortex cores have a very small diameter of about 10 nm, they can easily be pinned by small defects. The mobility of the vortex core may be compromised by impurities in the magnetic film, grain boundaries, or a local roughness of the underlying substrate. To avoid the selection of a square structure where a deflection of the vortex core is not possible, the core

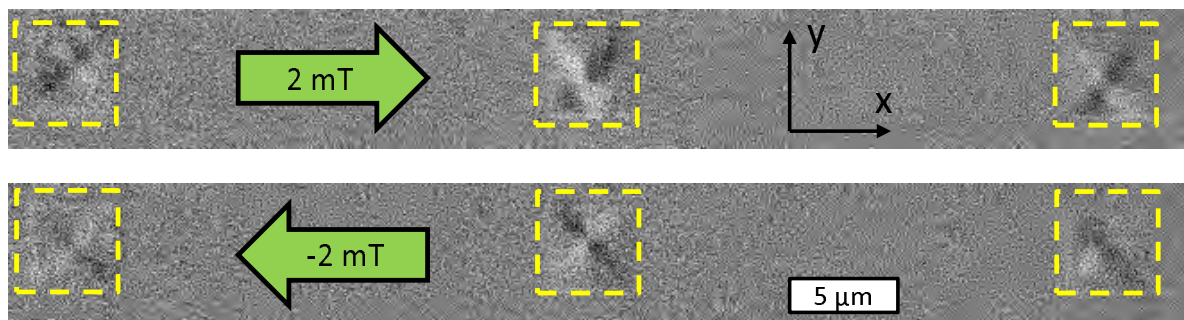


Figure 3.8: Differential Kerr microscope images of the field-induced vortex displacement in three $5\ \mu\text{m} \times 5\ \mu\text{m} \times 12\ \text{nm}$ nanostructures of pure iron prepared on a diamond substrate. The microscope was set to be sensitive to changes of the magnetization in y direction, while a magnetic field of $\pm 2\ \text{mT}$ was applied in x direction. An image of the undisturbed vortex state at $0\ \text{mT}$ was subtracted as a background image. Thus the displacement of the four Néel walls becomes directly visible as black and white contrast when the size of the particular domains giving dark or bright contrast (the vertical domains) de- or increases [304]. A wall displacement is visible for all three structures. Since the largest deflection is obtained for the nanostructure in the center, it was selected for a measurement in SEMPA and therefore electrically connected.

mobility of the vortex core is checked with a magneto optical Kerr microscope [303]. This is done before any of the square structures is electrically connected.

First, it is ensured that the Landau state is present in the nanostructure. A picture of the Landau state is then taken as a background image for the differential technique of Kerr microscopy. This makes it possible to spot small motions of the vortex core with the naked eye. Images of the nanostructure are then taken while a small external background field is applied. Some selected images for the sample with squares made of pure iron are shown in Fig. 3.8. For these squares a movement of the vortex core could be resolved for a magnetic field of $2\ \text{mT}$. One of the squares was subsequently electrically connected to the bonding pads and the sample was introduced into SEMPA.

SEMPA images of the vortex configuration were taken for current densities up to $j = 9 \times 10^{11}\ \text{A m}^{-2}$. The sample holder was kept at $T = 300\ \text{K}$. After a series of images was recorded, the position of the vortex core was determined from the images as described in chapter 7.1.1 on page 135. For this first series of images a significant movement of the vortex core could however not be observed (see Fig. 3.9). A small wobble field ($\sim 1\ \text{mT}$) was thus applied to loosen the vortex core from its pinning center. This procedure, however, only moved the vortex core to yet another pinning site, where its mobility under the influence of current remained insignificant.

An identical behavior was found for a square made of $\text{Fe}_{54}\text{Co}_{39}\text{Si}_7$ (see Fig. 3.9). It was previously observed by Kerr microscopy, that the vortex core in the given nanostructure was mobile under the influence of an external field ($\approx 1\ \text{mT}$). The application of a current density between $\pm 8 \times 10^{11}\ \text{A m}^{-2}$ however, did not suffice to induce a deflection of the vortex core. The sense of rotation in the Landau state was then changed by the application of a demagnetizing field. The core however remained fixed at the same position.

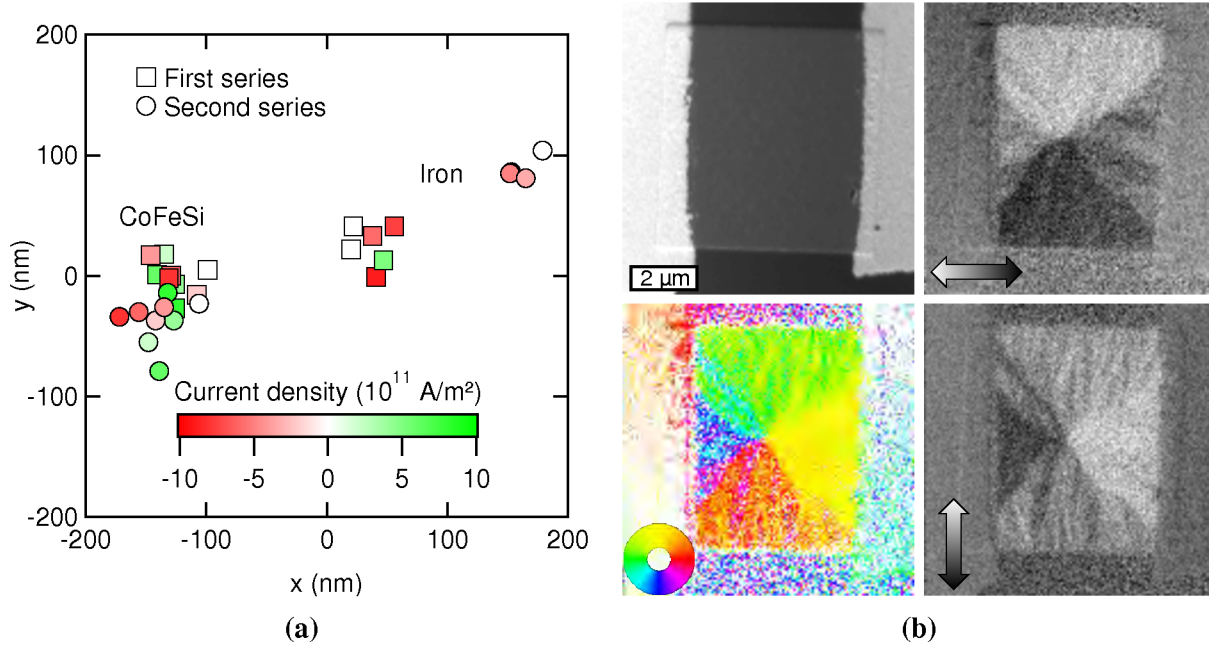


Figure 3.9: (a) Position of the vortex core in the central iron square of Fig. 3.8 ($x > 0$) and in a square of equal dimensions made of $\text{Fe}_{54}\text{Co}_{39}\text{Si}_7$ ($x < 0$). Images were taken with SEMPA while various current densities were sent through the structures. For visual reasons the error margins of $\pm 25 \text{ nm}$ in x - and y -direction are not shown. After the first series of measurements for the iron square was evaluated, it became clear that the vortex core did not move. A small wobble field of 2 mT was applied to remove the core from the pinning site and a second series was taken. The vortex core was now located in a different pinning site, however no significant effect of the electric current on the core position is visible. A similar behavior can be seen for the square made of $\text{Fe}_{54}\text{Co}_{39}\text{Si}_7$. Contrary to the iron square, a stronger wobble field was applied between the two series. The field was large enough to completely eject the vortex core from the structure and to bring in a new state with an opposing sense of rotation. Nevertheless, the vortex core still showed no significant movement. (b) SEMPA images of the iron square at a direct current density of $j = -5 \times 10^{11} \text{ Am}^{-2}$ after the wobble field was applied. The domain walls seem to follow a curved path, which could be an indicator for pinning sites along their way. Additionally, magnetization ripples are visible within the domains. The ripples might stem from magnetic impurities [305, 306] or a variation of the local anisotropy [306–308]. Both effects may contribute to an increased pinning of the vortex core.

For both samples, ripple structures were observed within the four domains of the Landau state (see Fig. 3.9b). These ripples are often observed in thin iron films [305, 307]. They indicate the presence of magnetic impurities [305, 306] or a variation of the local anisotropy [306–308] that is caused by “the random orientation of the crystallites, whose crystal anisotropies are superimposed on the uniaxial film anisotropy” [308]. It has been shown that magnetic impurities can act as an attractive potential for magnetic vortex cores [309–311]. A variation of the local anisotropy can however also act as a pinning center. A region in the sample where the local (in-plane) anisotropies coincide with the orientation of the magnetization around the vortex core would be a preferred spot for the vortex core position. The presence of ripples within a magnetic structure could therefore always be an indicator for the presence of pinning.

MOKE investigations of witness films that were prepared on SiO_2 simultaneously to the samples revealed a coercive field of $\mu_0 H_c = 6.4 \text{ mT}$ for the iron sample and $\mu_0 H_c = 5.2 \text{ mT}$ for the $\text{Fe}_{54}\text{Co}_{39}\text{Si}_7$ sample. The value for iron is quite low for a film that has been prepared by thermal evaporation [312, 313], which can be attributed to the slow evaporation rate of only 0.1 \AA s^{-1} . The value for $\text{Fe}_{54}\text{Co}_{39}\text{Si}_7$ however is quite common [192]. The pinning of a domain wall can be connected to the magnitude of the coercive field [314]. A further reduction of this property could therefore enhance the mobility of the magnetic vortex cores in Fe and $\text{Fe}_{54}\text{Co}_{39}\text{Si}_7$ thin films in future studies.

3.5 Vortex Displacement in Permalloy

A more promising material for observing a current induced deflection of the vortex core is permalloy ($\text{Ni}_{81}\text{Fe}_{19}$). The coercive field for permalloy thin films usually lies well below 1 mT [315] and represents a global minimum in composition of iron-nickel alloys [316, p. 115]. For a 20 nm thick permalloy film that was prepared on a diamond and on a sapphire (Al_2O_3) substrate, a coercivity of only $\mu_0 H_c = 0.5 \text{ mT}$ was found. Additionally, the uniaxial anisotropy of the evaporated permalloy films is usually so small that it can be neglected [317].

Kerr microscope investigations revealed that vortex cores are highly mobile in permalloy squares prepared on a diamond substrate (see Fig. 3.10). A change in core position can be observed for field steps as small as 0.1 mT . For a field of 1.8 mT the vortex core was completely expelled from the structure; a field strength where only a small core deflection was observed for the iron squares (compare Fig. 3.8).

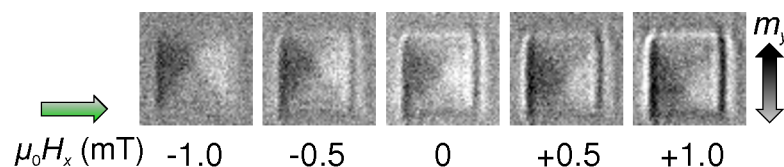


Figure 3.10: Kerr microscope images of a $5 \mu\text{m} \times 5 \mu\text{m} \times 12 \text{ nm}$ sized permalloy square prepared on a single-crystalline diamond substrate. For the displayed images that have been taken at field intervals of 0.5 mT a change in vortex position can be identified between each of the images. By looking at the full video data, where the individual frames were taken at 0.1 mT steps, a small change in core position can even be observed between each single frame.

Since a measurement of vortex states with an altered sense of rotation is required for the determination of β , the response of the squares to demagnetizing fields was also investigated with Kerr microscopy. An image of four neighboring squares was taken after a 50 mT field was applied for one second. The field was rotated from 0° to 90° in steps of 5° and during each step 50 demagnetization cycles were measured. The overall probability for each of the squares to show a Landau state lay between 93% and 98%. Although for specific angles a certain curling direction of the vortex state was favored, an observation that did not obey any regular pattern, the overall possibility to obtain each of the two rotational senses was about equal.

3.5.1 SEMPA Measurements

The square that is shown in Fig. 3.10 was then connected with gold leads from two sides as described in chapter 3.3.3. The mask for the gold leads was, however, not completely centered during the evaporation of the gold film. This step of the process therefore needed to be repeated a second time. After a finite resistance of $R = 359 \Omega$ was measured, the sample was mounted onto a polished copper plate and introduced into the SEMPA chamber. Since a clean surface is required for SEMPA imaging (see chapter 2.2) the sample was then sputtered at an accelerating voltage of 1 kV with an emission current of 20 mA (resulting in an ion current of $0.1 \mu\text{A}$ [192]) at an Argon partial pressure of 6.0×10^{-7} mbar for 25 minutes. Subsequent SEMPA imaging revealed that the structure was still in the Landau state with a positive sense of rotation ($c = +1$, see Fig. 3.11a), as it has been prepared in the Kerr microscope⁹. The polarity p of the vortex core can not be determined from these images. It will however be revealed from the direction of the core displacement along the y -axis via (3.41) as soon as direct current is sent through the structure.

To measure the current-induced displacement of the vortex core, a current density of $j_x = -3.2 \times 10^{11} \text{ A m}^{-2}$ was applied to the structure. A series of images was taken as the current density was increased in eight steps of $\Delta j_x = 0.8 \times 10^{11} \text{ A m}^{-2}$ until a current density of $j_x = 3.2 \times 10^{11} \text{ A m}^{-2}$ was reached. The temperature of the sample during this cycle was monitored by measuring the resistance R and comparing it to a calibration curve¹⁰ of $R(T)$. During the measurements the temperature fluctuated in the range of $T = (341 \pm 9) \text{ K}$.

SEM images of two opposing current-density steps ($\pm 2.4 \times 10^{11} \text{ A m}^{-2}$) are shown in Fig. 3.12. The voltage contrast [149], which is clearly visible in the images, serves as an additional check for the direction of current flow relative to the image orientation. A positive current $j_x > 0$ is defined for conduction electrons moving in negative x -direction. The difference in potential of $\Delta\phi = 5 \text{ V}$ between the two contacts gives rise to a constant electric field of $E = \nabla\phi = 1 \text{ MV m}^{-1}$ within the permalloy structure.

The asymmetry images that were taken simultaneously with the SEM images shown in Fig. 3.12 are shown in Fig. 3.13. When the current direction is reversed, all forces that act on the vortex core are inverted. This means that the two core positions for $j = \pm 2.4 \times 10^{11} \text{ A m}^{-2}$ (shown in Fig. 3.13) are point symmetric to the core position when no current is applied (shown in Fig. 3.11). It is, however, difficult to evaluate this quantitatively by just looking at the images because the position of the magnetic structure relative to the borders of the image is

⁹The state shown in Fig. 3.10 was not the final state that was transferred into SEMPA.

¹⁰The calibration curve was taken while the sample was cooled down to 80 K with LN_2 and then slowly defrosted.

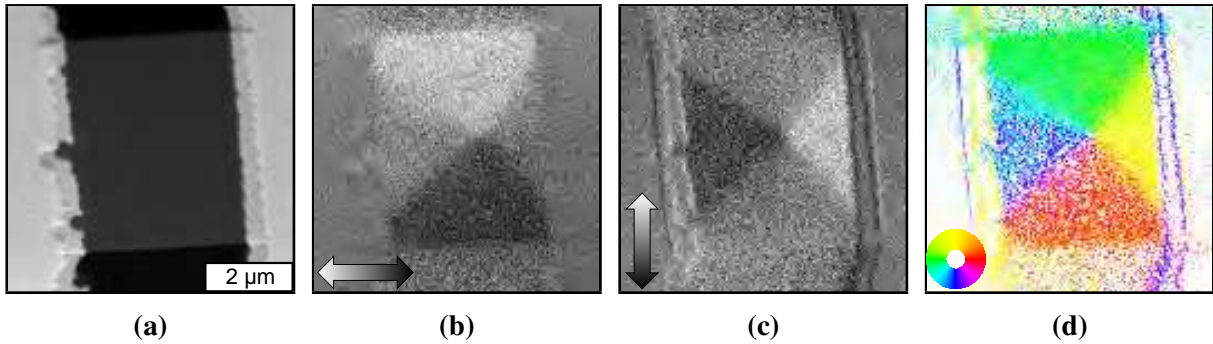


Figure 3.11: SEMPA images of the permalloy square shown in Fig. 3.10 after it has been contacted by gold leads. (a) SEM image of the structure. Two contacts are visible on each side of the permalloy square. As it was not possible to send a current through the structure after the first contact was prepared, the process shown in Fig. 3.5c had to be repeated to prepare a second, slightly shifted connection. (b-d) Magnetic images which have been taken simultaneously with the SEM image. The structure is in the magnetic Landau state with a positive sense of rotation (counterclockwise, $c = +1$). It can be seen, that the vortex core is not located in the center of the structure but is displaced a little to the right ($+x$). This is caused by a residual background field (~ 0.5 mT in $-y$ direction when the sample is tilted by 65° with respect to the gun) which is generated by the last objective lens of the SEM column and favors the left domain.

slightly shifted in every image. Yet it is qualitatively visible that the core moves to the top ($+y$) for increasing current densities, which allows for a determination of the core polarity of $p = -1$. The combined displacement caused by the Oersted field and the nonadiabatic spin-transfer torque on the Landau state with $c = +1$ causes a shift of the vortex core to the left for increasing current densities. This fits the description that has been found in Ref. [283] that a current flowing in $+x$ -direction generates an Oersted field in $+y$ -direction, which has a stronger effect on the vortex core position than the nonadiabatic spin-transfer torque. However the complete separation of the two effects can only be made once the displacement has been measured for two different curling directions $c = \pm 1$.

To change the curling direction, the sample was demagnetized with an alternating in-plane field with decaying amplitude. After four attempts, a state with a reversed rotation of $c = -1$ could be observed with SEMPA. Since the image contrast had already significantly weakened, the sample was ion milled for another 15 minutes with the same parameters as before. Another series of SEMPA images (not shown) was taken, which revealed an identical core polarity of $p = -1$.

Finally, a third magnetic state with the opposite core polarity $p = +1$ was prepared. To this end the current through the C3 objective lens of the SEM (and therefore the background field) was inverted during the demagnetization cycle. The z -component of the background field¹¹ of

¹¹The background field in SEMPA has a strength of 0.36 mT and the field vector points directly along the electron beam and out of the SEM column. The sample is fixed at an angle of 65° with respect to the SEM column (angle between surface normal and electron beam) [84]. In the reference frame of the sample, this field is split up into a component in $-y$ direction of 0.32 mT (which always favors the black domain in the “Asy13” image) and a component in $-z$ direction of 0.15 mT (which can be used to set the polarity p of the vortex core). The

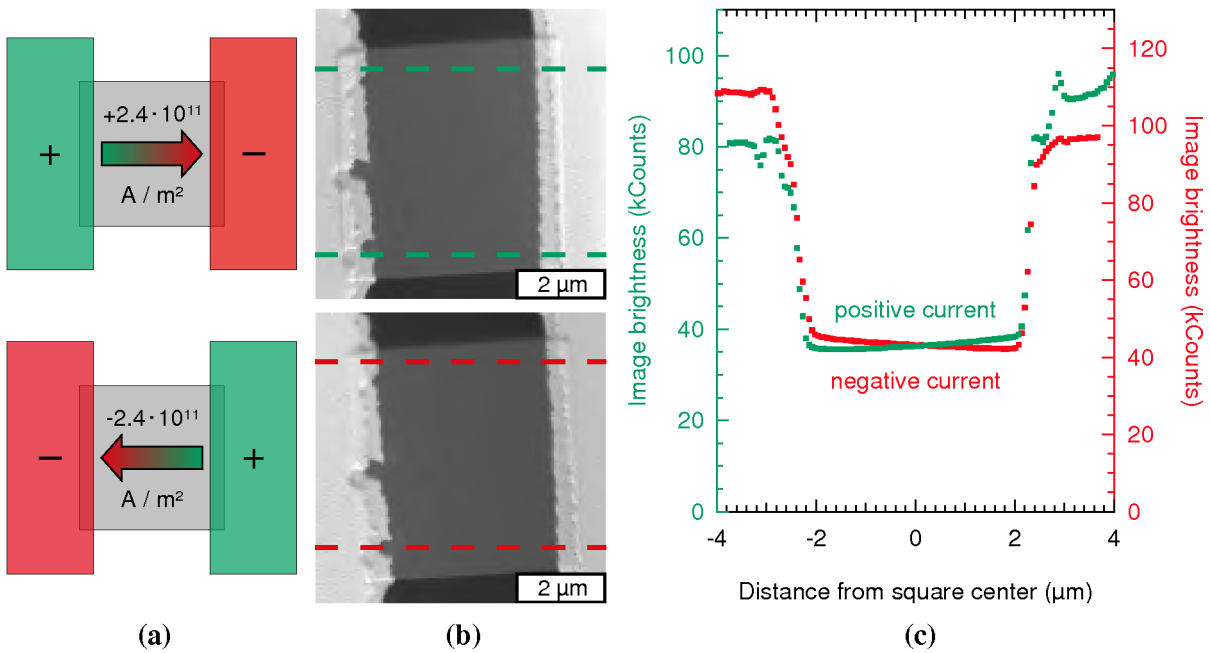


Figure 3.12: (a) Sketch of electric potential and direction and magnitude of current flow for two SEMPA measurements with opposing driving currents. (b) SEM images (128×128 px², 15 ms/px) reveal the polarity of the contact pads via voltage contrast [149]. The difference in potential between both pads is 5 V. The emission of secondary electrons from the contact pad with negative polarity (-) is enhanced compared to the emission from the contact pad with positive polarity (+). As a result the negatively charged contact pad is 12% brighter in the respective image than the positively charged contact pad. An additional effect that is due to a change in reflectivity R of the tungsten crystal (inside the spin detector) with the kinetic energy of the electrons (see Fig. 2.2b on page 14) might be superimposed. A line profile taken along the direction of current flow (parallel to the fast scanning direction) across the area indicated in (b) is shown in (c). The line profile additionally reveals a linear increase (decrease) in brightness of 12% across the uncovered region of the Py square (extending from $-2 \mu\text{m}$ to $2 \mu\text{m}$) for positive (negative) current.

roughly 0.15 mT is large enough to shift the magnetic moments slightly out-of-plane during the creation of the vortex core and thereby set a given core polarity. The third magnetic state showed a sense of rotation of $c = +1$. The sample was ion milled for 12 minutes before another series of SEMPA images was taken (also not shown), which confirmed the core polarity of $p = +1$.

To try and complete the data set by measuring the displacement for the fourth magnetic state ($c = -1, p = +1$) another demagnetization cycle was conducted with a reversed C3 current. The attempt to change the curling direction succeeded, but after another sequence of ion milling the creation of an undisturbed Landau state was no longer possible. Only diamond states or unclassified magnetization patterns could be observed. One cause for this might be that the vortex

field can be reversed by changing the polarity of the C3 lens current. The strength of the field was determined by comparing the field-induced deflection of the vortex core for a variety of samples to the deflection that is observed in hystereses in the Kerr microscope.

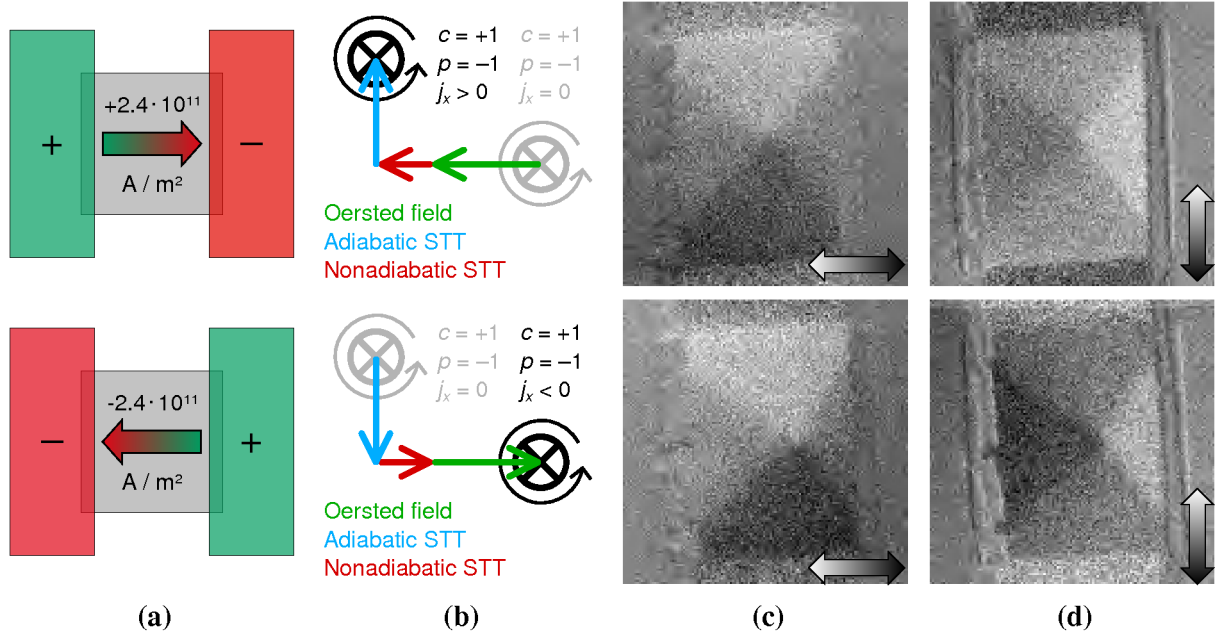


Figure 3.13: (a) Sketch of the electric potential and the direction and magnitude of the current flow for two SEMPA measurements with driving currents in positive (upper row) and negative (lower row) x -direction. (b) Displacement of a magnetic vortex core with a sense of rotation $c = +1$ and polarity $p = -1$ under the influence of the respective current densities shown in (a), as derived from (3.41). The vertical shift, perpendicular to the current flow, is caused by the adiabatic spin-transfer torque while the horizontal shift, parallel to the electron flow (anti-parallel to the current flow), is caused by the combined action of adiabatic spin-transfer torque and Oersted field. The direction of the Oersted field and its relative magnitude compared to the nonadiabatic spin-transfer torque are known from previous measurements [283]. (c-d) Magnetic images of the equilibrium position of the vortex core at the respective direct-current densities of $j = \pm 2.4 \times 10^{11} \text{ A m}^{-2}$. Since both core positions are affected by the same background field (compare Fig. 3.11) they are not aligned symmetrically around the center of the structure. In the images in the lower row, the core position is slightly shifted to the bottom right with respect to the images in the upper row. A shift of the vortex core to the top for increasing current densities indicates a negative core polarity $p = -1$ (see (3.41) on p. 41).

state is no longer the ground state for structures of very low thickness [318–320]. Another cause could be the variation in permalloy thickness between the two edge regions, which were protected from ion milling by the gold leads, and the central region of the square. Since no Landau state could be obtained, the sample was taken out of the SEMPA chamber to allow for a determination of the remaining permalloy thickness. This value is required for a determination of the sample thickness during the three measurement cycles.

Calibration of Sample Thickness

The final thickness of the permalloy square after one hour of ion milling $t_{f,AFM} = 7.3$ nm and the thickness of a witness film which corresponds to the initial thickness of the permalloy square $t_i = 11.8$ nm have been measured using atomic force microscopy (AFM). The final thickness that is measured with AFM is however influenced by a removal of the diamond substrate in the regions that are not covered by metallic films. Taking into account the sputtering yield of Diamond for 1 keV argon ions under the respective angle [321], about 0.9 nm of diamond were removed in the process. These have to be subtracted from the final thickness of the square as measured with AFM yielding a remaining thickness of the permalloy square of $t_f = 6.4$ nm.

For each milling step the same parameters were used for beam voltage, emission current and argon background pressure. The sample position, angle of incidence and area of exposure were also kept equal. It can therefore be assumed that the ion dose per unit area was more or less constant, leading to a steady removal of the sample material. A linear approximation can therefore be made for the decrease in permalloy thickness with milling time. From this approximation, the sample thickness for each of the three measurement cycles is calculated:

$$t_1 = 9.6 \text{ nm}$$

$$t_2 = 8.5 \text{ nm}$$

$$t_3 = 7.3 \text{ nm}$$

An exact knowledge of the permalloy thickness is required to calculate the respective current densities and to determine the magnitude of the geometric factors D_0/G_0 and G_0/mw_r^2 during each measurement cycle. Furthermore, the material parameters of the permalloy system need to be known before the geometric factors can be calculated. These were hence determined via ferromagnetic resonance (FMR).

3.5.2 Material Properties Obtained by Ferromagnetic Resonance

Ferromagnetic resonance (FMR) [322, 323] was used to determine the saturation magnetization, the Landé factor and the damping parameter of a permalloy witness film. The witness film was prepared simultaneously with the permalloy squares on a SiO₂ substrate. FMR is based on the collective excitation of the precessional motion of all the magnetic moments of a specific sample around the direction of an externally applied field, which has to be large enough to induce a single domain state [324]. The frequency at which resonance is observed, is of the order of GHz and increases with the strength of the external magnetic field [325].

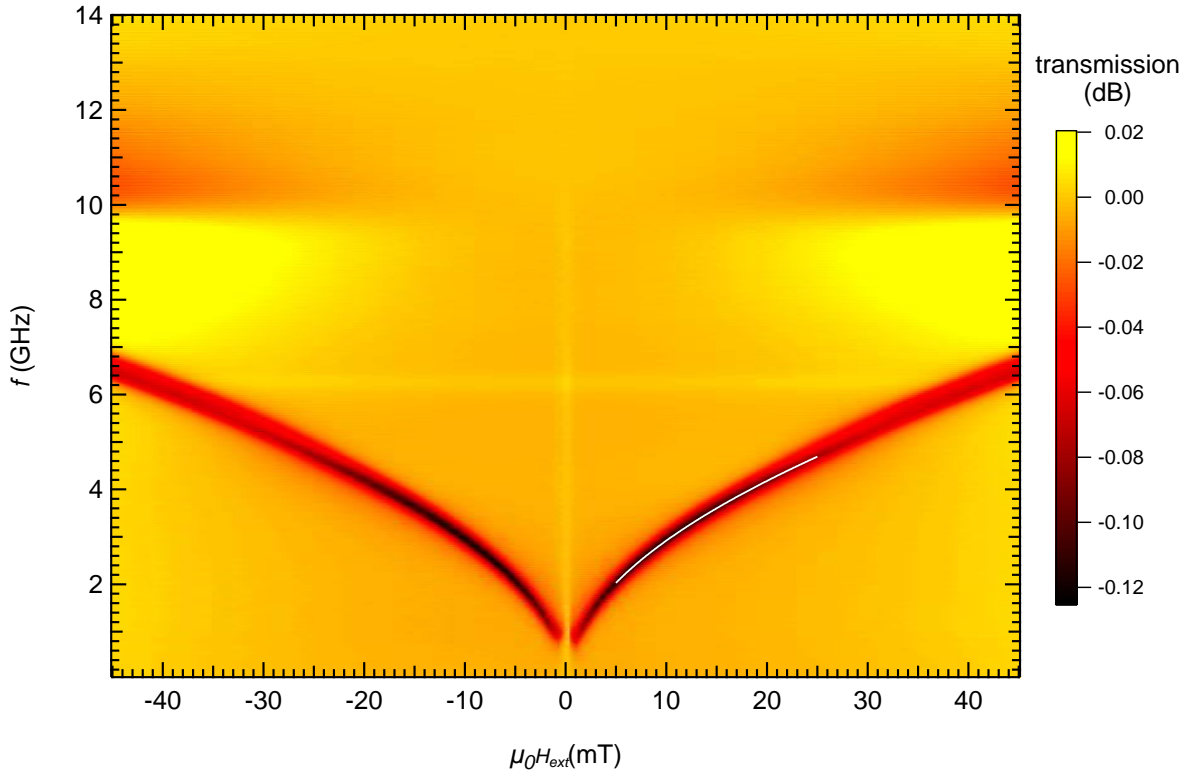


Figure 3.14: Absorption spectra measured for a 12 nm Py film grown on SiO₂. A minimum in transmission (black/red region) occurs, when a spin wave is excited in the ferromagnetic film. The energy is then dissipated within the spin wave via various damping mechanisms instead of being transmitted through the stripline. The thin white line represents a fit of the minima in transmission according to (3.46). The fit yields $g = 2.071 \pm 0.005$, $\mu_0 M_s = (1.035 \pm 0.006)$ T and $\mu_0 H_K = (-0.243 \pm 0.008)$ mT.

The sample investigated consisted of a 12 nm Py film, which was thermally evaporated at 0.8 \AA s^{-1} on a SiO₂ substrate at room temperature. FMR measurements are performed at room temperature (in cooperation with Felix Balhorn¹²). The sample is placed upside down onto a coplanar waveguide that carries the microwave signal. The microwave signal is provided by a vector network analyzer (VNA), which is also used to analyze the transmitted signal. The sample is saturated by an external magnetic field H_{ext} while the microwave frequency is swept from 0 to 14 GHz and the transmitted signal is recorded. Such frequency sweeps were obtained for magnetic fields between -45 mT and 45 mT in steps of 0.25 mT. The resulting absorption spectra are shown in Fig. 3.14. As expected, the position of the transmission minima moves towards higher frequencies (up to 6.5 GHz) for increasing strength of the external field (up to 45 mT).

The resonance condition for a thin film that is magnetized to saturation along its uniaxial easy axis is given by [325]

¹²Institute of Applied Physics, University of Hamburg.

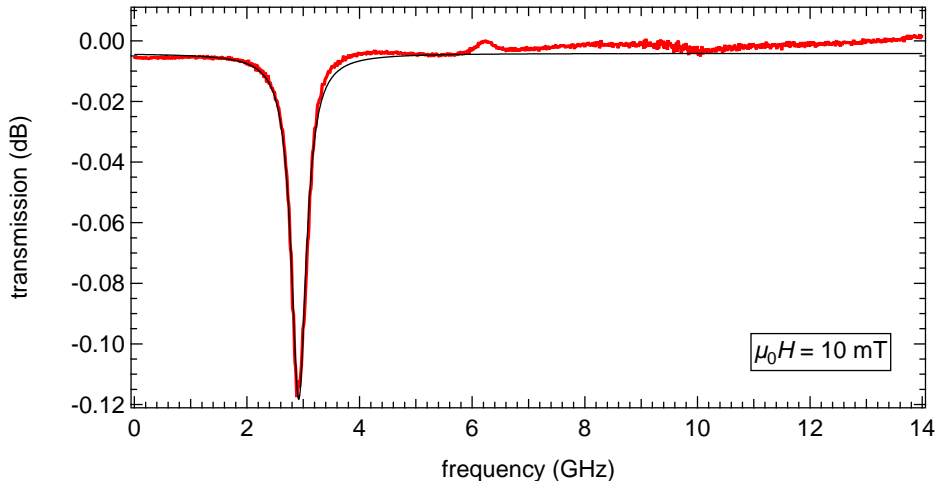


Figure 3.15: Single frequency sweep at $\mu_0 H_{\text{ext}} = 10 \text{ mT}$ (red line). This graph represents a vertical cut through Fig. 3.14 at $x = 10 \text{ mT}$. A Lorentzian function is fitted to extract the position and the width of the absorption peak (thin black line). The region that is taken into account for the fit has to be carefully chosen to make sure that the high-frequency noise of the setup (for instance the peak at 6 GHz) does not disturb the fit and alter the results.

$$f_{\text{Kittel}}(H_{\text{ext}}) = g \frac{e\mu_0}{4\pi m_e} \sqrt{(H_{\text{ext}} + H_{\text{K}})(H_{\text{ext}} + H_{\text{K}} + M_{\text{s}})} \quad (3.46)$$

with the Landé factor g , the applied background field H_{ext} and the anisotropy field H_{K} (see (3.21) on page 30). The position of the minima of the transmission spectrum and their linewidth are extracted from the measurement as shown in Fig. 3.14. The position of the minima is then fitted by (3.46) with g , H_{K} and M_{s} as free parameters. The fit is restricted to the area with the lowest background noise between 5 mT and 25 mT, where a single domain state is present. It yields a Landé factor $g = 2.071 \pm 0.005$, a saturation magnetization of $\mu_0 M_{\text{s}} = (1.035 \pm 0.006) \text{ T}$ and an anisotropy field of $\mu_0 H_{\text{K}} = (-0.243 \pm 0.008) \text{ mT}$.

The Landé factor is at the lower end of the range of bulk values of 2.07 [326], 2.08 [316, 327], 2.1 [328], 2.11 [329], 2.13 [330], 2.14 [331] and 2.07-2.13 [332]. The saturation magnetization of $M_{\text{s}} = (824 \pm 5) \text{ kA m}^{-1}$ is in good agreement with the room temperature (bulk) saturation magnetization for permalloy of $M_{\text{s}} \approx 820 \text{ kA m}^{-1}$ [316, 331, 333–335]¹³. A substantial decrease of M_{s} from the bulk value with film thickness is not expected above 40 Å at room temperature [336].

The anisotropy field translates into an anisotropy of $K = (100 \pm 3) \text{ J m}^{-3}$, which is a rather low value for permalloy [92]. However, the strength of the anisotropy field that is measured in FMR depends on the angle between the externally applied field H_{ext} and the easy axis of the material [337]. Since the FMR measurement was not performed in order to determine the strength of the anisotropy, the exact angle is unknown and the measured value of the anisotropy

¹³The measurement in Kobs *et al.* [334] is done for a permalloy film that was prepared in the exact same chamber. In this reference, the saturation magnetization was obtained with SQUID.

field can therefore lie between the uniaxial anisotropy field H_a and zero [337]. The uniaxial anisotropy H_a is induced by a magnetic field of roughly 1 mT that is applied during growth [338–340] and has a value of $(320 \pm 20) \text{ J m}^{-3}$ as determined with MOKE¹⁴ [92].

The Gilbert damping parameter α was determined by converting the linewidths in frequency Δf to the equivalent linewidths in field ΔH according to [341]:

$$\Delta H = \frac{\Delta f}{|\gamma| \sqrt{1 + \frac{|\gamma| \mu_0 M_s}{4\pi f}}} \quad (3.47)$$

Within the framework of inhomogenous broadening and Gilbert damping [342, 343] the Gilbert damping can then be determined by [341]

$$\Delta H = \Delta H_0 + \frac{4\pi\alpha f}{|\gamma|} \quad (3.48)$$

The inhomogenous broadening ΔH_0 “arises from the presence of magnetic inhomogeneities” [343] and is independent of frequency. The frequency-dependent term however gives direct access to the Gilbert damping. The gyromagnetic ratio can be calculated from the measurement of g via (3.8) to $\gamma/(2\pi) = (28.99 \pm 0.07) \text{ GHz T}^{-1}$, which is a common value for permalloy [344]. Application of (3.48) to the measured data yields $\alpha = 0.0085 \pm 0.0006$. For Py, α values of 0.0064 [345], 0.008 [332, 333, 346, 347] and 0.009 [348] have been published. Although the most common value of 0.008 lies within the error margin of our measurements a slight increase of α could be explained by the small film thickness [348] or a slightly higher nickel content [333].

Ferromagnetic resonance investigations of a 12 nm permalloy film yielded the Landé factor $g = 2.071 \pm 0.005$, the saturation magnetization $\mu_0 M_s = (1.035 \pm 0.006) \text{ T}$, and the Gilbert damping $\alpha = 0.0085 \pm 0.0006$ of the film. The film investigated here was a witness film to the permalloy squares that were prepared on the diamond substrate.

3.5.3 Determination of all Spin-Transfer-Torque Parameters

With all required material parameters being known, the spin-transfer torque parameters can be obtained from the current-induced displacement of the vortex core. The relative position of the vortex core for the three magnetic configurations was determined from the data as described in chapter 7.1.1 and chapter 7.1.2. Subsequently, the data was corrected for an offset in the vortex-core displacement that is caused by a residual field in y direction of -0.32 mT generated by the objective lens of the SEM column. The field causes an offset in x direction of about $\pm 500 \text{ nm}$, the sign of which depends on the curling direction c of the Landau state.

Fig. 3.16 shows the resulting data for the position of the vortex core. The data is theoretically described by Eq. (3.41) that was derived on p. 41:

$$\begin{pmatrix} x \\ y \end{pmatrix} = -\frac{|G_0|}{m\omega_r^2} \begin{pmatrix} \tilde{H}c + \left| \frac{D_0}{G_0} \right| \beta u \\ up \end{pmatrix} \quad (3.49)$$

¹⁴Magneto-optical Kerr effect.

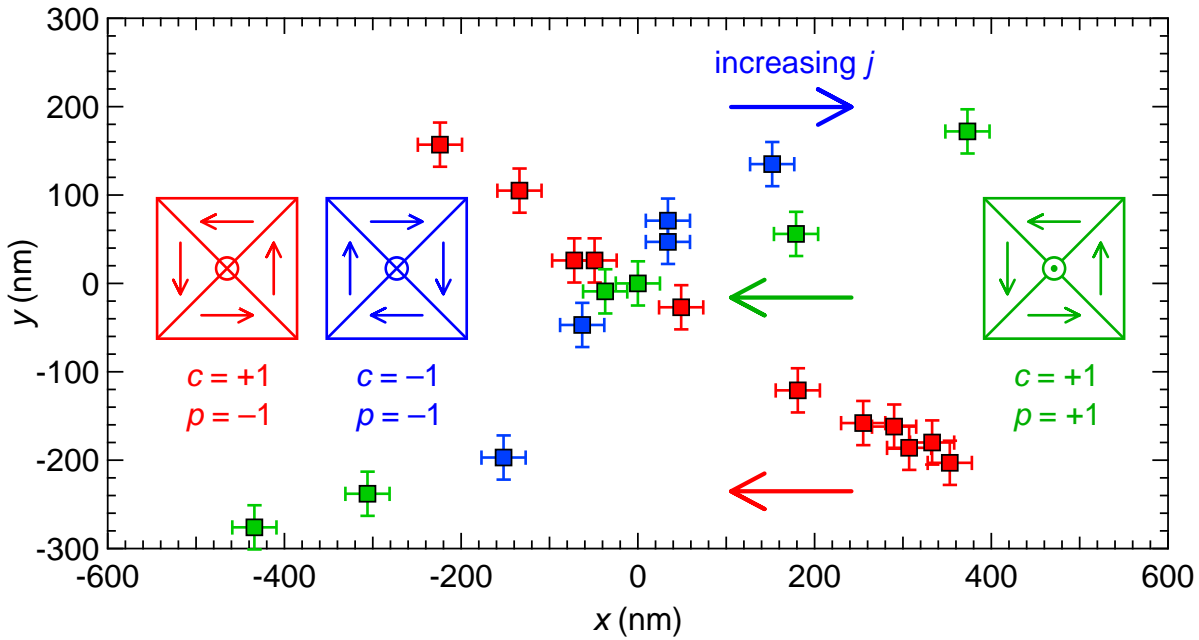


Figure 3.16: Geometric map of the vortex position in a permalloy square prepared on a diamond substrate for current densities in the range of $\pm 3.2 \times 10^{11} \text{ A m}^{-2}$ and three configurations of the Landau state. The direction of deflection for increasing current densities is indicated by the arrows. By comparing the three curves, it becomes clear that a change in circularity c has a major impact on the slope, as it reverses the core deflection in x direction. Since the nonadiabatic spin-transfer torque is independent of c , this effect can solely be attributed to the Oersted field contribution. It is thereby immediately clear that the Oersted field has a stronger influence on the vortex core position than the nonadiabatic spin-transfer torque. The direction of displacement along the y -axis is proportional to the core polarity p . Comparison to (3.41) therefore allows for a determination of the core polarity, which is not visible in the SEMPA images, as they show the projection of the magnetization vector on the film plane.

A linear correlation between the displacement in x and y -direction is observed in the measurement. This suggests that the Oersted field contribution is linear in current density, since all other contributions have a linear dependency on the current density. The figure also yields information about the relative strength of the Oersted field compared to the nonadiabatic spin-transfer torque. Since the direction of displacement is reversed with the curling direction of the structure c , it becomes clear that the Oersted field contribution dominates the displacement in x direction and outweighs the effects caused by the nonadiabatic spin-transfer torque. The latter is independent of c . Furthermore, the polarity of the vortex core is revealed via the direction of deflection that is detected parallel to the y -axis. In the as-prepared state shown in Fig. 3.11 the core has a negative polarity $p = -1$.

Quantitative values for the core displacement are shown in Tab. 3.2. The current density is calculated by considering the variation in thickness of the permalloy element and by taking into account the influence of parasitic current shunts (see chapter 7.2). The different values are however difficult to compare since the geometric factor $G_0/m\omega_r^2$ depends on film thickness (see

c	p	t (nm)	$x(j_0)$ (nm)	$y(j_0)$ (nm)
+1	-1	9.6 ± 0.2	-79 ± 4	$+48 \pm 3$
-1	-1	8.5 ± 0.2	$+45 \pm 5$	$+52 \pm 5$
+1	+1	7.3 ± 0.2	-129 ± 6	-67 ± 5

Table 3.2: Raw values for the displacement of the vortex core induced by a unit current-density of $j_0 = 1 \times 10^{11} \text{ A m}^{-2}$. The data has been extracted from the measurement shown in Fig. 3.16. A direct comparison of the measured values is not possible since the confining potential, which enters in each contribution, depends on film thickness. The confining potential is eliminated in Tab. 3.3.

chapter 3.3.2). An elimination of this quantity is therefore required before the spin drift velocity u and the parameter of the nonadiabatic spin-transfer torque β can be determined.

Spin Drift Velocity

To allow for an extraction of the spin drift velocity u from the measured data and to eliminate the thickness dependence of the geometric factors, knowledge about the confining potential $G_0/m\omega_f^2$ is required. To this end the magnitude of the confining potential has been determined by micromagnetic simulations (see chapter 3.3.2). It was shown in chapter 3.3.2 that the inverse confining potential equals the resonance frequency $\omega_{\text{res}} = m\omega_f^2/G_0$. Hence, a multiplication of the measured slopes by the resonance frequency eliminates all dependencies on the confining potential. The result can again be expressed as a vector similar to (3.41) and (3.49):

$$\begin{pmatrix} \omega_{\text{res}} \cdot x(j_0) \\ \omega_{\text{res}} \cdot y(j_0) \end{pmatrix} = \begin{pmatrix} -c\tilde{H}(j_0) - \left| \frac{D_0}{G_0} \right| \beta u(j_0) \\ -pu(j_0) \end{pmatrix} \quad (3.50)$$

The measured values for the individual components of this vector are shown in Tab. 3.3. It becomes clear that the magnitude of the displacement in x -direction depends on the curling direction c , which determines whether the two contributions point in the same or in opposite directions. Since the displacement has a positive sign for $c = -1$, the Oersted field term $\tilde{H}(j_0)$ has to be positive and outweighs the second contribution caused by the nonadiabatic spin-transfer torque. The fact that the displacement in x -direction is not equal for the two measurements with $c = +1$ shows that this property also depends on sample thickness. This will be crucial for the determination of β , which is discussed in the following section.

The displacement in y -direction, however, only depends on the spin drift velocity u multiplied by the core polarity p . The magnitude of this displacement is therefore directly identical to the spin drift velocity. The magnitude of u depends on the current density. It is hence most commonly given for the unit current-density $j_0 = 1 \times 10^{11} \text{ A m}^{-2}$ to allow for an easier comparison of the values. The resulting values shown in Tab. 3.3 reveal that the spin drift velocity is not influenced by ion milling and consequently also independent of thickness in the range that has been investigated. It is therefore legitimate to use the values of the three measurements

c	p	t (nm)	ω_{res} (MHz)	$\omega_{\text{res}} \cdot x(j_0)$ (m/s)	$\omega_{\text{res}} \cdot y(j_0)$ (m/s)	dx/dy
+1	-1	9.6 ± 0.2	99 ± 5	-7.8 ± 0.5	$+4.8 \pm 0.4$	-1.63 ± 0.14
-1	-1	8.5 ± 0.2	88 ± 4	$+4.0 \pm 0.5$	$+4.6 \pm 0.5$	$+0.87 \pm 0.14$
+1	+1	7.3 ± 0.2	76 ± 4	-9.8 ± 0.7	-5.1 ± 0.4	$+1.93 \pm 0.16$

Table 3.3: Corrected values for the displacement of the vortex core, induced by a unit current-density $j_0 = 1 \times 10^{11} \text{ A m}^{-2}$. The influence of the confining potential, which is identical to $1/\omega_{\text{res}}$, has been eliminated. The displacement in y -direction is now constant within the error margin. It corresponds to the spin drift velocity u , which can consequently also be considered as constant. The displacement in x -direction can only be directly compared for measurements with identical c , *i.e.* $c = +1$. The data suggests that either the Oersted field or the nonadiabatic contribution increases with decreasing thickness. An explanation of this observation will be given in chapter 3.5.4.

to obtain a value of higher statistical significance. For a temperature of $T = (341 \pm 9) \text{ K}$ we therefore obtain:

$$u(j_0) = (4.79 \pm 0.26) \text{ m s}^{-1}$$

The spin drift velocity can also be determined by sending a spin-polarized current through a spin wave. This results in a Doppler shift of the spin wave that is directly proportional to the spin drift velocity u [281]. The first measurement based on this approach has been conducted by Vlaminck and Bailleul [344] and yielded a value of $u(j_0) = 5 \text{ m s}^{-1}$ for permalloy. Further measurements by other groups produced values in the range of $4 - 6 \text{ m s}^{-1}$ at room temperature [81, 82, 349, 350].

The result obtained from the deflection of the vortex core is therefore in good agreement with recently published values for permalloy. It can furthermore be concluded that subsequent ion milling under the before-mentioned conditions does not change the magnetic properties of the sample system, as the spin drift velocity remained constant after each milling step.

Spin Polarization of the Current

The spin polarization of the driving current P can be calculated from the spin drift velocity u when the current density j and saturation magnetization M_s are known. A saturation magnetization at room temperature of $(824 \pm 5) \text{ kA m}^{-1}$ has been measured with FMR in a witness film (see chapter 3.5.2). To account for the slightly elevated temperature of $T = (341 \pm 9) \text{ K}$ during the measurement this value is reduced to $(811 \pm 5) \text{ kA m}^{-1}$ by the application of a calibration curve for permalloy [351]. From the definition of the spin drift velocity (3.25) follows:

$$P = \frac{2eM_s}{g\mu_B j} u \quad (3.51)$$

The insertion of u together with the values of g and M_s that were obtained with FMR (see chapter 3.5.2) yields:

$$P = (65 \pm 4)\%$$

yield results in the same range [362–364]. Although these values fit to theoretical models [360] there seems to be a fundamental difference when measuring the spin polarization with methods like PCAR spectroscopy, that “measures the spin polarization at the surface” [361]. A possible explanation lies in a reduction of the spin polarization at the surface with respect to the bulk value in the permalloy system. Another reason might be that the 1D approximation of the spin-diffusion model [366], that is often used to analyze the data, leads to an underestimation of the spin polarization [367, 368].

Parameter of Nonadiabaticity

The parameter of nonadiabaticity β is determined from the change in slope of the current-induced vortex core displacement when the sense of rotation c is reversed. While changing the sense of rotation reverses the Oersted-field-induced displacement it has no influence on the effects caused by spin-transfer torques. As described in chapter 3.3.1, β is determined by the application of

$$\beta = \frac{1}{2} \frac{G_0}{D_0} \left(p \cdot \frac{dx}{dy}(c, p) + p \cdot \frac{dx}{dy}(-c, p) \right) \quad (3.52)$$

using values for the ratio of gyrovector and dissipation tensor G_0/D_0 that have been obtained by performing micromagnetic simulations (see chapter 3.3.2). The correction for the confining potential that has been made in the previous section has no influence on the slope dx/dy , which is the only measured property used for the determination of β . The confining potential cancels out when $x(j_0)$ is divided by $y(j_0)$. The polarity of the vortex core p only changes the sign but not the magnitude of the slope dx/dy . Hence, measurements of different polarity can be used for the determination of the β parameter.

The magnitude of the slope dx/dy should be identical for the two measurements with a positive curling direction ($c = +1$). The measurement however reveals that there is a slight increase in this property when the film thickness is reduced (last column in Tab. 3.3). One reason for this might be an increase in the nonadiabatic contribution. The radius of the vortex core slightly decreases with decreasing film thickness [284, 287, 291, 369, 370], which leads to an increase in the truly nonadiabatic contribution β_{na} and causes a stronger displacement. When the film thickness is decreased from 12 nm to 8 nm, the radius of the vortex core decreases from 11 nm to 10 nm (assuming an exchange length $l_{\text{ex}} = 4$ nm for permalloy) [287].

Another reason might be that a stronger Oersted field is generated when the film thickness of the setup is reduced. On the basis of the available data, these two contributions can not be separated. To obtain a reliable value for β it is important to determine a value for the slope

$$dx/dy(c = +1, p = -1, t = 8.5 \text{ nm})$$

and to compare it to the slope that was directly measured:

$$dx/dy(c = -1, p = -1, t = 8.5 \text{ nm}) = 0.87 \pm 0.14$$

For $c = +1$ only measurements of the slope at $t = 9.6$ nm and $t = 7.3$ nm are available. To obtain a value for $t = 8.5$ nm the arithmetic mean of both values is calculated as¹⁵:

$$dx/dy(c = +1, p = -1, t = 8.5 \text{ nm}) = -1.78 \pm 0.10$$

The ratio of gyrovector and dissipation tensor for the corresponding thickness has been obtained by micromagnetic simulations (see chapter 3.3.2) as:

$$\frac{G_0}{D_0}(t = 8.5 \text{ nm}) = 3.75$$

Inserting all the values into (3.52) yields:

$$\beta = 0.12 \pm 0.02$$

The set of parameters (α see chapter 3.5.2, $u(j_0)$ see chapter 3.5.3) for a vortex core in a 8.5 nm thick permalloy element is hereby complete:

Vortex core

$$\alpha = 0.0085 \pm 0.0006$$

$$\beta = 0.12 \pm 0.02$$

$$u(j_0) = (4.8 \pm 0.3) \text{ m s}^{-1}$$

The value for β is in good agreement with results that were obtained from the observation of current-induced vortex displacement in 30 nm thick permalloy discs $\beta = 0.15 \pm 0.07$ ($\alpha = 0.008$) [283] and from the observation of the gyrotropic motion in 50 nm thick permalloy squares $\beta = 0.15 \pm 0.02$ ($\alpha = 0.016 \pm 0.001$) [88]. However, both measurements lack values for the spin-drift velocity u or the spin polarization P and all three β values (including the one that is obtained here) are equal within their error margin. A conclusion about the variation of β_{na} with the thickness dependent diameter of the vortex core can hence not yet be drawn.

It is however possible to estimate the magnitude of the truly nonadiabatic contribution β_{na} , by comparing the measured values to results obtained from experiments conducted with spin waves, as discussed in chapter 3.2. Since spin waves show a very shallow spatial variation of the magnetization, the truly nonadiabatic contribution β_{na} vanishes and only β_{sr} remains. The results of two spin-wave experiments, dedicated to the determination of β_{sr} , have been published until now [81, 82].

In 2012, Sekiguchi *et al.* [81] investigated the effect of an electrical current on the amplitude and frequency of spin waves in 35 nm thick permalloy stripes [81]. While the adiabatic spin-transfer torque slightly changes the frequency of the spin waves, the nonadiabatic spin-transfer torque alters their amplitude [280, 281]. For the given system they found $\alpha = 0.0082$, $\beta_{\text{sr}} =$

¹⁵It is physically reasonable to assume a monotonous increase of dx/dy with decreasing permalloy thickness. Whether this decrease is described by an exponential e^{-t} or a polynomial t^{-n} ($n \in \mathbb{N}, n > 0$) function, the fact that the property that is described by the function changes by only 15 % over a region where the thickness t changes by 30 % suggests that a rather flat region of the function is reached. Additionally, both values do not lie in the vicinity of the singularity of the function, which is expected at $t = 0$ nm. Therefore a linear approximation between both points is justified.

0.033 ± 0.012 , and $u(j_0) = 5 \text{ ms}^{-1}$. A slight overestimation of β_{sr} due to an inhomogeneous Oersted field could however not be excluded, hence $\beta_{\text{sr}} \leq 0.033 \pm 0.012$.

Two years later, in 2014, Chauleau *et al.* [82] used an improved setup with an additional optical detection of the spin waves via time-resolved scanning Kerr microscopy (see chapter 4.1). For a 15 nm thick permalloy stripe they obtained [82]:

Spin waves

$$\alpha = 0.0075 \pm 0.0003$$

$$\beta_{\text{sr}} = 0.035 \pm 0.011$$

$$u(j_0) = (5.1 \pm 0.2) \text{ ms}^{-1}$$

This set of parameters is identical with the one obtained by Sekiguchi *et al.* [81]. When comparing the values obtained for spin waves to the ones obtained for a vortex core, the damping α and spin drift velocity u are in perfect agreement. The nonadiabatic contribution β , however, is indeed enhanced by 340 % in a vortex state due to the strong gradient of the magnetization in the vortex core region.

By the application of (3.27) to the results of the two experiments, the truly nonadiabatic contribution β_{na} that is effective in a vortex core can be derived:

$$\beta_{\text{na}} = \beta - \beta_{\text{sr}} = 0.085 \pm 0.023 \quad (3.53)$$

The truly nonadiabatic term contributes to 71 % of the total nonadiabaticity for a vortex state in a 8.5 nm thick permalloy element. The next question is, whether and to what magnitude an influence of the lateral size of the vortex core on the truly nonadiabatic contribution would be expected within the three measurements [80, 88, 283] for vortex states? If we assume that the contribution β_{sr} is proportional to α , it should be the same in Heyne *et al.* [283] and it should be double in Pollard *et al.* [88] (compared to the other measurements). Hence the truly nonadiabatic contribution in these papers is $\beta_{\text{na}} = 0.11 \pm 0.07$ [283] and $\beta_{\text{na}} = 0.11 \pm 0.02$ [88]. Both values are identical to our value $\beta_{\text{na}} = 0.085 \pm 0.023$, although the vortex core in Pollard *et al.* [88] has roughly double the size of¹⁶ 21 nm because of the large film thickness of 50 nm. A further reduction of the experimental error and/or and investigation of a greater range in film thickness will be necessary before further conclusions can be drawn about the influence of the vortex-core size on the truly nonadiabatic contribution.

3.5.4 Experimental Sources of an Oersted Field

A long-standing mystery in the history of nanowires is, by which mechanisms and to what magnitude a current-induced Oersted field is created. Even though the experiments that were conducted with magnetic vortices can not fully solve this problem, they can at least give some hints about the relevance of the different contributions.

There are two possible mechanisms that give rise to an Oersted-field contribution: The geometry of the setup [372] and a gradient in conductivity within the permalloy structure [273].

¹⁶This measured value could be increased due to experimental broadening, which is not discussed in Pollard *et al.* [88].

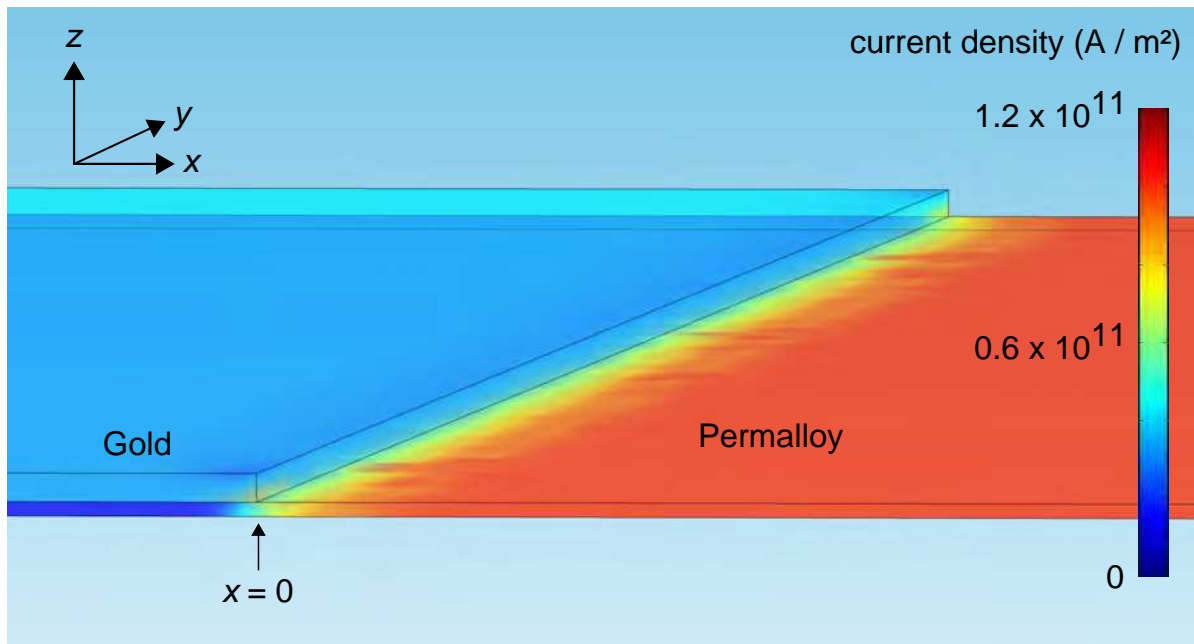


Figure 3.18: COMSOL [371] simulation of the current density distribution in a $5\ \mu\text{m}$ sized square permalloy element ($t = 10\ \text{nm}$) contacted by a gold lead ($t = 20\ \text{nm}$). The image shows the current density at the respective surfaces. Although interface resistances are not included in the model, the current density may be higher inside the material. As the current flows in from the left, most of the current remains in the gold lead as long as possible due to its high conductivity. Only a fraction of the total current is directed through the underlying permalloy square. It is only at the edge of the gold electrode, that the desired current density of $1 \times 10^{11}\ \text{A m}^{-2}$ is reached in the permalloy element.

The latter is caused by a thermal gradient in the magnetic structure or an asymmetry in interface scattering. Since the Oersted fields that are created by these two mechanisms both point in opposite directions, a clear identification of the leading contribution is possible. In the following sections the background behind both mechanisms will be explained, before a comparison to the experimental data is made.

Geometry of the Setup

The geometry of the setup is shown in Fig. 3.2a on page 38. The magnetic structure is contacted with gold electrodes on two sides. The technical current flows in $+x$ direction (electrons moving towards $-x$). The magnitude and distribution of the Oersted field that is generated in such a “nanowire geometry” has been calculated analytically by Moon *et al.* [372]. The electrical conductivity is more than one order of magnitude higher for gold than it is for permalloy. Additionally, the gold electrode is thicker than the permalloy structure (as prepared: $15\ \text{nm}$ compared to $12\ \text{nm}$). As a result, most of the current flows through the gold electrode in the overlap region (see Fig. 3.18), generating an Oersted field in $+y$ direction in the permalloy layer beneath it (see Fig. 3.19). When the current is injected into the nanostructure at the edge of the electrode, a vertical current flow emerges, which also generates an Oersted field. The vertical current flow

however creates Oersted fields of opposite signs around the injection region (see Fig. 3.19). This effect may thereby lead to a vortex deflection in both directions, depending on the exact position of the injection region. Overall the first effect has a greater influence (see Fig. 3.19) which means that we can consider a net Oersted field in $+y$ direction. This field is however strongly inhomogeneous although its influence on the vortex core position is described by an homogeneously distributed effective field in (3.50).

The numerical results of the calculation by Moon *et al.* [372], for the geometry that has been used, are shown in Fig. 3.19. A field of approximately 0.35 mT is expected in the region below the gold electrodes for a current density of $j = 1 \times 10^{11} \text{ A m}^{-2}$. It is slightly double-peaked below the tip of the electrode and then quickly decays to zero within a few hundred nanometers. This means that no Oersted field caused by the contact geometry is present in the center of the structure. Nevertheless the effect of the field on the magnetic microstructure near the edges may very well have an influence on the microstructure in the central region. It may therefore lead to a displacement of the magnetic vortex core.

Gradient in Conductivity

A gradient in conductivity within the permalloy layer is caused by two contributions. First, the ultrahigh current densities lead to a substantial Joule heating of the permalloy film. Due to the asymmetry of the setup with one interface of the film being permalloy/diamond whereas the opposing interface is permalloy/vacuum, the Joule heat can only be dissipated effectively through the diamond substrate. This leads to a temperature gradient in the magnetic film, parallel to the surface normal, resulting in an increase of temperature with increasing distance from the diamond substrate [273]. Since the electric conductivity decreases with increasing temperature, the current density is higher in layers that are closer to the diamond substrate. The upper layers will therefore feel an effective Oersted field which is slightly stronger than the one for the bottom layers¹⁷. For a technical current flowing in $+x$ direction (electrons moving towards $-x$) a net field is generated in $-y$ direction. Compared to the field that is caused by the contact geometry, it is therefore directed in the opposite direction. This can easily be understood by imagining that in the Joule-heating case more net current flows in the colder layers at the bottom, whereas the current in the gold electrode is localized above the nanostructure.

A second possible contribution to an inhomogeneous current density within the nanostructure is caused by an asymmetry in scattering of conduction electrons at the two film boundaries (permalloy/diamond and vacuum/permalloy). In the framework of the Fuchs-Sondheimer model [373, 374] the rates of specular scattering for the two interfaces are expressed by the parameters P and Q respectively (both ranging from 0 to 1). An asymmetry in scattering means $P \neq Q$. The magnitude of the two parameters was not investigated for our system. The two parameters exponentially depend on the RMS¹⁸ roughness σ_P or σ_Q of the respective interface by [375, 376]

¹⁷The Oersted field that is generated by the bottom layers and sensed in the top layers has the opposite sign than the one that is generated in the top layers and sensed in the bottom layers. For a homogeneous current flow both effects therefore cancel out.

¹⁸RMS = root mean square.

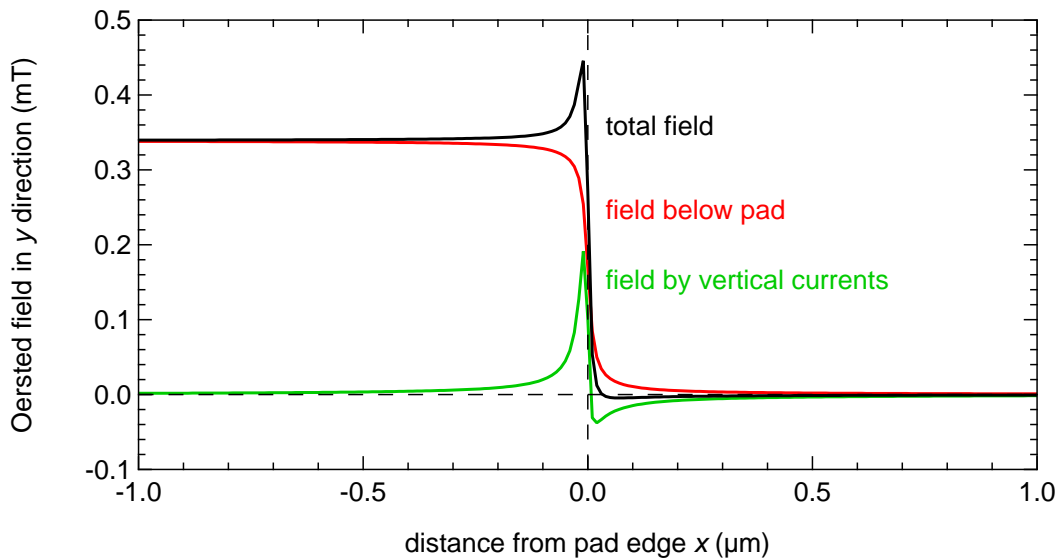


Figure 3.19: Magnitude of the Oersted field for the setup shown in Fig. 3.2a, calculated in the framework of the nanowire geometry [372]. A technical current of $j = 1 \times 10^{11} \text{ A m}^{-2}$ flowing in x direction is assumed. The parameters for the wire are width $w = 5 \mu\text{m}$ and thickness $t = 10 \text{ nm}$. The connection pad which is covering the nanostructure extends from $x = 0$ to $x = -\infty$, has a width of $L = 8 \mu\text{m}$ and a height $h = 10 \text{ nm}$. In our experimental setup the nanowire roughly extends from $-0.5 \mu\text{m}$ to $4.5 \mu\text{m}$. The strength of the field is calculated in the center of the nanowire ($y = w/2, z = t/2$) in dependence of the position along the wire x . The field vector points in $+y$ direction. The field consists of two contributions: The major part of the field is located beneath the Au connection pad (see Fig. 3.18). It stems from the unequally distributed current density: the main part of the current flows through the gold electrode (gold has a much higher conductivity). Since the main part of the current flows above the nanostructure in that region, a positive Oersted field is created below the current flow (check with the right-hand rule for technical current, left-hand for electrons). At the junction, where the current density is injected into the nanowire ($x = 0$), the field is strongly increased due to vertical paths of the current (parallel to z). These vertical current flows however create fields of opposite sign on both sides of the injection region.

$$P(\theta) = \exp\left(-\left(4\pi\sigma_P/\lambda_F\right)^2 \cos^2(\theta)\right) \quad (3.54)$$

with the Fermi wavelength λ_F (about 5 Å for nickel [377]) and the angle θ , which is measured between the wave vector of the electron and the interface normal. The surface roughness of the permalloy squares can not be distinguished from the surface roughness of the diamond substrate (which should be close to the roughness of the lower interface) via AFM measurements. Both are in the range of $\sigma_{\text{RMS}} = 5 - 7 \text{ \AA}$. For an exemplary electron that hits the surface under an incidence angle of 2° ($\theta = 88^\circ$) this translates to a reflectivity in the range of $P = 0.69 - 0.83$. The ratio between P and Q is proportional to $P/Q \propto \exp((\sigma_P - \sigma_Q)/\lambda_F)$, which means that it exponentially depends on the difference in RMS roughness for the two interfaces. Even a slight difference might therefore very well have an effect on the electrical conductivity near the interface. It would hence give rise to another Oersted field contribution¹⁹. A quantification of this contribution is however beyond the scope of this thesis.

Comparison to Experimental Data

Experiments with vortices using stationary currents (the samples investigated in this work and by Heyne *et al.* [283]) concurrently show an effective Oersted field in $+y$ direction for a current flowing in $+x$ direction. It therefore becomes clear that the main contribution to the Oersted field for the given geometry (Fig. 3.2a on page 38) stems from the geometry of the setup. The determination of the magnitude of the Oersted field is however difficult as all contributions give rise to a field which is by no means homogeneous. The displacement of the vortex core is only a sensor for the integrated action of this field on the magnetic structure, which is theoretically described as an homogeneous effective field \tilde{H} in the model by Krüger *et al.* [196] (see chapter 3.3.1). The strength of this field can be derived from the displacement in x direction as:

$$\mu_0 H(j_0) = -\frac{2\pi}{\gamma} \cdot \frac{1}{l} \cdot \left(c \cdot \omega_{\text{res}} \cdot x(j_0) + c \left| \frac{D_0}{G_0} \right| \beta \cdot u(j_0) \right) \quad (3.55)$$

The resulting effective homogeneous field for a thickness of 8.5 nm is $\mu_0 H(j_0)$ (43 ± 7) μT . In reality the field is however not homogeneously distributed. It furthermore consists of locally stronger contributions like the one calculated by Moon *et al.* [372] (see Fig. 3.19).

In the experimental data presented in the previous sections, an increase of the vortex displacement due to a field like contribution by 26 % was observed as the thickness of the sample was decreased from 9.6 nm to 7.3 nm. This effect can be explained by an increase in current density in the gold leads. The reference value for the current density, for which all experimental values are given, is calculated in the center of the permalloy square. The gold leads, however, with an initial thickness in the range of 15 - 30 nm²⁰ are removed faster during ion milling (see

¹⁹This contribution can occur in both in-plane directions that are perpendicular to the current ($\pm y$), depending on which of the interfaces is the rougher one.

²⁰The evaporation of gold had to be repeated a second time during the synthesis of the sample to achieve electrical connection, hence the inhomogeneous thickness.

chapter 7.2). As a result, the relative current density increases in the gold electrodes compared to the permalloy square. Depending on the initial thickness the relative increase is in the range of 5 - 50 %. Although a small fraction of the current is redistributed into the protected permalloy layer below the gold electrodes, this increase in current density is sufficient to explain the observed effect.

Although the exact strength of the field induced by a conductivity gradient is not known, it is also expected to decrease with film thickness²¹. Being the weaker contribution to the total field and pointing anti-parallel to the resulting field, a decrease in this property also leads to an increase in the total effective field.

3.6 Summary

The current-induced displacement of a magnetic vortex core has been investigated in three different material systems. In Iron and $\text{Fe}_{54}\text{Co}_{39}\text{Si}_7$, a significant deflection of the vortex core with an electric current could not be observed. Even though the vortex core was mobile during the application of an external magnetic field, pinning processes dominated its behavior when an electric current was applied.

In the soft-magnetic permalloy a current-induced deflection of the vortex core could be observed. All parameters that are relevant for the characterization of spin-transfer torque effects have been obtained and published [80]. These are (in alphabetical order and evaluated for the unit current density j_0 , as applicable):

$$\begin{aligned}
 \alpha &= 0.0085 \pm 0.0006 && \text{(Gilbert damping)} \\
 \beta &= 0.12 \pm 0.02 && \text{(Parameter of nonadiabaticity)} \\
 g &= 2.071 \pm 0.005 && \text{(Landé factor)} \\
 M_s &= (824 \pm 5) \text{ kA m}^{-1} && \text{(Saturation magnetization)} \\
 P &= (65 \pm 4) \% && \text{(Spin polarization)} \\
 u(j_0) &= (4.8 \pm 0.3) \text{ m s}^{-1} && \text{(Spin drift velocity)}
 \end{aligned}$$

By comparing these results to recent experiments conducted with spin waves [81, 82, 344, 349], an excellent agreement between all material parameters is found. Additionally, a substantial increase of the nonadiabaticity could be confirmed for the vortex core. The truly nonadiabatic contribution $\beta_{\text{na}} = 0.085 \pm 0.023$ accounts for 71 % of the total nonadiabaticity of the vortex structure in permalloy with a thickness of 8.5 nm. Yet another increase of this property is possible by further reducing the film thickness and thereby the size of the central core region of the vortex [287].

The velocity of a domain wall in a system with in-plane anisotropy is proportional to the nonadiabatic contribution [74]. Devices containing vortices are hence a promising candidate for enhancing the domain wall velocity in spin-transfer torque applications based on in-plane materials. They can then compete with systems with a perpendicular magnetic anisotropy (PMA).

²¹The temperature gradient becomes smaller for thinner films which on the other hand reduces the asymmetry of the current distribution.

In PMA systems narrow domain walls are inherently present²², leading to a strong spin-transfer torque and a subsequent enhancement of the domain wall velocity [378–381].

Vortex domain walls could for instance be used in Racetrack memory (RTM) [67] based on in-plane systems (for details about RTM see introduction chapter 1). Since the type of domain wall can be deliberately chosen by adjusting the geometry [382, 383], systems using vortex domain walls will have some advantages over transverse domain walls: The most important advantage is their higher speed which is due to the higher nonadiabatic contribution [239]. Additionally, the lateral position of the vortex core within a racetrack can be controlled by a number of factors. It is important to keep the core in the middle of the racetrack as it moves along the wire axis, to avoid a transformation of the wall type towards the transverse wall [384] (which reduces the speed). This could either be done by fabricating a small cut line in the middle of the racetrack which would provide an energetic minimum for the vortex core. Another possibility would be to deposit a thin line of PMA material in the center of the racetrack which couples to the polarity of the vortex core and would also help to keep it in the middle. The motion of vortex can even be controlled by tunable attractors [385], which could also be used to guide them along the racetrack.

Vortex cores themselves can also be utilized for data storage [386]. Information can either be stored in the polarity of the vortex core [387, 388] or in the combination of circularity and polarity (handedness) [389]. Both can be switched individually [390–407].

One means of switching the vortex core polarity and an additional way to determine it (instead of observing the static displacement of the vortex core under current) will be presented in the following chapter.

²²A large uniaxial anisotropy is required to overcome the stray field energy that is created when the magnetic moments are to be aligned perpendicular to the plane of a thin film. This anisotropy additionally leads to a short wall width.

4 Time-Resolved Magnetic Imaging

To extend the observable parameter space of the SEMPA microscope in Hamburg, and SEMPA in general, an improvement in the temporal resolution of the technique was aspired. The time-resolution of conventional SEMPA, which is of the order of minutes¹, was advanced to a temporal resolution of the order of nanoseconds.

In the context of the previous chapter, this allows for instance for the observation of the gyrotropic motion of a magnetic vortex core, which contains information about the local strength of the damping parameter α in a given structure [365]. The damping parameter can be slightly different in a nanostructure compared to an extended film [408, 409].

In the following chapters, an overview of the currently-established techniques for time-resolved magnetic imaging is given. The experimental approach to achieve an improvement of 10^9 in the temporal resolution of SEMPA, the concept of which was developed by Robert Frömter, will be shortly recapitulated. A more detailed description of the procedure and its experimental challenges is given in the Bachelor thesis of Fabian Kloodt² [410], who greatly contributed to the development of this technique here in Hamburg.

4.1 Time-Resolved Magnetic Imaging

Magnetization dynamics on fast timescales were first observed in 1963 when Dillon, Kamimura, and Remeika [112] visualized the ferromagnetic resonance, driven by a microwave excitation of 23 GHz, in an integrative way. The first magneto-optic camera with an ultra-short exposure time of 10 ns was constructed five years later by Kryder and Humphrey [411]. Nowadays a large variety of time-resolved magnetic imaging techniques is available. An overview of the temporal (dt) and spatial (dx) resolution of the different techniques is given in Tab. 4.1.

4.1.1 Photon-Based Techniques

Magneto-Optical Kerr Effect

Since the first high-frequency measurement using the magneto-optical Kerr effect (MOKE) in 1992 [427], a great variety of time-resolved techniques that utilize the MOKE has developed. The spatial resolution of the conventional time-resolved MOKE (TRMOKE) is rather poor [428] ($dt = 500$ fs, $dx = 600$ nm). By adding one or more dielectric layers on top of the sample, which act as a Fabry-Pérot cavity, the signal can be enhanced dramatically [429, 430]. This

¹The temporal resolution is limited by the integration time that is required to obtain a magnetic image with a significant signal-to-noise ratio.

²Institute of Applied Physics, University of Hamburg

Microscope	Particles	Geometry	dt	dx	Imaging
BLS [412, 413]	$\gamma \rightarrow \gamma$	trans.	2 ps	300 nm	parallel
Faraday [414]	$\gamma \rightarrow \gamma$	refl.	100 fs	1 μm	scanning
FMRFM [415]		probe	100 ps	90 nm	scanning
SKM [416]	$\gamma \rightarrow \gamma$	refl.	100 ps	300 nm	scanning
SEMPA [86]	$e \rightarrow e$	refl.	1 ns	3 nm	scanning
SP-STM [417, 418]	$e \rightarrow e$	probe	120 ps	0.1 nm	scanning
STXM [419, 420]	$\gamma \rightarrow \gamma$	trans.	60 ps	15 nm	scanning
Lorentz TEM [421]	$e \rightarrow e$	trans.	1 ns	10 nm	parallel
TXM [422, 423]	$\gamma \rightarrow \gamma$	trans.	< 100 ps	15 nm	parallel
XFTH [424]	$\gamma \rightarrow \gamma$	trans.	80 fs	80 nm	parallel
XPEEM [425, 426]	$\gamma \rightarrow e$	refl.	50 ps	2 nm	parallel

Table 4.1: Tabular overview of currently (October 2014) established time-resolved magnetic imaging techniques in alphabetical order. These include Brillouin light scattering (BLS), ferromagnetic resonance force microscopy (FMRFM), scanning Kerr microscopy (SKM), scanning electron microscopy with polarization analysis (SEMPA), spin-polarized scanning tunneling microscopy (SP-STM), scanning transmission X-ray microscopy (STXM), Lorentz transmission electron microscopy (Lorentz TEM), transmission X-ray microscopy (TXM), X-ray fourier transmission holography (XFTH), and X-ray photoelectron emission microscopy (XPEEM). The involved incoming and outgoing particles (electron e , photon γ), the geometry of the setup, the temporal resolution dt and the spatial resolution dx , as well as the imaging mode are given.

allows for the detection of much smaller nanostructures [431] ($dt = 100$ fs , $dx = 125$ nm). A further improvement is possible by using a setup where pump and probe beams are in a collinear alignment [432] ($dt = 100$ fs , $dx = 50$ nm).

It is however important to keep in mind that “quantifying the ability to observe magnetization dynamics in an individual isolated nanomagnet requires a different figure of merit than that used when laterally scanning arrays of magnets to determine spatial resolution” [433]. This means that the ultimate resolution that has been achieved in the latter examples is determined by, and therefore depends on, the size of the nanostructures. These occupy only a small fraction of the illuminated area that would determine the resolution in scanning mode. To allow for a better comparison to the other techniques, only the results from time-resolved scanning Kerr microscopy (TR-SKM) [416, 434–436] ($dt = 100$ fs , $dx = 300$ nm) are taken into account in Tab. 4.1. An excellent review of the various MOKE techniques is given in Ref. [432].

X-ray Magnetic Dichroism

Since the theoretical prediction in 1898 [437, 438] and the experimental discovery in 1947 [439, 440] of the strongly collimated emission of photons from an electron that is accelerated along a curved path (e.g. a synchrotron), a great variety of time-resolved imaging techniques utilizing this “synchrotron radiation” (X-rays) as an incident beam has been developed. The time-resolution is determined by the temporal width of the incoming X-ray pulse [441]. The

magnetic contrast is generated by a magnetization-dependent absorption of photons, the X-ray magnetic circular dichroism (XMCD) [120, 121]. One great advantage of this technique is that it is element specific [121], which means that the behavior of the single components in alloys or layered structures can be visualized.

The excitation of a given sample with X-rays results in two products that can be used for the generation of an image: the transmitted photons or the excited electrons. The transmitted photons are used for the generation of an image in transmission X-ray microscopy (TXM) [423]. With this approach a temporal resolution of less than 100 ps and a lateral resolution down to 15 nm is achieved [423]. TXM can be operated in full-field [422] or in scanning mode [442, 443]. A lens-less imaging mode working in transmission is X-ray Fourier transform holography (XFTH) where the real-space image is reconstructed from the hologram via Fourier transform (FTH) [125].

The electrons that are generated by photoemission are used for imaging in X-ray photoemission electron microscopy (XPEEM). The first time-resolved XPEEM (TR-XPEEM) was demonstrated in 2003 [444, 445]. While these very first experiments showed a temporal resolution of more than one nanosecond ($dt \geq 1$ ns, $dx = 150$ nm) it was quickly improved (within one year) into the 100 picosecond regime [441, 446] ($dt = 70$ ps, $dx = 100$ nm). Today the temporal resolution, which is only limited by the pulse width of the x-rays, has been enhanced to the lower picosecond regime [447] while the spatial resolution of aberration-corrected machines has reached 2 nm [448–451].

A further improvement of the temporal resolution of imaging techniques using X-rays far below the 100 ps regime is possible by using free electron lasers (FEL) [452–455].

Brillouin Light Scattering

Inelastic Brillouin Light Scattering (BLS) is another photon based approach that is very sensitive in the frequency regime [413]. The interaction of incoming photons with magnons³ in BLS allows to probe the wave vector and energy of the magnons that are involved in the process [413]. BLS allows for the investigation of dynamic phenomena in the range of 1 - 500 GHz. In modern micro-BLS setups, the incident laser beams can be focussed down to a spot of 300 nm [279, 412]. For the generation of an image, the beam is scanned across the sample surface. Since BLS is sensitive to the amplitude of the dynamic magnetization, it can not distinguish between the contributing wave vectors (directions) of the spin waves [413].

4.1.2 Electron-Based Techniques

Recent developments in the generation of ultrafast electron packets, which are generated with femtosecond laser pulses, have paved the way towards 4D ultrafast electron microscopy (UEM) [456]. The temporal resolution of the electron microscope is improved by using a stroboscopic (pump-probe) technique [457]. The technique has been shown to be applicable in Lorentz transmission electron microscopy (TEM) in the nanosecond mode and the authors claim that “femtosecond resolution should also be possible” [421]. The space-charge-induced broadening

³Magnons are the quasi-particles associated with spin waves.

of the incident electron pulse that either results in a decrease of temporal or spatial resolution can be avoided by using single-electron pulses [457].

The technique of time-resolved SEMPA, which is presented in this chapter, does not require the use of a pulsed beam of incident electrons. The temporal resolution is achieved solely by analyzing the response of the detector system in the high-frequency range. The development of a time-resolved SEMPA with a temporal resolution below 1 ns and a spatial resolution in the range of 10 nm is discussed in the following chapters. A further improvement in resolution down to 3 nm would be obtainable by using an aberration corrected lens [194].

4.1.3 Scanning Probe Techniques

If one is interested in effects that occur on the atomistic length scale, scanning tunneling microscopy is the method of choice [458, 459]. Just recently, Loth *et al.* [417] have improved the temporal resolution of the spin-polarized version of the STM (SP-STM) to a time scale (~ 50 ns) where the relaxation times of a single atomic spin could be measured. An optimization of the STM head for radio frequencies can further improve the temporal resolution. In a configuration with an uncoated (nonmagnetic) tip, a time-resolution of 120 ps has been shown to be within reach [418].

A different approach that combines the spatial resolution of AFM with the spectroscopic power of FMR is ferromagnetic resonance force microscopy (FMRFM) [460, 461]. In FMRFM the response of a cantilever with a small magnet on it to the resonance signal of a magnetic sample that is positioned directly on top of a stripline is monitored [462, 463]. This way the ferromagnetic resonance can be probed with a spatial resolution down to 90 nm [415].

4.2 Time-Resolved SEMPA

SEMPA is a *scanning* imaging technique, which means that one pixel of an image is taken after the other. Thereby the most convenient approach to enhance its temporal resolution lies in the improvement of the temporal resolution of each single pixel and a subsequent synchronization of all pixels in a given image.

In a conventional SEMPA (see chapter 2.2), an electron beam is focused onto a certain spot for 5 - 20 ms to acquire statistically relevant data for one pixel of an image (at least a few thousand events per channel are required). During this time, approximately one electron per nanosecond is detected in one of the four microchannel plates (MCP). A single temporal sweep over an event that happens on the timescale of nanoseconds (< 10 ns) would thus result in only a few events to be registered (< 10 events). It is evident that this is not sufficient to determine the orientation of the magnetization vector in a certain spot of the sample with any given precision. To obtain a statistically relevant amount of data, it is thus required to investigate a reproducible process at a particular frequency, which allows for a repeated acquisition of data.

The arrival of an electron in an MCP leads to the generation of a voltage pulse as it is shown in Fig. 4.1a. If the pulse height is above a given threshold voltage, it is registered as an event by a discriminator. Only the total number of events is of interest in conventional SEMPA. Time-resolved SEMPA, however, additionally requires a timestamp for each single event. This is

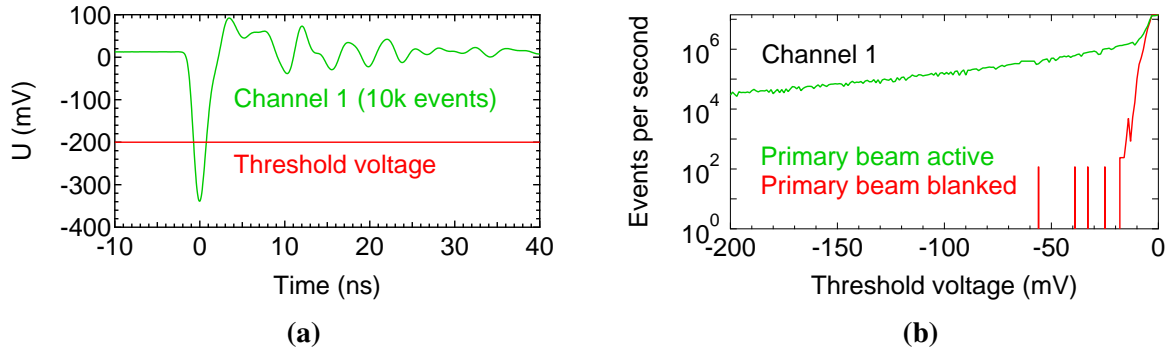


Figure 4.1: Detection of the arrival of a single electron at one of the four microchannel plates in SEMPA. (a) Exemplary shape of a pulse that is generated by a single electron event at $t = 0$ ns. The signal is averaged over 10k events that show a minimum pulse height of -200 mV (threshold voltage). Averaging eliminates any random noise, which has a peak-to-peak amplitude of about 50 mV. Echo peaks, which stem from a reflection of the pulse at the feedthrough and/or connections, are visible for $t > 0$ ns. Their magnitude lies only slightly above the noise floor. (b) Number of events that is registered in a counter, while the threshold voltage is ramped from -200 mV to 0 mV. The experiment was repeated while the primary electron beam was blanked, which means that no signal would be expected. In this case the level of the threshold voltage, where a significant amount of the noise floor is detected, becomes visible as “dark counts”. The statistical noise in the regime of low count rates (below 1×10^3) is rather high due to the short integration time of the measurement. This measurement allows for the determination of a working point with a good signal-to-noise ratio.

realized by replacing the conventional counters by an event time digitizer (TDC) [464] with 100 ps resolution.

The total number of events in a given time frame is stored in bins with a width of $2^n \cdot 100$ ps ($n \in \mathbb{N}, n \geq 0$). Subsequently all bins with an equal phase, relative to the frequency f of the process of interest, are added up. This means that events registered at times $t_i = t_0 + i/f$ ($i \in \mathbb{N}, i \geq 0$) are treated as equal. After the data is compressed in such manner to show only one single period of the process, it is further divided into a certain number of time slices. The length of each time slice must be greater or equal to the bin width. Usually each slice consists of several bins that are being summed up. By consecutively displaying these time slices, a video of the temporal evolution of the magnetization vector in a certain spot of the sample is generated for one pixel of the resulting image.

The primary electron beam is then moved to a neighboring spot, where the data for the next pixel is acquired. This is repeated until a complete set of time-resolved data is available. The data consists of a three-dimensional image (x, y, t) for each of the four channels. It is further processed into three additional images: In the first image the data of all four channels is summed up. It displays the surface morphology of the sample. In two further images the data of each two opposing channels is subtracted (and then divided by their sum). They display the x and y component of the magnetization vector.

4.3 Technical Improvement of the Setup

Several technical modifications were applied to the SEMPA setup to allow for the conduction of time-resolved measurements. The wiring inside the detector was optimized to reduce the height of the echo peaks that are shown in Fig. 4.1a. Additional improvements were necessary in the transmittance of high-frequency signals to the sample, which was not considered as a requirement when the machine was originally built. To that end, the original 5-pin feedthrough was replaced by two feedthroughs with SMA (SubMiniature version A) connections on both sides. The SMA feedthroughs are specified to show an impedance of $50\ \Omega$ up to a frequency of 6.5 GHz. Both feedthroughs come with a floating shield, which allows for the use of four separate connections in DC applications.

The main challenge, however, was the construction of a mobile sample carrier and an associated receptor (permanently placed inside the experimental chamber) that fulfilled the following requirements:

- High-frequency signals in the gigahertz range should be transmitted with low loss.
- The receptor must be connected to the feedthroughs via two SMA cables.
- The receptor and sample carrier need to be easily plugged and unplugged with a linear transfer rod in ultrahigh vacuum (UHV).
- The receptor must be bakeable to a minimum of $120\ ^\circ\text{C}$.
- The materials used must not degas under UHV conditions.
- The connection of the available cold finger to the sample holder should remain possible to allow for a variation of the sample temperature.
- The whole setup is required to be fully rotatable in the existing experimental chamber and must hence be of a compact size.
- It must remain possible to establish a connection to the sample via wire bonding.

The most convenient way to achieve a reliable electrical connection is by using commercially available plugs and jacks. Right-angle SMP plugs (for the sample carrier) and jacks (for the receptor) were found to fulfill most of the requirements. They are specified up to a frequency of 26.5 GHz and can directly be assembled on an SMA cable (jack) or soldered to a printed circuit board (plug). Plug and jack (see inset of Fig. 4.2b) have a small size with dimensions below 10 mm and the angle of 90° between jack and cable allow for a compact design of the setup.

Design of the Receptor

A photographic image of the receptor is shown in Fig. 4.2a. The receptor consists of two SMP jacks, a jack holder, and a metal piece that is designed to receive the sample carrier. The body of the SMP jacks consists of brass, which contains zinc and is therefore not suited for UHV. It is however plated with gold and may therefore be considered as safe as long as the plating is not

damaged. Thus one prerequisite was to firmly fix these jacks under UHV conditions without damaging their plating.

To solve this issue, a jack holder was designed⁴ (see Fig. 4.2a), which is made out of polyether ether ketone (PEEK). PEEK is a thermoplastic polymer with a glass transition at roughly 420 K and a melting point of 668 K [465]. It is therefore resistant to the baking that is required to achieve UHV conditions after the chamber was vented to atmosphere.

The jack holder contains two cubic cavities for the reception of SMP jacks. These cavities have the exact same dimension as the jacks. Additionally, a screw presses on one side wall of the cavity to increase the adhesion force on the jack. After the jacks are in place, the jack holder is attached to the titanium dovetail guide that receives the sample holder (see Fig. 4.2a).

After assembly, the receptor was mounted on the manipulator and introduced into the SEMPA chamber. During bakeout the manipulator was heated up to a temperature of 120 °C. After cooling down the previous pressure of 4×10^{-11} mbar was established inside the chamber. The materials used can hence be considered as suitable for an application in UHV.

Design of the Sample Carrier

A modification of the original sample holder (see Fig. 3.6b) was made to allow for the transmittance of a high-frequency signal to the sample. To this end a copper-clad ceramic board is additionally attached to the sample holder (see Fig. 4.2b). The ceramic board holds two SMP plugs that are connected to a coplanar waveguide (CPW) [466] on its surface. The signal connections on the sample can be wire-bonded towards the CPW.

The ceramic board has a thickness of 1.27 mm, a dielectric constant $\epsilon_r = 6.00 \pm 0.08$, and a surface resistivity of $10^9 \text{ M}\Omega$. It is clad with $17.5 \mu\text{m}$ of copper, which allows for the fabrication of a printed circuit board (PCB). The impedance of a design for the CPW was calculated with TXline [467]. For the given material parameters, a CPW geometry with a width of the central conductor of $1000 \mu\text{m}$ separated from the grounding lines by two gaps of $200 \mu\text{m}$ yields an impedance of 49.9Ω at 500 MHz. A design with these parameters is printed on transparent paper with a conventional laser printer as a mask. The PCB is manufactured by coating the copper plate with positive photoresist, shedding light through the transparent paper mask, development of the photoresist, and etching of the copper layer. After the copper plate is cut into the desired shape, the SMP plugs are attached to the ceramic board and connected to the CPW by soldering.

High-Frequency Test of the Setup

A PCB with the above-mentioned CPW design was fabricated, to test the high-frequency characteristics of the CPW layout, the SMP plugs and jacks, and the UHV-safe SMA cables (see inset images in Fig. 4.3). The SMP plugs needed to be modified mechanically to reduce the force for unplugging them from the SMP jacks. The force can not be too high since the linear transfer rod can translate a maximum force of roughly 10 N. Two of the mechanically modified SMP plugs were attached to the CPW by soldering. The PCB was then connected to a pulse generator and an oscilloscope with the respective SMP jacks and two SMA cables. A sine wave

⁴The jack holder was designed by Axel Frauen, Institute of Applied Physics, University of Hamburg.

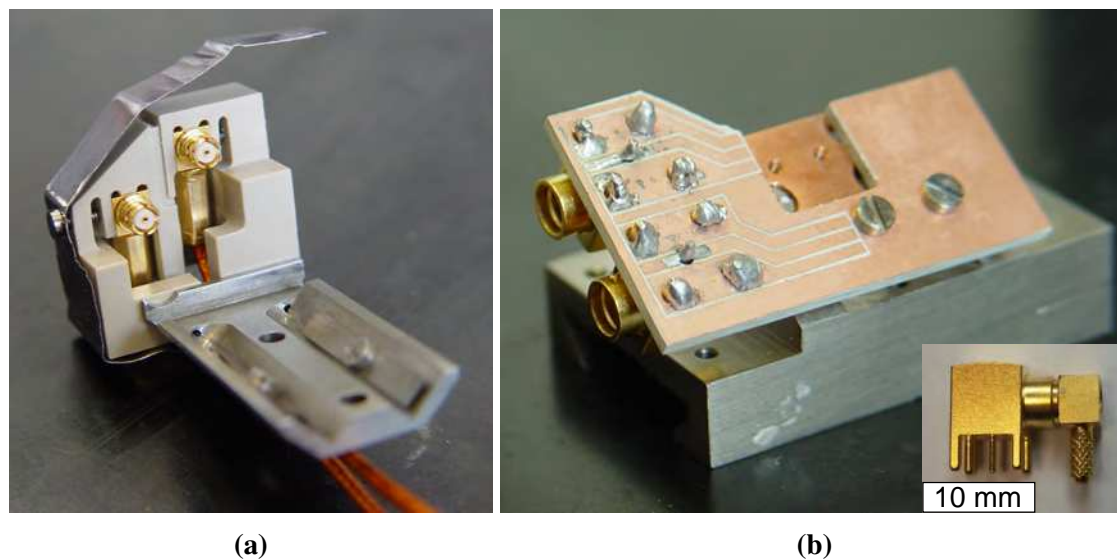


Figure 4.2: Photographs of the receptor (a) and sample carrier (b) that were constructed for time-resolved SEMPA (inset: plug and jack in the mated state). (a) The receptor consists of a dovetail titanium guide that can be attached to the manipulator stage of the SEMPA. A jack holder made of PEEK is positioned at the rear end of this piece. It firmly holds two SMP right-angle plugs that each provide one signal and one ground connection, which is isolated from the rest of the chamber. (b) The sample holder consists of a titanium block that can be slid onto the dovetail guide of the receptor. On top of the titanium block a polished copper plate is mounted. A copper block is positioned at the rear of the copper plate (not visible). The block contains a thread for the connection of a cold finger via copper braid. A ceramic plate with two coplanar waveguides (CPWs) is attached on top of the copper plate. At the left side of the plate two gold plated SMP plugs are mounted. The SMP plugs were slightly modified by removing some material in their inside to allow for a smooth transition onto their counterpart under UHV conditions. The sample is positioned directly onto the copper plate within the square opening in the ceramic plate. It is then connected electrically by bonding aluminum wires to the CPW.

(peak-to-peak voltage 500 mV, variable frequency) was sent through the test-setup and into the oscilloscope. At least 93 % of the amplitude was transmitted up to a frequency of 400 MHz. A pulse with a risetime of 820 ps (FWHM of its time derivative) was sent through the setup to test the response of the setup to higher frequency signals. The setup altered the shape of the pulse only slightly (see Fig. 4.3), leading to a shallow increase in its risetime to 825 ps. It is thus suitable for transmitting high-frequency signals into the SEMPA chamber and through a sample.

4.4 Time-Resolved Measurements

First time-resolved measurements were performed parallel to the improvement of the experimental setup and the preparation of a sample dedicated to the investigation of dynamic phe-

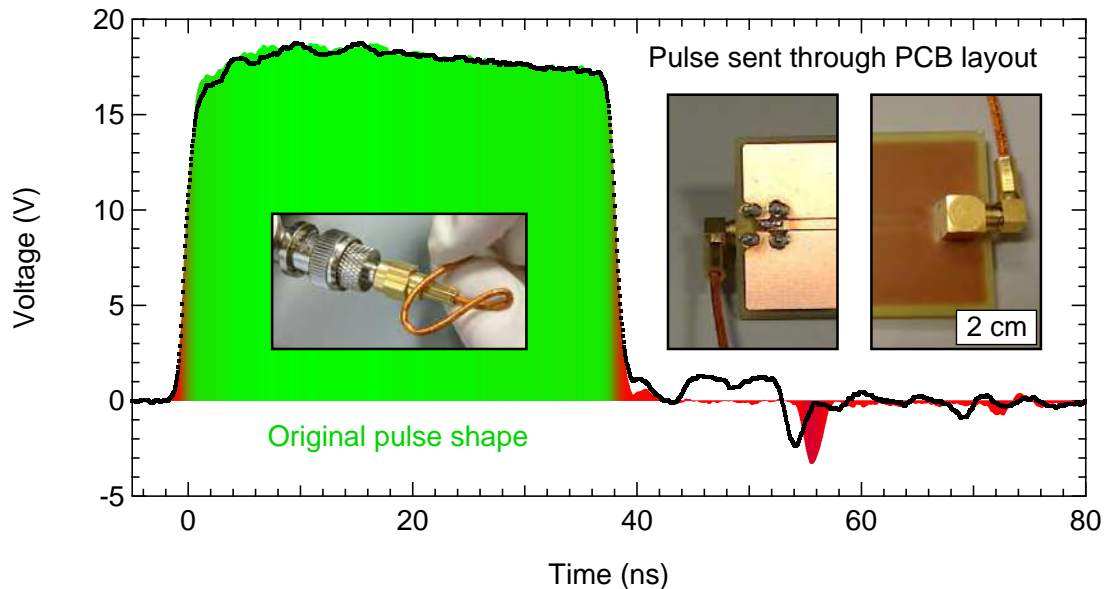


Figure 4.3: Experimental test of the printed circuit board (PCB) layout with a 18 V pulse of 40 ns duration. The original pulse shape (red/green shaded area in the background) was recorded by directly connecting a pulse generator to an oscilloscope with a 50 cm long RG58 cable (impedance 50Ω , BNC connections on both sides). The pulse was then sent through an SMA cable (40 cm), through the SMP plug and jack into the PCB (central inset image), through a 10 cm long coplanar waveguide (CPW) and finally through an identical SMP plug and jack back into another SMA cable (40 cm, rightmost inset image) and into the oscilloscope. The second inset image on the right hand side was taken after the PCB was rotated by 180° . The SMA cable was strongly bent (leftmost inset image) to test for the influence of mechanical stress on the cable, which it would also have to sustain in the vacuum chamber. This testing device conceptionally corresponds to the setup that is used in SEMPA, only without vacuum feedthroughs (they were tested before and did not alter the signal at all) and sample. The shape of the resulting pulse deviates only slightly from the shape of the original pulse. The risetime of the pulse is mostly limited by the characteristics of the pulse generator. The setup can therefore be considered as appropriate for high-frequency applications.

nomena. For a first proof of principle, one of the samples investigated in the previous chapter was used: The 5 μm sized iron square on a diamond substrate (see chapter 3.4).

4.4.1 Time-Resolved SEM

The first step on the way to a time-resolved SEMP is to ensure the time-resolved operation of the SEM mode of SEMP⁵. The question that should be answered by this experiment is, whether the current setup of the spin-detector allows for a temporal resolution in the range of nanoseconds. Before the experimental results are shown, the limits of the temporal resolution in SEMP will be discussed.

Limits on the Temporal Resolution

The temporal resolution in time-resolved SEMP is limited by the distribution of the initial energy that the secondary electrons possess, when they are emitted from the sample⁶ [84]. Two electrons of different energies (the difference is of a few eV for metals [183, p. 153]) will have different transit times on their way from the sample towards the detector plates.

Let us consider two electrons: one that is emitted from the sample without any initial energy (slow electron) and one that is emitted directly in direction of the spin detector with a kinetic energy of 10 eV (fast electron). More than 90 % of the electrons possess a kinetic energy well below 10 eV [183, p. 153]. The accelerating part of the electron path until they enter into the spin detector (8 mm through an electric field of 56 V mm⁻¹ [84]) takes 1.27 ns for the slow electron while it takes 1.10 ns for the fast electron. Moving at constant speed, the time t_{transit} that a nonrelativistic electron of energy E and mass m_e takes for a path of length s is given by:

$$t_{\text{transit}} = s \sqrt{\frac{m_e}{2E}} \quad (4.1)$$

The difference in transit times $\Delta t_{\text{transit}}$ for two electrons of energies E_1 and E_2 is given by:

$$\Delta t_{\text{transit}} = s \sqrt{\frac{m_e}{2}} \left| \frac{1}{\sqrt{E_1}} - \frac{1}{\sqrt{E_2}} \right| \quad (4.2)$$

During their way through the electron optics in the front part of the detector, the electrons are accelerated by voltages in the region of kilovolt. After being accelerated by a voltage of 1 kV the slow electron travels a distance of 10 cm in 5.33 ns while the fast electron takes 5.31 ns for the same distance. The difference in transit times is hence rather small for electrons passing through the electron optics. The electrons are, however, again decelerated to an energy of about 100 eV in the rear part of the detector, before they are elastically scattered at the tungsten crystal [84]. The lower energies (100 eV and 110 eV) increase $\Delta t_{\text{transit}}$ for the same distance to 0.78 ns

⁵Imaging without magnetic contrast is a lot simpler since only one of the four channels is required to work reliably and noise-free. Additionally, the imaging process is not interrupted by ion milling, which is required from time to time to refresh the magnetic contrast.

⁶Only the part of the kinetic energy that gives rise to a velocity that is parallel to the axis of the spin-detector is of interest. This means that the angular distribution of the secondary electron emission also needs to be considered.

while the traveling time for the slower electron increases to $t_{\text{transit}} = 16.86$ ns. The difference in electron speed during scattering will hence be critical for the ultimate time-resolution of the experiment. The distribution of the electrical potential throughout the spin-detector is however complex, which makes an analytical solution of the problem rather complicated. A temporal resolution in the region of one nanosecond seems however feasible from these simple theoretical considerations.

Experimental Results

The sample consisting of an iron square on a diamond substrate (see chapter 3.4) was used to probe the temporal resolution of the spin-detector. Additionally, the functionality of the evaluation and measurement software was tested, which is discussed elsewhere [410]. At the time of these experiments, the technical adjustments of the experimental chamber (see chapter 4.3) were not yet completed, which means that the hitherto existing setup of sample carrier and receptor was used.

A visual representation of the sample layout that has been obtained with SEM at zero current is shown in Fig. 4.4a. As soon as an AC signal is applied to the sample, an alternating Oersted field is generated that slightly moves the spot where the primary electron beam hits the surface by a few nanometers. With a sinusoidal current leading to a sinusoidal field a resulting sinusoidal movement of the spot is expected. This leads to a wobbling of the SEM image, that happens at the timescale of the excitation signal. The wobbling was observed by the operator and his coworkers. As a video cannot be presented here, a different visualization of the data is shown in Fig. 4.4b. Two regions of interest are chosen, where a modulation of the image brightness occurs as the electron beam moves between two materials that emit more or less secondary electrons (gold and iron). The sinusoidal shape of the excitation signal is perfectly reproduced in the count rates of the pixels in these regions of interest. The observation of a process that happens on the timescale of nanoseconds with SEM has therefore successfully been demonstrated.

4.4.2 Time-Resolved SEMPA

The gyrotropic motion of a permalloy vortex core, excited by an alternating magnetic field was chosen as a testing system for magnetic imaging in time-resolved SEMPA. Since its first experimental observation in 1984 [468] this system has been both theoretically [72, 87, 293, 294, 469–481] as well as experimentally [88, 310, 419, 436, 441, 473, 482–493] extensively studied. The system therefore represents an ideal candidate for testing purposes.

Driving the Gyration of a Vortex

When the equilibrium position of a magnetic vortex core is different from its actual position, the vortex core will start a circular motion around its energetic minimum [293]. If a damping mechanism is present in the magnetic system, the energy of the gyration will be dissipated and the radius of the gyration decreases until the vortex core has reached its equilibrium position. The gyration can however be sustained, by pumping energy into the system and thereby compensating for dissipative losses.

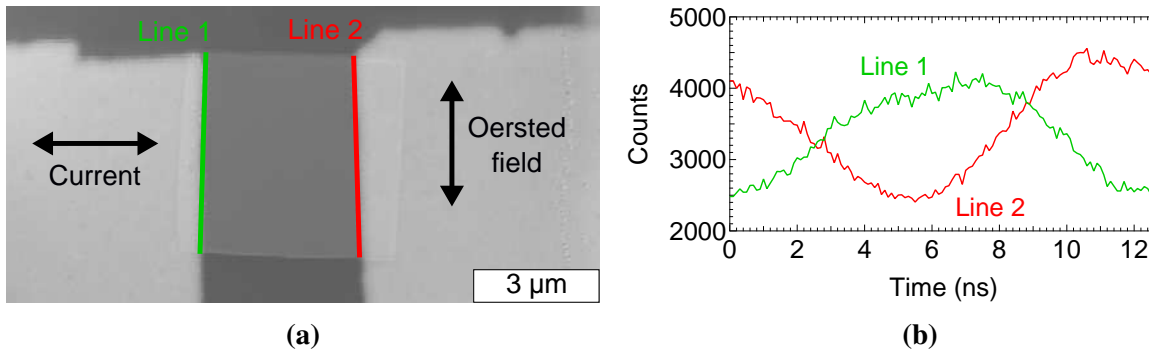


Figure 4.4: (a) SEM image of a 5 μm iron square, which is contacted by gold leads on two sides. When a sinusoidal voltage is applied between the contacts, an alternating current is generated that flows horizontally through the iron square. This gives rise to an Oersted field above the sample that has an influence on the primary electron beam. While the Oersted field is oriented perpendicular to the direction of current flow, the electron beam is deflected in the horizontal direction, parallel to the current flow. In a time-resolved SEM video this becomes visible as a horizontal movement of the whole image. The movement can however be visualized in a static image by integrating the signal of pixels that are aligned along the edge of the gold contacts (green and red line). The movement of the image leads to a modulation of the intensity in this “region of interest”. The temporal evolution of the integrated count rates of these pixels for an excitation signal of 5 V at 75 MHz is shown in (b) for one period of the excitation. For the pixels aligned along line 1, the signal increases during the first seven nanoseconds. The reason for this is that the left gold contact, which appears brighter in the image, is shifted to the right. Subsequently, as the current reaches its peak value and starts decreasing, the gold contact is shifted back to the left and the signal decreases again. For the pixels aligned along line 2 the situation is exactly the opposite, as the right gold contact is shifted away from the line at the beginning.

The transfer of energy is most efficient, when the frequency of the excitation signal matches the eigenfrequency of the vortex gyration. The eigenfrequency is proportional to the ratio of thickness t and radius r of the nanostructure that contains the vortex [293, 473, 474, 494]. For a flat permalloy element ($t/r < 0.1$), a frequency below 500 MHz is expected.

Another effect that occurs when exciting a magnetic Landau state with high-frequency signals is the creation of quantized and confined spin-wave eigenmodes [413, 422, 472, 495–500]. These are similar to the ones that are excited in the vortex state of a ferromagnetic disc [462, 501–508]. Since the latter effect appears in the higher-frequency regime ($> \text{GHz}$), a concurrent (and eventually competing) activity of both effects is unlikely.

Further information on vortex gyration can be found in review articles [509, 510].

Polarity Switching at the Critical Velocity

After reaching a critical velocity⁷ the vortex core switches its polarity [395, 396, 398, 511–514] regardless of the mechanism (AC magnetic field, spin-transfer torque, etc.) by which the vortex motion is excited [401]. The switching is mediated by a gyrotropic field that is generated by the vortex motion [403]. The gyrotropic field enables the creation of a vortex/antivortex pair with equal polarity that is opposite to the polarity of the original vortex. The antivortex moves toward the original vortex and annihilates it, leaving its partner with a switched polarity [394, 397, 512], a spin wave [391], and a Bloch point [515–517] behind. The Bloch point is topologically protected [518] and can thereby only be eliminated by another Bloch point (in the creation of which yet another Bloch point would appear) or at the edge of the structure.

In the scope of this experiment, a switching of the core polarity is a rather unwanted effect. First, it limits the maximum radius at which the vortex core can gyrate. Second, when enough energy is pumped into the system to allow for a switching of the polarity, a superposition of two vortex cores with opposite polarity moving in opposite directions would be observed like in Ref. [492]. For permalloy a critical velocity of approximately 250 m s^{-1} has been observed experimentally [396, 492, 514].

Sample Layout

A sample consisting of a $6 \mu\text{m}$ wide gold stripline with thirty-eight permalloy squares ($5 \mu\text{m} \times 5 \mu\text{m} \times 60 \text{ nm}$) on top (see Fig. 4.5, microstrip layout) was prepared by electron beam lithography [519] in cooperation with Lars Bocklage. The stripline is used to generate an alternating magnetic field at the position of the permalloy squares. The resonance frequency, at which the gyrotropic motion can most effectively be excited, can be calculated by (3.45) (see page 43). For the initial dimensions stated above, a resonance frequency of 100 MHz is expected. The frequency however decreases approximately linearly with thickness [293, 473, 474, 494] and will thus decrease when the sample is cleaned by ion milling.

The stripline is made of gold, has a thickness of 100 nm, a width of $6 \mu\text{m}$ and a DC resistance of 24Ω . For increasing frequency the resistance of the stripline increases due to the skin effect

⁷Sometimes a “critical radius” is related to the switching phenomenon. While the critical radius depends on the frequency of the gyration, the critical velocity provides a more universal description since it is independent of frequency [511].

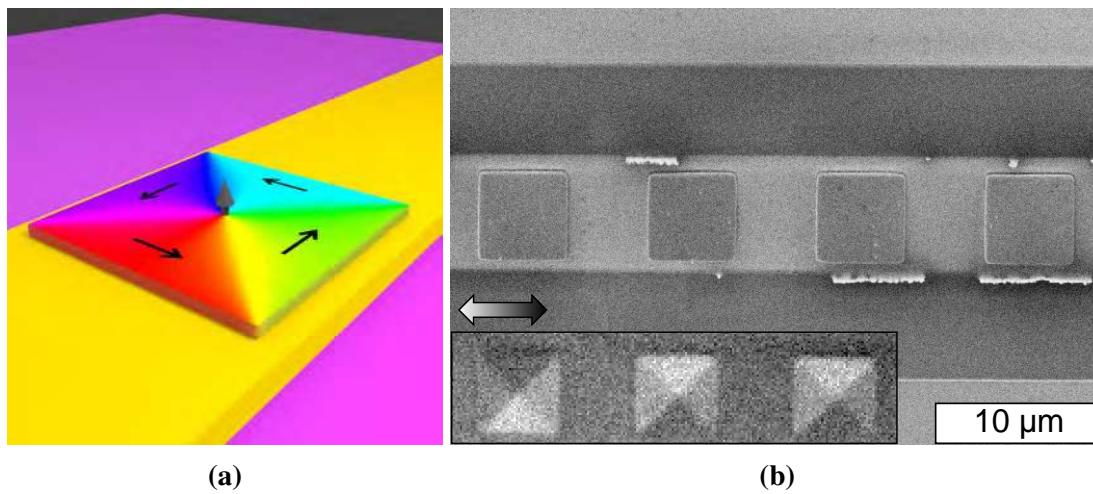


Figure 4.5: The first sample that was ever investigated with time-resolved SEMPA. (a) Schematic display of a permalloy square prepared upon a gold stripline. When a current is sent through the stripline, a magnetic field curling around the stripline is generated. Depending on its sign it affects the light-blue and red domains of the permalloy square on top, exerting a force on the vortex core. With an alternating current that corresponds to the resonance frequency of the vortex core, a strongly amplified gyrotropic motion of the core can be induced. (b) SEM image of the sample. The gold stripline has a width of $6\ \mu\text{m}$ and a thickness of $100\ \text{nm}$. It is supported by a bottom layer of $10\ \text{nm}$ chromium. The permalloy squares have a lateral dimension and separation of $5\ \mu\text{m}$ and an initial thickness of $t_1 = 60\ \text{nm}$. The magnetic configuration of the permalloy squares is shown in the inset. All are in the Landau state.

[520]: In a metal conductor, an alternating current only flows in a surface layer, the thickness of which is described by the skin depth. At a frequency of 100 MHz, gold has a skin depth of $\delta = 7.5 \mu\text{m}$. Since the skin depth is greater than the size of the stripline it should have no influence on its resistance in this frequency range.

Experimental Results

The technical improvements of the SEMPA chamber were completed when the stripline sample was ready for measurement. One of the four channels of the spin detector was however not yet ready for operation because it showed a small leakage current through the MCP stack. Only one component of the magnetization could hence be measured at the time.

The stripline sample was attached to the newly-designed sample holder and transferred into the chamber. After the sample holder was slid on the receptor, a little additional forward force was applied to the linear transfer rod, while the rotation of the stage (containing the receptor) was wobbled by a few degrees in both directions. In this way a reliable connection between the two SMP plugs is established. As a result, the *in-situ* DC resistance of 24Ω is identical to the one that was measured *ex-situ*.

Next, a harmonic sinusoidal signal is sent through the sample. With an excitation signal of 500 mV, 385 mV are transmitted at 10 MHz and 360 mV are transmitted at 100 MHz. Compared to the test-setup that was discussed before (p. 79), the transmittance at 100 MHz is reduced from 93 % to 72 % by the sample, bonding wires, and the longer cable connections that are required to get the signal into and out of the chamber. The previously-mentioned voltage gives rise to an Oersted field of 0.6 mT above the stripline [521].

Successful operation of sample and setup was confirmed by observing the Oersted field induced displacement of the electron beam⁸. The sample was again cleaned by ion milling and a thin iron film of approximately 1 nm was evaporated to enhance the signal contrast. After a few tries at different frequencies, the gyrotropic motion of the vortex core could clearly be observed at 70 MHz.

A single frame of the video, as well as the temporal evolution of the vertical position of vortex core and nanostructure are shown in Fig. 4.6. Although the movement of the vortex core is a superposition of the Oersted-field-induced movement of the image as a whole and the gyrotropic motion, the amplitude of the vortex gyration surpasses the background wobbling of the image by far. Both motions can be described by a sinusoidal function, the frequency of which is set to the frequency of the excitation signal:

$$y(t) = A_y \cdot \sin(2\pi \cdot 70 \text{ MHz} \cdot t + \phi_y) \quad (4.3)$$

Application of this formula to the raw data yields a vertical amplitude of $A_y = (210 \pm 30) \text{ nm}$ for the motion of the vortex core and an amplitude of $A_y = (23 \pm 3) \text{ nm}$ for the motion of the image. The vertical vortex gyration is shifted by $\phi_y = (152 \pm 9)^\circ$ with respect to the trigger signal of the

⁸For the stripline sample, the electron beam was found to move vertically, perpendicular to the direction of the current in the stripline. The resulting Oersted field has hence to stem from one of the bond wires, which is running perpendicular to the stripline. Since the bond location is right next to the stripline, in contrast to the previous sample where it was further away, a stronger influence of the Oersted field generated around the bond wire is expected.

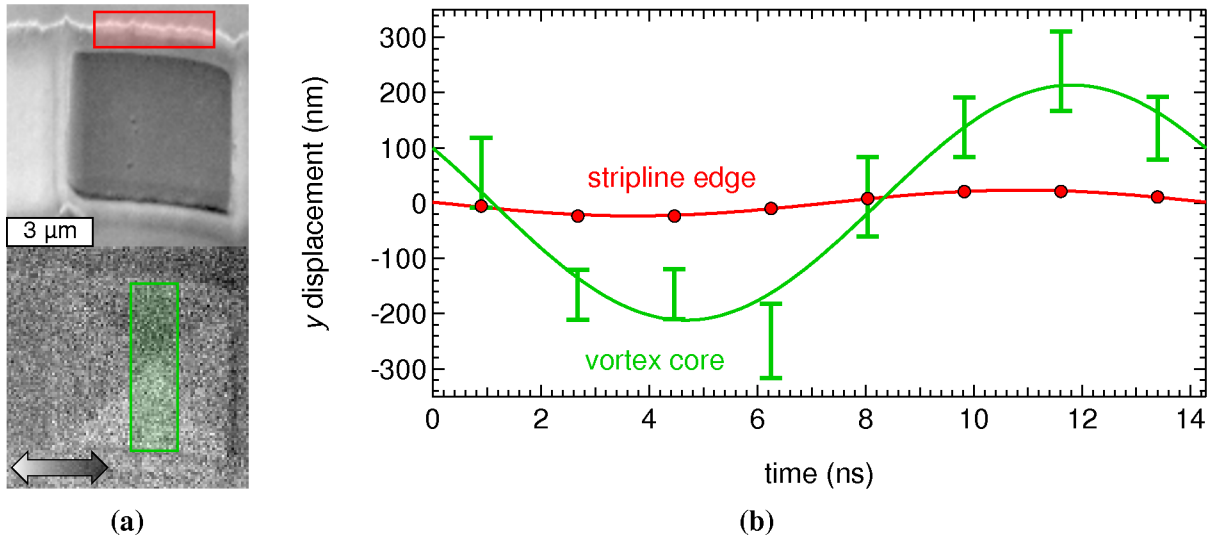


Figure 4.6: Data of the first time-resolved SEMPA video that has ever been obtained. A sinusoidal excitation signal of 350 mV (peak-to-peak) was applied at 70 MHz. **(a)** Shows the third of a total of eight frames of the video. One single frame consists of $100 \times 100 \text{ px}^2$ (the fast scan direction is vertical) with a dwell time of 7.23 ms/px. The third frame contains data from $1/8 = 1.78 \text{ ns}$ of the total period of 14.29 ns. The images of the morphology (top) and the x -component of the magnetization (bottom) were obtained simultaneously. They were obtained in a single scan of 15 minutes without any drift compensation and therefore appear slightly skewed. The gold stripline runs horizontally through the image. The magnetic configuration of the permalloy square can clearly be identified as a Landau state with a vortex core in its center. **(b)** Vertical displacement of the edge of the stripline (red, the error bars are smaller than the data points) and the vortex core (green) shown for one period (relative to the trigger signal at $t = 0 \text{ ns}$). The data was obtained from vertical line-profiles through the highlighted regions in (a) as discussed in chapter 7.1.1. The motion of the image as a whole (exemplary shown as a motion of the edge of the stripline) is caused by a harmonic deflection of the electron beam by the Oersted field that is generated around one of the bond wires. The displacement of the vortex core, however, surpasses the motion of the background by far and can hence be attributed to the gyrotropic motion of the vortex core which is driven by the Oersted field that is generated around the stripline. Both motions can very well be described by a sinusoidal function, the parameters of which are given in the main text.

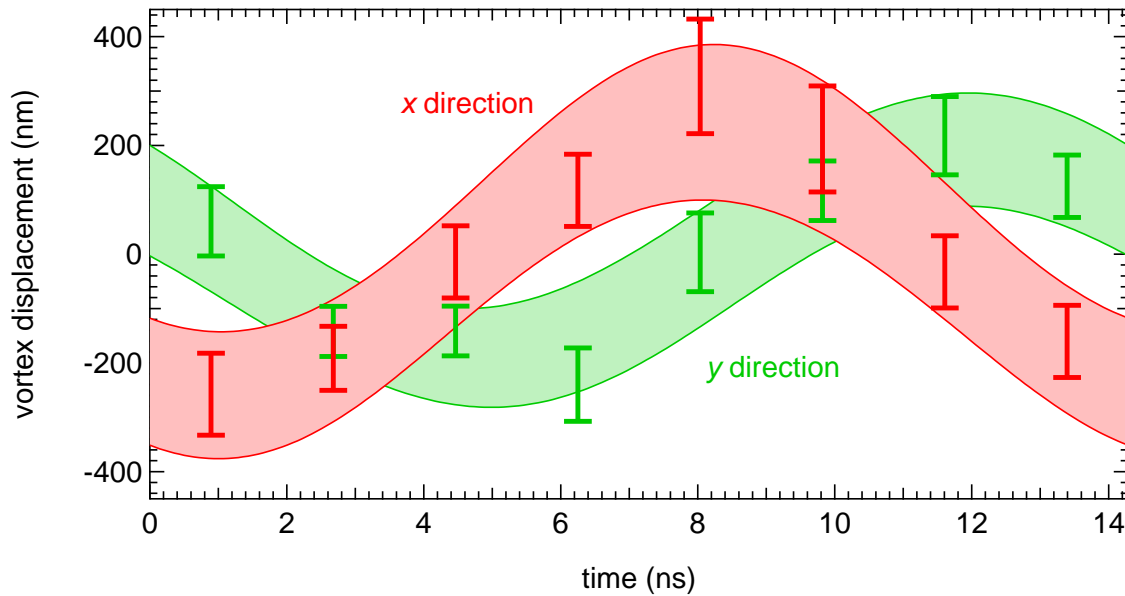


Figure 4.7: Displacement of the vortex core along the x and y directions during one period of its gyration. The data is corrected for the wobbling of the image that is caused by the action of the Oersted field on the primary electron beam. Both signals can be described by a sinusoidal function. The 95 % confidence bands of the fits are shown as a shaded area (details on fit parameters can be found in the main text). Since the vortex core moves along a harmonic circular path, the signals are phase shifted to one another by 90° . From the counterclockwise motion of the core, a positive core polarity $p = +1$ can be deduced [293].

frequency generator. The background motion of the image is shifted by $\phi_y = (176 \pm 7)^\circ$. While both, the mechanism, as well as the source of the underlying cause (the respective Oersted field coming from the bonding wire or the stripline), are different for the two motions, the phases are not expected to match. As a result, the observed superimposed signal of the vortex position can generally not be described by a single sinusoidal function. It was solely possible in this case because the background motion of the image was diminishingly small. For a more detailed evaluation of the data, however, the background motion has to be subtracted.

Evaluation of the Data

The x position of the vortex core was determined from the eight video frames of the x component of the magnetization⁹ as described in chapter 7.1.1. Additionally, the wobbling amplitude of the image in x direction (which is below 2 nm) was determined from the sum images. The background wobbling of the image was then subtracted from the two components of the core position. The resulting data for the vortex core displacement is shown in Fig. 4.7.

⁹As mentioned above, one channel of the spin-detector could not be used at the time since a leakage current prohibited the application of high voltages to its microchannel plate. Being one channel shy, only one component of the magnetization can reliably be obtained. The problem was solved after the chamber was again opened up.

A phase shift of roughly 90° can be observed between both signals, as the vortex core moves along a circular path. The amplitudes in both directions are different which means that the orbit is slightly elliptical. An elliptical orbit is observed when the frequency of the excitation signal does not match the resonance frequency [294].

Both trajectories can be described by sinusoidal functions (4.3). The parameters that fit the data best are:

	Amplitude (nm)	Phase ($^\circ$)
x	250 ± 40	244 ± 8
y	190 ± 30	149 ± 9

The resulting phase difference $\Delta\phi = (95 \pm 12)^\circ$ is in good agreement with a harmonic circular motion of the vortex core. A perfect circle could furthermore describe the trajectory of the vortex core as the amplitudes for both directions match within their respective error. Assuming a circular trajectory, the velocity of the vortex core at 70 MHz of $(98 \pm 11) \text{ m s}^{-1}$ is well below the critical velocity for switching of the vortex core polarity, which lies at 250 m s^{-1} [396, 492, 514].

There is however reason to believe that the difference in amplitudes is real and would therefore also sustain if the experimental error was reduced: First, a resonance frequency of slightly below 100 MHz (depending on how much material was removed by ion milling) is expected. A perfectly circular path can only be observed at resonance [294]. Second, the suspicion is substantiated by looking at the video data, which cannot be shown here. The video also suggests an elliptical path of the vortex core. Being off-resonance, the deviation of the frequency from resonance can be calculated: The ratio of excitation frequency f and resonance frequency f_{res} matches the ratio of the two amplitudes [294]:

$$f/f_{\text{res}} = A_y/A_x \quad (4.4)$$

From this relation a resonance frequency of $f_{\text{res}} = (90 \pm 20) \text{ MHz}$ is obtained. Considering a linear dependence of f_{res} on the thickness of the element [293, 473, 474, 494], a reduction of the resonance frequency by 10 % from 100 MHz to 90 MHz could be explained by a reduction of film thickness from 60 nm to 54 nm. Subsequent AFM measurements of the sample yield a remaining thickness of $(56 \pm 1) \text{ nm}$, which supports this theory.

4.5 Summary and Outlook

In the previous chapter, the development and successful operation of a time-resolved SEMPA was presented. The experimental approach of assigning a time stamp for each secondary electron that is detected was described. Several technical improvements including the construction of a new sample holder/receptor pair were discussed. The improvements allow for the application of high-frequency signals to a sample under UHV conditions. The sample thereby remains mobile and can be transferred into the chamber with a linear transfer rod.

After a high-frequency test of the setup, a measurement of the Oersted-field-induced motion of the primary electron beam on the timescale of nanoseconds was presented. Finally, the

gyrotropic motion of a vortex core in a permalloy square was investigated. The machine was proven to be able to capture magnetic images of the gyrotropic motion with a temporal resolution of approximately one nanosecond. At a frequency of 70 MHz, a harmonic circular motion of the vortex core along an elliptical path was observed. From the difference in amplitude along the direction parallel and perpendicular to the excitation signal the resonance frequency of $f_{\text{res}} = (90 \pm 20)$ MHz was determined.

Due to the fact that neither a drift compensation nor all four channels of the spin-detector were available for this first measurement, the lateral precision in the determination of the vortex core position is below the capabilities of the machine. Up until now, the technical issues have been resolved. Additionally, an imaging mode has been developed, in which multiple frames of an image are taken with a single-frame integration time of only a few seconds. In this mode, each frame is compared to the initial frame of the image. Subsequently the scanning region is shifted accordingly so that the primary electron beam follows the thermal movement of the sample. The frame mode with drift correction allows for integration times for a single video that lie above one hour, without any visible effects of thermal drift. This enables the recording of high quality time-resolved videos containing the complete information about the in-plane magnetization and resolving magnetic processes that occur on the temporal and lateral nanoscale.

With the extended temporal resolution, a greater variety of physical effects becomes accessible with SEMPA. For instance, a more detailed investigation of spin-transfer torques will be possible. In addition to the stationary displacement of a vortex core induced by a direct current [80], the harmonic behavior of the vortex core induced by an alternating current can be studied. This allows for an additional independent access to the relative strength of the nonadiabatic spin-transfer torque β [87, 88, 522]. The investigation further enables access to the local strength of the damping parameter α within the nanostructure, where it might slightly deviate from its value in an extended film [408, 409].

5 Interaction Between Ferroelectric and Ferromagnetic Domain Walls

The interaction between ferroelectric and ferromagnetic domain walls provides yet another interesting possibility of manipulating the position of a magnetic domain wall [90]. While ferroelectric materials are useful for quite a variety of applications themselves [523], the emergence of multiferroics has expanded and combined the areas of ferromagnetism and ferroelectricity [524]. Ferromagnetic domain walls can be pinned upon and moved along with ferroelectric domain walls [90] without the occurrence of a Walker breakdown limiting the maximum velocity [91]. Magnetic domain patterns can be written and erased by altering the underlying ferroelectric domain pattern [90]. From the technological point of view, the low power consumption (no currents are required to flow) renders the manipulation of ferromagnetic domain walls via the control of ferroelectric domain walls a very interesting field [90].

A model system where it has been shown that the magnetic domain wall motion can efficiently be controlled by an electric field, consists of thin ferromagnetic CoFe films on the ferroelectric crystal BaTiO₃ [90]. In this system, tetragonal BaTiO₃ crystals with in-plane polarization are used [525, 526]. “Stress relief in these substrates produces a regular ferroelastic stripe pattern whereby the elongated c -axis ($c = 4.036 \text{ \AA}$, $a = b = 3.992 \text{ \AA}$) rotates by 90° in the substrate plane” [527] (Fig. 5.1a). The modulation of the lateral strain between the a_1 and a_2 domains of this stripe pattern is 1.1 % [527, 528]. When a thin ferromagnetic Co₆₀Fe₄₀ film (10-20 nm) is evaporated upon such a crystal (showing the stripe pattern), a small percentage ($\approx 10\%$) of the lattice strain is transferred to the ferromagnetic film [90]. The strain induces a magnetoelastic uniaxial anisotropy with an easy axis along the elongated c -axis of the substrate [527, 528]. This effect leads to a direct transfer of the ferroelectric stripe domain pattern into the ferromagnetic film (Fig. 5.1a).

As a result of the domain pattern, 90° domain walls appear in the ferromagnetic film. They are located directly on top of the ferroelectric domain walls [527, 528]. Depending on the history of the magnetic material, there are two possible configurations for these domain walls [89]:

1. “Charged walls” are created when an in-plane magnetic field is applied parallel to the ferroelectric domain walls. The in-plane component of the magnetization that is perpendicular to the wall points in opposite directions on both sides of the wall.
2. “Uncharged walls” are created when an in-plane magnetic field is applied perpendicular to the ferroelectric domain walls. The in-plane component of the magnetization that is perpendicular to the wall points in the same direction on both sides of the wall.

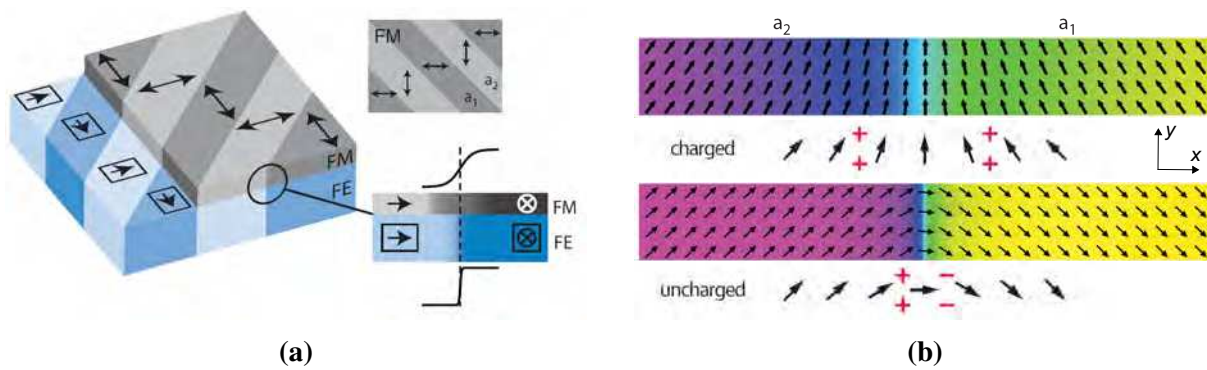


Figure 5.1: Schematic illustration of the ferroelectric and ferromagnetic domain pattern in $\text{Co}_{40}\text{Fe}_{40}\text{B}_{20}$ on BaTiO_3 (images slightly modified from [89]). (a) The ferroelectric (FE) tetragonal BaTiO_3 crystal with in-plane polarization shows a periodic stripe pattern in which the direction of the elongated c -axis (indicated by rectangular boxes) rotates by 90° to relieve mechanical stress. The respective regions are denoted as a_1 and a_2 domains. The rotation of the c -axis in the piezoelectric material is accompanied by a rotation of the polarization vector as indicated by the arrows. When a ferromagnetic film (FM) is grown on top of such a configuration, it adopts a small percentage of the lattice strain of the underlying substrate. This leads to the emergence of an alternating uniaxial magnetoelastic anisotropy that develops parallel to the polarization vector of the ferroelectric substrate. (b) Depending on the magnetic history, two types of domains have been identified in the ferromagnetic film in micromagnetic simulations: When a magnetic saturation field is applied parallel to the ferroelectric domain walls, charged walls develop (upper image). Charged walls are relatively broad because two neighboring domains repel each other like identical poles of two magnets. This is due to the net magnetic volume charges (indicated by red crosses). When the magnetic saturation field is applied perpendicular to the wall, uncharged walls develop. They contain no net magnetic volume charge and are therefore considerably thinner.

A visual representation of the two cases can be found in Fig. 5.1. The walls are named after their net charge considering magnetic volume charges. Magnetic volume charges ρ_m are defined as the divergence of the magnetization:

$$\rho_m := -\mu_0 M_s \nabla m \quad (5.1)$$

For a magnetization pattern that is translation invariant along the y and z axis as shown in Fig. 5.1b this simplifies to:

$$\rho_m = -\mu_0 M_s \frac{\partial m_x}{\partial x} \quad (5.2)$$

In the case of a symmetric charged wall, charges of equal sign emerge on both sides of the wall center. When integrating over the wall region a net magnetic volume charge remains, hence the name “charged wall”. In the case of a symmetric uncharged wall, equal charges of opposite sign emerge on both sides of the wall center. The charges therefore cancel out during integration and no net charge remains, hence the name “uncharged wall”. Charged walls are expected to be considerably broader than uncharged walls [89], as “A net magnetic charge generally widens the wall” [529]. Two neighboring domains that are separated by a charged wall repel each other like identical poles of two magnets.

The magnetization pattern and wall structure of the artificial 90° domain walls that appear in a 20 nm $\text{Co}_{40}\text{Fe}_{40}\text{B}_{20}$ film on BaTiO_3 were investigated with SEMPA in cooperation with Kévin J. A. Franke¹. The results of the investigation as well as further details on the two wall types are presented in the following sections.

5.1 Charged Walls

As discussed before, charged walls can be created by the application of a magnetic field parallel to the ferroelectric domain walls of a BaTiO_3 crystal. The orientation of the ferroelectric domain walls is determined using a polarization microscope [90, 530]. The behavior of the ferromagnetic domains under the influence of an external magnetic field is investigated with Kerr microscopy. As expected, the ferromagnetic domain walls are found to run parallel to the ferroelectric domain walls. The magnetization of the ferromagnetic domains can be switched by a field of 6 mT parallel to the walls. When the field is turned off, some of the domains reverse their magnetization, turning the neighbouring charged walls into uncharged walls and thus reducing the total energy. Most of the charged walls were however found to be stable in the remanent state.

To obtain saturation, a magnetic field pulse of 50 mT was consequently applied for a few seconds, parallel to the ferroelectric domain walls. An image of the resulting remanent magnetization pattern obtained with SEMPA is shown in Fig. 5.2a. The majority of the domains is oriented in the direction in which the external magnetic field was applied, only one domain is aligned in the opposite direction.

¹NanoSpin, Department of Applied Physics, Aalto University School of Science, Finland

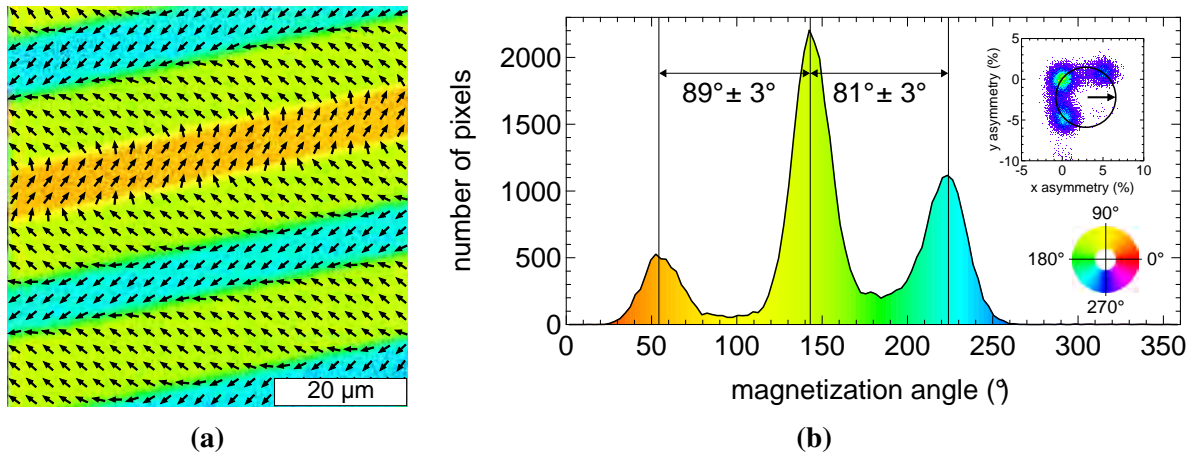


Figure 5.2: (a) SEMPA image of the magnetic configuration of $\text{Co}_{40}\text{Fe}_{40}\text{B}_{20}$ on BaTiO_3 after a magnetic field of 50 mT was applied. With respect to the image, the field vector pointed to the left. Charged walls are created when the external field is oriented parallel to the direction of the ferroelectric domain walls. An exception to this can be seen in the upper center of the image, where two uncharged walls appear. In this case the magnetization of the now orange domain switched back, replacing two charged walls by uncharged walls. (b) Histogram of the magnetization angle for each pixel of the image that is shown in (a). An angle of roughly 90° is present between two domains that are separated by an uncharged wall (orange and green). Two domains that are separated by a charged wall (green and blue), however, show a reduced angle. This issue is elucidated in Fig. 5.3. Inset: Two dimensional raw data of the histogram. The center of the distribution is shifted from zero due to the experimental asymmetry of the setup. The center and radius of the distribution were determined by fitting two-dimensional Gaussian functions to the three peaks. An image contrast of 3.7% is obtained from the radius of the distribution.

A histogram of the distribution of the magnetization angles (Fig. 5.2b) reveals an interesting detail: The angle between the magnetization of two domains that are separated by a charged wall is considerably smaller than 90° . Model calculations show that a deviation of the magnetization from the easy axis in the center of a domain occurs, when the width of the domain is smaller than approximately ten times the width of the enclosing domain walls [531].

To further illuminate this issue, a line profile was extracted from the image, oriented perfectly perpendicular to the walls. The result is shown in Fig. 5.3. Inside of the green and orange domains the magnetization is aligned pretty well along the easy axes, apart from a small offset. Inside the blue domain, however, the magnetization does not completely align with the easy axis as the rotation is reversed before the direction of the easy axis is reached. This effect can be attributed to the relatively small size of the blue domains when it is compared to the wall width. To obtain a quantitative access to the wall width, we will have to take a closer look at the internal structure of the charged wall and compare it to theoretical models.

Internal Wall Structure

To elucidate the internal structure of the charged wall, a higher-resolution image was taken around the region of one of the walls. The line profile that was obtained from this image is shown in the inset of Fig. 5.3. It reveals the internal structure of the charged wall: In the center of the wall, a relatively narrow core region can be observed. The rotation of the magnetization however extends deeply into the two domains. This shape of a charged Néel wall was described by Alex Hubert back in 1979 [529]. Hubert did a detailed numerical calculation for arbitrary:

- angles between the easy axes of the anisotropy θ , defined by $p = 180^\circ/\theta$ ($p = 2$ for the 90° configuration discussed here);
- angles between the wall and the direction $\mathbf{S} = \mathbf{M}_1 - \mathbf{M}_2$ ($\mathbf{M}_{1,2}$ are the directions of the magnetization in the two neighboring domains), defined by Ψ (with $\Psi = 90^\circ$ for a charged wall and $\Psi = 0^\circ$ for an uncharged wall);
- material parameters as the exchange constant A , saturation magnetization M_s , and the anisotropy constant K .

Hubert introduced two dimensionless parameters to simplify the calculations and get rid of all redundant² material constants: the quality factor Q and “the ratio of the material length of bubble theory [...] to film thickness” λ . In SI units these quantities are given by:

$$Q = \frac{K}{\frac{\mu_0}{2} M_s^2} \quad (5.3)$$

$$\lambda = \frac{2}{t} \cdot \frac{K}{\frac{\mu_0}{2} M_s^2} \cdot \sqrt{\frac{A}{K}} \quad (5.4)$$

For the sake of comparison to Hubert’s model, $Q = 0.01$ and $\lambda = 0.03$ are calculated for the system at hand, using values for $\text{Co}_{40}\text{Fe}_{40}\text{B}_{20}$ on BaTiO_3 that are found in [89, 531, 533, 534]

²Redundant for the problem at hand of course, not generally.

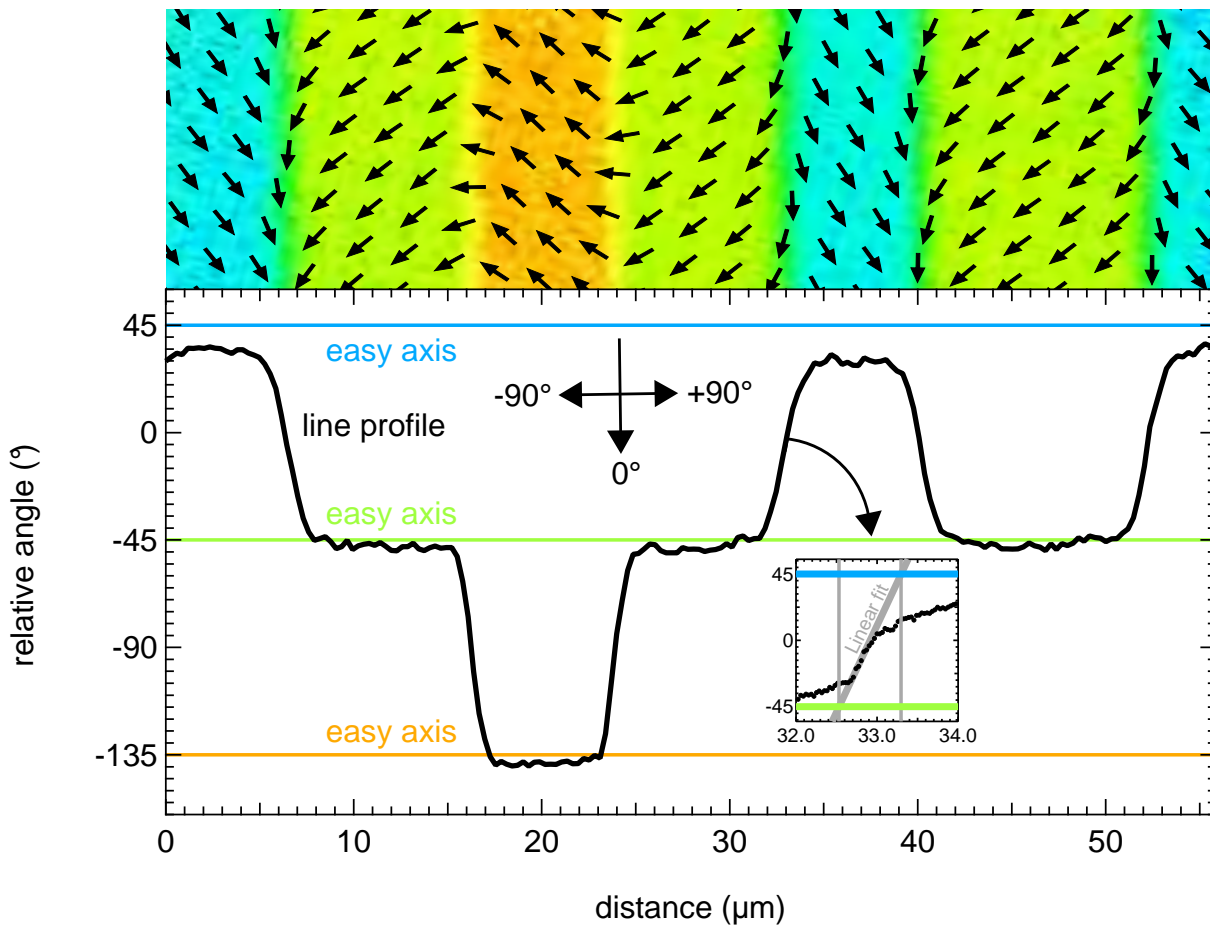


Figure 5.3: Line profile showing the magnetization angle taken along the full width of the image that is presented atop the graph. The line is drawn along a version of the image shown in Fig. 5.2 that is rotated by 78° . In contrast to the previous image, the definition of 0° is set to a direction that is parallel to the wall (see inset, don't let yourself be misguided by the optical delusion which suggests that the walls are askew: the grid to which the black arrows are attached to is not aligned parallel to the wall). The magnetization is slightly shifted from the easy axes inside the green and orange domains; an effect that might be attributed to a small external background field or systematic errors in the determination of the wall angle (the center of the SEMPA histogram (inset of Fig. 5.2b)) or a small misalignment in the scan rotation. Inside the blue domains the effect is however a lot stronger. It is evident, that the size (wall-to-wall distance) of the blue domains ($7\ \mu\text{m}$) is smaller than the size of the green domains ($9 - 12\ \mu\text{m}$). Model calculations for this system show that for the case of a charged wall the magnetization angle deviates from the easy axis inside a domain when the domain size is below about ten times the wall size [531]. A higher-magnification image was recorded (not shown) to obtain the wall width according to Lilley's definition [532] (see inset). A linear fit to the steepest region of the curve (slope $(117.45 \pm 9.12)^\circ \mu\text{m}^{-1}$) yields $\delta_L = (770 \pm 60)\ \text{nm}$. Considering this value, the size of the blue domains is 9 ± 1 times the wall width and below the above-mentioned limit. A reduction of the angle inside the domain is therefore expected, as a sharp reduction is observed below the critical limit [531].

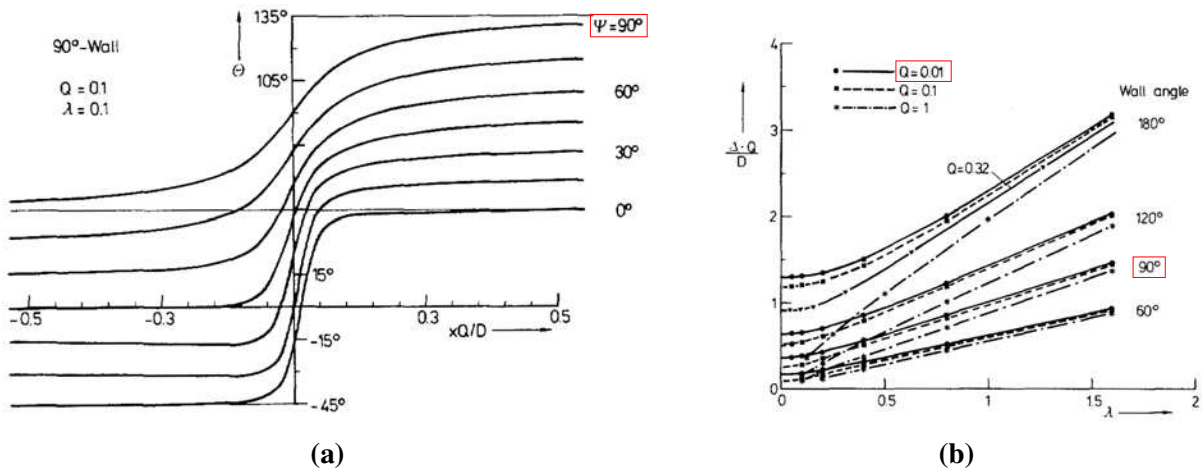


Figure 5.4: Original images reproduced from Alex Hubert’s paper “Charged Walls in Thin Magnetic Films” [529]. The relevant cases are highlighted. (a) Calculated wall profiles for $Q = 0.1$ and $\lambda = 0.1$ (parameters and angles are defined in the main text, D is the thickness). They show “The transition from charged walls ($\Psi = 90^\circ$) to Néel walls ($\Psi = 0^\circ$)” [529]. For $\Psi = 0^\circ$ the shape of the wall profile resembles a classical Néel wall. While Ψ increases towards $\Psi = 90^\circ$ the wall gets wider, a small core forms, and long tails emerge. (b) “Wall width [...] for [...] charged walls as a function of λ and Q ” [529]. The wall width is given as defined by Lilley [532] (see inset of Fig. 5.3). The system investigated here has $Q = 0.01$, $\lambda = 0.03$, and $D = 20$ nm. Due to the very low λ the leftmost region of the graph has to be considered (wall angle 90°). At this point the wall width is almost independent of λ . For the parameters of the $\text{Co}_{40}\text{Fe}_{40}\text{B}_{20}$ film, a wall width of ≈ 750 nm is expected.

($A = 2.1 \times 10^{-11} \text{ J m}^{-1}$, $M_s = 1.7 \times 10^6 \text{ A m}^{-1}$, $K = 1.7 \times 10^4 \text{ J m}^{-3}$) and a film thickness $t = 20$ nm. The wall profiles that have been calculated for a 90° wall are shown in Fig. 5.4a. When the charge of the wall is increased (by increasing Ψ), well separated tail and core regions develop. For a wall that consists of one core and two tail regions, two characteristic widths can be defined [529]:

- The width of the core region. It is most conveniently determined by fitting a line to the region where the swiftest rotation is observed (inset of Fig. 5.3). The line crosses the two respective lines of the final domain orientation ($\pm 45^\circ$) at two distinctive points. The distance between these two points gives the wall width. This is in accordance with Lilly’s definition δ_L [532]. Numerical values for the width of the core region have been obtained by Hubert [529] (see Fig. 5.4b).
- The width of the tail region. In the limit of vanishing exchange energy it is of the order of $\delta_{\text{tail}} = \frac{\pi}{2}t/Q$ [529].

The width of the core region of a charged wall $\delta_L = (770 \pm 60)$ nm is directly determined from the line profile shown in the inset of Fig. 5.3. The numerical calculations of Hubert, which are shown in Fig. 5.4b, yield an identical value of ≈ 750 nm for $Q = 0.01$, $\lambda = 0.03$,

and $t = 20$ nm. Wall widths around 700 nm are also found for this system in micromagnetic simulations (Fig. 4 in Ref. [531]).

The width of the tail region is not so easily obtained experimentally, due to the logarithmic nature of the tails [535]. Its order of magnitude can be approximated by $\delta_{\text{tail}} \approx \frac{\pi}{2} \cdot t/Q = 3 \mu\text{m}$ [529]. It now becomes clear why these tails cannot fully be observed in a domain that only measures a wall-to-wall distance of 7 μm . When the tail region starts to become confined, a steep reduction of the maximum rotation angle with decreasing domain size sets in [531].

5.2 Uncharged Walls

The investigation of uncharged walls was conducted on a second BaTiO₃ crystal. The second crystal was prepared simultaneously with the first one and can therefore be considered to be covered by a Co₄₀Fe₄₀B₂₀ film with identical properties as the first one. For SEMPA the second crystal was mounted in an orientation where the external magnetic field is applied perpendicular to the ferroelectric domain walls. With respect to the first crystal it was thereby rotated by 90°. In SEMPA it was saturated by the same magnetic field pulse of 50 mT as the first crystal prior to its investigation.

One of the SEMPA images that were consequently obtained is shown in Fig. 5.5. It was found that the whole Co₄₀Fe₄₀B₂₀ film only contained uncharged walls; a charged wall could not be found. The histogram (see Fig. 5.5b) reveals that the angle between the magnetization in two domains is $(88 \pm 4)^\circ$, exactly as it was observed for the first crystal (compare Fig. 5.2b). Although the size of the smaller (blue) domains is similar to the size of the smaller domains in the first crystal, the angle between the magnetization of two domains is not affected by the size. This is also an effect and/or an indication of the fact that uncharged walls are considerably smaller than charged walls. The size of the walls is determined in the following section.

5.2.1 Determination of Wall Width

The width of an uncharged wall was determined by zooming into the central wall region and recording a line profile through the wall. The resulting profile and an image of the surrounding area is shown in Fig. 5.6. When the line profile is obtained in a direction that is sufficiently perpendicular to the wall, the rotation of the magnetization component m_y (parallel to the wall) is described by a hyperbolic tangent [103, p. 217]:

$$m_y(x) = \frac{\sqrt{2}}{2} \cdot \tanh\left(\frac{2 \cdot (x - x_0)}{\delta_m}\right) \quad (5.5)$$

with the wall position x_0 , a factor of $\sqrt{2}/2$ for the 90° wall, and the width of the domain wall δ_m . While the measured quantity m_y corresponds to $\sin(\phi)$, with ϕ being the magnetization angle, this definition of the wall width δ_m is $2/\pi$ times [103, 175] the original definition of Lilley δ_L [532]. A fit of (5.5) to the measured signal (see Fig. 5.6) yields a width of:

$$\delta_m = (111 \pm 5) \text{ nm}$$

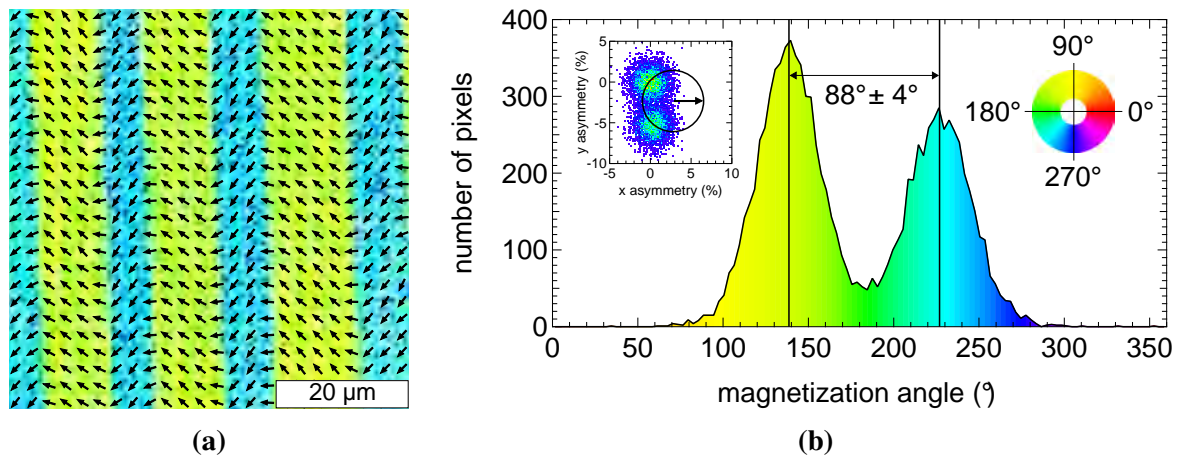


Figure 5.5: (a) SEMPA image of the magnetic configuration of $\text{Co}_{40}\text{Fe}_{40}\text{B}_{20}$ on the second BaTiO_3 crystal which was mounted perpendicular to the first one. The ferroelectric domain walls run vertical through the image. A magnetic saturation field of 50 mT, pointing to the left, was applied to the sample before imaging. As expected, uncharged walls are created in the $\text{Co}_{40}\text{Fe}_{40}\text{B}_{20}$, when the external field is applied perpendicular to the ferroelectric domain walls. In the color coding of the background pixels an abrupt transition between two domains can be seen, which means that the wall width is below the resolution of this image. Although several horizontal arrows suggest that the wall can be resolved, they only appear as a result of the averaging process over several pixels that belong to the one or the other domain. (b) Histogram of the magnetization angle for each pixel of the image that is shown in (a). An angle of roughly 90° is present between every two domains which are separated by an uncharged wall. Inset: Two dimensional raw data of the histogram. The center of the distribution is not easily obtained when only two domains (spots) are present. To this end the expected asymmetry (3.75 %) was determined from images that were measured shortly before and after the one that is shown here and then used as the radius. The center of the histogram is shifted from zero due to the experimental asymmetry of the setup. The raw data of the color images can be found in the appendix (see chapter 7.3).

$$\delta_L = (174 \pm 8) \text{ nm}$$

A wall profile that has been obtained by simulation is also shown in Fig. 5.6b. It is evident that it differs from the measured line profile. Before a more detailed analysis of the wall width can be done, we will have to take a look at how the experimentally measured wall profile is affected by experimental broadening.

5.2.2 Experimental Broadening

The width of a domain wall as measured with SEMPA is usually larger than the intrinsic wall width. When a length scale is measured with SEM, it is altered by experimental inaccuracies that stem from a finite width of the probing beam, thermal drift and 50 Hz noise. Additional broadening, which is related to multiple scattering processes, occurs in SEMPA. While the width of the probing beam and 50 Hz noise increase the apparent wall width, thermal drift may de- or increase it, depending on its direction relative to the scanning direction of the probing beam. It has to be noted that the change in the quantity that one is interested in should always be observed in the fast scanning direction to minimize experimental broadening. The influence of the different inaccuracies on the wall width will be discussed and quantified in the following sections.

Thermal Drift

Common to all scanning imaging techniques is the possible distortion of images due to thermal drift. Since perfect thermal stability can never be established for an experimental setup, slow thermal expansions of the materials that are involved lead to a relative movement between the source of the primary electron beam and the sample. Thermal drift may occur in every possible direction (x, y, z) whereas each will have a slightly different influence on the image.

Let us assume an image of a surface is taken with a fast scan direction along the x -axis and a slow scan direction along the y -axis. In this case, a constant thermal drift in x direction leads to a skewed image, whereas a constant drift in y direction leads to an elongated or condensed image. An additional drift along the z axis causes the sample to move out of the focussed region of the electron beam. The image hence becomes increasingly unfocussed or blurred.

There are several possibilities of correcting for the drift of an image after its acquisition, for instance rescanning the area while the slow and fast scan axes are reversed [536, 537]. Considering a line scan, this option is not available. One remaining option however is repeating multiple scans of the same line and subsequently aligning them. The line scan that is shown in Fig. 5.6 consists of ten single scans. Each of these scans took 50 seconds of which approximately 10 seconds were spent in the region of the domain wall. The single line scans were aligned by comparing the center position of the domain wall. A more solid option for the alignment would have been provided by small particles of dirt. A region without dirt was however deliberately chosen for the measurement, to allow for an undisturbed measurement of the wall profile.

In the integrated line scan that is shown in Fig. 5.6, the maximum shift between two single frames amounts to $\Delta x = (-10 \pm 1) \text{ nm/frame}$. For the time in which the primary electron beam moves through the wall region (10 of 50 seconds of a frame) the maximum drift is

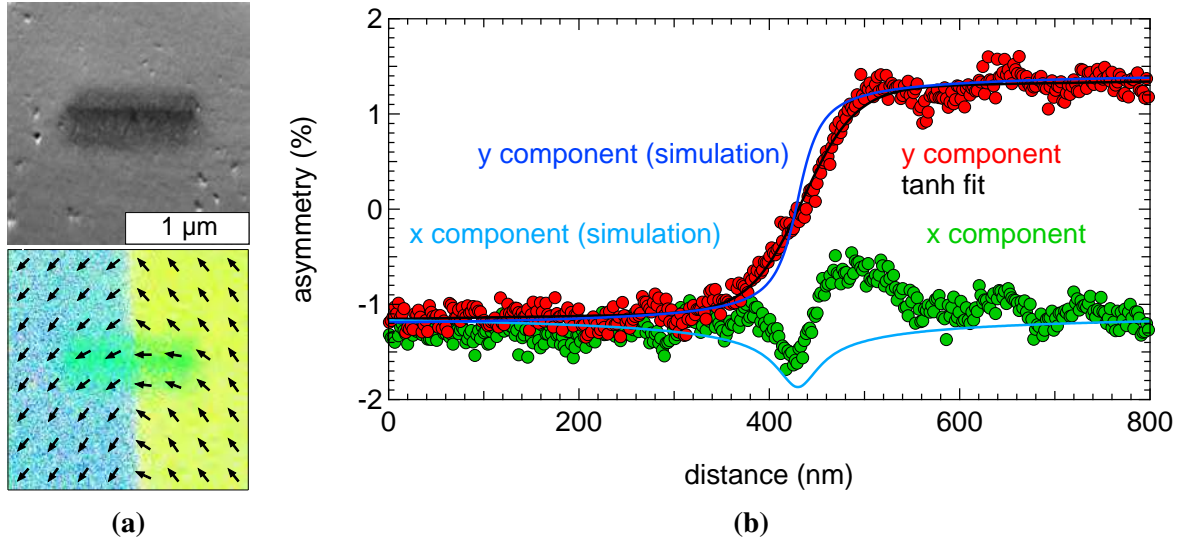


Figure 5.6: SEMPA measurement of a line profile obtained perpendicular to an uncharged domain wall. (a) Top: SEM image of the surrounding area, taken directly after the line scan. The region where the line scan was conducted shows an increased accumulation of carbon, which stems from residual-gas molecules that were cracked by the primary electron beam. Bottom: Simultaneously obtained SEMPA data showing the uncharged domain wall. The green region in the center has to be considered with care as it is impaired by the carbon. (b) Central region of the line profile in comparison to simulations (courtesy of Kevin J.A. Franke). The total line-profile consists of 500 pixels with a dwell time of 100 ms/px and was repeatedly measured ten times. It was then corrected for drift and averaged (this operation was checked to not alter the wall width, it just decreased the noise of the data). A steady increase of the y component of the magnetization is visible. It can be described by a hyperbolic tangent that yields a width of $\delta_m = (111 \pm 5)$ nm. The magnitude of the x component of the magnetization slightly increases in the center of the wall before it settles to a value that is a little bit smaller in magnitude than the one that is present on the left side of the wall. The profiles are not completely symmetric as the wall does not run perfectly vertical (or parallel) to the symmetry axes of the spin detector, which leads to a slight intermixing of the two components. The simulation was conducted with OOMMF [296] using the parameters for $\text{Co}_{40}\text{Fe}_{40}\text{B}_{20}$ ($A = 2.1 \times 10^{-11} \text{ J m}^{-1}$, $M_s = 1.7 \times 10^6 \text{ A m}^{-1}$, $K = 1.7 \times 10^4 \text{ J m}^{-3}$), a film thickness $t = 20 \text{ nm}$ and a cell size of $2 \text{ nm} \times 2 \text{ nm} \times 20 \text{ nm}$. The wall width is increased in the measurement compared to the simulations $\delta_{m,\text{sim}} = 90 \text{ nm}$. Reasons for this are the experimental broadening, the abrupt transition of the easy axis in the simulation (neglecting the finite width of the ferroelectric wall), and a possible difference in parameters like the anisotropy.

$\Delta x = (-2.0 \pm 0.2) \text{ nm}/10 \text{ s}$. Since the sample drifts in negative x direction and the primary electron beam moves in positive x direction, this leads to a shortening of the measured wall profile by $\Delta\delta_m = (-2.0 \pm 0.2) \text{ nm}$.

To check whether the values obtained from the line scans were reasonable, the thermal drift of the primary electron beam was analyzed relatively to the surface of a different sample in a later measurement. The gun was set to identical parameters and was allowed to run for 90 min prior to the measurement to reproduce the conditions that were present during the original measurement of the wall profile. A concurrent thermal drift in x direction of $(-2.5 \pm 0.4) \text{ nm}/10 \text{ s}$ was found. The drift in y direction is of a similar magnitude $(-1.5 \pm 0.4) \text{ nm}/10 \text{ s}$ and can thereby be neglected even if the wall does not run 100 % parallel to the y direction.

In summary, considering a domain wall that runs sufficiently vertical through the image, the drift in y direction has no influence on the measured wall width. The drift in x direction however decreases the measured domain wall width by $\Delta\delta_m = (-2.0 \pm 0.2) \text{ nm}$.

Width of the Probing Beam

The width of the primary electron beam is increased by a variety of factors that are discussed elsewhere [191]. “In practice, the incident beam will have a finite area of cross section and the electron distribution over this area will probably be approximately Gaussian.” [191]. Astigmatism may lead to a different width of this Gaussian shape when the beam is cut along the x or the y axis due to the elliptical shape of the spot on the surface of the sample [538]. This effect is increased by the inclined incidence of the primary electron beam that is present in our SEMPA [84]. In this case the inclined incidence decreases the maximum resolution in y direction by $1/(\cos 65^\circ) \approx 2.36$. However only the width in x direction is of importance here as it is the one perpendicular to the wall.

Additionally to its finite width, the probing beam is wobbled over the surface due to 50 Hz noise affecting the scanning unit. This periodic wobbling is observed as an additional broadening of the beam. During the measurement the noise was minimized as far as possible and all unnecessary devices and turbomolecular pumps were turned off.

An upper boundary for the approximate width of the beam can directly be obtained from the image that is shown in Fig. 5.6a (the upper image). To this end a line profile is drawn through a region where a small dirt particle is present. Assuming that the dirt particle has ultimately sharp edges, the profile of the beam is directly obtained from the derivative of the line profile at the position of the edge (not shown). It is indeed of Gaussian shape and has a full width at half maximum (FWHM) of $(17 \pm 3) \text{ nm}$.

The effect of the beam width on the measured property (wall width) is however rather indirect. As a result of a finite width of the beam, a convolution of the real wall profile with the beam profile is measured. The convolution of a wall profile of 111 nm width with a Gaussian peak of the above-mentioned FWHM yields a wall profile with a width of 112.5 nm.

The broadening that is caused by a finite width of the probing beam can in this case be approximated as $\Delta\delta_m = 1.5 \text{ nm}$. It has to be noted that the influence of this effect increases with decreasing dimensions of the object that is investigated and that the above-mentioned value is only valid for a wall of 111 nm width.

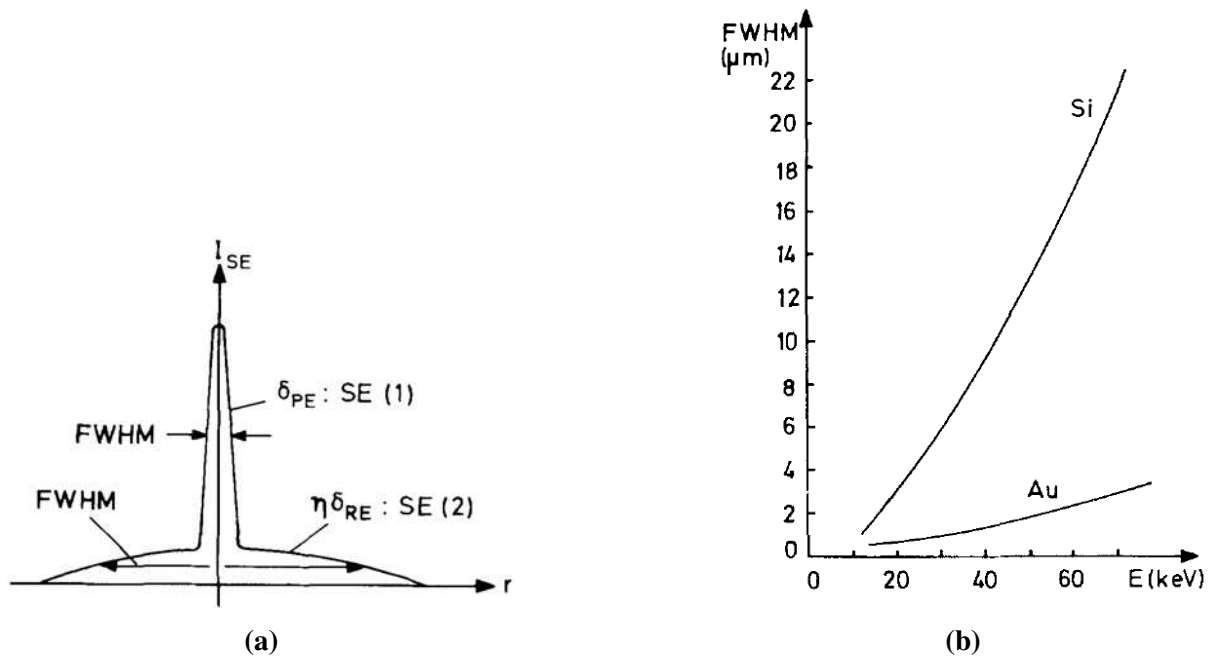


Figure 5.7: (a) Profiles for the emission of secondary electrons (SE) showing the emission of SE_1 and SE_2 (images reprinted from [149]). The SE_1 that are generated by the primary beam show a relatively narrow profile. Its width is determined by the focusing capabilities of the experimentalist and the electron column. The SE_2 that are generated by backscattered electrons (BSE) show a substantially wider profile. The width of the profile depends on the energy of the primary electrons as shown in (b). During the measurements that are shown here, the SEMPA was operated at a primary energy of 6 keV. At this energy, the width of the SE_2 distribution should be between 100 - 500 nm. When scanning a beam with an SE profile as shown in (a) over a sharp wall, the narrow part of the profile will cause a slight broadening of the observed wall profile while the shallow part will cause the seemingly appearance of wall tails.

Additional Broadening in SEMPA

Compared to conventional SEM, the ultimate resolution of SEMPA is usually decreased due to mechanical vibration that has a stronger effect as the imaging times in SEMPA are longer [194]. The SEMPA II in Hamburg is however equipped with a state of the art system for vibration isolation, so that these effects are no longer visible. The largest contribution now stems from electrical noise (50 Hz noise).

The width of the probing beam was determined from a SEM(PA) image (Fig. 5.6a) where the dwell time per pixel (5 ms) was 20 times shorter than it was for the line scan of Fig. 5.6. Comparing a single line from the magnetic image that was taken simultaneously with the SEM image however shows that the additional broadening does not have a drastic effect on the line profile. It is approximated to be below 10 nm.

An additional decrease in resolution stems from the emission of secondary electrons that are excited by primary electrons (PE) which have been scattered multiple times [169, 539]. These backscattered electrons (BSE) may eject secondary electrons from surface-near regions of the

sample where a different polarization is present. The secondary electrons that stem from BSE are named SE_2 in contrast to the SE that stem from primary electrons, which are named SE_1 . The SE_2 come from a much larger region of the sample (Fig. 5.7). Their influence however depends on the relative number N of SE_1 and SE_2 . The ratio is given by [149]

$$N(SE_2)/N(SE_1) = \beta\eta \quad (5.6)$$

with the back-scattering factor η and the ratio $\beta = \delta_{BSE}/\delta_{PE}$ that gives the difference in SE yield between backscattered and primary electrons. For Fe, Co, or Ni and a primary beam energy of 6 kV, $\eta \approx 0.27$ [183, p. 145] and $\beta = 4 - 5$ [149, 540, 541]. This means that the ratio is close to unity and the integral over the two profiles that are shown in Fig. 5.7 should be equal, as it actually nearly is in this representation. In this case, the wall profile measured by such a beam is composed of two different profiles: a narrow one that is expected from the rather narrow distribution and a broader one that is caused by the broader distribution. The FWHM of the broad profile lies in the range of 100 - 500 nm which is also the length scale on which broadening should be observed. Although these effects are hard to quantify, they might very well be responsible for the broadening of the measured line profile compared to the line profile that is obtained by micromagnetic simulations (see Fig. 5.6). More information on the influence of SE_2 on resolution can be found in Refs. [542–544].

In summary, the contributions to a broadening of the wall that are due to thermal drift and a finite width of the probing beam almost cancel out. The remaining broadening that is due to electric noise during the increased imaging time is approximately 10 nm. The measured wall profile is additionally altered by a contribution of secondary electrons of the second type (caused by BSE), which make up approximately half of the total secondary electron population.

5.2.3 Wall Width in Theory and Experiment

When experimental broadening is taken into account, the broadening of the measured line profile compared to the one obtained by simulation (see Fig. 5.6b) can be explained. The real width of the uncharged wall, should be in the range of $\delta_m = 90 - 120$ nm. The real wall width may however also be increased by the following factors that are not completely included in the micromagnetic simulation:

- The internal structure and size of the ferromagnetic wall (and particularly its core) could be affected by the finite width and internal structure of the ferroelectric wall. The width of the region where the polarization changes has been found to lie in the range of 1 - 25 nm in $BaTiO_3$ (see Tab. 1 in Ref. [545]). The ferroelectric wall was further found to reveal a complex internal structure [546]. It is however unclear how the strain is distributed inside the crystal around the region of the ferroelectric domain wall on the nanoscale [547, 548] and how this affects the strain transfer to the ferromagnetic film and therefore the induced anisotropy. The length scale on which the strength of the uniaxial anisotropy is build up in the ferromagnetic film with increasing distance from the wall center (in the one or the other direction) will be the important factor that ultimately determines the width of the ferromagnetic domain wall.

- The width of the ferromagnetic domain wall on BaTiO₃ can further be increased by an out-of-plane electric field [549]. An out-of-plane field of typically 56 kV m⁻¹ is caused by the spin-detector in SEMPA [84]. A field of this magnitude will cause a strain below 0.01 % [550], which is two orders of magnitude below the strain modulation between two ferroelectric domains [528]. This effect can very well be neglected.

5.3 Summary

The width and internal structure of charged and uncharged walls that appear in a Co₄₀Fe₄₀B₂₀ film on top of the ferroelectric domain walls in BaTiO₃ were investigated with SEMPA. Charged and uncharged walls could respectively be induced by applying a magnetic field either parallel or perpendicular to the ferroelectric domain walls. Some domains of the crystal in which charged walls were meant to be produced switched by 180° and turned two charged walls into uncharged walls, as they are energetically favorable.

SEMPA images of the charged walls reveal that they consist of a core region with a width of

$$\delta_L = (770 \pm 60) \text{ nm}$$

that is accompanied by two tails. Numerical calculations provide an identical core width $\delta_L \approx 750 \text{ nm}$ [529]. They further suggest a width of the tail region of $\delta_{\text{tail}} = 3.1 \mu\text{m}$ [529]. The tails can however not fully be observed with SEMPA in all domains because the size of smaller domains (7 μm) limits the maximum rotation angle of the magnetization [531]. As predicted [531], this effect sets in when the domain size w_{dw} is around tenfold the width of the core of the surrounding charged walls δ_L .

A full rotation of $(88 \pm 4)^\circ$ is observed for domains that are separated by uncharged walls. SEMPA images of uncharged walls reveal that they are indeed relatively narrow:

$$\delta_m = 90 - 120 \text{ nm}$$

$$\delta_L = 140 - 190 \text{ nm}$$

Compared to micromagnetic simulations the experimentally obtained wall profile is a little bit broader. There are two main reasons for this: First, the finite width of the region where the easy axis of the anisotropy rotates is not accounted for in the simulation. Second, the wall profile is altered by the profile of the probing beam and the lateral distribution of secondary electrons.

When comparing the measured widths of charged walls to that of uncharged walls, an increase of $(500 \pm 100) \%$ is observed when magnetic volume charges are introduced. A reproducible switching between both wall types is possible by the application of a small magnetic field. The possibility of switching between two domain wall states “could be used to store information or function as a magnetic switch in magnonic crystals, and tunable ferromagnetic domain walls could form the basis of tunable microwave resonators” [89].

6 Uniaxial Anisotropy of a Rippled Magnetic Film

As we have seen in the previous chapter, magnetic charges can have a tremendous effect on the width of a domain wall. As we will see in this chapter, they can also induce a magnetic anisotropy in a ferromagnetic film that has a wave-like, or a periodically modulated structure.

Magnetic thin films that show such a structure can for instance be prepared by evaporating the ferromagnetic material under oblique-incidence [551], by preparing it on top of a stepped [552, 553] or a wavy [554] substrate, or by a subsequent ion milling of the magnetic film (again at oblique-incidence) [555]. These thin magnetic films show a modulation of either one or of both of their interfaces.

The appearance of a uniaxial anisotropy in a modulated film, with an easy axis that is aligned perpendicular to the modulation (along the direction of the hills and valleys) was observed in various experiments [551, 553, 556–567]. In most cases, a quantitative description of the anisotropy is possible by using a model that has been developed by Schlömann [568]. Within this model, the demagnetizing factors of a magnetic film with a corrugated surface are derived, under the assumption that the magnetization is aligned perfectly uniform within the magnetic film (rigid magnetization) [568]. The anisotropy equals the stray field energy that is generated by such a pattern. The stray field energy is found to depend on the square of the RMS¹ roughness of the modulation divided by its corresponding wavelength [568].

An extension of the dipolar mechanism that includes magnetic volume charges and exchange energy was published by Arias and Mills [569]. They derived the roughness-induced anisotropy for small modulations of the surface profile, *i.e.* the film thickness is much larger than the corrugation. In their case, the surface modulation is treated as a perturbation of first order and the magnetization is allowed to vary locally. Two limiting cases could be identified: In the first case the length scale of the spatial variation is shorter than the exchange length of the material. In this case the magnetization can not follow the variation of the interfaces and “the rigid magnetization picture works well” [569]. Hence a “dipole only” description of the problem [568] is sufficient [569]. In the second case the length scale of the variation is longer than the exchange length², the exchange energy, which stems from a local variation of the magnetic moments, has to be taken into account [569]. The model was found to provide a good description for the anisotropy that is induced in films grown on a stepped surface [569].

Within this chapter, a model is developed that is able to describe the energy contributions that arise in two extreme cases: The distribution of magnetic surface charges as well as the stray field energy are derived in the case of rigid, or “uniform magnetization”. In comparison, the distribution of magnetic volume charges, the corresponding stray field energy, and the exchange energy

¹RMS = root mean square

²And the magnetization is not pulled straight by an external field.

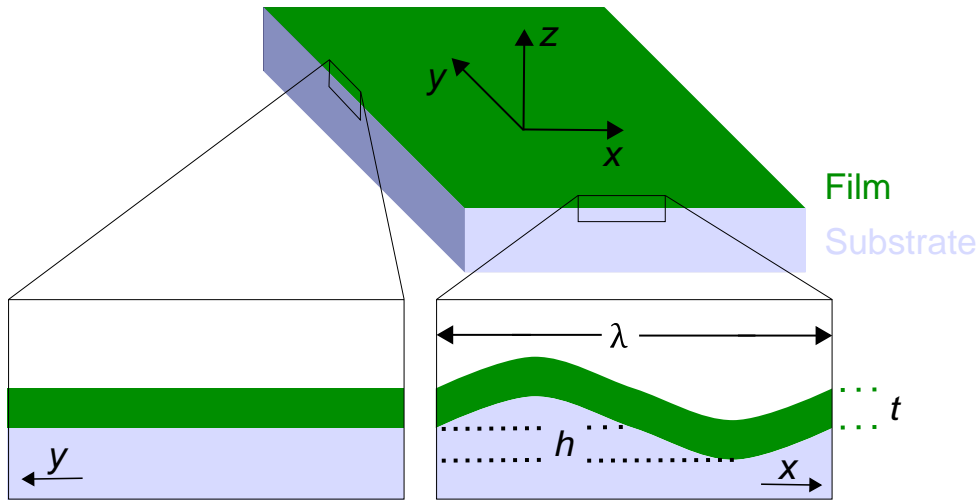


Figure 6.1: Schematic of the model system. A ferromagnetic film of thickness t (green) is placed on top of a rippled substrate (blue). Both extend infinitely within the xy -plane. On the macroscopic scale film and substrate seem to be plain. On the microscopic scale however the true morphology of the substrate is revealed. It shows a wavy structure along the x direction while it remains plain along the y direction. The waviness along the x direction can be described by a sinusoidal function of amplitude h and wavelength λ .

are derived in the case of undulating³, or “wavy magnetization”. The transition between both cases is derived by comparing the wavelength of the modulation to the film thickness. Finally, the results are compared to experimental studies. By comparing the theory to an experimental example [566], the region that is close to the transition region is explored and the reduction of energy by choosing a configuration that lies between the two extreme cases is quantified.

6.1 Model System and Possible Magnetic Configurations

The system that is used to describe and to calculate the magnetic anisotropy induced by a wavy substrate is pictured in Fig. 6.1. Film and substrate extend infinitely within the xy -plane, external fields and temperature are zero. With this being the case, the total energy of the system equals zero⁴ when all magnetic moments are aligned parallel to each other and directed along the y -axis.

When the magnetic moments are aligned along the x -axis, the total energy of the system is inevitably raised. Two different mechanisms are responsible for this increase, depending on the micromagnetic configuration that is present within the film. Regarding the micromagnetic configuration two fundamental cases can be distinguished, a mixture of which can describe every other case that is physically reasonable (see Fig. 6.2):

³The denotation “undulating” was chosen in Ref. [570] where quite the contrary, a reduction in the anisotropy of a magnetic thin film by a non-directional (isotropic) surface roughness, was analyzed.

⁴The potential energy of the system is in this configuration also set to be zero.

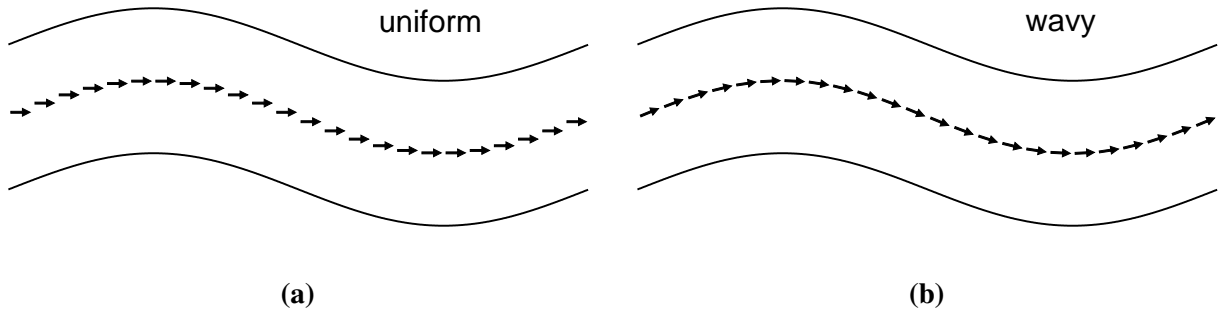


Figure 6.2: Prototype configurations for an alignment of the magnetization along the hard axis. (a) All magnetic moments are aligned parallel to each other and point exactly in x direction ($m_x = 1$). In this case the exchange energy is zero. The uncompensated magnetic moments at the interfaces cause a stray magnetic field that determines the total energy of the system. (b) The second possibility is that all magnetic moments exactly follow the wavy structure of the film and stay aligned parallel to the interfaces. In this case the generation of stray field at the interfaces is avoided. The exchange energy is however no longer zero and in addition magnetic volume charges emerge, giving rise to yet another stray field contribution to the total energy.

1. **Uniform magnetization** (Fig. 6.2a): All magnetic moments are aligned exactly parallel to the x -axis ($m_x = 1$). The exchange energy remains zero, but stray field emerges from the sample and raises the magnetostatic energy. The stray field energy will be calculated in the framework of magnetic surface charges.
2. **Wavy magnetization** (Fig. 6.2b): All magnetic moments follow the wavy structure of the film and stay aligned parallel to the interfaces. In this case no stray field emerges from the sample. The exchange energy however no longer remains zero because the magnetization varies locally. Additionally, magnetic volume charges appear and give rise to stray field energy.

One immediately sees that the energy of the first configuration arises from the interaction of the magnetization with the interfaces. The energy of the second configuration however arises solely from within the magnetic volume. The dependence of energy on thickness is therefore expected to be different for both configurations. Whereas the energy density decreases with thickness for an interface effect, it stays constant for an effect that occurs within the volume material. Further pursuing this thought, the uniform configuration should be present in films that are thick (compared to some characteristic value) whereas the wavy configuration should be present in very thin films. Somewhere in between a mixture of both should exist.

The physical system has two distinguished axes that lie within the film plane. The energy for an alignment of the magnetization along the x -axis is higher than it is for an alignment along the y -axis. The resulting anisotropy can hence be described as uniaxial. The y -axis is the easy axis of the system. While the qualitative situation is already quite clear from these simple theoretical considerations, the calculation of the different energy terms will provide a quantitative measure for the transition region between both configurations and give us an estimate for the strength of the resulting anisotropy.

To allow for an analytical solution of the problem, the morphology of the two interfaces that surround the film needs to be approximated by a mathematical function:

$$z(x,y) = h \cdot \sin \left[2\pi \frac{x}{\lambda} \right] \pm \frac{t}{2} \quad (6.1)$$

The function $z(x,y)$ describes a two-dimensional plane in three-dimensional space. It is composed of the parameters h (the amplitude of the modulation) and λ (the wavelength of the modulation). Both parameters can be used to adjust the function to the modulation that is present in the respective experiment. The upper and the lower interface of the film are described by shifting the plane up or down by one half of the film thickness $\Delta z = \pm t/2$ respectively. Note that although the function is two-dimensional, it does not depend on y and is hence invariant to translation along the y -axis.

To simplify the calculations, it is furthermore convenient to introduce a few dimensionless parameters in reduced units. These are the reduced length \bar{x} , the reduced thickness \bar{t} , and the reduced height of the modulation \bar{h} :

$$\bar{x} := \frac{x}{\lambda} \quad (6.2)$$

$$\bar{t} := \frac{t}{\lambda} \quad (6.3)$$

$$\bar{h} := \frac{h}{\lambda} \quad (6.4)$$

Note that all length scales are compared to the wavelength of the modulation λ . The use of dimensionless parameters allows for an immediate scaling of the system. If an energy contribution only depends on dimensionless parameters, it will stay constant when the system is scaled up or down accordingly⁵. As we will later see (chapter 6.5), the parameters \bar{t} and \bar{h} are typically smaller than one in nanoscale experiments [551, 553, 556–567].

Since it will appear quite frequently, an additional abbreviation $z_{dx}(x)$ is defined for the sake of simplicity. It gives the derivative of the surface function $z(x,y)$ (defined in Eq. (6.1)) along the x -axis:

$$z_{dx}(x) := \frac{\partial z(x,y)}{\partial x} = 2\pi\bar{h} \cdot \cos(2\pi\bar{x}) \quad (6.5)$$

A detailed calculation of the individual stray field and exchange energy contributions will be presented in the following sections. A shorter version (which is partially⁶ only valid for $\bar{h} = 0.1$) can be found in Ref. [564].

⁵The system is scale invariant when the wavelength λ , thickness t , and height h are multiplied by the same factor. This operation will not change the dimensionless parameters.

⁶The Fourier coefficients of the volume charge distribution were only calculated for the value of $\bar{h} = 0.1$. A derivation for arbitrary \bar{h} (as long as $2\pi\bar{h} < 1$) is made here.

6.2 Stray Field Energy

Stray field energy emerges when the magnetic flux of a magnetization pattern is broken. This can either occur by a variation in the direction of the magnetic moments or by an (abrupt) change in their strength. The latter is for instance the case, when the magnetization hits a surface or an interface.

The stray field energy is most conveniently derived in the framework of magnetic charges. These consist of magnetic volume and surface charges. The determination of these charges is discussed in the following chapter. As a first step, a mathematical expression for the distribution of the respective charges shall be derived.

6.2.1 Surface and Volume Magnetic Charges

The density of surface charges σ_m at a given point $\mathbf{r} = (x, y, z)$ is given in the continuum approximation by the dot product of the magnetization unit vector $\mathbf{m}(\mathbf{r})$ and the surface normal $\mathbf{n}(\mathbf{r})$ [103, p. 130][571]:

$$\sigma_m(\mathbf{r}) = \mu_0 M_s \mathbf{m}(\mathbf{r}) \cdot \mathbf{n}(\mathbf{r}) \quad (6.6)$$

Note that the vector field of the surface normal $\mathbf{n}(\mathbf{r})$ is zero in all space, except for the immediate region of an interface. The vector field hence includes a delta function in z direction, which reduces the effective dimension of the resulting scalar field $\sigma_m(\mathbf{r})$ by one. The unit of the two dimensional area charge density is $[\sigma_m] = V \cdot s/m^2$. The charge density is proportional to the magnetic flux that streams through an interface.

The density of volume charges ρ_m is obtained quite similarly by the dot product of the Nabla operator ∇ with the unit vector of the magnetization \mathbf{m} , which yields the divergence of the magnetization [103, p. 130][571]:

$$\rho_m := -\mu_0 M_s \nabla \cdot \mathbf{m} \quad (6.7)$$

The additional unit of the nabla operator $[\nabla] = 1/m$ leads to the resulting unit of $[\rho_m] = V \cdot s/m^3$ for the three-dimensional volume charge density.

Usually all magnetic charges appear in pairs. The existence of magnetic monopoles (unpaired charges) has been proposed in 1931 by Dirac [572, 573] to explain the quantization of the electric charge in units of e . Up until now, the existence of magnetic monopoles has not yet been proven experimentally. This might be due to their high (expected) mass [574], their low abundance [575, 576], or the large attractive force between two monopoles of opposite sign [572]. A quasiparticle that has some similarity with two single interacting volume charges was just recently observed in spin-ice systems [577–579].

Uniform Magnetization

Let us first calculate the distribution of magnetic charges in the case of uniform magnetization (Fig. 6.2a). In this case the magnetization vector \mathbf{m} is simply given by:

$$\mathbf{m}(\mathbf{r}) = \begin{pmatrix} 1 \\ 0 \\ 0 \end{pmatrix} \quad (6.8)$$

When all magnetic moments are aligned parallel to the x -axis, no magnetic volume charges appear since the divergence in magnetization vanishes⁷. Since most of the magnetic moments are, however, not aligned parallel to the surface, magnetic surface charges appear. To calculate the distribution of surface charges the vector field of the surface normal is required additionally to the vector field of the magnetization (6.8). The vector field of the surface normal is zero in all space except for the two interfaces. For the sake of simplicity, the direction of the surface normal in a given point on the respective upper or lower interface is calculated without including any delta functions that would determine the base point of the vector by putting constrictions on the allowed z values. The calculation is conducted by only considering the x coordinate of surface normal, magnetization, and charge. The exact position of a given point of the interface can be derived from x by means of (6.1) for the upper and lower surface respectively.

Two trivial requirements for the surface normal \mathbf{n} are that \mathbf{n} must be a unit vector and that its component n_y must vanish⁸, hence:

$$n_x^2 + n_y^2 + n_z^2 = 1 \quad (6.9)$$

$$n_y = 0 \quad (6.10)$$

The ratio of n_z to n_x for the upper and the lower surface can further be connected to the slope $z_{dx}(x,y)$ of the function $z(x,y)$ by a simple geometrical consideration⁹:

$$z_{dx} = \frac{\partial z}{\partial x} = -\frac{n_x}{n_z} \quad (6.11)$$

A combination of (6.9), (6.10), and (6.11) yields n_z and n_x for the upper (lower) surface:

⁷No changes in magnetization are present at zero temperature. For higher temperatures, a fluctuation of the volume charge density is expected. On the temporal average however the magnetic volume charge remains zero.

⁸The surface normal can not be tilted in y direction due to the translational invariance of the surface function z along the y -axis.

⁹The slope of a function $z(x)$ at a given point x is often motivated by drawing a triangle below the function. The triangle shows two orthogonal sides of (infinitesimal) length Δx and Δz . The ratio of these lengths $\Delta z/\Delta x$ is directly given by the derivative of the function dz/dx . To get access to the components of the two vectors that are perpendicular to the function z , the triangle can be rotated by $\pm 90^\circ$, which means nothing more than interchanging Δx and Δz .

$$1 = n_x^2 + n_z^2 = n_z^2 z_{dx}^2 + n_z^2 = n_z^2 (1 + z_{dx}^2) \quad (6.12)$$

$$n_z = \pm \sqrt{\frac{1}{1 + z_{dx}^2}} \quad (6.13)$$

$$n_x = \mp z_{dx} \cdot \sqrt{\frac{1}{1 + z_{dx}^2}} \quad (6.14)$$

The assignment of the signs of n_x and n_z is consistent with:

- n_z is always positive (negative) for the upper (lower) surface.
- When the slope z_{dx} of the surface function z is positive, n_x is negative (positive) for the upper (lower) surface.

Now that \mathbf{m} (6.8) and n_x (6.14) are known, the distribution of surface charges (6.6) can be calculated for the upper (lower) surface:

$$\sigma_m = \mp 2\pi \bar{h} \mu_0 M_s \cdot \cos(2\pi \bar{x}) \cdot \sqrt{\frac{1}{1 + (2\pi \bar{h} \cdot \cos(2\pi \bar{x}))^2}} \quad (6.15)$$

The magnitude of the surface charges is proportional to the height of the modulation \bar{h} and varies along the x direction with the exact same frequency as the modulation of the surface. The results of (6.15) are shown in Fig. 6.3 for a sample system with $\bar{h} = 0.01$ and $\bar{t} = 4\bar{h}$.

Wavy Magnetization

Let us now calculate the distribution of magnetic charges in the case of wavy magnetization (Fig. 6.2b). When all magnetic moments follow the variation of the surface structure, they are parallel to the interfaces in every row of the magnetic film (row means $x = \text{const.}$). The creation of surface charges is hence avoided. However, as a divergence in magnetization is present, magnetic volume charges emerge. To get access to the distribution of volume charges, a mathematical expression for the variation in magnetization is required.

In the wavy case it comes in handy that the magnetization \mathbf{m} is perpendicular to the surface normal \mathbf{n} of both interfaces (see Fig. 6.2b) and that the components of \mathbf{n} were already determined in the previous section (n_x (6.14), n_y (6.10), and n_z (6.13)). The magnetization unit vector \mathbf{m} is therefore directly obtained from \mathbf{n} by a rotation of $\pm 90^\circ$ (depending on the normal of which interface is used):

$$\mathbf{m} = \begin{pmatrix} \sqrt{\frac{1}{1 + z_{dx}^2}} \\ 0 \\ z_{dx} \cdot \sqrt{\frac{1}{1 + z_{dx}^2}} \end{pmatrix} \quad (6.16)$$

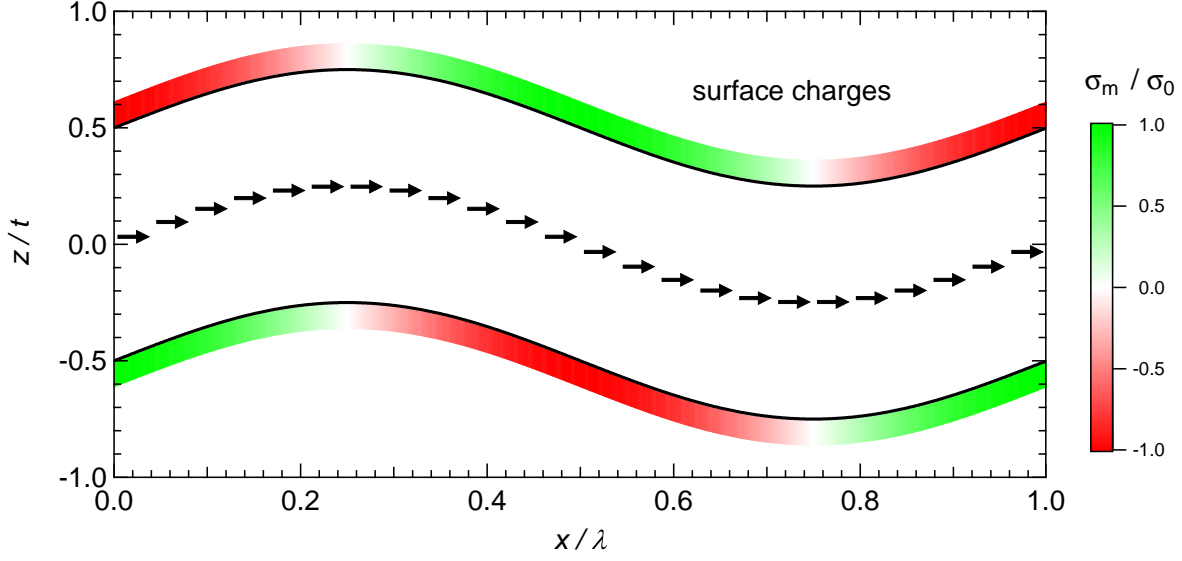


Figure 6.3: Distribution of magnetic charges on the surface of a wavy film that is homogeneously magnetized (black arrows, translation invariant in $\pm z$ within the film) as calculated by (6.15). The charge distribution is localized directly at the interfaces and extends deeply into the image plane (until $y = \pm\infty$). A finite height of the distribution was chosen for the sake of illustration. The parameters are $\bar{h} = 0.01$ and $\bar{t} = 4\bar{h}$, which means that the height of the modulation h is smaller than the film thickness t and much smaller than the wavelength of the modulation λ . The unit of the surface charges is $\sigma_0 = 2\pi\bar{h}\mu_0 M_s$. In strict agreement with (6.6), a positive surface charge is generated when the angle between magnetization \mathbf{m} and surface normal is $< 90^\circ$ while a negative surface charge is generated when the angle is $> 90^\circ$. For a perpendicular alignment ($= 90^\circ$), which is present at the hills and valleys, no surface charges are generated.

Note that z_{dx} is small when \bar{h} is small¹⁰ (as it usually is), which means that the main component of the magnetization points in x direction. The distribution of magnetic volume charges (6.7) then reads:

$$\rho_m = -\mu_0 M_s \nabla \cdot \mathbf{m} = -\mu_0 M_s \begin{pmatrix} \partial/\partial x \\ \partial/\partial y \\ \partial/\partial z \end{pmatrix} \cdot \begin{pmatrix} \sqrt{\frac{1}{1+z_{dx}^2}} \\ 0 \\ z_{dx} \cdot \sqrt{\frac{1}{1+z_{dx}^2}} \end{pmatrix} \quad (6.17)$$

Since z_{dx} does not depend on the z coordinate, the third component of (6.16) vanishes and the equation simplifies to:

$$\rho_m = \frac{\mu_0 M_s}{2} (1+z_{dx}^2)^{-\frac{3}{2}} z_{dx} \frac{\partial z_{dx}}{\partial x} \quad (6.18)$$

¹⁰The maximum value of the function z_{dx} is $2\pi\bar{h}$.

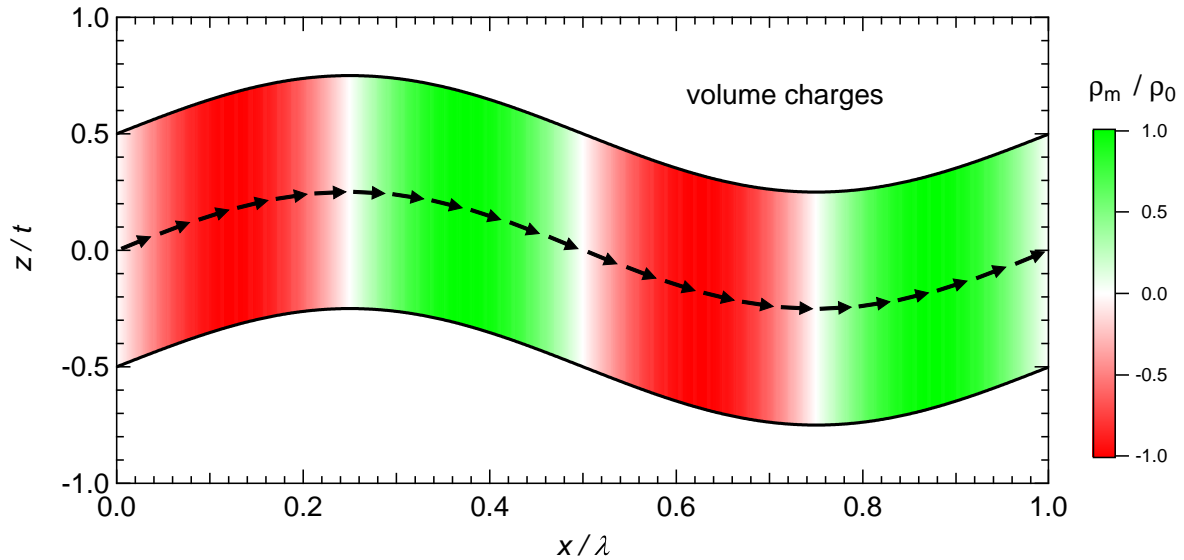


Figure 6.4: Distribution of magnetic charges in the volume of a wavy film in which the magnetization follows the wavy structure (black arrows, translation invariant in $\pm z$ within the film) as calculated with (6.19). The parameters are $\bar{h} = 0.01$ and $\bar{t} = 4\bar{h}$ as before (see Fig. 6.3). The magnitude of the charges is given proportional to the unit charge $\rho_0 = (\pi/\lambda)(2\pi\bar{h})^2$. Compared to the distribution of magnetic surface charges, the volume charge distribution has double the periodicity. It is positive when the component of \mathbf{m} that is parallel to the divergence ∇ increases, and negative when it decreases. In this case only the deviation in x direction gives rise to volume magnetic charges.

After a re-substitution of z_{dx} the distribution of volume charges inside a wavy magnetization pattern is finally revealed:

$$\rho_m = -\frac{1}{2} \frac{2\pi}{\lambda} (2\pi\bar{h})^2 \mu_0 M_s \sin(4\pi\bar{x}) [1 + (2\pi\bar{h} \cdot \cos(2\pi\bar{x}))^2]^{-3/2} \quad (6.19)$$

It is evident that the leading term of the volume charge distribution $\sin(4\pi\bar{x})$ varies with double the frequency compared to the modulation of the surface (and therefore the magnetization). In contrast to the distribution of magnetic surface charges (6.15), the distribution of volume charges is *not* scalable as it explicitly depends on $1/\lambda$. This behavior stems from the divergence in (6.7) where the length scale of the variation in magnetization enters. The distribution of volume charges in the case of wavy magnetization is plotted for $\bar{h} = 0.01$ and $\bar{t} = 4\bar{h}$ in Fig. 6.4.

6.2.2 From Charges to Energy

The stray field energy density f_m can be calculated by means of a Fourier expansion of the charge distribution [103, p. 132][580]. Two conditions need to be fulfilled to be able to apply this approach:

1. The energy is calculated for a charge distribution in a perfectly flat film. The wavy structure of the film therefore needs to be sufficiently shallow ($2\pi\bar{h} < 1$) so that the film can be approximated as flat.
2. The model assumes that surface charges on one side of the magnetic film are paired by opposite charges on the other side of the film. This condition is fulfilled in the model that is presented here.

Under these assumptions, the stray field energy density f for surface σ and volume ρ magnetic charges reads [103, p. 132][580, 581]:

$$f_{\sigma} = \frac{\mu_0 M_s^2}{2} \sum_j |v_j|^2 \frac{1 - \exp(-2\pi|\mathbf{q}_j|t)}{2\pi|\mathbf{q}_j|t} \quad (6.20)$$

$$f_{\rho} = \frac{\mu_0 M_s^2}{2} \sum_j |v_j|^2 \left(1 - \frac{1 - \exp(-2\pi|\mathbf{q}_j|t)}{2\pi|\mathbf{q}_j|t} \right) \quad (6.21)$$

The Fourier coefficients v_j and the respective wave vectors \mathbf{q}_j (with $|\mathbf{q}_j| = j/\lambda$) of the magnetization pattern are required for the calculation of the energy density. Both are defined in the complex form of the Fourier series [582] of a function $m_{\sigma,\rho}(\bar{x})$, which is characteristic for the change in magnetic flux, as:

$$m_{\sigma,\rho}(\bar{x}) = \sum_{j=-\infty}^{+\infty} v_j \exp(ij2\pi\bar{x}) \quad (6.22)$$

The complex Fourier coefficients are obtained by [582]:

$$v_j = \frac{1}{\lambda} \int_0^{\lambda} m_{\sigma,\rho}(\bar{x}) \exp(i2\pi j\bar{x}) d\bar{x} \quad (6.23)$$

In the case of the rippled magnetic film, the $m_{\sigma,\rho}(\bar{x})$ are [564]:

$$m_{\sigma}(\bar{x}) = 2\pi\bar{h} \cdot \cos(2\pi\bar{x}) \sqrt{\frac{1}{1 + (2\pi\bar{h} \cdot \cos(2\pi\bar{x}))^2}} \quad (6.24)$$

$$m_{\rho}(\bar{x}) = \sqrt{\frac{1}{1 + (2\pi\bar{h} \cdot \cos(2\pi\bar{x}))^2}} \quad (6.25)$$

The function $m_{\sigma}(\bar{x})$ describes the variation in the strength of magnetic flux that passes through each of the two interfaces in the case of uniform magnetization (see Fig. 6.2a). The calculation of the energy is identical for an out-of-plane stripe pattern with a saturation magnetization that is reduced by the factor $2\pi\bar{h}$ [564].

The function $m_{\rho}(\bar{x})$ describes the variation of the x component of the magnetization in the wavy magnetization pattern (Fig. 6.2b). As we have seen before (compare (6.17) and (6.18)),

only the x component gives rise to magnetic volume charges, because the magnetic pattern does not change along the y - or the z -axis.

Since both functions $m_{\sigma,\rho}(\bar{x})$ are real, it directly follows from the definition of the Fourier coefficient (6.23) that [582]

$$v_{-j} = v_{+j}^* \implies |v_{-j}| = |v_{+j}| \quad (6.26)$$

where v^* is the complex conjugate of v . For the determination of the stray field energy via (6.20) or (6.21) only the absolute value $|v_j|$ is of importance. It is hence sufficient to calculate v_j for all positive values of j and multiply the result by a factor of two¹¹.

To be able to solve the problem analytically, it is however convenient to develop the term below the square root of (6.24) and (6.25) into a Taylor series [583] to obtain a function that is easily integrable. To simplify the calculations, the root is defined as $g(c)$ and developed in a Taylor series around the point $c = 0$:

$$c(\bar{x}) := 2\pi\bar{h} \cdot \cos(2\pi\bar{x}) \quad (6.27)$$

$$g(c) := \sqrt{\frac{1}{1+c^2}} = \sum_{n=0}^{\infty} \frac{g(c)^{(n)}(0)}{n!} (c)^n \quad (6.28)$$

Hereby $g(c)^{(n)}$ denotes the n -th derivation of g with respect to c . The Taylor series of $g(c)$ reads:

$$g(c) = 1 + \sum_{n=1}^{\infty} \frac{(-1)^{(n)}}{2 \cdot 4^{(n-1)}} \binom{2n-1}{n-1} \cdot c^{(2n)} \quad (6.29)$$

The Taylor series converges if $|c| < 1$ [584]. This means that the function $g(c(\bar{x}))$ can be appropriately described by a Taylor expansion for all $\bar{x} \in \mathbb{R}$ if $2\pi\bar{h} \leq 1$. Since this condition needed to be fulfilled for the model to be applicable, the convergence of the series can be presumed.

The set of formulae presented in this section is sufficient to evaluate the energy density that is caused by magnetic charges for the two cases that are shown in Fig. 6.2. Since the derivation is very similar, both cases will be evaluated in parallel.

Stray Field Energies of the Charge Distributions

The energies f_{σ} (surface charge distribution, Fig. 6.3) and f_{ρ} (volume charge distribution, Fig. 6.4) are calculated from (6.20) and (6.21) by a Fourier expansion of m_{σ} (6.24) and m_{ρ} (6.25) respectively [580]. A multiplication of $g(c)$ (6.29) by $c = 2\pi\bar{h} \cdot \cos(2\pi\bar{x})$, yields the Taylor expansion of the surface charge distribution:

$$m_{\sigma} = 2\pi\bar{h} \cdot \cos(2\pi\bar{x}) + \sum_{n=1}^{\infty} \frac{(-1)^n}{2 \cdot 4^{(n-1)}} \binom{2n-1}{n-1} \cdot (2\pi\bar{h} \cdot \cos(2\pi\bar{x}))^{(2n+1)} \quad (6.30)$$

¹¹As we will later see, the values for $j = 0$ do not contribute to the total energy.

The Taylor expansion of the volume charge distribution (6.25) is simply given by $g(c)$ alone (6.29):

$$m_\rho = 1 + \sum_{n=1}^{\infty} \frac{(-1)^{(n)}}{2 \cdot 4^{(n-1)}} \binom{2n-1}{n-1} \cdot (\cos(2\pi\bar{x}))^{(2n)} \quad (6.31)$$

Note that for m_σ all even terms are zero whereas for m_ρ all odd terms are zero. This is because the original functions ((6.24) and (6.25)) are once even and once odd in c with regard to $c = 0$.

For the calculation of the Fourier coefficients from this power series, an integration is required. Since switching summation and integration is a commutative operation for a polynomial function, the calculation of the respective Fourier coefficient can be done individually for each single addend.

The Fourier coefficients of each single addend are derived by using the identities¹²:

$$v_{(2k+1)}(\cos^{(2m+1)}(2\pi\bar{x})) = 2^{-(2m+1)} \binom{2m+1}{m-k} \quad (6.32)$$

$$v_{(2k)}(\cos^{(2m)}(2\pi\bar{x})) = 2^{-(2m)} \binom{2m}{m-k} \quad (6.33)$$

The identities are valid¹³ $\forall m \wedge k \in \mathbb{N}$ with $m \geq k$. The application of (6.32) on (6.30) and of (6.33) on (6.31) yields:

odd	even	
$v_\sigma(j = 2k + 1) = \sum_{n=0}^{\infty} \alpha_{n,k} \cdot (2\pi\bar{h})^{2n+1}$	$v_\sigma(j = 2k) = 0$	(6.34)

$v_\rho(j = 2k + 1) = 0$	$v_\rho(j = 2k) = \sum_{n=0}^{\infty} \beta_{n,k} \cdot (2\pi\bar{h})^{2n}$	(6.35)
--------------------------	-----------------------------------------------------------------------------	--------

The coefficients $\alpha_{n,k}$ and $\beta_{n,k}$ are given by:

$$\alpha_{n,k} = \begin{cases} \frac{1}{2} & n = k = 0 \\ \frac{(-1)^n}{2 \cdot 4^{(n-1)} 2^{(2n+1)}} \cdot \binom{2n-1}{n-1} \cdot \binom{2n+1}{n-k} & n \geq k \wedge n > 0 \\ 0 & n < k \end{cases} \quad (6.36)$$

$$\beta_{n,k} = \begin{cases} 1 & n = k = 0 \\ \frac{(-1)^n}{2 \cdot 4^{(n-1)} 2^{(2n)}} \cdot \binom{2n-1}{n-1} \cdot \binom{2n}{n-k} & n \geq k \wedge n > 0 \\ 0 & n < k \end{cases} \quad (6.37)$$

¹²These functions are not so easily obtained. The author would like to explicitly thank Mahmoud Reza Rahbar Azad for his profound and enduring help in obtaining them with MATHEMATICA [584]. I am sure that the formulae may also be found in the one or other book about Fourier transformation, which is however not part of my shelf. A hint for their derivation is given in the integration of \cos^n which can for instance be found in Ref. [585, p. 318].

¹³Within this thesis \mathbb{N} includes zero.

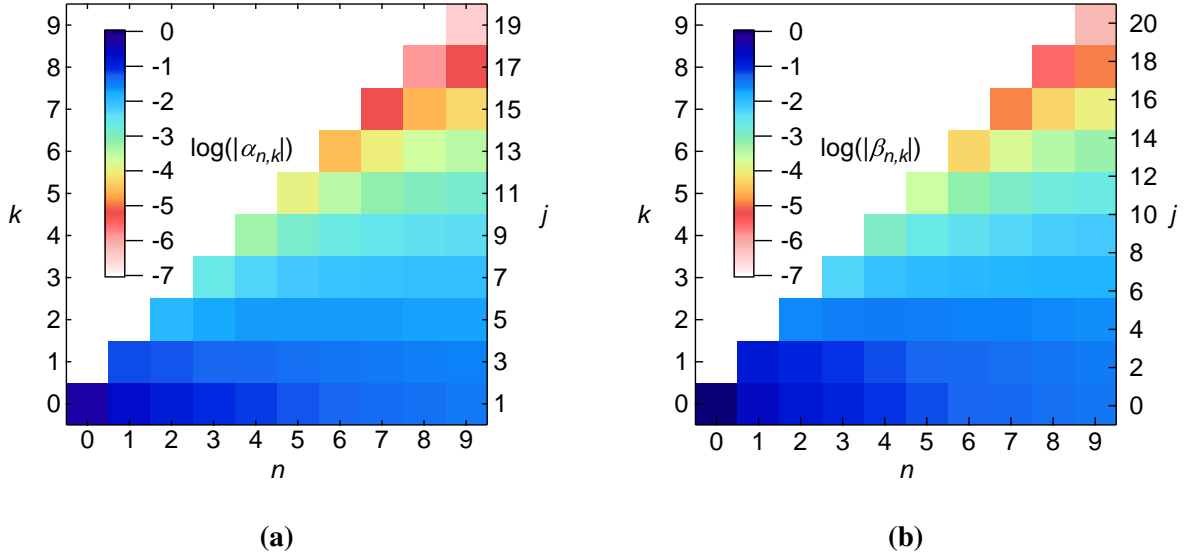


Figure 6.5: Dependence of the coefficients (a) $\alpha_{n,k}$ and (b) $\beta_{n,k}$ on n and k . The value of n gives the order of the Taylor expansion in the magnetic flux component that gives rise to surface ($m_\sigma, \alpha_{n,k}$) or volume charges ($m_\rho, \beta_{n,k}$). The value of k is proportional to the order j of the Fourier expansion of these functions. For the distribution of surface charges the only non-vanishing contribution stems from odd powers of $j = 2k + 1$, whereas for the distribution of volume charges only even powers $j = 2k$ contribute. When the energy is calculated, the contribution that stems from $k = 0$ in (b) is multiplied by zero, the lowest row in (b) hence has no physical meaning. The coefficients quickly decay with increasing n and k as indicated by the logarithmic scale.

Note that when developing an odd (even) function to a Fourier series, only odd (even) Fourier coefficients are non-zero because the function is approximated by odd (even) powers of sine and cosine functions [582]. Depending on the magnitude of $(2\pi\bar{h})$, the summation can be stopped at a given value of n when the desired accuracy is reached. For small values of $(2\pi\bar{h})$ it is usually sufficient to derive the first-order of the approximation. The decay of the coefficients $\alpha_{n,k}$ and $\beta_{n,k}$ with increasing n and k is visualized in Fig. 6.5a.

With the Fourier coefficients being known, the stray field energies generated by the two charge distributions (Fig. 6.3 and Fig. 6.4) can be calculated for a given sample system. A reformulation of Eqs. (6.20) and (6.21) accounting for the symmetry in v_j (see Eq. (6.26)) by replacing j by k reads:

$$f_\sigma = \frac{\mu_0 M_s^2}{2} \cdot 2 \sum_{k=0}^{\infty} |v_{2k+1}|^2 \left(\frac{1 - \exp(-2\pi|2k+1|\bar{l})}{2\pi|2k+1|\bar{l}} \right) \quad (6.38)$$

$$f_\rho = \frac{\mu_0 M_s^2}{2} \cdot 2 \sum_{k=0}^{\infty} |v_{2k}|^2 \left(1 - \frac{1 - \exp(-2\pi|2k|\bar{l})}{2\pi|2k|\bar{l}} \right) \quad (6.39)$$

These solutions are absolutely exact within the two boundary conditions stated on page 117. The formulae are however not very nifty for an evaluation of the physical connection. The physical background can easier be seen in the first order approximations. The first order in f_σ is given by $k = 0, n = 0$. The first order in f_ρ is given by¹⁴ $k = 1, n = 1$. They read:

$$f_\sigma = \frac{\mu_0 M_s^2}{2} \frac{(2\pi\bar{h})^2}{2} \left(\frac{1 - \exp(-2\pi\bar{t})}{2\pi\bar{t}} \right) + \mathcal{O}((2\pi\bar{h})^6) \quad (6.40)$$

$$f_\rho = \frac{\mu_0 M_s^2}{2} \frac{(2\pi\bar{h})^4}{32} \left(1 - \frac{1 - \exp(-4\pi\bar{t})}{4\pi\bar{t}} \right) + \mathcal{O}((2\pi\bar{h})^8) \quad (6.41)$$

These approximations are also obtained in Ref. [564]¹⁵. The stray field energy that is caused by magnetic surface charges (Fig. 6.3) f_σ , is in first approximation proportional to $1/\bar{t}$, which is typical for an interface effect. For small \bar{t} the term in brackets saturates at one. The stray field energy further grows proportional to the square height of the modulation \bar{h}^2 , as the charge density of the upper and the lower interface grow proportional to \bar{h} . The energy however remains constant when the system is properly scaled up or down as it only depends on the dimensionless parameters of reduced length \bar{h} and \bar{t} . Note that without the exponential contribution, Eq. (6.40) corresponds to the first order approximation of Schlömann¹⁶ (Eq. (33) in [568]).

The stray field energy that is caused by magnetic volume charges (Fig. 6.4) f_ρ , is in first approximation independent of \bar{t} . It however exponentially approaches zero for very small thicknesses. While the charge density of volume charges (6.19) is proportional to the square height of the modulation \bar{h}^2 the energy grows with the fourth power of \bar{h} .

The dependence on the parameters \bar{h} and \bar{t} of the stray field energy in the first order approximation is visualized in comparison to the exchange energy in Fig. 6.7a on page 126. Now that the stray field energies are known, the only remaining unknown contribution remains in the exchange energy that is generated in the wavy configuration.

6.3 Exchange Energy

The exchange energy of a ferromagnetic substance is increased, when the magnetic moments of two neighboring atoms are not aligned parallel to each other. In the continuum approximation of micromagnetics (see chapter 3.1) the local exchange energy density $f_{\text{ex}}(x)$ can be calculated by [564]:

$$f_{\text{ex}}(x) = A \left(\frac{\partial \theta}{\partial x} \right)^2 \quad (6.42)$$

¹⁴It has to be noted, that the contribution that stems from $k = 0$ ($j = 0$) vanishes when the energy is calculated. Although the Fourier coefficients are relatively large, the fact that $q_0 = 0$ leads to a multiplication of the Fourier coefficient v_0 by zero in eq. (6.21), which results in a contribution of zero to the total energy. For your information: $\lim_{x \rightarrow 0} [(1 - \exp(-x))/x] = 1$.

¹⁵In the calculation of the energy due to volume charges in Ref. [564], a discrete value for \bar{h} was set and the summation was carried out from $n = 0$ to $n = \infty$. In the general case that is presented here, the full summation can not be conducted.

¹⁶To get access to the energy Eq. (33) has to be used in combination with Eq. (16). Additionally a factor of two needs to be applied since Schlömann worked with a modulation of only one of the two interfaces.

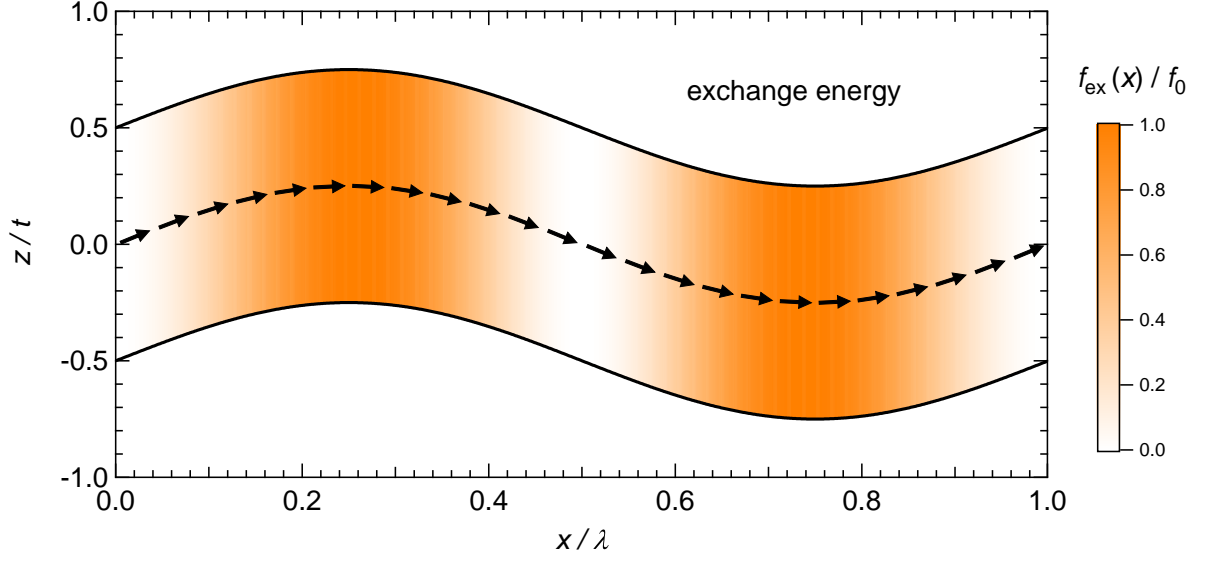


Figure 6.6: Variation of the local exchange energy $f_{\text{ex}}(x)$ in a film with wavy magnetization. The strength is given relatively to the unit exchange energy $f_0 = A (2\pi\hbar)^2 (2\pi/\lambda)^2$. The exchange energy density reaches its maximum value around the curves of the magnetic pattern. In this region, the largest angle is present between two individual magnetic moments. The exchange energy reaches zero in the regions where the second order derivation of the sine function that gives the pattern vanishes. This corresponds to the point where the rotation of the magnetization is reversed.

The parameter A denotes the exchange stiffness of the material. In our model system (see Fig. 6.2), the angle θ is defined between the magnetization vector and the $+x$ axis and is measured within the xz plane. In the case of uniform magnetization presented in Fig. 6.2a, the exchange energy $f_{\text{ex}}(x)$ equals zero, as θ is constant within the magnetic film. In the case of wavy magnetization, the angle θ can be obtained from the ratio of the two magnetization components m_z and m_x as defined in (6.16) by:

$$\theta = \arctan \left[\frac{m_z}{m_x} \right] = \arctan [2\pi\bar{h} \cdot \cos [2\pi\bar{x}]] \quad (6.43)$$

The derivation of θ with respect to x yields

$$\frac{\partial \theta}{\partial x} = (2\pi\bar{h}) \frac{2\pi}{\lambda} \frac{\sin [2\pi\bar{x}]}{1 + (2\pi\bar{h})^2 \cos^2 [2\pi\bar{x}]} \quad (6.44)$$

which yields the local exchange energy $f_{\text{ex}}(\bar{x})$ as:

$$f_{\text{ex}}(\bar{x}) = A (2\pi\bar{h})^2 \left(\frac{2\pi}{\lambda} \right)^2 \left(\frac{\sin [2\pi\bar{x}]}{1 + (2\pi\bar{h})^2 \cos^2 [2\pi\bar{x}]} \right)^2 \quad (6.45)$$

The variation of the local exchange energy $f_{\text{ex}}(x)$ is shown in Fig. 6.6. The energy is highest in the regions where the magnetization rotates swiftly, *i.e.* the peaks and valleys of the wavy magnetic film.

To obtain a quantity that can be compared to the stray field energy of the system, it is convenient to define the average exchange energy density f_{ex} . It is calculated as the average of $f_{\text{ex}}(\bar{x})$ over one wavelength:

$$f_{\text{ex}} = \int_0^1 f_{\text{ex}}(\bar{x}) d\bar{x} \quad (6.46)$$

MATHEMATICA [584] yields the result [564]:

$$f_{\text{ex}} = \frac{A}{2} (2\pi\bar{h})^2 \left(\frac{2\pi}{\lambda}\right)^2 \sqrt{\frac{1}{1 + (2\pi\bar{h})^2}} \quad (6.47)$$

Which is, again, exact within the boundary conditions of the system (see page 117). The exchange energy density f_{ex} :

- depends on the square of the maximum slope of the wavy magnetic film $(2\pi\bar{h})$, with an additional correction by higher order terms¹⁷ $\mathcal{O}(2\pi\bar{h})^4$, which become important when $(2\pi\bar{h})$ is close to unity;
- depends on the square of the wave vector of the system $2\pi/\lambda$;
- and is independent of film thickness t .

6.4 Comparison of the Energy Contributions

The magnetic system in a wavy film that is aligned along the hard axis (perpendicular to the waves) will chose the configuration that has the lowest total energy. This might be one of the two configurations that are shown in Fig. 6.2 or some configuration that is a mixture between them. To be able to decide which of the two configurations matches the system better, the energy of both configurations has to be compared for the parameters of the given sample setup. A comparison of the two respective energy contributions will be made in the limit of a shallow variation of the surface $(2\pi\bar{h}) \ll 1$.

When the system is in the state of uniform magnetization (Fig. 6.2a), its total energy f_{uniform} consists of the stray field energy which is generated by magnetic surface charges f_{σ} :

$$f_{\text{uniform}} = f_{\sigma} \stackrel{(2\pi\bar{h} \ll 1)}{\approx} \frac{\mu_0 M_s^2}{2} \frac{(2\pi\bar{h})^2}{2} \left(\frac{1 - \exp(-2\pi\bar{t})}{2\pi\bar{t}} \right) \quad (6.48)$$

¹⁷The Taylor series of the expression below the square root is given in (6.29) on page 119.

When the system is in the state of wavy magnetization (Fig. 6.2b), its total energy f_{wavy} consists of the sum of the exchange energy f_{ex} and the stray field energy that is generated by magnetic volume charges f_{ρ} :

$$\begin{aligned}
 f_{\text{wavy}} &= f_{\text{ex}} + f_{\rho} \\
 &\stackrel{(2\pi\bar{h} \ll 1)}{\approx} \frac{A}{2} (2\pi\bar{h})^2 \left(\frac{2\pi}{\lambda}\right)^2 \sqrt{\frac{1}{1 + (2\pi\bar{h})^2}} \\
 &\quad + \frac{\mu_0 M_s^2}{2} \frac{(2\pi\bar{h})^4}{32} \left(1 - \frac{1 - \exp(-4\pi\bar{t})}{4\pi\bar{t}}\right)
 \end{aligned} \tag{6.49}$$

The relative strength of the volume charge contribution f_{ρ} with respect to the exchange energy f_{ex} can be estimated by comparing the parameters of the modulation to the exchange length of the system l_{ex} [199]

$$l_{\text{ex}} = \sqrt{\frac{2A}{\mu_0 M_s^2}} \tag{6.50}$$

and using the first order in \bar{t} for f_{ρ} (thin film limit) and the first order in \bar{h} for f_{ex} :

$$\frac{f_{\rho}}{f_{\text{ex}}} = \frac{\pi}{4} \cdot \bar{t} \cdot \bar{h}^2 \left(\frac{\lambda}{l_{\text{ex}}}\right)^2 \tag{6.51}$$

It becomes clear that the volume charge contribution to the energy of the wavy state will only play a role in systems where the wave length of the modulation is substantially larger than the exchange length¹⁸.

The dependence of the individual contributions on the film thickness t is shown in Fig. 6.7a, using the example system of permalloy with $(2\pi\bar{h}) = 0.1$ and $\lambda = 100\text{nm}$. In this case the contribution that stems from magnetic volume charges is three orders of magnitude smaller than the other two contributions. To be able to decide which of the two micromagnetic configurations (wavy or uniform) is chosen, it is convenient to introduce the asymmetry in energy A_{E} :

$$A_{\text{E}} = \frac{f_{\text{wavy}} - f_{\text{uniform}}}{f_{\text{wavy}} + f_{\text{uniform}}} \approx \frac{f_{\text{ex}} - f_{\sigma}}{f_{\text{ex}} + f_{\sigma}} \tag{6.52}$$

The asymmetry is in the range of $[-1, +1]$ and indicates for:

- $A_{\text{E}} = -1$, that the exchange energy is considerably smaller than the stray field energy. In this case the wavy configuration will be present.
- $A_{\text{E}} = 0$, that both energies are equal. In this case a mixture of the two configurations will be present.

¹⁸The parameter \bar{h} is not allowed to rise beyond unity, because if it does, the model will fail. If \bar{t} approaches unity (thick film limit), it will vanish from the equation (in this case, divide Eq. (6.51) by $4\pi\bar{t}$) because the energy of volume charges then becomes independent of thickness.

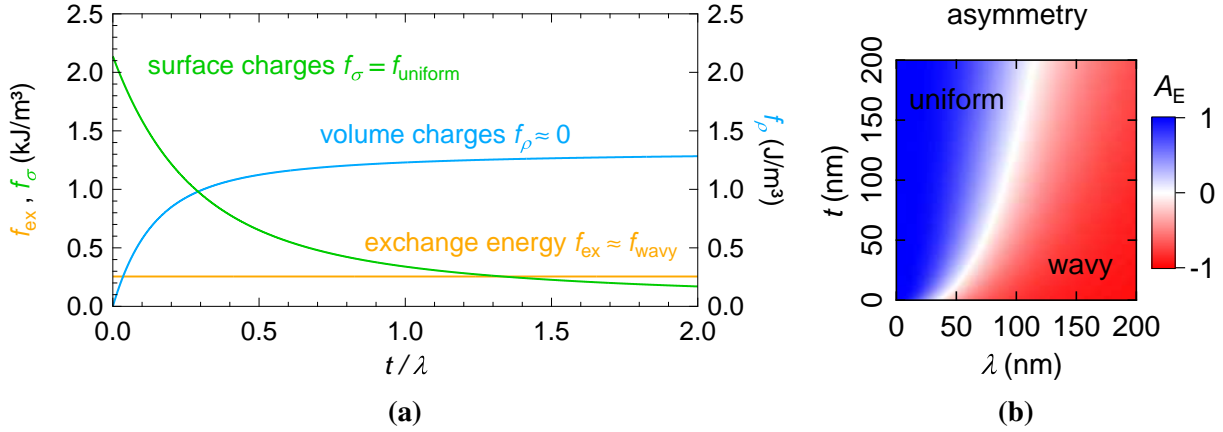


Figure 6.7: (a) Thickness dependence of the individual contributions for a system with the following parameters: $(2\pi\bar{h}) = 0.1$, $\lambda = 100\text{nm}$, $\mu_0 M_s^2 = 855\text{kJ}$, $A = 1.3 \times 10^{-11}\text{Jm}^{-2}$. The magnetic properties resemble permalloy ($\text{Ni}_{80}\text{Fe}_{20}$). Note that the scale for the energy contribution of magnetic volume charges f_ρ is three orders of magnitude smaller than for the other two contributions f_σ and f_{ex} . To determine the micromagnetic state with the lowest energy, it is thereby sufficient to compare the exchange energy of the wavy configuration to the stray field energy of the uniform configuration. The asymmetry in energy A_E , defined in (6.48), yields a direct measure for the relative magnitude of these two energies. In Fig. (b) the dependence of A_E on wavelength λ and film thickness t is shown for $(2\pi\bar{h}) = 0.1$. For small values of λ the uniform configuration is always favored. When λ is increased, the wavy configuration becomes more and more favorable. The uniform configuration will however still be present above a critical thickness.

- $A_E = +1$, that the stray field energy is considerably smaller than the exchange energy. In this case the uniform configuration will be present.

The dependence of the asymmetry on film thickness t and the wavelength of the modulation λ is plotted in Fig. 6.7b for the permalloy system with $(2\pi\bar{h}) = 0.1$. This representation emphasizes the fact that the exchange energy is not invariant against a scaling of the system. If it was, the transition region (white stripe) would be a straight line. The magnetostatic energy is invariant against a scaling as long as the dimensionless parameters \bar{h} and \bar{t} are kept constant. The exchange energy however increases dramatically with $1/\lambda^2$ as the system is scaled down.

A transition between the two micromagnetic configurations is experimentally most easily driven by a variation of the film thickness t . When the thickness of a film t is increased, a transition from the wavy to the uniform configuration will occur at a critical thickness t_{crit} . This transition region is visible as a white stripe in Fig. 6.7b. When the wavelength of the system λ is increased, t_{crit} also increases. With increasing λ the wavy configuration becomes more and more favorable as the exchange energy becomes smaller and smaller.

Above a certain wavelength (or film thickness), the two approximations $\exp[-2\pi t/\lambda] \ll 1$ and $(2\pi\bar{h})^2 \ll 1$ are valid around the transition region of Fig. 6.7b. In this limit the energy

of volume charges can be neglected and the remaining energies can be greatly simplified. The critical thickness can then be expressed as:

$$t_{\text{crit}} = \frac{\mu_0 M_s^2}{2A} \left(\frac{\lambda}{2\pi} \right)^3 = \frac{\lambda}{2\pi} \left(\frac{\lambda/(2\pi)}{l_{\text{ex}}} \right)^2 \quad (6.53)$$

This approximation shows that the increase in the critical thickness t_{crit} is proportional to λ^3 . The critical thickness further depends on the ratio of magnetostatic and exchange energy, which is related to the magnetostatic exchange length l_{ex} of the magnetic system by (6.50). When $(\lambda/(2\pi))$ is of the order of the exchange length l_{ex} , the critical thickness is also of the order of the exchange length.

6.5 Comparison of Model Values to Experimental Data

Now that the full model is available, it shall be compared to three selected experimental systems. In the first two experimental studies (permalloy on diamond [92] and cobalt on magnesium oxide [564]), the wavy configuration is present. In the last study (permalloy, cobalt, and iron on silicon [566]) the transition region between the wavy and the uniform configuration is explored.

6.5.1 Permalloy on Diamond

The model presented here was initially developed to describe the uniaxial anisotropy that arises in a permalloy film grown on top of a polished diamond substrate. The mechanical polishing of the diamond substrate results in periodic polishing lines that run across the surface in parallel [92]. A uniaxial anisotropy of $K_u = (470 \pm 30) \text{ J m}^{-3}$ with an easy axis aligned parallel to the polishing lines has been measured in a 20 nm permalloy film with MOKE¹⁹ [92]. The film was constantly rotated during evaporation to avoid the emergence of an additional field-induced contribution to the anisotropy during growth.

A surface profile perpendicular to the polishing lines (Fig. 6.8b) shows a height of $h = 1.0 - 1.5 \text{ nm}$ and a wavelength of $\lambda = 100 - 125 \text{ nm}$ for the larger modulations [92, 302]. With the exchange length of permalloy, $l_{\text{ex}} = 5.5 \text{ nm}$, this translates to a critical thickness of $t_{\text{crit}} = 130 - 260 \text{ nm}$. The film investigated in [92] has a thickness of 20 nm and is therefore well below this limit. As a result the wavy configuration is expected to be present when the magnetization is aligned along the hard axis. The contribution that stems from the stray field energy of the magnetic volume charges is below 1 % in this case and can be neglected.

The anisotropy induced by the largest modulations of the film structure is in the range of 50 - 250 J m^{-3} . A slightly higher value in the range of 200 - 800 J m^{-3} is obtained when the exchange energy is calculated directly from the surface function $z(x, y)$ obtained by AFM measurements [92]. This emphasizes the fact that smaller modulations also have to be taken into account when the anisotropy is calculated, to make sure it will not be underestimated.

Overall, the values which are obtained from the model fit very well to the anisotropies of permalloy thin films on a corrugated diamond substrate.

¹⁹MOKE = Magneto-optical Kerr effect.

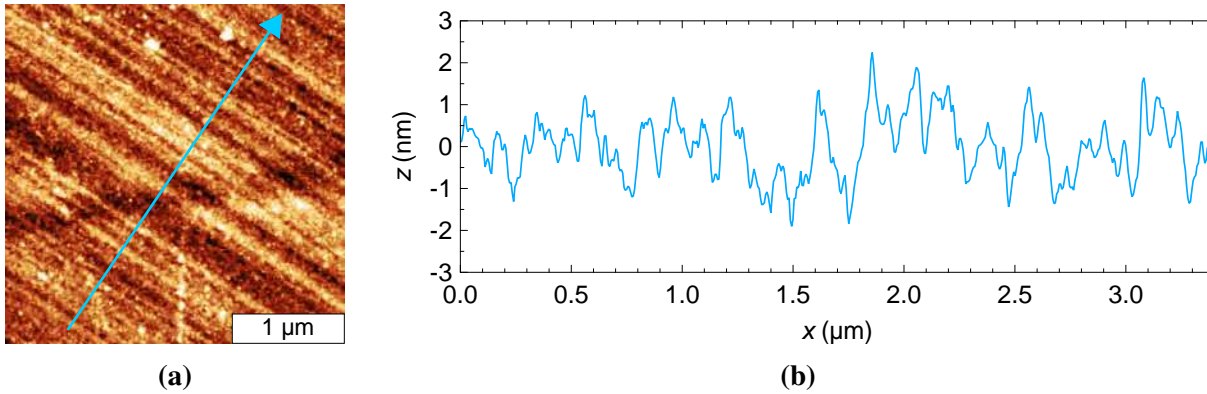


Figure 6.8: (a) AFM image of the diamond surface. Polishing lines are clearly visible. (b) A line profile drawn perpendicular to the polishing lines reveals that the wavelength and amplitude of the corrugation are rather random. Two major contributions can however be spotted. A larger one with an amplitude of approximately $h = 1.5$ nm and a wavelength of roughly $\lambda = 100$ nm, and a smaller one with $h = 0.5$ nm and $\lambda = 50$ nm.

6.5.2 Cobalt on Magnesium Oxide

The model was also applied to the system of a thin film of cobalt on the sputtered surface of magnesium oxide (MgO) [564]. After ion milling at oblique incidence, the surface of the MgO shows a periodic modulation with a wavelength of $\lambda = 100$ nm and an amplitude of $h = 10$ nm, as measured with AFM [564]. When a 10 nm cobalt film is evaporated on top, the measured amplitude is decreased to 6 nm, which suggests that the corrugation is smoothed and not completely reproduced in the upper interface [564].

When the MgO(001) surface is ion milled at normal incidence, the subsequently evaporated cobalt film shows an in-plane biaxial anisotropy with easy axes along the Co(110) directions [564]. Ion milling at oblique incidence produces a uniaxial anisotropy with the easy axis aligned along the tilting direction of the incoming ion beam. This behavior could be reproduced for directions of the ion beam along MgO[100], MgO[110], and MgO[010]. The additional anisotropy was found to be a volume-like contribution and attributed to the exchange energy of the wavy configuration.

For the exchange length of cobalt $l_{\text{ex}} = 4.7$ nm [586, 587] and $\lambda = 100$ nm the critical thickness is $t_{\text{crit}} = 180$ nm. This value is well above the thickness range that was investigated in the experiment, which is below 10 nm [564]. The magnetization is therefore indeed expected to be in the wavy configuration when it is aligned along the hard axis.

Using the exchange constant of fcc cobalt $A = 2.73 \times 10^{-11}$ Jm⁻¹ [586, 587], the exchange energy for the wavy configuration is $f_{\text{ex}} = 7$ kJm⁻³ for $h = 6$ nm and $f_{\text{ex}} = 18$ kJm⁻³ for $h = 10$ nm respectively. A volume contribution to the uniaxial anisotropy of $K_{\text{u}} = 21.5$ kJm⁻³ is measured with MOKE in films with a thickness in the range of 2.1 - 4.6 nm [564]. This value is closer to the exchange energy that stems from the higher modulation amplitude, which might suggest that the smoothing of the upper interface is not as distinct as it is for the 10 nm film. A smoothing of one of the interfaces would result in a reduction of the measured anisotropy. As before, the exchange energy might however also be underestimated by neglecting contributions

from smaller wavelengths. Additionally, the inclusion of volume charges into the calculation can further increase the energy by up to 0.9 kJ m^{-3} (for $t = 4.6 \text{ nm}$ and $M_s(\text{Co}) = 1440 \text{ kA m}^{-1}$ [209, p. 99]).

Chen *et al.* [564] report about an additional surface contribution to the anisotropy that “favors the direction perpendicular to the ripples” [564]. A contribution perpendicular to the ripples can neither be explained by the model presented here nor by Chen *et al.* [564] (where the same model was applied). In the following chapter we will however see that such a contribution is also present in other experimental systems.

In summary the wavy configuration of the model provides a good description for the volume contribution to the anisotropy that develops in cobalt films on MgO that have been ion milled at oblique incidence.

6.5.3 Permalloy, Cobalt, and Iron on Silicon

A recent paper by Liedke *et al.* [566] reports about the uniaxial anisotropy of permalloy, cobalt and iron thin films on a rippled silicon substrate. The strength of the anisotropy field is investigated in dependence on ripple wavelength λ and film thickness t . A rippling of the surface of the Si(100) substrates is obtained by Xe^+ ion bombardment under incidence angles of 65° and 70° [554]. A self organized ripple structure with a well defined periodicity is created by the sputtering process. Since the wavelength of the ripple pattern increases proportional to the ion dose, samples with different ripple wavelengths could be prepared [561, 566]. Permalloy, cobalt, and iron films (thickness 10 nm) were grown with MBE²⁰ on templates with various wavelengths. Subsequently their magnetic properties were investigated with MOKE and FMR [566].

Liedke *et al.* [566] calculate their model values [568] from the surface roughness ω_{rms} of the ripple structure. The same is done here to ensure comparability²¹. Moreover, the authors give the anisotropy in units of the anisotropy field, which is connected to the uniaxial anisotropy K_u by:

$$H_a = \frac{2K_u}{\mu_0 M_s} \quad (6.54)$$

The uniaxial anisotropy K_u is equal to the stray field or exchange energy of the respective hard-axis configuration. Measured [566] and model values of the anisotropy field in dependence of λ are shown in Fig. 6.9. The overall trend of the data is described very well by the model. Since all measured points are in the vicinity of the transition region (where both energies are equal) a mixture between both configurations (uniform and wavy) is expected. The energy of a mixed configuration is always below the energies of the two individual configurations.

It is however intriguing that the measured anisotropy fields lie above the modeled values for $\lambda \geq 70 \text{ nm}$. One reason for this might be that the amplitude of the surface modulation increases for larger wavelengths [566], whereas it is kept constant in the model for the sake of simplicity. Additionally, the influence of smaller wavelengths is greater on the exchange energy ($\propto \lambda^{-4}$)

²⁰MBE = molecular beam epitaxy

²¹The surface roughness is related to the amplitude h of a sine function by $h = \sqrt{2}\omega_{\text{rms}}$.

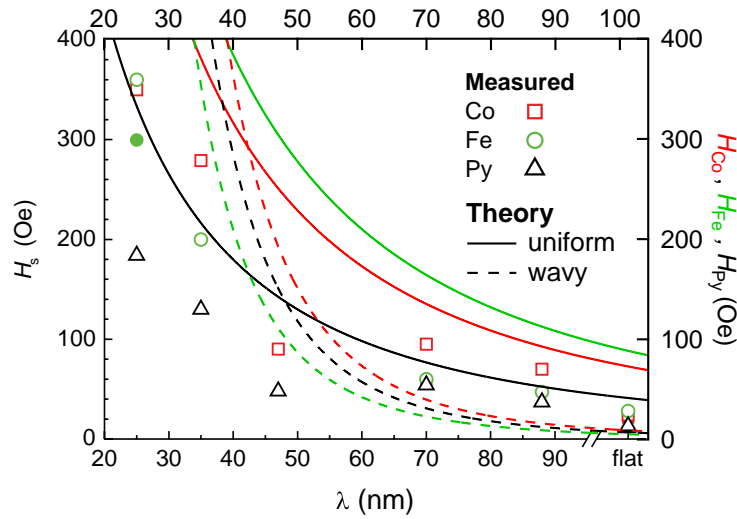


Figure 6.9: Measured values for the anisotropy field in 10 nm Co, Fe, and Py thin films (open symbols plotted against the left and bottom axis, data from [566]). The films were prepared on different substrates with various wavelengths of the ripple pattern λ . The anisotropy field corresponding to the stray field energy of the uniform magnetization pattern (solid lines) as well as the exchange energy of the wavy magnetization pattern (dashed lines) are calculated from Eqs. (6.48) and (6.49) respectively and plotted against the top and right axis for $h = 1.7$ nm. The modelled curves describe the general trend of the measured data very well. When the system is close to the transition region around $\lambda = 40 - 50$ nm a mixture of both states should be present, which leads to a reduction in total energy. Liedke *et al.* [566] report an increase in roughness for larger wavelengths, which would explain an increase in energy. Contributions from variations of smaller wavelengths may lead to an additional increase in energy (see main text).

than it is on the stray field energy ($\propto \lambda^{-2}$). The value of λ that is plotted on the bottom axis of the graph corresponds to the center of the first satellite peak of the Fourier transformation (FFT) of the corresponding AFM image [566]. Calculating the energy from this value alone might lead to an underestimation of the exchange energy, as smaller wavelengths, which have a lower occurrence in the spectra but a higher impact on the energy, are neglected. For instance, a decrease in wavelength by 10 % leads to an increase in energy by more than 50 %.

Liedke *et al.* [566] also investigated the dependence of the anisotropy field on film thickness t . To that end wedges with thickness gradients from 0 - 50 nm were prepared on $\lambda = 25$ nm ripple templates. The results are compared to theoretical values that are obtained by using the model of Schlömann [566, 568], which gives an approximation for the stray field energy of the uniform configuration (see Fig. 6.10). The anisotropy field that is calculated from the energy of the uniform configuration (6.48) (in combination with (6.54)) as well as the values obtained from Schlömann's model provide a good approximation for the general behavior and the magnitude of the anisotropy field for thickness above 10 nm.

In these systems of short $\lambda = 25$ nm, the critical thickness is of the order of the exchange length, and therefore around 5 nm. Below 10 nm one is hence in the intermediate regime, where

both energy contributions have an influence. Liedke *et al.* [566] claim that the magnetization deviates from its perfect alignment along the x -axis by a maximum angle β_{\max} for thickness below 10 nm, which leads to a reduction of the stray field energy. In a micromagnetic simulation β_{\max} increased up to 8° with decreasing film thickness in an iron film [566]. This tilting could indeed lead to a reduction of total energy. The question however remains if this decrease is sufficient to explain the experimental data?

Reducing the Energy by Tilting Towards the Wavy Configuration

Let us estimate the energy that would be saved in the 10 nm permalloy film of Fig. 6.10a if the uniform magnetization was slightly tilted towards the wavy configuration by a maximum angle of $\beta_{\max} = 2^\circ$.

The exchange energy for a configuration with a maximum angle β_{\max} can be obtained by replacing $(2\pi\bar{h})$ by $\tan(\beta_{\max})$ in Eq. (6.47), which can be understood by considering Eq. (6.43)²². For $\beta_{\max} = 2^\circ$, the anisotropy field due to the exchange energy is 26 Oe for $\lambda = 25$ nm and the parameters of permalloy.

Simultaneously, the effective magnetization $M_{\text{eff}} = (2\pi\bar{h}) M_s$ that gives rise to the emergence of surface charges is further reduced. In the uniform configuration ($\beta_{\max} = 0$), the maximum angle at which the magnetization hits the surface is already reduced from 90° due to the shallowness of the surface function. The effective angle θ_{eff} that gives rise to the effective magnetization M_{eff} can be calculated as $\theta_{\text{eff}} = \arcsin(2\pi\bar{h})$, which results from a simple geometrical consideration. Using this angle, the effective magnetization can be written as $M_{\text{eff}} = \sin(\theta_{\text{eff}}) \cdot M_s$.

The additional reduction of the effective magnetization $M_{\text{eff,red}}$ by a further rotation of the magnetization towards parallel alignment with the surface by $\beta_{\max} \leq \theta_{\text{eff}}$ is then given as:

$$M_{\text{eff,red}} = \sin(\theta_{\text{eff}} - \beta_{\max}) \cdot M_s = \sin(\arcsin(2\pi\bar{h}) - \beta_{\max}) \cdot M_s \quad (6.55)$$

The stray field energy that arises from surface charges is proportional to the square of the effective magnetization M_{eff} [564]. Hence, a reduced effective magnetization leads to a reduction of the stray field energy by a factor α_{red} of:

$$\alpha_{\text{red}} = \left(\frac{\sin(\arcsin(2\pi\bar{h}) - \beta_{\max})}{2\pi\bar{h}} \right)^2 \quad (6.56)$$

Which amounts to $\alpha_{\text{red}} = 0.85$ for $(2\pi\bar{h}) = 0.41$ and $\beta_{\max} = 2^\circ$. The stray-field-induced anisotropy field of the 10 nm permalloy film is therefore reduced by 45 Oe from 300 Oe to 255 Oe.

To summarize, a rotation of the uniform magnetization towards the wavy configuration by a maximum angle of $\beta_{\max} = 2^\circ$ would reduce the stray field energy²³ by 45 Oe while increasing the exchange energy by only 26 Oe. The total energy would hence be reduced by 19 Oe.

One would tend to believe that a further tilting might lead to an even larger reduction in energy for this system. The value of $\beta_{\max} = 2^\circ$ is however quite close to the energetic minimum, which is located at 2.3° .

²²The maximum angle is reached when the cosine function in Eq. (6.43) equals one.

²³In this context “... energy” means “anisotropy field that stems from the ... energy contribution”.

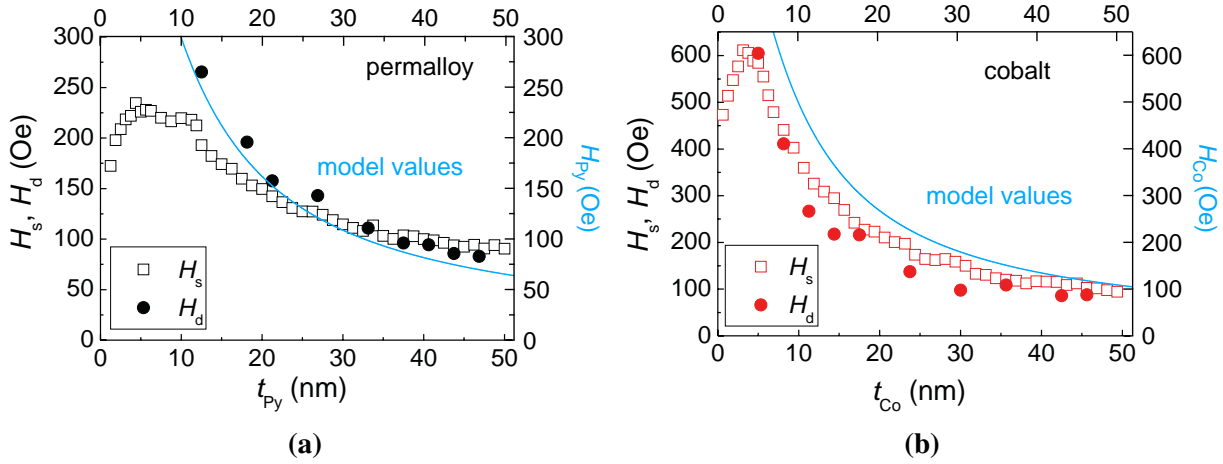


Figure 6.10: Dependence of the anisotropy field on Py and Co thickness on a $\lambda = 25$ nm ripple substrate obtained by: measurement [566] (open symbols), Schlömann's model [566, 568] (solid symbols), and the model that is presented here (solid lines, uniform configuration). In the application of Schlömann's model, thickness-dependent values for the roughness and literature values for the saturation magnetization were used by Liedke *et al.* [566]. For our model, a ripple amplitude of $(2\pi\hbar) = 0.41$ (obtained from ω_{rms}) was assumed. A saturation magnetization of $M_s = 1300 \text{ kA m}^{-1}$ for cobalt and of $M_s = 775 \text{ kA m}^{-1}$ for permalloy was chosen, as measured by Liedke *et al.* [566] for the $\lambda = 25$ nm samples. The energy of the uniform configuration f_{uniform} is calculated using these values and (6.48) on p. 124 (the difference to Schlömann's formula is the exponential term). The energy is converted to the anisotropy field H by (6.54). Although only the first order approximation is used, the error that is made by omitting higher orders is still below 20 % in this case. The model provides a good description for the measured data for thicknesses above 10 nm. The modeled curves slightly deviate from the ones that were modeled by Liedke *et al.* [566] due to the difference in the model as well as in the M_s and ω_{rms} values (the exact values that have been used are not printed in Ref. [566]). Below 10 nm a leveling of the anisotropy is observed. This can be attributed to the influence of a surface anisotropy that is directed perpendicular to the ripple direction and to a beginning tilting of the uniform magnetization towards the wavy configuration. Details about this issue are discussed in the main text. The anisotropy field of the wavy configuration (obtained from f_{ex} in (6.47) on p. 124) is $H_{\text{Py}} = 1779$ Oe and $H_{\text{Co}} = 2272$ Oe respectively (independent of thickness). It is way above the range of the graph and therefore not shown.

Overall, a slight tilting of the magnetization away from the uniform configuration could possibly explain a part of the leveling of the data observed in Fig. 6.10 for low permalloy thickness. The tilting can however not explain a reduction of the anisotropy field with decreasing thickness. While the exchange energy is independent of thickness, the stray field energy will always increase when the thickness is decreased.

The reduction in anisotropy field needs to be explained by factors that lie beyond the scope of this model. Liedke *et al.* [566] claim, that the influence of a surface anisotropy, which “is aligned perpendicular to the ripple crests” [566] causes an in-plane spin-reorientation transition (SRT). They explain the SRT with “the ripple dislocations in combination with thin films giving rise to a broken symmetry” [566]. A non-continuous film growth leading to a re-orientation of the easy axis could explain the measured data.

6.6 Summary

Within this chapter, the emergence of a uniaxial anisotropy in a wavy magnetic film of sinusoidal shape is reviewed. A model is developed that can be used to calculate the energy of two prototype micromagnetic states: the uniform and the wavy configuration. The energy of the uniform state is given by the stray field energy caused by magnetic charges on the interfaces of the magnetic film. The energy of the wavy configuration is governed by the exchange energy with a correction due to magnetic volume charges. The contribution of volume charges is small and mostly negligible in systems on the nanoscale. It will however be of importance in systems where the length scales are considerably larger than the exchange length l_{ex} .

The distribution of surface and volume magnetic charges is calculated. While the distribution of magnetic surface charges varies with the same frequency as the modulation, the distribution of volume charges varies with double the frequency. In the limit where the height of the modulation h is small compared to its wavelength λ , the stray field energy of the two cases is calculated by a Fourier expansion of the magnetic flux. The resulting energy terms are found to be proportional to powers of $(h/\lambda)^n$, with $n = \{2, 6, 10, \dots\}$ for surface charges generated in the uniform configuration and $n = \{4, 8, 12, \dots\}$ for volume charges generated in the wavy configuration. The volume-charge energy is found to be mostly independent of film thickness t , whereas the energy that stems from surface charges is proportional to $1/t$. In ultrathin films, the stray field energy in the uniform case saturates at a finite value; while it approaches zero in the wavy case.

The exchange energy of the wavy configuration is derived without any limitations on the shape of the wave. The local exchange energy varies in strength throughout the magnetic film. It is strongest in the regions around the curves of the wave pattern. The average exchange density of the system is proportional to $(h/\lambda)^2$ times $(1/\lambda)^2$. In contrast to the stray field energy contributions, which only depend on the relative scaling, the exchange energy thus depends on the absolute scale of the system (λ).

Driven by the change in the relative strength of exchange and stray field energy, a thickness-dependent transition can be identified between the wavy and the uniform configuration. Except for small wavelengths ($\lambda < 2\pi l_{\text{ex}}$), the wavy configuration is preferred in thin films below a critical thickness t_{crit} . The critical thickness is proportional to the square ratio $(\lambda/l_{\text{ex}})^2$ of

wavelength and exchange length. The transition between the two regimes can also be driven by a variation in λ , which is however harder to establish experimentally.

The theory was compared to two experimental systems that are well below the critical thickness and hence in the wavy configuration: permalloy on polished diamond [92] and cobalt on magnesium oxide [564]. In both cases the surface of the substrate exhibits a wave-like structure with wavelengths in the range of 100 nm. The exchange energy of the wavy configuration was found to reproduce the uniaxial anisotropies that are found in experiment very well.

An experimental template that provides a wide range of modulation wavelengths ($\lambda = 25 - 100$ nm) is sputtered silicon [554]. The dependence of the uniaxial anisotropy on λ and t was investigated for cobalt, iron, and permalloy thin films and reported in a recent paper [566]. The parameter ranges in both cases included the regime where a transition from the one to the other configuration would be expected. In the variation of λ , the stray field energy of the uniform configuration fits the measured data very well. A sharp transition to the wavy configuration, which might be expected at the upper end of the measured λ range, could however not be observed.

The change in anisotropy through the variation of t is also well reproduced by the stray field energy of the uniform configuration above the critical thickness. In the regime close to the critical thickness, additional effects are superimposed to the measured anisotropy [566]. These effects cannot ultimately be separated from the effects that occur due to the beginning transition to an exchange-dominated picture. Measuring the thickness dependence on a template with a larger wavelength and hence shifting the critical thickness to a higher value would allow to gain a deeper insight into the nature of physics in this system.

The experimental and theoretical results show that a detailed control of the direction and magnitude of a uniaxial anisotropy is possible by tailoring the parameters of a wavy magnetic film. Materials with fine-tuned anisotropies have their application for instance in magnetic field sensors [565]. Well-defined regions that are sensitive to different field directions can be defined on one and the same template by patterning the magnetic film in the respective regions accordingly [563]. These sensors can be applied in the fabrication of low-cost navigation systems [588].

A patterning of the magnetic film can also be useful in storage applications that are based on in-plane systems to enhance the intrinsically small anisotropy fields [562]. The texturing of a surface was found to improve not only the thermal stability but also the signal-to-noise ratio of magnetic recording media [589].

7 Appendix

7.1 Evaluation Tools for SEMPA Data

A precise evaluation of the vortex core position under the influence of current is required for the determination of the spin-transfer torque parameters. The tools that have been used to achieve quantitative data for the vortex displacement from a SEMPA image are described in the following sections.

7.1.1 Determination of the Vortex Core Position from SEMPA Data

The determination of the vortex core position from an image is most conveniently done by identifying the point where the z -component of the magnetization vector reaches its maximum [282]. The lateral size of this region is ~ 10 nm [79] for thin iron films (8 - 10 monolayers) and depends on the ratio of exchange stiffness A and the squared saturation magnetization M_s^2 [286, 287]. With the SEMPA setup that has been used throughout this thesis, both in-plane components of the magnetization are accessible, whereas the out-of-plane component cannot be visualized (see chapter 2.2). Thereby an alternate approach has to be used for the determination of the vortex core position.

A micromagnetic simulation of the magnetic Landau state is shown in Fig. 3.3 on page 43. The four domains are clearly visible in the in-plane images. Also visible are four domain walls of Néel type running from the four edges of the structure to the core in the center. It is these four walls that give us the best idea of the core position when looking at in-plane images.

One way of determining the core position from this data is by taking the measurement of the y component of the magnetization (Fig. 3.3c) to identify the x position of the vortex core and vice versa. This is done by identifying the point where the vertical domains are separated from one another. The point can most conveniently be found by taking line profiles perpendicular to the line of separation. Some line profiles that have been taken across a simulated Landau state are shown in Fig. 7.1. In the vicinity of the vortex core their shape can be described by a hyperbolic tangent. This description is still valid for line profiles taken as far as 150 nm away from the central core. It is therefore possible to determine the core position from lines all across this area, at least from undisturbed images. It can further be concluded that an integration over multiple line profiles (or a line profile with a finite width) does not have an influence on the vortex core position that is obtained, as long as all contributing line profiles are in close vicinity of the vortex core.

For measured images, which show an observable amount of noise, an integrative and iterative approach is chosen (see Fig. 7.2 for one iteration of the process): First, an initial guess of the core position is made by looking at the images with the naked eye. The iteration then starts with the selection of a rectangular region of interest (ROI) for the image of m_y , with the core

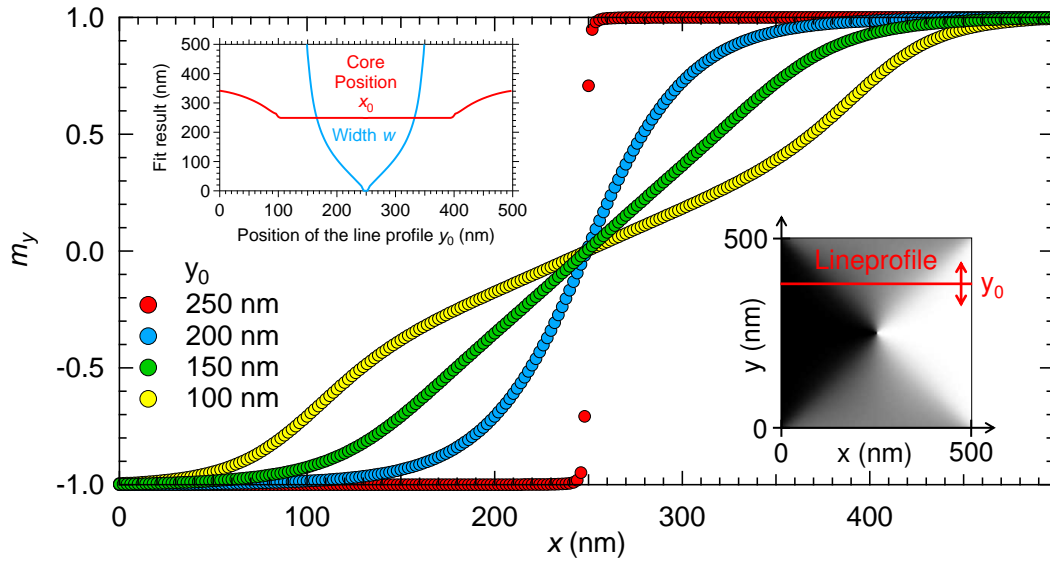


Figure 7.1: Line profiles drawn at different positions y_0 of a simulation of the magnetization's y -component m_y (inset at the bottom right). In this picture of the undisturbed state, the vortex core is located in the center at $x_0 = y_0 = 250$ nm. For small deviations from the middle of the structure, a hyperbolic tangent describes the shape of the profile very well (red, blue and green points). Further away from the central core region, the features of the two 90° domain walls become visible (yellow points). The parameters of a hyperbolic tangent (\tanh) that was fitted to the data are shown in the inset at the top left. While the width increases when the profile is taken further away from the center, the position can still be determined with great accuracy. It is just close to the corner of the image, where the details of the two domain walls start to develop (see yellow curve), that the procedure fails. At this point the position of one of the two domain walls is fitted instead of the core position. As a result one can however say that the summation of line profiles taken in close vicinity of the vortex core does not alter the resulting core position.

position lying directly in the middle of the ROI. Afterward, the data within the ROI is projected onto the x axis to reduce the noise and the central point is identified by fitting a hyperbolic tangent of the following shape:

$$A(x) = A_0 \cdot \tanh\left(\frac{x - x_0}{w}\right) + A_{\text{off}} + a \cdot x \quad (7.1)$$

Hereby A_0 is the amplitude in asymmetry in the center of the image, x_0 is the x position of the vortex core, w is the width of the steep transition region, A_{off} is the experimental offset in asymmetry, and a accounts for a linear background (caused by the contribution of the off-centered line profiles, for instance the green curve in Fig. 7.1).

The point x_0 now replaces the initially guessed x coordinate of the core position. The process is then executed similarly for the image of m_x . This time the data within the ROI is projected onto the y axis, which allows for a determination of the y coordinate of the core position. The

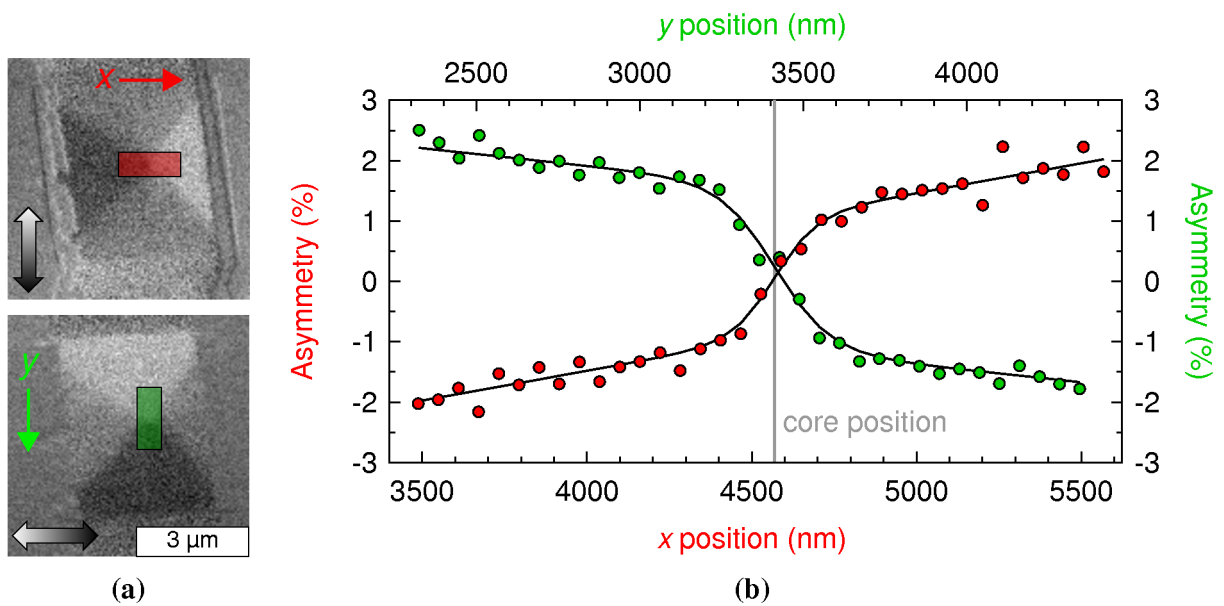


Figure 7.2: Determination of the vortex core position from the SEMPA images that are shown in Fig. 3.11 on page 53. (a) Raw asymmetry images with no corrections applied to the data. The origin of the coordinate system lies in the top left corner of the images. The x position of the vortex core is determined from the upper image, which shows the y component of the magnetization. To this end a line profile is drawn along the x direction in the red shaded area. The red box is centered around the vortex position that was found in the previous iteration (or initially guessed). The width of the lineprofile is 800 nm (13 pixel), its length spans 2000 nm (33 pixel). (b) The line profile is fit by the function (7.1) that yields one component of the core position, which then replaces the value from the previous iteration. Subsequently the whole process is repeated for the x component of the magnetization (shown in green) to determine a new value for the y position of the vortex core. The two line profiles do not intersect at the core position due to a small experimental asymmetry A_{off} (discussed in chapter 2.2.2 on page 21).

newly obtained position of the vortex core is then fed into the next iteration as a starting parameter. Usually the whole process converges after less than ten iterations. The last iteration of the evaluation of the core position is shown in Fig. 7.2 for the measurement presented in Fig. 3.11 on p. 53.

Obtaining Both Components of the Vortex Core Position from a Single Image

When only one component of the magnetization is available, a different approach has to be chosen to determine the position of the vortex core. While one component of the position can still be obtained by the approach that was previously discussed (without the iterative part), the second one is completely inaccessible. One rather subjective approach is trying to determine the core position with the naked eye. As this is principally possible and may yield reasonable results, a slightly different method is chosen here.

The method is exemplary shown at hand of an image with very low statistics in Fig. 7.3. When a substantial amount of noise is visible, the image is first smoothed by using a Gaussian

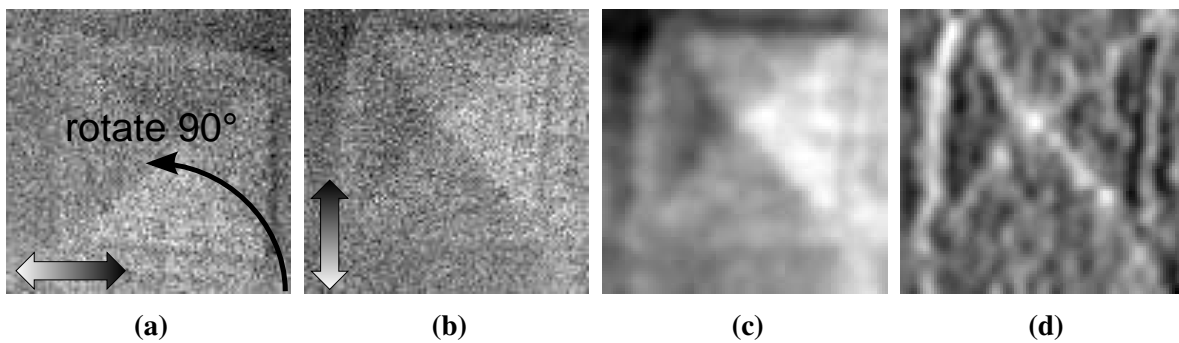


Figure 7.3: Determination of the vortex core position from one single SEMPA image. (a) The image of Fig. 4.6a showing a $5\ \mu\text{m}$ sized square structure. Only one component of the magnetization vector was obtained. First (a) was rotated counterclockwise by 90° (b). Because of a relatively low integration time for this single frame of the video, the statistical noise of the image is rather high. (c) The image was passed through a Gaussian filter (five passes averaging over 5 pixels) to reduce the statistical noise. (d) Finally, the derivation of the image along the horizontal axis is calculated from the left to the right. The vortex core is now visible as a bright spot in the center. Additionally the four domain walls and the edges of the structure appear as bright or dark lines.

filter. Afterward, the derivation of the image along the axis that runs perpendicular to the magnetic contrast is calculated. The edges of the structure as well as the domain walls become visible as bright/dark lines in the derivative image. In the middle of the structure, where all domain walls meet, the vortex core appears as a bright spot. The spot is not to be confused with the out of plane component of the magnetization in the center of the vortex core. It moreover shows the strong gradient of the magnetization that is present in the central core region.

The position of the vortex core is now determined from the derivative image. One possibility is to take the apex of the central peak as the vortex core position. The peak can also be described by a two-dimensional Gaussian function. The area of the fit has however to be carefully constrained as the signal of the domain walls considerably alters the background.

This method allows for a demonstrative visual representation of the core position. It is thus also used when both in-plane components of the magnetization are available, for instance for a clearer visualization of the core motion in a video file. The contrast can then further be enhanced by adding up the absolute (or squared) values of the derived images of both components in one single image.

7.1.2 Determination of Position and Orientation of the Magnetic Structure

The sole knowledge of the position of the vortex core is not sufficient to calculate its displacement from equilibrium. Sequences of images have lateral offsets from one another and may also be skewed or elongated in one direction. It is thus of equal importance to determine the position and the orientation of the magnetic square element that confines the vortex core with the same precision as the core position.

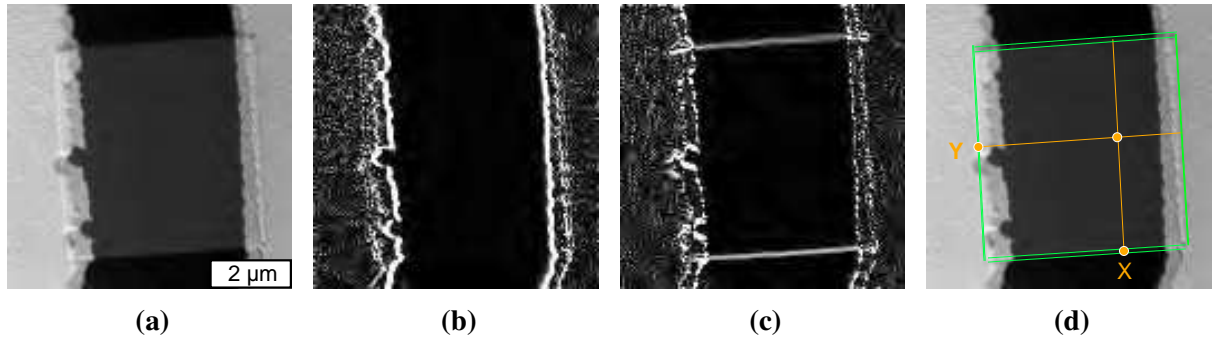


Figure 7.4: Example of the positional determination for the edges of a structure. (a) SEM image of a permalloy square with an applied DC current density of $j = 2.4 \times 10^{11} \text{ A m}^{-2}$. The structure had to be contacted twice to achieve electrical contact. As a result of this three vertical lines are visible at either side of the structure. The absolute value of the data differentiated by rows and columns is shown in (b) and (c) respectively. After differentiation the vertical (b) and horizontal (c) edges are clearly visible. A train of Gaussian functions aligned along a variable line (7.2) is then fitted to a region of interest around each of the four edges. In (d) green contour lines identify the points where the Gaussian functions reach half of their maximum value. The distance between two neighbouring lines equals the full width at half maximum (FWHM) of the Gaussian functions. The position of the vortex core (orange spot) was determined from magnetic images. It is now correlated with the structural position to calculate the relative displacement of the vortex core in x - and y -direction. This is done by calculating lines that run through the vortex core and are parallel to the horizontal or vertical edges. Their intersection with the edges is then taken as the x and y coordinate of the vortex core position.

An exemplary demonstration of the edge determination is shown in Fig. 7.4. The SEM image of the structure is differentiated along its rows and columns. Since there is always a change in contrast at the edge, the mostly vertical or mostly horizontal lines become clearly visible after differentiation in rows and columns respectively. They can then be fitted by a two-dimensional train of Gaussian functions that are aligned along a straight line. For instance a horizontal line can be described by $y = y_0 + mx$ which leads to the fit function:

$$f(x,y) = A \cdot \exp\left(\frac{-(y - y_0 - mx)^2}{w^2}\right) + f_0 \quad (7.2)$$

The shape of the function can be brought to mind by considering the following argument: When the two-dimensional function is cut along the yz -plane it looks like a Gaussian function, when it is cut along the xz -plane it looks like a linear function. Free parameters for the fit are:

- A the amplitude of the Gaussian functions;
- w their width, which is related to the steepness of the underlying edge;
- f_0 a possible offset that emerges in the differential image when an image is not evenly illuminated.

With the four linear equations for the edges, it is now possible to calculate the core position in the coordinate system of the square element as shown in Fig. 7.4d. This coordinate system may be translated, stretched or skewed with respect to the coordinate system of the original image. These are effects of a thermal drift that occurs during the imaging process [590], which usually takes several minutes. By calculating the displacement relatively, all influences by drift that are constant in time are eliminated. When the relative coordinates of the core with respect to the square element are known they are multiplied by the true lateral dimensions of the square. The lateral dimensions are determined from an SEM image with an integration time of only a few seconds, so that they cannot be impaired by thermal drift.

7.2 Correction of Current Density for Parasitic Shunt Resistances

In most experiments parasitic shunt resistances are neglected, since their resistance lies well above the resistance of the sample. However when shunt and sample resistances are of the same order of magnitude, they need to be taken into account. The required argon milling of the specimen prior to SEMPA investigations causes a transformation of the diamond surface to amorphous carbon [591]. This leads to a parasitic shunt resistance (in the “insulating” channel) which is of the same order of magnitude as the resistance of the sample [192]. For the sample of permalloy on diamond that is discussed in chapter 3.5, an additional shunt resistance had to be taken into account. It is caused by a thin iron film which was evaporated in a previous investigation. In the previous investigation a sample holder was used that did not protect the electric contacts inside the chamber from being metallized.

Since shunt and sample resistances appear in series to one another it is convenient to introduce the electrical conductance $G = R^{-1}$ to simplify the calculations. The measured conductance and the different contributions contained in the theoretical model are shown in the upper left corner of Fig. 7.5. The model contains a permalloy structure that is contacted by gold leads on either side. Additionally, two shunt conductance channels are considered. The one caused by the thin iron film and the one caused by graphitization of the diamond surface in the channel between the two pads.

The conductance G_{PyAu} of the fresh grown sample mounted and contacted to the sample holder was measured before its introduction into the chamber $G_{\text{PyAu}} = \frac{1}{358.9\Omega} = 2.786 \text{ mS}$. After transfer of the sample into the chamber the conductance increased by the initial conductance of the iron film $G_{\text{Fe,i}}$ to $G_{\text{PyAu+Fe}} = 5.687 \text{ mS}$. By comparing this value to the conductance of the sample at air, the initial conductance of the iron film $G_{\text{Fe,i}}$ can be determined:

$$G_{\text{Fe,i}} = G_{\text{PyAu}} - G_{\text{PyAu+Fe}} = 2.901 \text{ mS} \quad (7.3)$$

During the first ion milling process (see Fig. 7.5) an additional conduction channel via the transformation of the diamond surface is created and the conductance increases. After a protective surface layer is formed, the process saturates at a permalloy thickness of $t_{\text{Py}} = 10.6 \text{ nm}$. Extrapolation of the saturated values allows for a determination of the shunt conductance that is caused by the amorphous carbon layer $G_{\text{C}} = 1.164 \text{ mS}$.

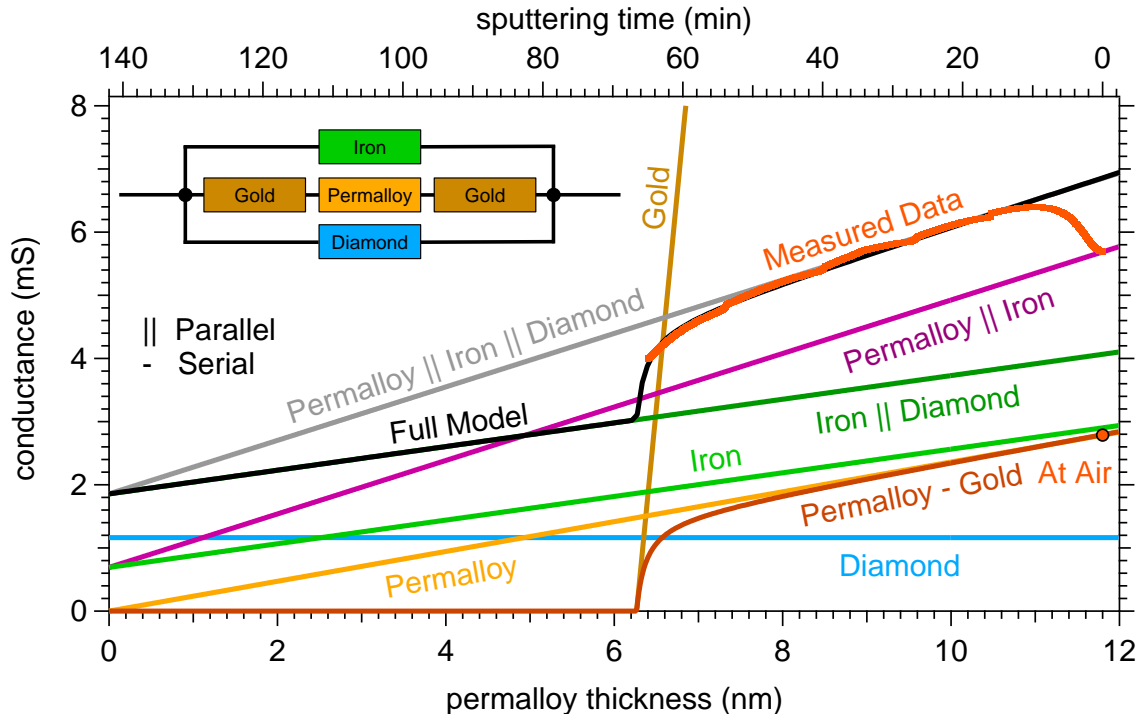


Figure 7.5: Contributions to the conductance of the permalloy sample contacted with gold leads prepared on a diamond substrate including a parasitic shunt resistance due to a thin iron film (see main text). Before ion milling ($t_{Py} = 11.8$ nm) the conductance is composed of the conductance of the sample and the iron shunt. During the first milling process the conductance is increased due to graphitisation of the diamond surface [591]. When an amorphous carbon layer is formed on top of the diamond, the surface is protected and its contribution to the conductance stays constant below $t_{Py} \approx 10.6$ nm. From then on the conductance decreases linearly. The linear contribution is caused by the removal of the permalloy square and its gold contacts and a simultaneous removal of the iron film. Since the sputtering yield of gold is more than double the sputtering yield of permalloy the gold contacts are removed preferentially. This leads to a rapid decrease in the sample conductance below $t_{Py} = 7$ nm. Although the sample was not sputtered that far, the measured data suggests that the gold contacts would have failed at a permalloy thickness of $t_{Py} = 6.27$ nm.

Further ion milling decreases the conductance of the sample and the iron shunt linearly. Initially the conductance of the gold leads is more than one order of magnitude higher than the conductance of the permalloy structure. Therefore the conductance of the sample is dominated by the conductance of the permalloy square. The decrease of sample conductance with permalloy thickness is assumed to be linear. Since the conductances for $t_{\text{Py}} = 11.8 \text{ nm}$ and $t_{\text{Py}} = 0 \text{ nm}$ are known, the contribution of the sample to the gradient can be separated:

$$\frac{\partial G_{\text{Py}}(t_{\text{Py}})}{\partial t_{\text{Py}}} = \frac{G_{\text{Py}}(11.8 \text{ nm}) - G_{\text{Py}}(0 \text{ nm})}{11.8 \text{ nm}} = 0.236 \text{ mS nm}^{-1} \quad (7.4)$$

Comparing this to the measured data yields:

$$\frac{\partial G_{\text{Fe}}}{\partial t_{\text{Py}}} = \frac{\partial G_{\text{Measured}}}{\partial t_{\text{Py}}} - \frac{\partial G_{\text{Py}}}{\partial t_{\text{Py}}} = 0.187 \text{ mS nm}^{-1} \quad (7.5)$$

Below a permalloy thickness of $t_{\text{Py}} = 7 \text{ nm}$ the conductance starts to decrease more rapidly. This can be understood by an approaching failure of the gold leads. The gold leads had to be evaporated twice to achieve contact to the square structure. While this leads to a large region where the gold thickness was double the usual thickness ($t_{\text{Au}} = 15 \text{ nm}$), also a small overlap region with the usual thickness was generated (see Fig. 7.4a). The measured data can be fitted by allowing for a faster removal of gold by a factor of 2.3. By comparing the sputtering yields for 1 keV Ar^+ Ions [592–594] of Iron ($\gamma = 1.77$), Nickel ($\gamma = 1.96$) and Gold ($\gamma = 3.03$), taking into account the atomic densities, a factor of 2.4 is expected. This confirms the theory that the decrease in conductance is caused by an approaching failure of the gold leads.

The development of current density in dependence of the permalloy thickness is shown in Fig. 7.6. The importance of taking shunt resistances into account for the calculation of the experimental driving current is obvious in this example. The percentage of current flowing through the sample j_{Py}/j_0 lay below 40% at all times. Subsequent ion milling between the three measurement series further decreased the percentage of current flowing through the permalloy structure. The resulting current density ratios for the three measurement series are:

$$\begin{aligned} \frac{j_{\text{Py}}}{j_0}(t_{\text{Py}} = 9.6 \text{ nm}) &= 38.0 \% \pm 0.8 \% \\ \frac{j_{\text{Py}}}{j_0}(t_{\text{Py}} = 8.5 \text{ nm}) &= 36.2 \% \pm 0.8 \% \\ \frac{j_{\text{Py}}}{j_0}(t_{\text{Py}} = 7.3 \text{ nm}) &= 33.2 \% \pm 0.7 \% \end{aligned}$$

7.3 Raw Data of SEMPA Images

This section contains the raw data for the SEMPA images of chapter 5.

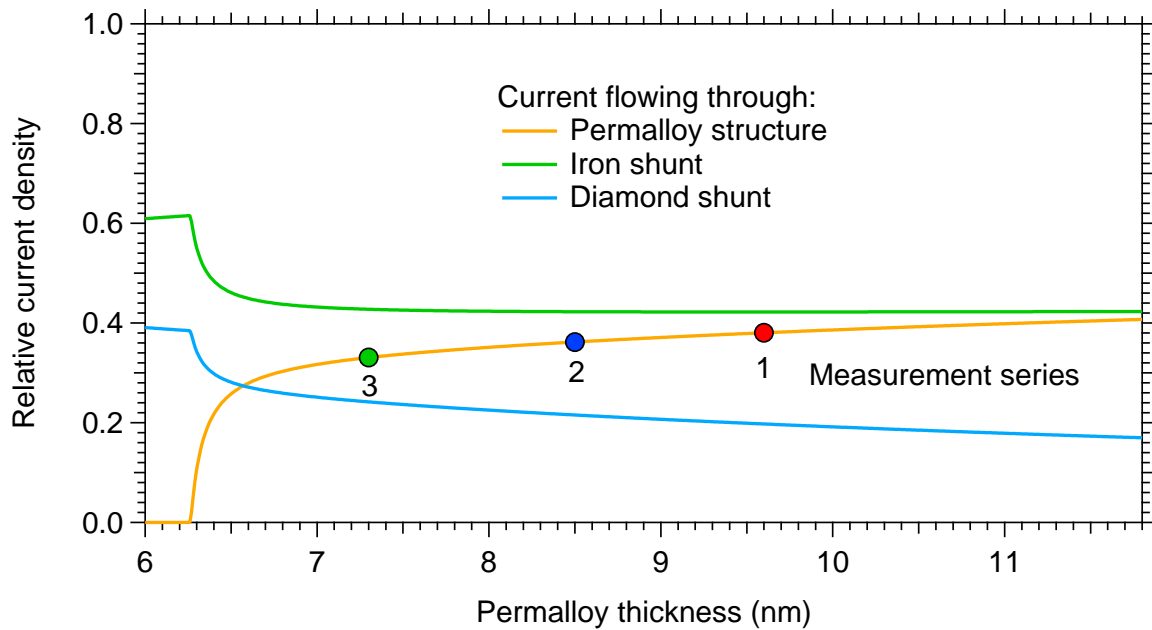


Figure 7.6: Distribution of the current density on the different conductance channels including changes in conductance due to ion milling of the sample. The carbon shunt is assumed to be constant, since its formation was finished well before the first measurement series. During ion milling the conductance of the sample decreases faster than the conductance of the iron shunt. Therefore the relative current density flowing through the permalloy structure decreases with thickness whereas the current flowing through the iron shunt stays almost constant.

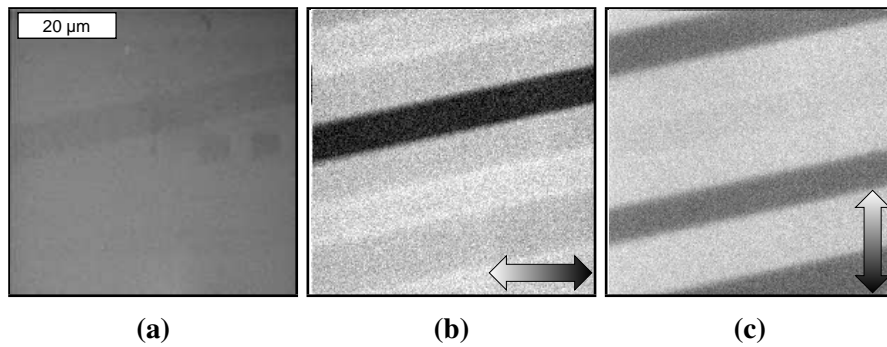


Figure 7.7: Raw data of Fig. 5.2 on p. 96. The sum image is shown in (a). The images of the x and y component of the magnetization are shown in (b) and (c) respectively.

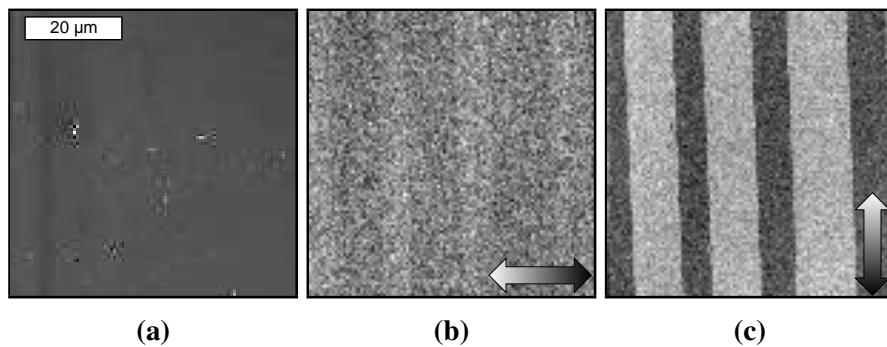


Figure 7.8: Raw data of Fig. 5.5 on p. 101. The sum image is shown in (a). The images of the x and y component of the magnetization are shown in (b) and (c) respectively.

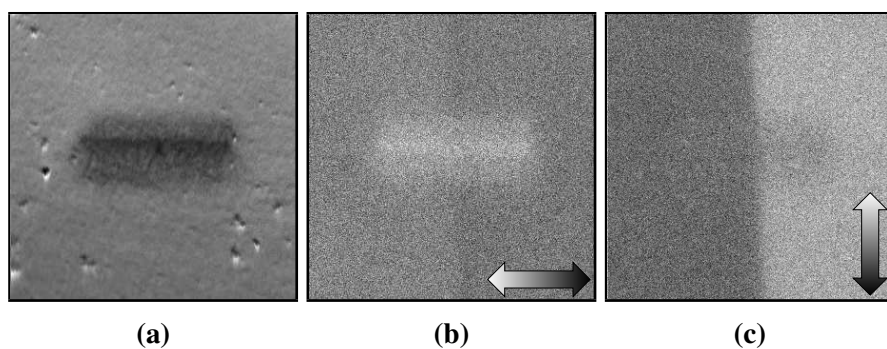


Figure 7.9: Raw data of Fig. 5.6 on p. 103. The sum image is shown in (a). The images of the x and y component of the magnetization are shown in (b) and (c) respectively.

References

- [1] W. Melody, R. Mansell, and B. Richards, *Information and Communication Technologies: An over-view of research* (Economic and Social Research Council, 1986).
- [2] S. Crawford, *Bull Med Libr Assoc.* **71**, 380 (1983).
- [3] T. M. Cover and J. A. Thomas, *Elements of Information Theory* (John Wiley & Sons, Inc., 2005).
- [4] C. E. Shannon, *Bell Syst. Tech. J.* **27**, 379 (1948).
- [5] M. Hilbert and P. López, *Science* **332**, 60 (2011).
- [6] G. Moore, *Proc. IEEE* **86**, 82 (1998).
- [7] N. Cowan, in *Essence of Memory*, Vol. 169, edited by W. S. Sossin, J.-C. Lacaille, V. F. Castellucci, and S. Belleville (Elsevier, 2008) pp. 323–338.
- [8] S. Lubar, *J. Am. Cult.* **15**, 43 (1992).
- [9] A. Tanenbaum, *Computer Networks* (Prentice Hall PTR, 2003).
- [10] P. Vettiger, G. Cross, M. Despont, U. Drechsler, U. Durig, B. Gotsmann, W. Haberle, M. Lantz, H. Rothuizen, R. Stutz, and G. Binnig, *IEEE Trans. Nanotechnol.* **1**, 39 (2002).
- [11] E. Eleftheriou, T. Antonakopoulos, G. Binnig, G. Cherubini, M. Despont, A. Dholakia, U. Durig, M. Lantz, H. Pozidis, H. Rothuizen, and P. Vettiger, *IEEE Trans. Magn.* **39**, 938 (2003).
- [12] *Fifty years of storage innovation - Magnetic tape and beyond*, IBM Archives (2014).
- [13] *650 RAMAC announcement*, IBM Archives (2014).
- [14] *VelociRaptor WD1000DHTZ*, Western Digital Corporation (2014).
- [15] W. Brinkman, D. Haggan, and W. Troutman, *IEEE J. Solid-State Circuits* **32**, 1858 (1997).
- [16] A. Saxena, in *Technical Proceedings of the 2007 Nanotechnology Conference and Trade Show*, Vol. 3 (2007) pp. 460–474.
- [17] J. W. Forrester, *J. Appl. Phys.* **22**, 44 (1951).
- [18] C. Chappert, A. Fert, and F. N. Van Dau, *Nat. Mater.* **6**, 813 (2007).

- [19] J. Mathon and A. Umerski, *Phys. Rev. B* **63**, 220403 (2001).
- [20] J. S. Moodera, L. R. Kinder, T. M. Wong, and R. Meservey, *Phys. Rev. Lett.* **74**, 3273 (1995).
- [21] T. Miyazaki and N. Tezuka, *J. Magn. Magn. Mater.* **139**, L231 (1995).
- [22] S. Narasimha *et al.*, in *2012 IEEE International Electron Devices Meeting (IEDM)* (2012) pp. 3.3.1–3.3.4.
- [23] *Spansion Announces Industry's First 8Gb NOR Flash Memory at 45nm*, Spansion Inc. (2012).
- [24] S. A. Wolf, J. Lu, M. Stan, E. Chen, and D. Treger, *Proc. IEEE* **98**, 2155 (2010).
- [25] H. McAdams, R. Acklin, T. Blake, J. Fong, D. Liu, S. Madan, T. Moise, S. Natarajan, N. Qian, Y. Qui, J. Roscher, A. Seshadri, S. Summerfelt, X. Du, J. Eliason, W. Kraus, R. Lanham, F. Li, C. Pietrzyk, and J. Rickes, in *2003 Symposium on VLSI Circuits* (2003) pp. 175–176.
- [26] C. Lin, S. Kang, Y. Wang, K. Lee, X. Zhu, W. Chen, X. Li, W. Hsu, Y. C. Kao, M. T. Liu, W. Chen, Y. Lin, M. Nowak, N. Yu, and L. Tran, in *2009 IEEE International Electron Devices Meeting (IEDM)* (2009) pp. 1–4.
- [27] K. L. Wang, J. G. Alzate, and P. K. Amiri, *J. Phys. D: Appl. Phys.* **46**, 074003 (2013).
- [28] A. Hirohata and K. Takanashi, *J. Phys. D: Appl. Phys.* **47**, 193001 (2014).
- [29] B. Krzanich, in *Intel Developer Forum IDF13* (2013) - The presentation of the first 14 nm device starts at video minute 10:15.
- [30] R. Dennard, “Us patent no. 3,387,286,” (1968).
- [31] P. K. Chatterjee, G. Taylor, R. Easley, H.-S. Fu, and J. Tasch, AF., *IEEE Trans. Electron Devices* **26**, 827 (1979).
- [32] M. L. Roukes, M. R. Freeman, R. S. Germain, R. C. Richardson, and M. B. Ketchen, *Phys. Rev. Lett.* **55**, 422 (1985).
- [33] F. C. Wellstood, C. Urbina, and J. Clarke, *Phys. Rev. B* **49**, 5942 (1994).
- [34] M. Lenzlinger and E. H. Snow, *J. Appl. Phys.* **40**, 278 (1969).
- [35] F. Masuoka, M. Momodomi, Y. Iwata, and R. Shirota, in *1987 International Electron Devices Meeting (IEDM)*, Vol. 33 (1987) pp. 552–555.
- [36] S. M. Thatte, in *Proceedings on the 1986 international workshop on Object-oriented database systems* (IEEE Computer Society Press, Pacific Grove, California, USA, 1986) pp. 148–159.

- [37] T. McGuire and R. Potter, *IEEE Trans. Magn.* **11**, 1018 (1975).
- [38] A. Pohm, J. S. T. Huang, J. Daughton, D. Krahn, and V. Mehra, *IEEE Trans. Magn.* **24**, 3117 (1988).
- [39] W. J. Gallagher, S. S. P. Parkin, Y. Lu, X. P. Bian, A. Marley, K. P. Roche, R. A. Altman, S. A. Rishton, C. Jahnes, T. M. Shaw, and G. Xiao, *J. Appl. Phys.* **81**, 3741 (1997).
- [40] S. Tehrani, J. Slaughter, E. Chen, M. Durlam, J. Shi, and M. DeHerren, *IEEE Trans. Magn.* **35**, 2814 (1999).
- [41] B. N. Engel, J. Akerman, B. Butcher, R. Dave, M. DeHerrera, M. Durlam, G. Grynkewich, J. Janesky, S. Pietambaram, N. Rizzo, J. Slaughter, K. Smith, J. J. Sun, and S. Tehrani, *IEEE Trans. Magn.* **41**, 132 (2005).
- [42] M. Julliere, *Phys. Lett. A* **54**, 225 (1975).
- [43] S. Yuasa, T. Nagahama, A. Fukushima, Y. Suzuki, and K. Ando, *Nat. Mater.* **3**, 868 (2004).
- [44] S. S. P. Parkin, C. Kaiser, A. Panchula, P. M. Rice, B. Hughes, M. Samant, and S.-H. Yang, *Nat. Mater.* **3**, 862 (2004).
- [45] W. H. Butler and A. Gupta, *Nat. Mater.* **3**, 845 (2004).
- [46] R. Leuschner, U. Klostermann, H. Park, F. Dahmani, R. Dittrich, C. Grigis, K. Hernan, S. Mege, C. Park, M. C. Clech, G. Y. Lee, S. Bournat, L. Altimime, and G. Mueller, in *2006 International Electron Devices Meeting (IEDM)* (2006) pp. 1–4.
- [47] I. L. Prejbeanu, M. Kerekes, R. C. Sousa, H. Sibuet, O. Redon, B. Dieny, and J. P. Nozières, *J. Phys.: Condens. Matter* **19**, 165218 (2007).
- [48] J.-H. Song, J. Kim, S. H. Kang, S.-S. Yoon, and S.-O. Jung, *Int. J. Circ. Theor. Appl.* **39**, 313 (2011).
- [49] S. Ikeda, K. Miura, H. Yamamoto, K. Mizunuma, H. D. Gan, M. Endo, S. Kanai, J. Hayakawa, F. Matsukura, and H. Ohno, *Nat. Mater.* **9**, 721 (2010).
- [50] A. Brataas, A. D. Kent, and H. Ohno, *Nat. Mater.* **11**, 372 (2012).
- [51] RUSNANO, *RUSNANO Portfolio Company Crocus Nano Electronics Launches First Production Line* (2013).
- [52] L. Berger, *Phys. Rev. B* **54**, 9353 (1996).
- [53] J. C. Slonczewski, *J. Magn. Magn. Mater.* **159**, L1 (1996).
- [54] Y. Huai, F. Albert, P. Nguyen, M. Pakala, and T. Valet, *Appl. Phys. Lett.* **84**, 3118 (2004).

- [55] Z. Diao, D. Apalkov, M. Pakala, Y. Ding, A. Panchula, and Y. Huai, *Appl. Phys. Lett.* **87**, (2005).
- [56] A. V. Khvalkovskiy, D. Apalkov, S. Watts, R. Chepulskii, R. S. Beach, A. Ong, X. Tang, A. Driskill-Smith, W. H. Butler, P. B. Visscher, D. Lottis, E. Chen, V. Nikitin, and M. Krounbi, *J. Phys. D: Appl. Phys.* **46**, 074001 (2013).
- [57] E. B. Myers, D. Ralph, J. Katine, R. Louie, and R. Buhrman, *Science* **285**, 867 (1999).
- [58] M. Hosomi, H. Yamagishi, T. Yamamoto, K. Bessho, Y. Higo, K. Yamane, H. Yamada, M. Shoji, H. Hachino, C. Fukumoto, H. Nagao, and H. Kano, in *2005 IEEE International Electron Devices Meeting (IEDM)* (2005) pp. 459–462.
- [59] K. C. Chun, H. Zhao, J. Harms, T.-H. Kim, J. ping Wang, and C. Kim, *IEEE J. Solid-State Circuits* **48**, 598 (2013).
- [60] J. Scott, *Ferroelectric Random Access Memories - Fundamentals and Applications*, edited by H. Ishiwara, M. Okuyama, and Y. Arimoto, Vol. 93 (Springer Berlin Heidelberg, 2004).
- [61] T. Davenport and S. Mitra, *Integr. Ferroelectr.* **31**, 213 (2000).
- [62] M. Wuttig and N. Yamada, *Nat. Mater.* **6**, 824 (2007).
- [63] I. Friedrich, V. Weidenhof, W. Njoroge, P. Franz, and M. Wuttig, *J. Appl. Phys.* **87**, 4130 (2000).
- [64] Y. Choi *et al.*, in *2012 IEEE International Solid-State Circuits Conference (ISSCC)* (2012) pp. 46–48.
- [65] X. Dong, X. Wu, G. Sun, Y. Xie, H. Li, and Y. Chen, in *45th ACM/IEEE Design Automation Conference (DAC)* (2008) pp. 554–559.
- [66] J. Akerman, *Science* **308**, 508 (2005).
- [67] S. S. P. Parkin, M. Hayashi, and L. Thomas, *Science* **320**, 190 (2008).
- [68] S. Parkin, *Meeting Abstracts MA2012-02*, 2813 (2012).
- [69] M. Hayashi, L. Thomas, R. Moriya, C. Rettner, and S. S. P. Parkin, *Science* **320**, 209 (2008).
- [70] A. J. Annunziata, M. Gaidis, L. Thomas, C. Chien, C.-C. Hung, P. Chevalier, E. O’Sullivan, J. Hummel, E. Joseph, Y. Zhu, T. Topuria, E. Delenia, P. Rice, S. Parkin, and W. Gallagher, in *2011 IEEE International Electron Devices Meeting (IEDM)* (2011) pp. 24.3.1–24.3.4.
- [71] L. Landau and E. Lifshitz, *Phys. Z. Sowjetunion* **8**, 153 (1935).
- [72] A. A. Thiele, *Phys. Rev. Lett.* **30**, 230 (1973).

-
- [73] S. Zhang and Z. Li, *Phys. Rev. Lett.* **93**, 127204 (2004).
- [74] A. Thiaville, Y. Nakatani, J. Miltat, and Y. Suzuki, *Europhys. Lett.* **69**, 990 (2005).
- [75] G. Tatara and P. Entel, *Phys. Rev. B* **78**, 064429 (2008).
- [76] K.-J. Lee, M. Stiles, H.-W. Lee, J.-H. Moon, K.-W. Kim, and S.-W. Lee, *Phys. Rep.* **531**, 89 (2013).
- [77] T. Gilbert, *IEEE Trans. Magn.* **40**, 3443 (2004).
- [78] G. Tatara, H. Kohno, and J. Shibata, *Phys. Rep.* **468**, 213 (2008).
- [79] A. Wachowiak, J. Wiebe, M. Bode, O. Pietzsch, M. Morgenstern, and R. Wiesendanger, *Science* **298**, 577 (2002).
- [80] S. Rößler, S. Hankemeier, B. Krüger, F. Balhorn, R. Frömter, and H. P. Oepen, *Phys. Rev. B* **89**, 174426 (2014).
- [81] K. Sekiguchi, K. Yamada, S.-M. Seo, K.-J. Lee, D. Chiba, K. Kobayashi, and T. Ono, *Phys. Rev. Lett.* **108**, 017203 (2012).
- [82] J.-Y. Chauleau, H. G. Bauer, H. S. Körner, J. Stigloher, M. Härtinger, G. Woltersdorf, and C. H. Back, *Phys. Rev. B* **89**, 020403 (2014).
- [83] H. Hopster and H. Oepen, eds., *Magnetic Microscopy of Nanostructures* (Springer Berlin Heidelberg, 2005).
- [84] R. Frömter, S. Hankemeier, H. P. Oepen, and J. Kirschner, *Rev. Sci. Instrum.* **82**, 033704 (2011).
- [85] B. Hillebrands and K. Ounadjela, eds., *Spin Dynamics in Confined Magnetic Structures*, Vol. 83 (Springer Berlin Heidelberg, 2002).
- [86] R. Frömter, S. Rössler, F. Klodt, D. R. Cavicchia, L. Bocklage, and H. P. Oepen, in *59th Annual Magnetism & Magnetic Materials Conference, Honolulu, Hawaii* (2014).
- [87] B. Krüger, A. Drews, M. Bolte, U. Merkt, D. Pfannkuche, and G. Meier, *Phys. Rev. B* **76**, 224426 (2007).
- [88] S. Pollard, L. Huang, K. Buchanan, D. Arena, and Y. Zhu, *Nat. Commun.* **3**, 1028 (2012).
- [89] K. J. A. Franke, T. H. E. Lahtinen, and S. van Dijken, *Phys. Rev. B* **85**, 094423 (2012).
- [90] T. H. E. Lahtinen, K. J. A. Franke, and S. van Dijken, *Sci. Rep.* **2**, (2012).
- [91] B. Van de Wiele, L. Laurson, K. J. A. Franke, and S. van Dijken, *Appl. Phys. Lett.* **104**, (2014).
- [92] S. Rößler, *Auswirkungen einer gewellten Substratoberfläche auf magnetische Filme und Strukturen*, Master's thesis, Universität Hamburg (2010).

- [93] C. P. Bean and J. D. Livingston, *J. Appl. Phys.* **30**, S120 (1959).
- [94] W. T. Coffey and Y. P. Kalmykov, *J. Appl. Phys.* **112**, (2012).
- [95] A. Neumann, *Magnetisierungsverhalten einzelner ferromagnetischer Nanostrukturen*, Ph.D. thesis, Universität Hamburg (2014).
- [96] E. O. Wilson, *Consilience - The Unity of Knowledge*, edited by E. O. Wilson (Random House Inc. New York, 1999).
- [97] L. v. Hámós and P. Thiessen, *Z. f. Physik* **71**, 442 (1931).
- [98] F. Bitter, *Phys. Rev.* **38**, 1903 (1931).
- [99] K. Hoselitz, *Rep. Prog. Phys.* **52**, 227 (1989).
- [100] H. J. Williams, R. M. Bozorth, and W. Shockley, *Phys. Rev.* **75**, 155 (1949).
- [101] P. Weiss, *J. Phys. Theor. Appl.* **6**, 661 (1907).
- [102] P. Weiss, *Le Magnetisme* (Librairie Armand Colin, 1926).
- [103] A. Hubert and R. Schäfer, *Magnetic Domains* (Springer, Berlin, 2009).
- [104] W. Szmaja, *J. Magn. Magn. Mater.* **234**, 13 (2001).
- [105] A. M. Kalashnikova, V. V. Pavlov, A. V. Kimel, A. Kirilyuk, T. Rasing, and R. V. Pisarev, *Low Temp. Phys.* **38**, 863 (2012).
- [106] P. Fischer, T. Eimüller, G. Schütz, P. Guttman, G. Schmahl, K. Pruegl, and G. Bayreuther, *J. Phys. D: Appl. Phys.* **31**, 649 (1998).
- [107] A. Kubetzka, M. Bode, O. Pietzsch, and R. Wiesendanger, *Phys. Rev. Lett.* **88**, 057201 (2002).
- [108] K. Goto and T. Sakurai, *Appl. Phys. Lett.* **30**, 355 (1977).
- [109] P. Rice and J. Moreland, *Rev. Sci. Instrum.* **62**, 844 (1991).
- [110] J. Fowler, Charles A. and E. M. Fryer, *Phys. Rev.* **104**, 552 (1956).
- [111] H. Boersch and M. Lambeck, *Z f. Physik* **165**, 176 (1961).
- [112] J. F. Dillon, H. Kamimura, and J. P. Remeika, *J. Appl. Phys.* **34**, 1240 (1963).
- [113] H. J. Williams, F. G. Foster, and E. A. Wood, *Phys. Rev.* **82**, 119 (1951).
- [114] J. Fowler, Charles A. and E. M. Fryer, *Phys. Rev.* **94**, 52 (1954).
- [115] A. Green and M. Prutton, *J. Sci. Instrum.* **39**, 244 (1962).

-
- [116] J. McCord, H. Brendel, A. Hubert, and S. Parkin, *J. Magn. Magn. Mater.* **148**, 244 (1995).
- [117] S. Egelkamp and L. Reimer, *Meas. Sci. Technol.* **1**, 79 (1990).
- [118] W. Clegg, N. Heyes, E. Hill, and C. Wright, *J. Magn. Magn. Mater.* **95**, 49 (1991).
- [119] G. L. Ping, C. W. See, M. G. Somekh, M. B. Suddendorf, J. H. Vincent, and P. K. Footner, *Scanning* **18**, 8 (1996).
- [120] G. Schütz, W. Wagner, W. Wilhelm, P. Kienle, R. Zeller, R. Frahm, and G. Materlik, *Phys. Rev. Lett.* **58**, 737 (1987).
- [121] L. Baumgarten, C. M. Schneider, H. Petersen, F. Schäfers, and J. Kirschner, *Phys. Rev. Lett.* **65**, 492 (1990).
- [122] J. Stöhr, Y. Wu, B. D. Hermsmeier, M. G. Samant, G. R. Harp, S. Koranda, D. Dunham, and B. P. Tonner, *Science* **259**, 658 (1993).
- [123] P. Fischer, G. Schütz, G. Schmahl, P. Guttman, and D. Raasch, *Z. f. Physik B* **101**, 313 (1996).
- [124] P. Fischer, T. Eimüller, G. Schütz, G. Bayreuther, S. Tsunashima, N. Takagi, G. Denbeaux, and D. Attwood, *J. Synchr. Rad.* **8**, 325 (2001).
- [125] S. Eisebitt, J. Lüning, W. F. Schlotter, M. Lörger, O. Hellwig, W. Eberhardt, and J. Stöhr, *Nature* **432**, 885 (2004).
- [126] W. Swiech, G. Fecher, C. Ziethen, O. Schmidt, G. Schönhense, K. Grzelakowski, C. M. Schneider, R. Frömter, H. Oepen, and J. Kirschner, *J. Electron Spectros. Relat. Phenomena.* **84**, 171 (1997).
- [127] G. Schönhense, *J. Phys.: Condens. Matter* **11**, 9517 (1999).
- [128] C. M. Schneider and G. Schönhense, *Rep. Prog. Phys.* **65**, 1785 (2002).
- [129] J. N. Chapman, *J. Phys. D: Appl. Phys.* **17**, 623 (1984).
- [130] M. E. Hale, H. W. Fuller, and H. Rubinstein, *J. Appl. Phys.* **30**, 789 (1959).
- [131] H. Boersch and H. Raith, *Naturwiss.* **46**, 574 (1959).
- [132] M. Cohen, *IEEE Trans. Magn.* **1**, 156 (1965).
- [133] J. Chapman, P. Batson, E. Waddell, and R. Ferrier, *Ultramicroscopy* **3**, 203 (1978).
- [134] J. Philibert and R. Tixier, *Micron* **1**, 174 (1969).
- [135] W. Pauli, *Z. f. Physik* **31**, 765 (1925).

- [136] M. S. Altman, H. Pinkvos, J. Hurst, H. Poppa, G. Marx, and E. Bauer, *Mat. Res. Soc. Symp. Proc.* **232**, 125 (1991).
- [137] U. Hartmann, *J. Magn. Magn. Mater.* **157-158**, 545 (1996).
- [138] Y. Martin and H. K. Wickramasinghe, *Appl. Phys. Lett.* **50**, 1455 (1987).
- [139] R. Wiesendanger, H.-J. Güntherodt, G. Güntherodt, R. J. Gambino, and R. Ruf, *Phys. Rev. Lett.* **65**, 247 (1990).
- [140] B. M. Chernobrod and G. P. Berman, *J. Appl. Phys.* **97**, (2005).
- [141] R. S. Schoenfeld and W. Harneit, *Phys. Rev. Lett.* **106**, 030802 (2011).
- [142] J.-P. Tetienne, T. Hingant, L. Rondin, S. Rohart, A. Thiaville, J.-F. Roch, and V. Jacques, *Phys. Rev. B* **88**, 214408 (2013).
- [143] E. Betzig, J. K. Trautman, T. D. Harris, J. S. Weiner, and R. L. Kostelak, *Science* **251**, 1468 (1991).
- [144] E. Betzig, J. K. Trautman, J. S. Weiner, T. D. Harris, and R. Wolfe, *Appl. Opt.* **31**, 4563 (1992).
- [145] J. J. Thomson, *Philos. Mag.* **44**, 293 (1897).
- [146] J. J. Thomson, *Philos. Mag.* **90**, 25 (2010).
- [147] L. d. Broglie, *Philosophical Magazine Series 6* **47**, 446 (1924).
- [148] M. Ardenne, *Z. f. Physik* **109**, 553 (1938).
- [149] H. Seiler, *J. Appl. Phys.* **54**, R1 (1983).
- [150] W. Gerlach and O. Stern, *Z. f. Physik* **9**, 353 (1922).
- [151] G. E. Uhlenbeck and S. Goudsmit, *Naturwiss.* **47**, 662 (1925).
- [152] G. Chrobok and M. Hofmann, *Phys. Lett. A* **57**, 257 (1976).
- [153] J. Kessler, *Polarized Electrons*, 2nd ed. (Springer Berlin Heidelberg, 1985).
- [154] J. Unguris, D. T. Pierce, A. Galejs, and R. J. Celotta, *Phys. Rev. Lett.* **49**, 72 (1982).
- [155] J. Kirschner and K. Koike, *Surf. Sci.* **273**, 147 (1992).
- [156] J. Kirschner, *Polarized Electrons at Surfaces* (Springer Berlin Heidelberg, 1985).
- [157] M. Van Hove, W. Weinberg, and C.-M. Chan, *Low-Energy Electron Diffraction*, edited by G. Ertl and R. Gomer (Springer-Verlag Berlin Heidelberg New York London Paris Tokyo, 1986).

-
- [158] N. F. Mott, *Proc. Phys. Soc. London Sect. A* **124**, 425 (1929).
- [159] K. Koike and K. Hayakawa, *Jpn. J. Appl. Phys.* **22**, 1332 (1983).
- [160] K. Koike and K. Hayakawa, *Jpn. J. Appl. Phys.* **23**, L187 (1984).
- [161] K. Koike and K. Hayakawa, *Appl. Phys. Lett.* **45**, 585 (1984).
- [162] L. A. Hodge, T. J. Moravec, F. B. Dunning, and G. K. Walters, *Rev. Sci. Instrum.* **50**, 5 (1979).
- [163] K. Jost, F. Kaussen, and J. Kessler, *J. Phys. E* **14**, 735 (1981).
- [164] L. G. Gray, M. W. Hart, F. B. Dunning, and G. K. Walters, *Rev. Sci. Instrum.* **55**, 88 (1984).
- [165] D. M. Campbell, C. Hermann, G. Lampel, and R. Owen, *J. Phys. E* **18**, 664 (1985).
- [166] F. B. Dunning, L. G. Gray, J. M. Ratliff, F. Tang, X. Zhang, and G. K. Walters, *Rev. Sci. Instrum.* **58**, 1706 (1987).
- [167] D. D. Neufeld, H. Aliabadi, and F. B. Dunning, *Rev. Sci. Instrum.* **78**, (2007).
- [168] V. N. Petrov, V. V. Grebenshikov, A. N. Andronov, P. G. Gabdullin, and A. V. Maslevt-cov, *Rev. Sci. Instrum.* **78**, (2007).
- [169] M. R. Scheinfein, J. Unguris, M. H. Kelley, D. T. Pierce, and R. J. Celotta, *Rev. Sci. Instrum.* **61**, 2501 (1990).
- [170] J. Unguris, D. T. Pierce, and R. J. Celotta, *Rev. Sci. Instrum.* **57**, 1314 (1986).
- [171] M. R. Scheinfein, D. T. Pierce, J. Unguris, J. J. McClelland, R. J. Celotta, and M. H. Kelley, *Rev. Sci. Instrum.* **60**, 1 (1989).
- [172] J. Kirschner and R. Feder, *Phys. Rev. Lett.* **42**, 1008 (1979).
- [173] G.-C. Wang, R. J. Celotta, and D. T. Pierce, *Phys. Rev. B* **23**, 1761 (1981).
- [174] H. P. Oepen and J. Kirschner, *J. Phys. (Paris)* **49**, 1853 (1988).
- [175] H. P. Oepen and J. Kirschner, *Phys. Rev. Lett.* **62**, 819 (1989).
- [176] R. Frömter, H. P. Oepen, and J. Kirschner, *Appl. Phys. A* **76**, 869 (2003).
- [177] S.-H. Chung, D. Pierce, and J. Unguris, *Ultramicroscopy* **110**, 177 (2010).
- [178] T. Kohashi, H. Matsuyama, and K. Koike, *Rev. Sci. Instrum.* **66**, 5537 (1995).
- [179] T. Kohashi, M. Konoto, and K. Koike, *Rev. Sci. Instrum.* **75**, 2003 (2004).
- [180] W. C. Wiley and C. F. Hendee, *IRE Trans. Nucl. Sci.* **9**, 103 (1962).

- [181] J. Adams and B. W. Manley, [IEEE Trans. Nucl. Sci.](#) **13**, 88 (1966).
- [182] J. Ladislav Wiza, [Nucl. Instrum. Methods](#) **162**, 587 (1979).
- [183] L. Reimer, in *Springer Series in Optical Sciences*, Vol. 45 (Springer Berlin Heidelberg, 1998).
- [184] F. Lofink, S. Hankemeier, R. Frömter, J. Kirschner, and H. P. Oepen, [Rev. Sci. Instrum.](#) **83**, (2012).
- [185] G. Schönhense and H. C. Siegmann, [Ann. Phys.](#) **2**, 465 (1993).
- [186] J. Kirschner, *Spinabhängige Phänomene bei Elektronenbeugung und Photoemission an unmagnetischen Kristallen* (1982).
- [187] N. Sherman, [Phys. Rev.](#) **103**, 1601 (1956).
- [188] R. Cortenraad, S. Ermolov, V. Semenov, A. Denier van der Gon, V. Glebovsky, S. Bozhko, and H. Brongersma, [J. Cryst. Growth](#) **222**, 154 (2001).
- [189] K. Zakeri, T. Peixoto, Y. Zhang, J. Prokop, and J. Kirschner, [Surf. Sci.](#) **604**, L1 (2010).
- [190] J. S. Allen, [Phys. Rev.](#) **55**, 966 (1939).
- [191] T. E. Everhart, O. O. Wells, and C. W. Oatley, [J. Electr. Contr](#) **7**, 97 (1959).
- [192] S. Hankemeier, *The Magnetic Fine Structure of Thin-Film Elements*, [Ph.d. thesis](#), Universität Hamburg (2010).
- [193] F. Lofink, *Oberflächensensitive Abbildung magnetischer Feinstrukturen des Domänenmusters von Ni(111) und geknickter Nanodrähte*, [Ph.d. thesis](#), Universität Hamburg (2013).
- [194] K. Koike, [Microscopy](#) **62**, 177 (2013).
- [195] G. Steierl, G. Liu, D. Iorgov, and J. Kirschner, [Rev. Sci. Instrum.](#) **73**, 4264 (2002).
- [196] B. Krüger, M. Najafi, S. Bohlens, R. Frömter, D. P. F. Möller, and D. Pfannkuche, [Phys. Rev. Lett.](#) **104**, 077201 (2010).
- [197] B. Odom, D. Hanneke, B. D’Urso, and G. Gabrielse, [Phys. Rev. Lett.](#) **97**, 030801 (2006).
- [198] C. Kittel, [Rev. Mod. Phys.](#) **21**, 541 (1949).
- [199] R. Hertel, *Spintronics*, edited by S. Blügel, D. Bürgler, M. Morgenstern, C. M. Schneider, and R. Waser, Micromagnetism, Vol. 10 (Forschungszentrum Jülich GmbH, 2009) p. D1.
- [200] M. Krawczyk, M. L. Sokolovskyy, J. W. Klos, and S. Mamica, [Adv. Condens. Matter Phys.](#) **2012**, 1 (2012).

-
- [201] W. F. Brown, Jr., ed., *Magnetostatic Principles in Ferromagnetism* (North-Holland publishing company, Amsterdam, 1962).
- [202] W. F. Brown, Jr., ed., *Micromagnetics* (Interscience Publishers, John Wiley & Sons, New York, London, 1963).
- [203] T. Gilbert, *Phys. Rev.* **100**, 1243 (1955).
- [204] L. Berger, *J. Appl. Phys.* **49**, 2156 (1978).
- [205] Y. B. Bazaliy, B. A. Jones, and S. C. Zhang, *Phys. Rev. B* **57**, R3213 (1998).
- [206] G. Bertotti, I. Mayergoyz, and C. Serpico, *Nonlinear Magnetization Dynamics in Nanosystems* (Elsevier Science & Technology, 2008).
- [207] W. Heisenberg, *Z. f. Physik* **38**, 411 (1926).
- [208] P. A. M. Dirac, *Proc. Phys. Soc. London Sect. A* **112**, 661 (1926).
- [209] R. C. O'Handley, *Modern Magnetic Materials* (John Wiley & Sons, Inc, 2000).
- [210] P. Weiss and R. Forrer, *Ann. Phys.* **5**, 153 (1926).
- [211] H. Kronmüller, in *Handbook of Magnetism and Advanced Magnetic Materials* (John Wiley & Sons, Ltd, 2007).
- [212] M. D. Stiles, W. M. Saslow, M. J. Donahue, and A. Zangwill, *Phys. Rev. B* **75**, 214423 (2007).
- [213] V. Kamberský, *Czech. J. Phys. B* **26**, 1366 (1976).
- [214] K. Gilmore, Y. U. Idzerda, and M. D. Stiles, *Phys. Rev. Lett.* **99**, 027204 (2007).
- [215] M. C. Hickey and J. S. Moodera, *Phys. Rev. Lett.* **102**, 137601 (2009).
- [216] L. Berger, *Phys. Rev. B* **83**, 054410 (2011).
- [217] M. Sparks, R. Loudon, and C. Kittel, *Phys. Rev.* **122**, 791 (1961).
- [218] R. Arias and D. L. Mills, *Phys. Rev. B* **60**, 7395 (1999).
- [219] B. K. Kuanr, R. Camley, and Z. Celinski, *J. Magn. Magn. Mater.* **286**, 276 (2005).
- [220] D. Mills and S. Rezende, in *Spin Dynamics in Confined Magnetic Structures II*, edited by B. Hillebrands and K. Ounadjela (Springer Berlin Heidelberg, 2003) pp. 27–59–.
- [221] L. Berger, *J. Appl. Phys.* **55**, 1954 (1984).
- [222] M. Hayashi, L. Thomas, C. Rettner, R. Moriya, Y. B. Bazaliy, and S. S. P. Parkin, *Phys. Rev. Lett.* **98**, 037204 (2007).

- [223] M. D. Stiles and A. Zangwill, *Phys. Rev. B* **66**, 014407 (2002).
- [224] A. Shpiro, P. M. Levy, and S. Zhang, *Phys. Rev. B* **67**, 104430 (2003).
- [225] J. Xiao, A. Zangwill, and M. D. Stiles, *Phys. Rev. B* **70**, 172405 (2004).
- [226] Z. Li and S. Zhang, *Phys. Rev. Lett.* **92**, 207203 (2004).
- [227] R. J. Elliott, *Phys. Rev.* **96**, 266 (1954).
- [228] S. Takahashi and S. Maekawa, *J. Phys. Soc. Jpn.* **77**, 031009 (2008).
- [229] J. Bass and W. P. Pratt Jr, *J. Phys.: Condens. Matter* **19**, 183201 (2007).
- [230] Y. Tserkovnyak, H. J. Skadsem, A. Brataas, and G. E. W. Bauer, *Phys. Rev. B* **74**, 144405 (2006).
- [231] L. Berger, *Phys. Rev. B* **80**, 144427 (2009).
- [232] H. Kohno, G. Tatara, and J. Shibata, *J. Phys. Soc. Jpn.* **75**, 113706 (2006).
- [233] M. Thorwart and R. Egger, *Phys. Rev. B* **76**, 214418 (2007).
- [234] I. Garate, K. Gilmore, M. D. Stiles, and A. H. MacDonald, *Phys. Rev. B* **79**, 104416 (2009).
- [235] P. Baláz, V. K. Dugaev, and J. Barnaś, *Phys. Rev. B* **85**, 024416 (2012).
- [236] V. Kamberský, *Can. J. Phys.* **48**, 2906 (1970).
- [237] G. Tatara and H. Kohno, *Phys. Rev. Lett.* **92**, 086601 (2004).
- [238] A. Manchon, W.-S. Kim, and K.-J. Lee, *arXiv:1110.3487* (2011).
- [239] D. Claudio-Gonzalez, A. Thiaville, and J. Miltat, *Phys. Rev. Lett.* **108**, 227208 (2012).
- [240] C. Petitjean, D. Luc, and X. Waintal, *Phys. Rev. Lett.* **109**, 117204 (2012).
- [241] J. Xiao, A. Zangwill, and M. D. Stiles, *Phys. Rev. B* **73**, 054428 (2006).
- [242] G. Tatara, H. Kohno, J. Shibata, Y. Lemaho, and K.-J. Lee, *J. Phys. Soc. Jpn.* **76**, 054707 (2007).
- [243] C. H. Marrows, *Adv. Phys.* **54**, 585 (2005).
- [244] L. Thomas and S. Parkin, in *Handbook of Magnetism and Advanced Magnetic Materials* (John Wiley & Sons, Ltd, 2007).
- [245] G. Beach, M. Tsoi, and J. Erskine, *J. Magn. Magn. Mater.* **320**, 1272 (2008).
- [246] Y. Tserkovnyak, A. Brataas, and G. E. Bauer, *J. Magn. Magn. Mater.* **320**, 1282 (2008).

-
- [247] M. Kläui, *J. Phys.: Condens. Matter* **20**, 313001 (2008).
- [248] J. Shibata, G. Tatara, and H. Kohno, *J. Phys. D: Appl. Phys.* **44**, 384004 (2011).
- [249] G. Malinowski, O. Boulle, and M. Kläui, *J. Phys. D: Appl. Phys.* **44**, 384005 (2011).
- [250] P. Gambardella and I. M. Miron, *Phil. Trans. R. Soc. A* **369**, 3175 (2011).
- [251] A. Brataas and K. M. D. Hals, *Nat. Nano.* **9**, 86 (2014).
- [252] V. Edelstein, *Solid State Commun.* **73**, 233 (1990).
- [253] A. Manchon and S. Zhang, *Phys. Rev. B* **78**, 212405 (2008).
- [254] N. L. Schryer and L. R. Walker, *J. Appl. Phys.* **45**, 5406 (1974).
- [255] Y. Nakatani, A. Thiaville, and J. Miltat, *Nat. Mater.* **2**, 521 (2003).
- [256] A. Thiaville, Y. Nakatani, J. Miltat, and N. Vernier, *J. Appl. Phys.* **95**, 7049 (2004).
- [257] N. Vernier, D. A. Allwood, D. Atkinson, M. D. Cooke, and R. P. Cowburn, *Europhys. Lett.* **65**, 526 (2004).
- [258] A. Yamaguchi, T. Ono, S. Nasu, K. Miyake, K. Mibu, and T. Shinjo, *Phys. Rev. Lett.* **92**, 077205 (2004).
- [259] M. Yamanouchi, D. Chiba, F. Matsukura, T. Dietl, and H. Ohno, *Phys. Rev. Lett.* **96**, 096601 (2006).
- [260] M. Hayashi, L. Thomas, Y. B. Bazaliy, C. Rettner, R. Moriya, X. Jiang, and S. S. P. Parkin, *Phys. Rev. Lett.* **96**, 197207 (2006).
- [261] G. S. D. Beach, C. Knutson, C. Nistor, M. Tsoi, and J. L. Erskine, *Phys. Rev. Lett.* **97**, 057203 (2006).
- [262] L. Thomas, M. Hayashi, X. Jiang, R. Moriya, C. Rettner, and S. S. P. Parkin, *Nature* **443**, 197 (2006).
- [263] D. Bedau, M. Kläui, S. Krzyk, U. Rüdiger, G. Faini, and L. Vila, *Phys. Rev. Lett.* **99**, 146601 (2007).
- [264] E. Martinez, L. Lopez-Diaz, O. Alejos, and L. Torres, *Phys. Rev. B* **77**, 144417 (2008).
- [265] S. Lepadatu, A. Vanhaverbeke, D. Atkinson, R. Allenspach, and C. H. Marrows, *Phys. Rev. Lett.* **102**, 127203 (2009).
- [266] M. Hayashi, L. Thomas, C. Rettner, R. Moriya, and S. S. P. Parkin, *Nat. Phys.* **3**, 21 (2007).
- [267] M. Kläui, C. A. F. Vaz, J. A. C. Bland, W. Wernsdorfer, G. Faini, E. Cambril, L. J. Heyderman, F. Nolting, and U. Rüdiger, *Phys. Rev. Lett.* **94**, 106601 (2005).

- [268] M. Hayashi, L. Thomas, C. Rettner, R. Moriya, X. Jiang, and S. S. P. Parkin, *Phys. Rev. Lett.* **97**, 207205 (2006).
- [269] M. Eltschka, M. Wötzel, J. Rhensius, S. Krzyk, U. Nowak, M. Kläui, T. Kasama, R. E. Dunin-Borkowski, L. J. Heyderman, H. J. van Driel, and R. A. Duine, *Phys. Rev. Lett.* **105**, 056601 (2010).
- [270] A. Yamaguchi, S. Nasu, H. Tanigawa, T. Ono, K. Miyake, K. Mibu, and T. Shinjo, *Appl. Phys. Lett.* **86**, 012511 (2005).
- [271] F. Junginger, M. Kläui, D. Backes, U. Rüdiger, T. Kasama, R. E. Dunin-Borkowski, L. J. Heyderman, C. A. F. Vaz, and J. A. C. Bland, *Appl. Phys. Lett.* **90**, 132506 (2007).
- [272] M. Dagrás, M. Laufenberg, D. Bedau, L. Vila, G. Faini, C. A. F. Vaz, and Bland, *J. Phys. D: Appl. Phys.* **40**, 1247 (2007).
- [273] H. Fangohr, D. S. Chernyshenko, M. Franchin, T. Fischbacher, and G. Meier, *Phys. Rev. B* **84**, 054437 (2011).
- [274] P. P. Freitas and L. Berger, *J. Appl. Phys.* **57**, 1266 (1985).
- [275] L. Bocklage, B. Krüger, T. Matsuyama, M. Bolte, U. Merkt, D. Pfannkuche, and G. Meier, *Phys. Rev. Lett.* **103**, 197204 (2009).
- [276] H. H. Langner, L. Bocklage, B. Krüger, T. Matsuyama, and G. Meier, *Appl. Phys. Lett.* **97**, 242503 (2010).
- [277] G. Malinowski, *J. Phys. D: Appl. Phys.* **43**, 045003 (2010).
- [278] S. Lepadatu, M. C. Hickey, A. Potenza, H. Marchetto, T. R. Charlton, S. Langridge, S. S. Dhesi, and C. H. Marrows, *Phys. Rev. B* **79**, 094402 (2009).
- [279] V. E. Demidov, M. P. Kostylev, K. Rott, J. Münchenberger, G. Reiss, and S. O. Demokritov, *Appl. Phys. Lett.* **99**, (2011).
- [280] P. Lederer and D. L. Mills, *Phys. Rev.* **148**, 542 (1966).
- [281] J. Fernández-Rossier, M. Braun, A. S. Núñez, and A. H. MacDonald, *Phys. Rev. B* **69**, 174412 (2004).
- [282] T. Shinjo, T. Okuno, R. Hassdorf, K. Shigeto, and T. Ono, *Science* **289**, 930 (2000).
- [283] L. Heyne, J. Rhensius, D. Ilgaz, A. Bisig, U. Rüdiger, M. Kläui, L. Joly, F. Nolting, L. J. Heyderman, J. U. Thiele, and F. Kronast, *Phys. Rev. Lett.* **105**, 187203 (2010).
- [284] P. Fischer, M.-Y. Im, S. Kasai, K. Yamada, T. Ono, and A. Thiaville, *Phys. Rev. B* **83**, 212402 (2011).
- [285] L. Rondin, J. P. Tetienne, S. Rohart, A. Thiaville, T. Hingant, P. Spinicelli, J. F. Roch, and V. Jacques, *Nat. Commun.* **4**, (2013).

- [286] E. Feldtkeller and H. Thomas, *Phys. Kondens. Materie* **4**, 8 (1965).
- [287] K. L. Metlov, *J. Magn. Magn. Mater.* **343**, 55 (2013).
- [288] S. Hankemeier, K. Sachse, Y. Stark, R. Frömter, and H. P. Oepen, *Appl. Phys. Lett.* **92**, 242503 (2008).
- [289] J. Shibata, Y. Nakatani, G. Tatara, H. Kohno, and Y. Otani, *Phys. Rev. B* **73**, 020403 (2006).
- [290] R. P. Cowburn and M. E. Welland, *Appl. Phys. Lett.* **72**, 2041 (1998).
- [291] J. Raabe, R. Pulwey, R. Sattler, T. Schweinbock, J. Zweck, and D. Weiss, *J. Appl. Phys.* **88**, 4437 (2000).
- [292] B. Krüger, *Current-Driven Magnetization Dynamics: Analytical Modeling and Numerical Simulation*, *Ph.D. thesis*, Universität Hamburg (2011).
- [293] K. Y. Guslienko, B. A. Ivanov, V. Novosad, Y. Otani, H. Shima, and K. Fukamichi, *Appl. Phys. Lett.* **91**, 8037 (2002).
- [294] K.-S. Lee and S.-K. Kim, *Appl. Phys. Lett.* **91**, 132511 (2007).
- [295] W. F. Brown and A. E. LaBonte, *J. Appl. Phys.* **36**, 1380 (1965).
- [296] M. Donahue and D. Porter, *Interagency Report NISTIR 6376*, National Institute of Standards and Technology, Gaithersburg, MD (1999).
- [297] A. Drews, *Fast Micromagnetic Simulator for Computations on CPU and Graphics Processing Unit (GPU)* (2014).
- [298] M. Albert, M. Franchin, T. Fischbacher, G. Meier, and H. Fangohr, *J. Phys.: Condens. Matter* **24**, 024219 (2012).
- [299] S. Barman and G. P. Srivastava, *J. Appl. Phys.* **101**, 123507 (2007).
- [300] J. Kühnle and O. Weis, *Surf. Sci.* **340**, 16 (1995).
- [301] *Almax easyLab* (2014).
- [302] A. Frauen, *Gleichstrominduzierte Verschiebung von Domänenwänden in Permalloy-Nanodrähten auf Saphirsubstrat*, *Master's thesis*, Universität Hamburg (2011).
- [303] J. McCord and A. Hubert, *Phys. Status Solidi A* **171**, 555 (1999).
- [304] A. Neudert, J. McCord, D. Chumakov, R. Schäfer, and L. Schultz, *Phys. Rev. B* **71**, 134405 (2005).
- [305] H. Boersch, H. Raith, and D. Wohlleben, *Z. f. Physik* **159**, 388 (1960).
- [306] K. J. Harte, *J. Appl. Phys.* **39**, 1503 (1968).

- [307] H. W. Fuller and M. E. Hale, *J. Appl. Phys.* **31**, 238 (1960).
- [308] H. Riedel, *Phys. Status Solidi A* **24**, 449 (1974).
- [309] A. R. Pereira, L. A. S. Mól, S. A. Leonel, P. Z. Coura, and B. V. Costa, *Phys. Rev. B* **68**, 132409 (2003).
- [310] R. L. Compton and P. A. Crowell, *Phys. Rev. Lett.* **97**, 137202 (2006).
- [311] D. Toscano, S. A. Leonel, R. A. Dias, P. Z. Coura, and B. V. Costa, *J. Appl. Phys.* **109**, (2011).
- [312] A. J. Sorensen, *Phys. Rev.* **24**, 658 (1924).
- [313] R. L. Edwards, *Phys. Rev.* **29**, 321 (1927).
- [314] H. Kronmüller and B. Gröger, *J. Phys. France* **42**, 1285 (1981).
- [315] K. Y. Ahn, *J. Appl. Phys.* **37**, 1481 (1966).
- [316] R. M. Bozorth, *Ferromagnetism* (D. Van Nostrand Company, Inc., 1951).
- [317] S. Hankemeier, R. Frömter, N. Mikuszeit, D. Stickler, H. Stillrich, S. Pütter, E. Y. Vedmedenko, and H. P. Oepen, *Phys. Rev. Lett.* **103**, 147204 (2009).
- [318] J. K. Ha, R. Hertel, and J. Kirschner, *Phys. Rev. B* **67**, 224432 (2003).
- [319] Y. B. Grebenshchikov, N. A. Usov, and K. S. Pestchanyi, *J. Appl. Phys.* **94**, 6649 (2003).
- [320] L. J. Heyderman, S. Czekaj, F. Nolting, E. Müller, P. Fischer, P. Gasser, and L. López-Díaz, *J. Appl. Phys.* **99**, 063904 (2006).
- [321] T. J. Whetten, A. A. Armstead, T. A. Grzybowski, and A. L. Ruoff, *J. Vac. Sci. Technol. A* **2**, 477 (1984).
- [322] J. H. E. Griffiths, *Nature* **158**, 670 (1946).
- [323] W. A. Yager and R. M. Bozorth, *Phys. Rev.* **72**, 80 (1947).
- [324] S. Chikazumi, *Physics of Ferromagnetism* (Oxford Science Publications, 1999).
- [325] C. Kittel, *Phys. Rev.* **73**, 155 (1948).
- [326] E. Nazaretski, J. D. Thompson, R. Movshovich, M. Zalalutdinov, J. W. Baldwin, B. Houston, T. Mewes, D. V. Pelekhov, P. Wigen, and P. C. Hammel, *J. Appl. Phys.* **101**, 074905 (2007).
- [327] M. H. Seavey, Jr. and P. E. Tannenwald, *J. Appl. Phys.* **29**, 292 (1958).
- [328] J. P. Nibarger, R. Lopusnik, Z. Celinski, and T. J. Silva, *Appl. Phys. Lett.* **83**, 93 (2003).

- [329] D. T. Ngo, *J. Appl. Phys.* **34**, 3626 (1963).
- [330] H. Wijn, ed., *Magnetic Properties of Metals*, Vol. 19 a (Springer-Verlag Berlin, 1986).
- [331] T. Maeda, H. Yamauchi, and H. Watanabe, *J. Phys. Soc. Jpn.* **35**, 1635 (1973).
- [332] H. Hurdequint, *J. Magn. Magn. Mater.* **310**, 2061 (2007).
- [333] R. Bonin, M. L. Schneider, T. J. Silva, and J. P. Nibarger, *J. Appl. Phys.* **98**, 123904 (2005).
- [334] A. Kobs, H. Spahr, D. Stickler, S. Hankemeier, R. Frömter, and H. P. Oepen, *Phys. Rev. B* **80**, 134415 (2009).
- [335] A. Kobs, *Magnetogalvanic effects in ferromagnets of reduced dimensions*, Ph.D. thesis, Staats- und Universitätsbibliothek Hamburg, Von-Melle-Park 3, 20146 Hamburg (2013).
- [336] S. Ingvarsson, G. Xiao, S. Parkin, and W. Gallagher, *J. Magn. Magn. Mater.* **251**, 202 (2002).
- [337] S. Vonsovskii, *Ferromagnetic Resonance: (Ferromagnitnyi Rezonans); the Phenomenon of Resonance Absorption of HF Electromagnetic Field Energy in Ferromagnetic Materials* (Israel Program for Scientific Translations, 1964).
- [338] M. Goto, H. Tange, and T. Kamimori, *J. Magn. Magn. Mater.* **62**, 251 (1986).
- [339] J. Han-Min, C.-O. Kim, T.-D. Lee, and H.-J. Kim, *Chin. Phys.* **16**, 3520 (2007).
- [340] E. B. Park, S.-U. Jang, J.-H. Kim, and S.-J. Kwon, *Thin Solid Films* **520**, 5981 (2012).
- [341] S. S. Kalarickal, P. Krivosik, M. Wu, C. E. Patton, M. L. Schneider, P. Kabos, T. J. Silva, and J. P. Nibarger, *J. Appl. Phys.* **99**, 093909 (2006).
- [342] B. Heinrich, J. F. Cochran, and R. Hasegawa, *J. Appl. Phys.* **57**, 3690 (1985).
- [343] X. Liu, J. Rantschler, C. Alexander, and G. Zangari, *IEEE Trans. Magn.* **39**, 2362 (2003).
- [344] V. Vlaminck and M. Bailleul, *Science* **322**, 410 (2008).
- [345] G. Nahrwold, J. M. Scholtyssek, S. Motl-Ziegler, O. Albrecht, U. Merkt, and G. Meier, *J. Appl. Phys.* **108**, 013907 (2010).
- [346] W. K. Hiebert, A. Stankiewicz, and M. R. Freeman, *Phys. Rev. Lett.* **79**, 1134 (1997).
- [347] K. Kobayashi, N. Inaba, N. Fujita, Y. Sudo, T. Tanaka, M. Ohtake, M. Futamoto, and F. Kirino, *IEEE Trans. Magn.* **45**, 2541 (2009).
- [348] S. Ingvarsson, L. Ritchie, X. Y. Liu, G. Xiao, J. C. Slonczewski, P. L. Trouilloud, and R. H. Koch, *Phys. Rev. B* **66**, 214416 (2002).
- [349] M. Zhu, C. L. Dennis, and R. D. McMichael, *Phys. Rev. B* **81**, 140407 (2010).

- [350] R. L. Thomas, M. Zhu, C. L. Dennis, V. Misra, and R. D. McMichael, *J. Appl. Phys.* **110**, 033902 (2011).
- [351] J. Crangle and G. C. Hallam, *Proc. Phys. Soc. London Sect. A* **272**, 119 (1963).
- [352] M. Haidar and M. Bailleul, *Phys. Rev. B* **88**, 054417 (2013).
- [353] I. I. Mazin, *Phys. Rev. Lett.* **83**, 1427 (1999).
- [354] I. Zutic, J. Fabian, and S. Das Sarma, *Rev. Mod. Phys.* **76**, 323 (2004).
- [355] P. A. Dowben, N. Wu, and C. Binek, *J. Phys.: Condens. Matter* **23**, 171001 (2011).
- [356] B. Krüger, private communications (2013).
- [357] S. Dubois, L. Piraux, J. M. George, K. Ounadjela, J. L. Duvail, and A. Fert, *Phys. Rev. B* **60**, 477 (1999).
- [358] L. Vila, W. Park, J. A. Caballero, D. Bozec, R. Loloee, W. P. Pratt, Jr., and J. Bass, *J. Appl. Phys.* **87**, 8610 (2000).
- [359] R. J. Soulen, J. M. Byers, M. S. Osofsky, B. Nadgorny, T. Ambrose, S. F. Cheng, P. R. Broussard, C. T. Tanaka, J. Nowak, J. S. Moodera, A. Barry, and J. M. D. Coey, *Science* **282**, 85 (1998).
- [360] B. Nadgorny, R. J. Soulen Jr, M. S. Osofsky, I. I. Mazin, G. Laprade, R. J. M. van de Veerdonk, A. A. Smits, S. F. Cheng, E. F. Skelton, and S. B. Qadri, *Phys. Rev. B* **61**, R3788 (2000).
- [361] L. Bocklage, J. M. Scholtyssek, U. Merkt, and G. Meier, *J. Appl. Phys.* **101**, 09J512 (2007).
- [362] D. Ilgaz, J. Nievendick, L. Heyne, D. Backes, J. Rhensius, T. A. Moore, M. Niño, A. Locatelli, T. O. Menteş, A. v. Schmidfeld, A. v. Bieren, S. Krzyk, L. J. Heyderman, and M. Kläui, *Phys. Rev. Lett.* **105**, 076601 (2010).
- [363] T. Kimura, N. Hashimoto, S. Yamada, M. Miyao, and K. Hamaya, *NPG Asia Mater.* **4**, e9 (2012).
- [364] P. Laczkowski, L. Vila, V.-D. Nguyen, A. Marty, J.-P. Attané, H. Jaffrès, J.-M. George, and A. Fert, *Phys. Rev. B* **85**, 220404 (2012).
- [365] S. Kasai, P. Fischer, M.-Y. Im, K. Yamada, Y. Nakatani, K. Kobayashi, H. Kohno, and T. Ono, *Phys. Rev. Lett.* **101**, 237203 (2008).
- [366] T. Valet and A. Fert, *Phys. Rev. B* **48**, 7099 (1993).
- [367] Y. Niimi, Y. Kawanishi, D. H. Wei, C. Deranlot, H. X. Yang, M. Chshiev, T. Valet, A. Fert, and Y. Otani, *Phys. Rev. Lett.* **109**, 156602 (2012).

-
- [368] E. Villamor, M. Isasa, L. E. Hueso, and F. Casanova, *Phys. Rev. B* **88**, 184411 (2013).
- [369] N. Usov and S. Peschany, *J. Magn. Magn. Mater.* **118**, L290 (1993).
- [370] S. Gliga, *Ultrafast vortex core dynamics investigated by finite-element micromagnetic simulations*, *Ph.D. thesis*, Forschungszentrums Jülich (2010).
- [371] *COMSOL Multiphysics* (2014).
- [372] K.-W. Moon, J.-C. Lee, K. Rhie, K.-H. Shin, and S.-B. Choe, *IEEE Trans. Magn.* **47**, 2508 (2011).
- [373] K. Fuchs, *Math. Proc. Cambridge* **34**, 100 (1938).
- [374] E. Sondheimer, *Adv. Phys.* **1**, 1 (1952).
- [375] S. B. Soffer, *J. Appl. Phys.* **38**, 1710 (1967).
- [376] G. Kästle, H.-G. Boyen, A. Schröder, A. Plettl, and P. Ziemann, *Phys. Rev. B* **70**, 165414 (2004).
- [377] C. Chappert, D. Renard, P. Beauvillain, J. Renard, and J. Seiden, *J. Magn. Magn. Mater.* **54-57, Part 2**, 795 (1986).
- [378] O. Boulle, J. Kimling, P. Warnicke, M. Kläui, U. Rüdiger, G. Malinowski, H. J. M. Swagten, B. Koopmans, C. Ulysse, and G. Faini, *Phys. Rev. Lett.* **101**, 216601 (2008).
- [379] C. Burrowes, A. P. Mihai, D. Ravelosona, J.-V. Kim, C. Chappert, L. Vila, A. Marty, Y. Samson, F. Garcia-Sanchez, L. D. Buda-Prejbeanu, I. Tudosa, E. E. Fullerton, and J.-P. Attane, *Nat. Phys.* **6**, 17 (2010).
- [380] L. San Emeterio Alvarez, K.-Y. Wang, S. Lepadatu, S. Landi, S. J. Bending, and C. H. Marrows, *Phys. Rev. Lett.* **104**, 137205 (2010).
- [381] J. Heinen, D. Hinzke, O. Boulle, G. Malinowski, H. J. M. Swagten, B. Koopmans, C. Ulysse, G. Faini, B. Ocker, J. Wrona, and M. M, *J. Phys.: Condens. Matter* **24**, 024220 (2012).
- [382] R. McMichael and M. Donahue, *IEEE Trans. Magn.* **33**, 4167 (1997).
- [383] Y. Nakatani, A. Thiaville, and J. Miltat, *J. Magn. Magn. Mater.* **290-291**, 750 (2005).
- [384] A. Thiaville, Y. Nakatani, F. Piéchon, J. Miltat, and T. Ono, *Eur. Phys. J. B* **60**, 15 (2007).
- [385] M. Manfrini, J.-V. Kim, S. Petit-Watelot, W. Van Roy, L. Lagae, C. Chappert, and T. Devolder, *Nat. Nano.* **9**, 121 (2014).
- [386] A. Drews, *Dynamics of magnetic vortices and antivortices*, *Ph.D. thesis*, Universität Hamburg (2009).

- [387] B. Pigeau, G. de Loubens, O. Klein, A. Riegler, F. Lochner, G. Schmidt, L. W. Molenkamp, V. S. Tiberkevich, and A. N. Slavin, *Appl. Phys. Lett.* **96**, (2010).
- [388] D. Mitin, D. Nissen, P. Schädlich, S. S. P. K. Arekapudi, and M. Albrecht, *J. Appl. Phys.* **115**, (2014).
- [389] S. Bohlens, B. Krüger, A. Drews, M. Bolte, G. Meier, and D. Pfannkuche, *Appl. Phys. Lett.* **93**, 142508 (2008).
- [390] M. Schneider, H. Hoffmann, and J. Zweck, *Appl. Phys. Lett.* **79**, 3113 (2001).
- [391] Q. F. Xiao, J. Rudge, B. C. Choi, Y. K. Hong, and G. Donohoe, *Appl. Phys. Lett.* **89**, (2006).
- [392] B. C. Choi, J. Rudge, E. Girgis, J. Kolthammer, Y. K. Hong, and A. Lyle, *Appl. Phys. Lett.* **91**, 022501 (2007).
- [393] Y. Liu, S. Gliga, R. Hertel, and C. M. Schneider, *Appl. Phys. Lett.* **91**, 112501 (2007).
- [394] V. P. Kravchuk, D. D. Sheka, Y. Gaididei, and F. G. Mertens, *J. Appl. Phys.* **102**, (2007).
- [395] D. D. Sheka, Y. Gaididei, and F. G. Mertens, *Appl. Phys. Lett.* **91**, 082509 (2007).
- [396] K. Yamada, S. Kasai, Y. Nakatani, K. Kobayashi, H. Kohno, A. Thiaville, and T. Ono, *Nat. Mater.* **6**, 270 (2007).
- [397] R. Hertel, S. Gliga, M. Fähnle, and C. M. Schneider, *Phys. Rev. Lett.* **98**, 117201 (2007).
- [398] J.-G. Caputo, Y. Gaididei, F. G. Mertens, and D. D. Sheka, *Phys. Rev. Lett.* **98**, 056604 (2007).
- [399] K. Yamada, S. Kasai, Y. Nakatani, K. Kobayashi, and T. Ono, *Appl. Phys. Lett.* **93**, 152502 (2008).
- [400] Y. Gaididei, D. D. Sheka, and F. G. Mertens, *Appl. Phys. Lett.* **92**, 012503 (2008).
- [401] Y. B. Gaididei, V. P. Kravchuk, D. D. Sheka, and F. G. Mertens, *Low Temp. Phys.* **34**, 528 (2008).
- [402] K.-S. Lee, S.-K. Kim, Y.-S. Yu, Y.-S. Choi, K. Y. Guslienko, H. Jung, and P. Fischer, *Phys. Rev. Lett.* **101**, 267206 (2008).
- [403] K. Y. Guslienko, K.-S. Lee, and S.-K. Kim, *Phys. Rev. Lett.* **100**, 027203 (2008).
- [404] S.-K. Kim, K.-S. Lee, Y.-S. Yu, and Y.-S. Choi, *Appl. Phys. Lett.* **92**, 022509 (2008).
- [405] W. Jin, H. He, Y. Chen, and Y. Liu, *J. Appl. Phys.* **105**, 013906 (2009).
- [406] D. J. Keavney, X. M. Cheng, and K. S. Buchanan, *Appl. Phys. Lett.* **94**, 172506 (2009).
- [407] Y. Liu and A. Du, *J. Appl. Phys.* **107**, (2010).

- [408] A. Barman, V. V. Kruglyak, R. J. Hicken, A. Kundrotaite, and M. Rahman, *Appl. Phys. Lett.* **82**, 3065 (2003).
- [409] A. Barman, V. V. Kruglyak, R. J. Hicken, J. Scott, A. Kundrotaite, and M. Rahman, *J. Appl. Phys.* **95**, 6998 (2004).
- [410] F. Kloodt, *Realisierung eines Messverfahrens zur zeitaufgelösten Rasterelektronenmikroskopie mit Polarisationsanalyse mit 100ps Auflösung*, Bachelor thesis, Universität Hamburg (2013).
- [411] M. H. Kryder and F. B. Humphrey, *Rev. Sci. Instrum.* **40**, 829 (1969).
- [412] V. E. Demidov, B. Hillebrands, S. O. Demokritov, M. Laufenberg, and P. P. Freitas, *J. Appl. Phys.* **97**, (2005).
- [413] S. O. Demokritov and V. E. Demidov, *IEEE Trans. Magn.* **44**, 6 (2008).
- [414] K. Vahaplar, A. M. Kalashnikova, A. V. Kimel, S. Gerlach, D. Hinzke, U. Nowak, R. Chantrell, A. Tsukamoto, A. Itoh, A. Kirilyuk, and T. Rasing, *Phys. Rev. B* **85**, 104402 (2012).
- [415] H. Mamin, M. Poggio, C. Degen, and D. Rugar, *Nat. Nano.* **2**, 301 (2007).
- [416] P. S. Keatley, V. V. Kruglyak, P. Gangmei, and R. J. Hicken, *Phil. Trans. R. Soc. A* **369**, 3115 (2011).
- [417] S. Loth, M. Etzkorn, C. P. Lutz, D. M. Eigler, and A. J. Heinrich, *Science* **329**, 1628 (2010).
- [418] C. Saunus, J. Raphael Bindel, M. Pratzner, and M. Morgenstern, *Appl. Phys. Lett.* **102**, (2013).
- [419] M. Bolte, G. Meier, B. Krüger, A. Drews, R. Eiselt, L. Bocklage, S. Bohlens, T. Tyliczszak, A. Vansteenkiste, B. Van Waeyenberge, K. W. Chou, A. Puzic, and H. Stoll, *Phys. Rev. Lett.* **100**, 176601 (2008).
- [420] C. Cheng, K. Kaznatcheev, and W. E. Bailey, *J. Appl. Phys.* **111**, (2012).
- [421] H. S. Park, J. S. Baskin, and A. H. Zewail, *Nano Lett.* **10**, 3796 (2010).
- [422] H. Stoll, A. Puzic, B. van Waeyenberge, P. Fischer, J. Raabe, M. Buess, T. Haug, R. Höllinger, C. Back, D. Weiss, and G. Denbeaux, *Appl. Phys. Lett.* **84**, 3328 (2004).
- [423] P. Fischer, D.-H. Kim, B. Mesler, W. Chao, and E. Anderson, *J. Magn. Magn. Mater.* **310**, 2689 (2007).
- [424] T. Wang *et al.*, *Phys. Rev. Lett.* **108**, 267403 (2012).
- [425] C. M. Schneider, A. Krasyuk, S. Nepijko, A. Oelsner, and G. Schönhense, *J. Magn. Magn. Mater.* **304**, 6 (2006).

- [426] A. Locatelli and E. Bauer, *J. Phys.: Condens. Matter* **20**, 093002 (2008).
- [427] M. R. Freeman, M. J. Brady, and J. Smyth, *Appl. Phys. Lett.* **60**, 2555 (1992).
- [428] A. Barman, T. Kimura, Y. Otani, Y. Fukuma, K. Akahane, and S. Meguro, *Rev. Sci. Instrum.* **79**, (2008).
- [429] A. Hubert, *Phys. Stat. Sol. (b)* **22**, 709 (1967).
- [430] N. Qureshi, H. Schmidt, and A. R. Hawkins, *Appl. Phys. Lett.* **85**, 431 (2004).
- [431] A. Barman, S. Wang, J. D. Maas, A. R. Hawkins, S. Kwon, A. Liddle, J. Bokor, and H. Schmidt, *Nano Lett.* **6**, 2939 (2006).
- [432] B. Rana and A. Barman, *Spin* **3**, 1330001 (2013).
- [433] N. Qureshi, S. Wang, M. A. Lowther, A. R. Hawkins, S. Kwon, A. Liddle, J. Bokor, and H. Schmidt, *Nano Lett.* **5**, 1413 (2005).
- [434] Y. Acremann, C. H. Back, M. Buess, O. Portmann, A. Vaterlaus, D. Pescia, and H. Melchior, *Science* **290**, 492 (2000).
- [435] P. Gangmei, P. S. Keatley, W. Yu, R. J. Hicken, M. A. Gubbins, P. J. Czoschke, and R. Lopusnik, *Appl. Phys. Lett.* **99**, 232503 (2011).
- [436] Y.-S. Yu, D.-S. Han, M.-W. Yoo, K.-S. Lee, Y.-S. Choi, H. Jung, J. Lee, M.-Y. Im, P. Fischer, and S.-K. Kim, *Sci. Rep.* **3**, (2013).
- [437] A. Liénard, *L'éclairage électrique* **16**, 5 (1898).
- [438] G. A. Schott, *Ann. Phys.* **329**, 635 (1907).
- [439] F. R. Elder, A. M. Gurewitsch, R. V. Langmuir, and H. C. Pollock, *Phys. Rev.* **71**, 829 (1947).
- [440] F. R. Elder, R. V. Langmuir, and H. C. Pollock, *Phys. Rev.* **74**, 52 (1948).
- [441] S.-B. Choe, Y. Acremann, A. Scholl, A. Bauer, A. Doran, J. Stöhr, and H. A. Padmore, *Science* **304**, 420 (2004).
- [442] S.-K. Kim, J. B. Kortright, and S.-C. Shin, *Appl. Phys. Lett.* **78**, 2742 (2001).
- [443] F.-U. Stein, L. Bocklage, M. Weigand, and G. Meier, *Sci. Rep.* **3**, (2013).
- [444] A. Krasnyuk, A. Oelsner, S. Nepijko, A. Kuksov, C. Schneider, and G. Schönhense, *Appl. Phys. A* **76**, 863 (2003).
- [445] J. Vogel, W. Kuch, M. Bonfim, J. Camarero, Y. Pennec, F. Offi, K. Fukumoto, J. Kirschner, A. Fontaine, and S. Pizzini, *Appl. Phys. Lett.* **82**, 2299 (2003).

-
- [446] C. M. Schneider, A. Kuksov, A. Krasnyuk, A. Oelsner, D. Neeb, S. A. Nepijko, G. Schönhense, I. Mönch, R. Kaltofen, J. Morais, C. de Nadaï, and N. B. Brookes, [Appl. Phys. Lett.](#) **85**, 2562 (2004).
- [447] T. Ohkochi, H. Fujiwara, M. Kotsugi, A. Tsukamoto, K. Arai, S. Isogami, A. Sekiyama, J. Yamaguchi, K. Fukushima, R. Adam, C. M. Schneider, T. Nakamura, K. Kodama, M. Tsunoda, T. Kinoshita, and S. Suga, [Jpn. J. Appl. Phys.](#) **51**, 073001 (2012).
- [448] R. Tromp, J. Hannon, A. Ellis, W. Wan, A. Berghaus, and O. Schaff, [Ultramicroscopy](#) **110**, 852 (2010).
- [449] T. Schmidt, A. Sala, H. Marchetto, E. Umbach, and H.-J. Freund, [Ultramicroscopy](#) **126**, 23 (2013).
- [450] R. Tromp, J. Hannon, W. Wan, A. Berghaus, and O. Schaff, [Ultramicroscopy](#) **127**, 25 (2013).
- [451] F. Nickel, D. Gottlob, I. Krug, H. Doganay, S. Cramm, A. Kaiser, G. Lin, D. Makarov, O. Schmidt, and C. Schneider, [Ultramicroscopy](#) **130**, 54 (2013).
- [452] W. Ackermann *et al.*, [Nat. Photon.](#) **1**, 336 (2007).
- [453] C. Gutt *et al.*, [Phys. Rev. B](#) **79**, 212406 (2009).
- [454] C. Gutt, S. Streit-Nierobisch, L.-M. Stadler, B. Pfau, C. M. Günther, R. Könnecke, R. Frömter, A. Kobs, D. Stickler, H. P. Oepen, R. R. Fäustlin, R. Treusch, J. Feldhaus, E. Weckert, I. A. Vartanyants, M. Grunze, A. Rosenhahn, T. Wilhein, S. Eisebitt, and G. Grübel, [Phys. Rev. B](#) **81**, 100401 (2010).
- [455] L. Müller *et al.*, [Synchrotron Radiat. News](#) **26**, 27 (2013).
- [456] V. A. Lobastov, R. Srinivasan, and A. H. Zewail, [Proc. Natl. Acad. Sci. U. S. A.](#) **102**, 7069 (2005).
- [457] B. Barwick, H. S. Park, O.-H. Kwon, J. S. Baskin, and A. H. Zewail, [Science](#) **322**, 1227 (2008).
- [458] G. Binnig, H. Rohrer, C. Gerber, and E. Weibel, [Phys. Rev. Lett.](#) **49**, 57 (1982).
- [459] G. Binnig and H. Rohrer, [Surf. Sci.](#) **126**, 236 (1983).
- [460] D. Rugar, C. S. Yannoni, and J. A. Sidles, [Nature](#) **360**, 563 (1992).
- [461] Z. Zhang, P. C. Hammel, and P. E. Wigen, [Appl. Phys. Lett.](#) **68**, 2005 (1996).
- [462] O. Klein, G. de Loubens, V. V. Naletov, F. Boust, T. Guillet, H. Hurdequint, A. Leksikov, A. N. Slavin, V. S. Tiberkevich, and N. Vukadinovic, [Phys. Rev. B](#) **78**, 144410 (2008).
- [463] H.-J. Chia, F. Guo, L. M. Belova, and R. D. McMichael, [Appl. Phys. Lett.](#) **101**, (2012).

- [464] D. I. Porat, *IEEE Trans. Nucl. Sci.* **20**, 36 (1973).
- [465] S. Z. D. Cheng, M. Y. Cao, and B. Wunderlich, *Macromolecules* **19**, 1868 (1986).
- [466] R. N. Simons, in *Coplanar Waveguide Circuits, Components, and Systems* (John Wiley & Sons, Inc., 2002) pp. 112–126.
- [467] *TX-LINE: Transmission Line Calculator* (2014).
- [468] B. E. Argyle, E. Terrenzio, and J. C. Slonczewski, *Phys. Rev. Lett.* **53**, 190 (1984).
- [469] J. Slonczewski, *J. Magn. Magn. Mater.* **12**, 108 (1979).
- [470] D. L. Huber, *J. Appl. Phys.* **53**, 1899 (1982).
- [471] A. R. Völkel, G. M. Wysin, F. G. Mertens, A. R. Bishop, and H. J. Schnitzer, *Phys. Rev. B* **50**, 12711 (1994).
- [472] J. P. Park, P. Eames, D. M. Engebretson, J. Berezovsky, and P. A. Crowell, *Phys. Rev. B* **67**, 020403 (2003).
- [473] V. Novosad, F. Y. Fradin, P. E. Roy, K. S. Buchanan, K. Y. Guslienko, and S. D. Bader, *Phys. Rev. B* **72**, 024455 (2005).
- [474] K. Y. Guslienko, X. F. Han, D. J. Keavney, R. Divan, and S. D. Bader, *Phys. Rev. Lett.* **96**, 067205 (2006).
- [475] O. V. Sukhostavets, J. M. Gonzalez, and K. Y. Guslienko, *Appl. Phys. Express* **4**, 065003 (2011).
- [476] H. Min, R. D. McMichael, J. Miltat, and M. D. Stiles, *Phys. Rev. B* **83**, 064411 (2011).
- [477] A. Drews, B. Krüger, G. Selke, T. Kamionka, A. Vogel, M. Martens, U. Merkt, D. Möller, and G. Meier, *Phys. Rev. B* **85**, 144417 (2012).
- [478] Y. Liu, H. Li, Y. Hu, and A. Du, *J. Appl. Phys.* **112**, 093905 (2012).
- [479] S. O. Parreiras, G. B. M. Fior, F. Garcia, and M. D. Martins, *J. Appl. Phys.* **114**, (2013).
- [480] P. E. Roy, *Appl. Phys. Lett.* **102**, 162411 (2013).
- [481] C. Andreas, A. Kákay, and R. Hertel, *Phys. Rev. B* **89**, 134403 (2014).
- [482] A. Puzic, B. Van Waeyenberge, K. W. Chou, P. Fischer, H. Stoll, G. Schutz, T. Tyliczszak, K. Rott, H. Bruckl, G. Reiss, I. Neudecker, T. Haug, M. Buess, and C. H. Back, *J. Appl. Phys.* **97**, 10E704 (2005).
- [483] K. W. Chou, A. Puzic, H. Stoll, D. Dolgos, G. Schutz, B. Van Waeyenberge, A. Vansteenkiste, T. Tyliczszak, G. Woltersdorf, and C. H. Back, *Appl. Phys. Lett.* **90**, 202505 (2007).

-
- [484] J.-Y. Lee, K.-S. Lee, S. Choi, K. Y. Guslienko, and S.-K. Kim, *Phys. Rev. B* **76**, 184408 (2007).
- [485] A. Vansteenkiste, J. De Baerdemaeker, K. W. Chou, H. Stoll, M. Curcic, T. Tyliczszak, G. Woltersdorf, C. H. Back, G. Schütz, and B. Van Waeyenberge, *Phys. Rev. B* **77**, 144420 (2008).
- [486] R. L. Compton, T. Y. Chen, and P. A. Crowell, *Phys. Rev. B* **81**, 144412 (2010).
- [487] J.-S. Kim, O. Boulle, S. Verstoep, L. Heyne, J. Rhensius, M. Kläui, L. J. Heyderman, F. Kronast, R. Mattheis, C. Ulysse, and G. Faini, *Phys. Rev. B* **82**, 104427 (2010).
- [488] T. Kamionka, M. Martens, A. Drews, B. Krüger, O. Albrecht, and G. Meier, *Phys. Rev. B* **83**, 224424 (2011).
- [489] T. Y. Chen, A. T. Galkiewicz, and P. A. Crowell, *Phys. Rev. B* **85**, 180406 (2012).
- [490] T. Ohkochi, A. Yamaguchi, M. Kotsugi, H. Hata, M. Goto, Y. Nozaki, T. Nakamura, H. Osawa, and T. Kinoshita, *Jpn. J. Appl. Phys.* **51**, 128001 (2012).
- [491] H. H. Langner, L. Bocklage, T. Matsuyama, and G. Meier, *Phys. Rev. B* **87**, 064420 (2013).
- [492] M. Martens, T. Kamionka, M. Weigand, H. Stoll, T. Tyliczszak, and G. Meier, *Phys. Rev. B* **87**, 054426 (2013).
- [493] S. E. Stevenson, C. Moutafis, G. Heldt, R. V. Chopdekar, C. Quitmann, L. J. Heyderman, and J. Raabe, *Phys. Rev. B* **87**, 054423 (2013).
- [494] B. A. Ivanov, H. J. Schnitzer, F. G. Mertens, and G. M. Wysin, *Phys. Rev. B* **58**, 8464 (1998).
- [495] K. Perzmaier, M. Buess, C. H. Back, V. E. Demidov, B. Hillebrands, and S. O. Demokritov, *Phys. Rev. Lett.* **94**, 057202 (2005).
- [496] J. Raabe, C. Quitmann, C. H. Back, F. Nolting, S. Johnson, and C. Buehler, *Phys. Rev. Lett.* **94**, 217204 (2005).
- [497] M. Bolte, G. Meier, and C. Bayer, *Phys. Rev. B* **73**, 052406 (2006).
- [498] M. Bolte, G. Meier, and C. Bayer, *J. Magn. Magn. Mater.* **316**, e526 (2007).
- [499] Y. Liu, H. He, and Z. Zhang, *Appl. Phys. Lett.* **91**, (2007).
- [500] G. Shimon, A. O. Adeyeye, and C. A. Ross, *Phys. Rev. B* **87**, 214422 (2013).
- [501] B. A. Ivanov and C. E. Zaspel, *Appl. Phys. Lett.* **81**, 1261 (2002).
- [502] V. Novosad, M. Grimsditch, K. Y. Guslienko, P. Vavassori, Y. Otani, and S. D. Bader, *Phys. Rev. B* **66**, 052407 (2002).

- [503] M. Buess, R. Höllinger, T. Haug, K. Perzlmaier, U. Krey, D. Pescia, M. R. Scheinfein, D. Weiss, and C. H. Back, [Phys. Rev. Lett. **93**, 077207 \(2004\)](#).
- [504] L. Giovannini, F. Montoncello, F. Nizzoli, G. Gubbiotti, G. Carlotti, T. Okuno, T. Shinjo, and M. Grimsditch, [Phys. Rev. B **70**, 172404 \(2004\)](#).
- [505] I. Neudecker, K. Perzlmaier, F. Hoffmann, G. Woltersdorf, M. Buess, D. Weiss, and C. H. Back, [Phys. Rev. B **73**, 134426 \(2006\)](#).
- [506] I. Neudecker, F. Hoffmann, G. Woltersdorf, and C. H. Back, [J. Phys. D: Appl. Phys. **41**, 164010 \(2008\)](#).
- [507] B. Zhang, W. Wang, C. Mu, Q. Liu, and J. Wang, [J. Magn. Magn. Mater. **322**, 2480 \(2010\)](#).
- [508] K. Vogt, O. Sukhostavets, H. Schultheiss, B. Obry, P. Pirro, A. A. Serga, T. Sebastian, J. Gonzalez, K. Y. Guslienko, and B. Hillebrands, [Phys. Rev. B **84**, 174401 \(2011\)](#).
- [509] R. Antos, Y. Otani, and J. Shibata, [J. Phys. Soc. Jpn. **77**, 031004 \(2008\)](#).
- [510] N. Vukadinovic, [J. Magn. Magn. Mater. **321**, 2074 \(2009\)](#).
- [511] S.-K. Kim, Y.-S. Choi, K.-S. Lee, K. Y. Guslienko, and D.-E. Jeong, [Appl. Phys. Lett. **91**, 082506 \(2007\)](#).
- [512] B. Van Waeyenberge, A. Puzic, H. Stoll, K. W. Chou, T. Tyliczszak, R. Hertel, M. Fahnle, H. Bruckl, K. Rott, G. Reiss, I. Neudecker, D. Weiss, C. H. Back, and G. Schutz, [Nature **444**, 461 \(2006\)](#).
- [513] K.-S. Lee, K. Y. Guslienko, J.-Y. Lee, and S.-K. Kim, [Phys. Rev. B **76**, 174410 \(2007\)](#).
- [514] A. Vansteenkiste, K. W. Chou, M. Weigand, M. Curcic, V. Sackmann, H. Stoll, T. Tyliczszak, G. Woltersdorf, C. H. Back, G. Schutz, and B. Van Waeyenberge, [Nat. Phys. **5**, 332 \(2009\)](#).
- [515] R. Feldkeller, [Z. Angew. Physik **19**, 530 \(1965\)](#).
- [516] W. Döring, [J. Appl. Phys. **39**, 1006 \(1968\)](#).
- [517] A. Thiaville, J. M. García, R. Dittrich, J. Miltat, and T. Schrefl, [Phys. Rev. B **67**, 094410 \(2003\)](#).
- [518] S. Da Col, S. Jamet, N. Rougemaille, A. Locatelli, T. O. Mendes, B. S. Burgos, R. Afid, M. Darques, L. Cagnon, J. C. Toussaint, and O. Fruchart, [Phys. Rev. B **89**, 180405 \(2014\)](#).
- [519] A. Tseng, K. Chen, C. Chen, and K. Ma, [IEEE Trans. Electron. Packag. Manufact. **26**, 141 \(2003\)](#).
- [520] G. S. Smith, [Eur. J. Phys. **35**, 025002 \(2014\)](#).

-
- [521] T. J. Silva, C. S. Lee, T. M. Crawford, and C. T. Rogers, *J. Appl. Phys.* **85**, 7849 (1999).
- [522] J.-H. Moon, D.-H. Kim, M. H. Jung, and K.-J. Lee, *Phys. Rev. B* **79**, 134410 (2009).
- [523] N. Setter, D. Damjanovic, L. Eng, G. Fox, S. Gevorgian, S. Hong, A. Kingon, H. Kohlstedt, N. Y. Park, G. B. Stephenson, I. Stolitchnov, A. K. Taganstev, D. V. Taylor, T. Yamada, and S. Streiffer, *J. Appl. Phys.* **100**, (2006).
- [524] H. Schmid, *Ferroelectrics* **162**, 317 (1994).
- [525] P. W. Forsbergh, *Phys. Rev.* **76**, 1187 (1949).
- [526] W. J. Merz, *Phys. Rev.* **95**, 690 (1954).
- [527] T. H. E. Lahtinen, J. O. Tuomi, and S. van Dijken, *Adv. Mater.* **23**, 3187 (2011).
- [528] T. Lahtinen, J. Tuomi, and S. van Dijken, *IEEE Trans. Magn.* **47**, 3768 (2011).
- [529] A. Hubert, *IEEE Trans. Magn.* **15**, 1251 (1979).
- [530] E. Soergel, *Appl. Phys. B* **81**, 729 (2005).
- [531] K. J. A. Franke, D. López González, S. J. Hämäläinen, and S. van Dijken, *Phys. Rev. Lett.* **112**, 017201 (2014).
- [532] B. Lilley, *Philos. Mag. Series 7* **41**, 792 (1950).
- [533] K. J. A. Franke, private communications (2014).
- [534] F. Brandl, K. Franke, T. Lahtinen, S. van Dijken, and D. Grundler, *Solid State Commun.*, (2014).
- [535] V. S. Semenov, *Phys. Status Solidi A* **103**, K51 (1987).
- [536] B. S. Salmons, D. R. Katz, and M. L. Trawick, *Ultramicroscopy* **110**, 339 (2010).
- [537] N. D. Follin, K. D. Taylor, C. J. Musalo, and M. L. Trawick, *Rev. Sci. Instrum.* **83**, (2012).
- [538] W. Zhou, R. Apkarian, Z. Wang, and D. Joy, in *Scanning Microscopy for Nanotechnology*, edited by W. Zhou and Z. Wang (Springer New York, 2007) pp. 1–40–.
- [539] H. P. Oepen and J. Kirschner, *Scanning Microsc.* **5**, 1 (1991).
- [540] I. M. Bronshtein and S. S. Denisov, *Sov. Phys.-Solid State* **9**, 731 (1967).
- [541] I. M. Bronshtein and V. A. Dolinin, *Sov. Phys.-Solid State* **9**, 2133 (1968).
- [542] J. Cazaux, *J. Microsc.* **214**, 341 (2004).
- [543] J. Cazaux, *J. Microsc.* **217**, 16 (2005).

- [544] J. Cazaux, *J. Electron Microsc.* **61**, 261 (2012).
- [545] A. S. Sidorkin, *J. Adv. Dielectr.* **02**, 1230013 (2012).
- [546] Q. Zhang and W. A. Goddard, *Appl. Phys. Lett.* **89**, (2006).
- [547] R. C. Rogan, N. Tamura, G. A. Swift, and E. Ustundag, *Nat. Mater.* **2**, 379 (2003).
- [548] A. Pramanick, J. L. Jones, G. Tutuncu, D. Ghosh, A. D. Stoica, and K. An, *Sci. Rep.* **2**, (2012).
- [549] H. T. Chen, Y. Ni, and A. K. Soh, *J. Appl. Phys.* **113**, (2013).
- [550] B. Ertuğ, *Am. J. Eng. Res.* **02**, 01 (2013).
- [551] D. O. Smith, M. S. Cohen, and G. P. Weiss, *J. Appl. Phys.* **31**, 1755 (1960).
- [552] J. Chen and J. L. Erskine, *Phys. Rev. Lett.* **68**, 1212 (1992).
- [553] A. Berger, U. Linke, and H. P. Oepen, *Phys. Rev. Lett.* **68**, 839 (1992).
- [554] A. Biermanns, U. Pietsch, J. Grenzer, A. Hanisch, S. Facsko, G. Carbone, and T. H. Metzger, *J. Appl. Phys.* **104**, (2008).
- [555] Q.-f. Zhan, S. Vandezande, C. Van Haesendonck, and K. Temst, *Appl. Phys. Lett.* **91**, (2007).
- [556] W. Oepts, R. Coehoorn, J. C. S. Kools, and W. J. M. de Jonge, *J. Magn. Magn. Mater.* **218**, 114 (2000).
- [557] J. H. Wolfe, R. K. Kawakami, W. L. Ling, Z. Q. Qiu, R. Arias, and D. L. Mills, *J. Magn. Magn. Mater.* **232**, 36 (2001).
- [558] R. Moroni, D. Sekiba, F. Buatier de Mongeot, G. Gonella, C. Boragno, L. Mattera, and U. Valbusa, *Phys. Rev. Lett.* **91**, 167207 (2003).
- [559] F. Bisio, R. Moroni, F. Buatier de Mongeot, M. Canepa, and L. Mattera, *Phys. Rev. Lett.* **96**, 057204 (2006).
- [560] S. J. Steinmuller, C. A. F. Vaz, V. Ström, C. Moutafis, D. H. Y. Tse, C. M. Gürtler, M. Kläui, J. A. C. Bland, and Z. Cui, *Phys. Rev. B* **76**, 054429 (2007).
- [561] J. Fassbender, T. Strache, M. O. Liedke, D. Markó, S. Wintz, K. Lenz, A. Keller, S. Facsko, I. Mönch, and J. McCord, *New J. Phys.* **11**, 125002 (2009).
- [562] Y. Fukuma, Z. Lu, H. Fujiwara, G. J. Mankey, W. H. Butler, and S. Matsunuma, *J. Appl. Phys.* **106**, (2009).
- [563] J. Briones, F. Montaigne, D. Lacour, G. Lengaigne, S. Girod, and M. Hehn, *Appl. Phys. Express* **3**, 073002 (2010).

-
- [564] K. Chen, R. Frömter, S. Rössler, N. Mikuszeit, and H. P. Oepen, *Phys. Rev. B* **86**, 064432 (2012).
- [565] M. O. Liedke, M. Körner, K. Lenz, F. Grossmann, S. Facsko, and J. Fassbender, *Appl. Phys. Lett.* **100**, (2012).
- [566] M. O. Liedke, M. Körner, K. Lenz, M. Fritzsche, M. Ranjan, A. Keller, E. Čížmár, S. A. Zvyagin, S. Facsko, K. Potzger, J. Lindner, and J. Fassbender, *Phys. Rev. B* **87**, 024424 (2013).
- [567] M. A. Arranz, J. M. Colino, and F. J. Palomares, *J. Appl. Phys.* **115**, (2014).
- [568] E. Schlömann, *J. Appl. Phys.* **41**, 1617 (1970).
- [569] R. Arias and D. L. Mills, *Phys. Rev. B* **59**, 11871 (1999).
- [570] C. A. F. Vaz, S. J. Steinmuller, and J. A. C. Bland, *Phys. Rev. B* **75**, 132402 (2007).
- [571] N. Mikuszeit, *Streufeldinduzierte Ordnung und Anisotropie wechselwirkender Teilchen in zweidimensionalen periodischen und quasiperiodischen Anordnungen*, Ph.d. thesis, Universität Hamburg (2004).
- [572] P. A. M. Dirac, *Proc. Phys. Soc. London Sect. A* **133**, 60 (1931).
- [573] P. A. M. Dirac, *Phys. Rev.* **74**, 817 (1948).
- [574] G. 't Hooft, *Nucl. Phys. B* **79**, 276 (1974).
- [575] W. V. R. Malkus, *Phys. Rev.* **83**, 899 (1951).
- [576] K. Bendtz, D. Milstead, H.-P. Hächler, A. M. Hirt, P. Mermoud, P. Michael, T. Sloan, C. Tegner, and S. B. Thorarinnsson, *Phys. Rev. Lett.* **110**, 121803 (2013).
- [577] D. J. P. Morris, D. A. Tennant, S. A. Grigera, B. Klemke, C. Castelnovo, R. Moessner, C. Czternasty, M. Meissner, K. C. Rule, J.-U. Hoffmann, K. Kiefer, S. Gerischer, D. Slobinsky, and R. S. Perry, *Science* **326**, 411 (2009).
- [578] T. Fennell, P. P. Deen, A. R. Wildes, K. Schmalzl, D. Prabhakaran, A. T. Boothroyd, R. J. Aldus, D. F. McMorrow, and S. T. Bramwell, *Science* **326**, 415 (2009).
- [579] S. Ladak, D. E. Read, G. K. Perkins, L. F. Cohen, and W. R. Branford, *Nat. Phys.* **6**, 359 (2010).
- [580] N. Mikuszeit, S. Meckler, R. Wiesendanger, and R. Miranda, *Phys. Rev. B* **84**, 054404 (2011).
- [581] E. Y. Tsybal, *Appl. Phys. Lett.* **77**, 2740 (2000).
- [582] B. Osgood, ed., *The Fourier Transform and its Applications* (Electrical Engineering Department Stanford University, 2007).

- [583] K. Weltner, S. John, W. Weber, P. Schuster, and J. Grosjean, in *Mathematics for Physicists and Engineers* (Springer Berlin Heidelberg, 2014) pp. 229–248–.
- [584] *Mathematica*, Wolfram Research, Inc., Champaign, Illinois, version 9.0 ed. (2012).
- [585] I. Bronstein and K. Semendjajew, eds., *Taschenbuch der Mathematik*, Vol. 13 (Verlag Harri Deutsch, Frankfurt (Main) und Zürich, 1973).
- [586] X. Liu, M. M. Steiner, R. Sooryakumar, G. A. Prinz, R. F. C. Farrow, and G. Harp, *Phys. Rev. B* **53**, 12166 (1996).
- [587] J. Hamrle, O. Gaier, S.-G. Min, B. Hillebrands, Y. Sakuraba, and Y. Ando, *J. Phys. D: Appl. Phys.* **42**, 084005 (2009).
- [588] M. Caruso, in *IEEE 2000 Position Location and Navigation Symposium* (2000) pp. 177–184.
- [589] K. Sato, I. Okamoto, Y. Kitamoto, and S. Ishida, *Jpn. J. Appl. Phys.* **46**, 5139 (2007).
- [590] P. Cizmar, A. E. Vladár, and M. T. Postek, *Microsc. Microanal.* **17**, 302 (2011).
- [591] P. Olivero, S. Rubanov, P. Reichart, B. C. Gibson, S. T. Huntington, J. Rabeau, A. D. Greentree, J. Salzman, D. Moore, D. N. Jamieson, and S. Prawer, *Adv. Mater.* **17**, 2427 (2005).
- [592] R. Behrisch and W. Eckstein, eds., *Sputtering by Particle Bombardment* (Springer Berlin / Heidelberg, 2007).
- [593] M. P. Seah, C. A. Clifford, F. M. Green, and I. S. Gilmore, *Surf. Interface Anal.* **37**, 444 (2005).
- [594] M. Seah, *Nucl. Instrum. Methods* **229**, 348 (2005).

Publications

Published

Stefan Rößler, Sebastian Hankemeier, Benjamin Krüger, Felix Balhorn, Robert Frömter, and Hans Peter Oepen, “Nonadiabatic spin-transfer torque of magnetic vortex structures in a permalloy square”, *Phys. Rev. B*, **89**, 174426 (2014)

Marietta Seifert, Ludwig Schultz, Rudolf Schäfer, Volker Neu, Sebastian Hankemeier, Stefan Rössler, Robert Frömter, and Hans Peter Oepen, “Domain evolution during the spin-reorientation transition in epitaxial NdCo 5 thin films”, *New Journal of Physics*, **15**, 013019 (2013)

Björn Beyersdorff, Sebastian Hankemeier, Stefan Rößler, Yuliya Stark, Germar Hoffmann, Robert Frömter, Hans Peter Oepen, and Benjamin Krüger, “Thermal effects in spin-torque assisted domain wall depinning”, *Phys. Rev. B*, **86**, 184427 (2012)

Kai Chen, Robert Frömter, Stefan Rössler, Nikolai Mikuszeit, and Hans Peter Oepen, “Uniaxial magnetic anisotropy of cobalt films deposited on sputtered MgO(001) substrates”, *Phys. Rev. B*, **86**, 064432 (2012)

In Preparation

Arianna Casiraghi, Teresa Rincón Domínguez, Stefan Rößler, Kévin J. A. Franke, Sampo J. Hämäläinen, Hans Peter Oepen, and Sebastiaan van Dijken, “Influence of elastically pinned domain walls on the magnetization reversal process in a multiferroic heterostructure”, *Phys. Rev. B* (2014)

Edna C. Corredor, José I. Arnaudas, Miguel Ciria, Fabian Lofink, Stefan Rößler, Robert Frömter, and Hans Peter Oepen, “Strain-induced spin reorientation of bcc-like iron films grown on Cu(001)”, *Phys. Rev. B* (2014)

Conference Contributions

Robert Frömter, Stefan Rössler, Fabian Kloodt, Demetrio R. Cavicchia, Lars Bocklage, and Hans Peter Oepen, “Incorporating Nanosecond Time Resolution into Scanning Electron Microscopy with Polarization Analysis”, *59th Annual Magnetism & Magnetic Materials Conference, Honolulu, Hawaii* (2014)

Stefan Roessler, Sebastian Hankemeier, Benjamin Krueger, Felix Balhorn, Robert Froemter, and Hans Peter Oepen, “Determination of all Spin-Transfer-Torque Parameters for a Magnetic Vortex in Permalloy”, [IEEE International Magnetism Conference INTERMAG, Dresden, Germany \(2014\)](#)

Marietta Seifert, Ludwig Schultz, Rudolf Schaefer, Volker Neu, Sebastian Hankemeier, Stefan Roessler, Robert Froemter, and Hans Peter Oepen, “Observation of the domain evolution during the spin-reorientation transition in epitaxial NdCo₅ thin films”, [IEEE International Magnetism Conference INTERMAG, Dresden, Germany \(2014\)](#)

Stefan Rößler, “Investigating the domain structure of magnetic thin-film elements with SEMPA” [READi Workshop, Hamburg, Germany \(2014\)](#)

Stefan Rößler, “Time-resolved SEMPA” [SFB 668 Seminar, Hamburg, Germany \(2013\)](#)

Stefan Rößler, Sebastian Hankemeier, Robert Frömter, Hans Peter Oepen, and Benjamin Krüger “Determination of the nonadiabatic spin transfer torque parameter via SEMPA investigations”, [Spring Meeting of the German Physical Society DPG, Berlin, Germany \(2012\)](#)

Stefan Rößler, Sebastian Hankemeier, Robert Frömter, and Hans Peter Oepen, “Different Methods for the Investigation of a Substrate Induced Uniaxial Anisotropy”, [Spring Meeting of the German Physical Society DPG, Dresden, Germany \(2011\)](#)

Stefan Rößler, Sebastian Hankemeier, Robert Frömter, and Hans Peter Oepen, “Effect of substrate morphology on magnetic anisotropy and domain-structure”, [Spring Meeting of the German Physical Society DPG, Regensburg, Germany \(2010\)](#)

Acknowledgement

Sincere thanks to all who contributed to this book and supported me during the last years. In particular I would like to thank:

Prof. Hans Peter Oepen for giving me the opportunity to conduct this thesis in his group at the Institute of Applied physics in Hamburg and for providing me with the funds and machines (especially SEMPA) that were so essential for my research. I would also like to thank him for many fruitful discussions and his profound help in writing scientific publications.

Prof. André Thiaville for reading the manuscript and providing an assessment about it. I am also grateful for his fundamental work in including the current-induced effects into the Thiele equation, without which this thesis would not have been possible.

Dr. Robert Frömter for his profound supervision during the last five years at SEMPA, his solid advice regarding not only technical but also physical issues, and extensive proof-reading of this manuscript.

Dr. Sebastian Hankemeier for introducing me to the world of SEMPA and into the group.

Dr. Lars Bocklage for the good collaboration and his help with the fabrication of a stripline sample.

Dr. Benjamin Krüger for providing the results of theoretical calculations and micromagnetic simulations.

Dr. Edna C. Corredor for joining me at SEMPA and collaborating in the research of iron on copper.

Dr. Felix Balhorn for measuring the ferromagnetic resonance of our samples and helping me with its evaluation.

Dr. Nikolai Mikuszeit for his support in the calculation of magnetic charges and stray fields.

Dr. Martin Stier for giving insights into the theory of non-local spin torques.

Tim Boehne for giving me access to and helping me with the laser cutter.

Kévin J. A. Franke for visiting our lab, providing the ferroelectric samples, and supporting me during their measurement.

Axel Frauen for his excellent work during the extension of the machine for time-resolved SEMPA.

Fabian Kloodt for greatly contributing to the project of time-resolved SEMPA and for coding the measurement software.

Dr. André Kobs for his elaborate proof-reading and solid advice and for jointly supporting our team during the 2014 world championship.

Dr. Fabian Lofink for supporting our mutual spin-injection project and his advice regarding SEMPA.

Jim Duden for providing AFM measurements.

Mahmoud Reza Rahbar Azad for his extensive help regarding MATHEMATICA.

Gerrit Winkler for a good collaboration during many years of studies.

Carsten Thönnißen for supporting me in repairing the Philips SEM.

Dr. Matthias Hille for always having an idea about what to do after a good meal.

Björn Beyersdorff for providing some FIB structures and for having a jointly good time at the beach-volleyball facilities.

Demetrio R. Cavicchia for bringing the italian spirit into the group and taking over the SEMPA project.

Alexander Neumann for his help with the calculation of sputtering yields and for providing citations regarding the thermal switching of nanoparticles.

Judith Bach for her creative ideas about how to improve things.

Philipp Staeck for expanding into the world of MTJs and for always having a funny story to tell.

Barend Jonathan Jacobsohn for spelling corrections and interesting nights of table tennis.

Brigitte Muhlack and Sonja Hesselmann for caring for the infrastructure of our group.

Wolfgang Pfützner for technical support.

Dr. Moritz Bubek for his unhesitating support not only regarding practical work but also L^AT_EX.

Stephanie Baer for her profound help concerning all bureaucratic issues.

All other former and current members of the “Surface Science Physics” group in Hamburg.

Johannes Friedlein for sharing information about time-resolved measurements.

Falk Stein, Matthias Pues, Josef Grenz, Manuel Steinbrecher, Bernhard Bugenhagen, and all other Members of the SFB 668 for fruitful discussions.

Sabine Hilger and Manuela Doose for providing me with numerous books and publications.

Horst Biedermann and his crew of the electronic shop for his invaluable help with the construction and repair of electronic devices.

Rolf-Peter Benecke, Jens Path, and their crew of the mechanical shop for their help in the adjustment, extension, and development of experimental setups.

The “Deutsche Forschungsgemeinschaft” for funding via SFB 668.

Christopher Preuß and Andreas Rathjen for offering a filling station for good mood.

My close family, especially Veronika Hierl, Claus Rößler, and Sabine Engelhardt for their enduring support during all the years of studying.

Lara August and Luna for a wonderful time, proof-reading of the manuscript, and teaching me everything I need to know about horsemanship.



Within this thesis, static and dynamic states in magnetic systems of reduced dimensions are investigated by means of the advanced magnetic imaging technique “scanning electron microscopy with polarization analysis” (SEMPA). After a short introductory overview of the historical development of storage media, its current status is described with a focus on random access memory (RAM). The basic concepts of modern non-volatile storage devices based on magnetism are introduced and the physical mechanisms behind the phenomena that are used to manipulate and access the data are discussed. Magnetic imaging is a powerful, yet illustrative tool to further explore the physics behind these mechanisms. After a short overview of the history and current status of magnetic imaging techniques, the working principle of SEM-

PA is explained. The imaging capabilities of SEMPA are used to investigate the current-driven stationary displacement of a magnetic vortex core confined in a square permalloy element. The full set of spin-transfer torque parameters is obtained from the measurement. In the course of the investigation, the physical origin of the nonadiabatic contribution ($\beta = 0.12 \pm 0.02$) is explored. It is shown to consist of one component that depends on the intrinsic properties of the material (29%) and one component that depends on the divergence of the magnetic texture (71%).

A concept for enhancing the temporal resolution of SEMPA into the regime of one nanosecond is presented. The feasibility of the concept is proven by observing the gyration of a magnetic vortex core that is excited by a high-frequency field ($f = 70$ MHz). From the elliptical shape of the movement pattern, the resonance frequency of the square permalloy element that contains the vortex core is derived.

In another project of this thesis, the interplay between ferromagnetic and ferroelectric domain walls is investigated. In 20 nm thick $\text{Co}_{40}\text{Fe}_{40}\text{B}_{20}$ on BaTiO_3 , the ferromagnetic domain walls are pinned on top of the ferroelectric ones. Two types of magnetic 90° domain walls are identified: Charged walls are created after an external field was applied parallel to the ferroelectric domain walls. When the field is applied perpendicular to the ferroelectric domain walls, uncharged walls are created. The width of both wall types is compared with SEMPA. The width is found to be enhanced by 500% for the charged walls (~ 770 nm) compared to the uncharged walls (~ 150 nm).

The thesis concludes with a theoretical chapter in which the uniaxial anisotropy is derived that emerges when a magnetic film is prepared on top of a rippled substrate. The strength of the anisotropy is calculated for an alignment of the magnetization along the hard in-plane axis, perpendicular to the ripple pattern. Two magnetic configurations are considered: In the wavy configuration, the local magnetization follows the ripple structure of the film. In the uniform configuration, a rigid magnetization is present. A thickness-dependent transition between both states is identified. The results are compared to experimental studies.

ISBN 978-3-8440-3523-0



9

783844

035230